CYPRUS UNIVERSITY OF TECHNOLOGY

FACULTY OF ENGINEERING AND TECHNOLOGY

PhD Thesis

THERMAL ANALYSIS OF NATURALLY VENTILATED BIPV SYSTEMS

Agathokleous Rafaela

Limassol, November 2017

CYPRUS UNIVERSITY OF TECHNOLOGY

FACULTY OF ENGINEERING AND TECHNOLOGY

DEPARTMENT OF MECHANICAL ENGINEERING AND MATERIALS SCIENCE ENGINEERING

PhD Thesis

THERMAL ANALYSIS OF NATURALLY VENTILATED BIPV SYSTEMS

by

Agathokleous Rafaela

Limassol, November 2017

FORM FOR APPROVAL

PhD Thesis

Thermal Analysis of Naturally Ventilated BIPV systems

by

Rafaela Agathokleous

Supervisor: Prof. Soteris Kalogirou

Cyprus University of Technology

Limassol, November 2017

Acknowledgements

I would like to thank my thesis supervisor Professor Soteris Kalogirou for his expert guidance. His dedication in research and his expertise in the energy field has been a source of motivation during this work. I want also to thank him for giving me the opportunity to work in this field through several projects and participate in various conferences in Europe.

Besides my advisor, I would also like to acknowledge Professor Tasos Georgiades who supported me and all the PhD students of the department through these years.

I would also like to thank my parents for their continuous support and encouragement.

Copyright

The approval of the report by the Department of Mechanical Engineering and Science Cyprus University of Technology Engineering Materials not necessarily implies acceptance of the views of the author by the Department.

Abstract

The aim of this study is to investigate the thermal behaviour of naturally ventilated BIPV systems. This study focuses on the systems with natural ventilation because it is believed that there is a good potential to improve their performance with design configurations, in order to provide sufficient ventilation to circulate the air and avoid the use of a fan with extra cost, noise and maintenance requirements. The ultimate goal is to estimate the convective heat transfer coefficients in all sections of a BIPV system.

An extensive experimental analysis is carried out in outdoor environmental conditions and in indoor controlled conditions with the use of a solar simulator. It was pointed out that the air exits the duct at around 10^{o}C hotter than it enters and for this reason the PV's temperature increases from the bottom to the top. Regarding the inclination angles tested, it is observed that the system develops higher temperature when is inclined at 30^{o} and less when is placed vertically (90^{o}). Subsequently, an analysis of the natural convection is carried out using fundamental convection equations and as a result, two correlations for the estimation of the convective heat transfer coefficients (CHTC) are extracted for the first time. These can be applied to estimate the CHTC in the air gap between the PV panels and the outer skin of the building, in double skin BIPV systems, for windy and no windy conditions. Afterwards, a 3D computational fluid dynamic (CFD) model was built in COMSOL Multiphysics and it is validated with the experimental results. The general conclusion is that the experimental results were in a good agreement with the simulation results.

Additionally, based on the measured temperature distribution of the system from the experimental procedures, energy and exergy analyses are carried out and the correlations for the estimation of the energy and exergy efficiencies are presented for the first time for a naturally ventilated BIPV system. The energy efficiency of the system is estimated to be up to 26.5-33.5% while the exergy efficiency is estimated to be between 13-16%.

Finally, the gained knowledge is applied to a real BIPV demonstration system. A building simulation model is carried out to predict the temperature of the PV panels and the energy production of the system for one year. A good agreement is observed between the calculated and measured data.

Table of Contents

List of Tables

List of Figures

Abbreviations

AM:	Air Mass
ASEL:	Archimedes Solar Energy Laboratory
BAPV:	Building Applied Photovoltaics
BIPV/T:	Building Integrated Photovoltaic/Thermal
BIPV:	Building Integrated Photovoltaics
BISTS:	Building Integrated Solar Thermal System
CFD:	Computational Fluid Dynamics
CHTC:	Convective heat transfer coefficients
CPD:	Construction Product Directive
CPU:	Central Processing Unit
DC:	Direct Current
DOF:	Degrees of Freedom
DSF:	Double Skin Facades
DSVF:	Double Skin Ventilated Façade
EU:	European Union
FEM:	Finite Element Method
FF:	Fill Factor
GUI:	Graphical User Interface
HVAC:	Heating Ventilation Air Conditioning
IR:	Infrared
MVF:	Mechanically Ventilated Facade
NOCT:	Nominal Operating Cell Temperature
NVF	Naturally Ventilated Façade
NZEB:	Nearly Zero Energy Building
OJVF:	Open Joints Ventilated Facade
PCM:	Phase Change Materials
PDEs:	Partial Differential Equations
PIV:	Particle Image Velocimetry
PRE:	Percentage Relative Error
PSP:	Precision Spectral Pyranometer
PV/T:	Photovoltaic/Thermal

PV:	Photovoltaics
RANS:	Reynolds Averaged Navier Stokes
RES:	Renewable Energy Systems
SE:	Standard Error
SS conditions:	Steady State conditions
SS:	Solar Simulator
STC:	Standard Test Conditions
TAS:	Thermal Analysis Simulations
TMY:	Typical Meteorological Year
TR:	Transient
TRNSYS:	Transient System Simulations
UTC:	Unglazed Transpired Solar Collectors
ZEB:	Zero Energy Building

Nomenclature

English Symbols:

A_c:	Cross sectional area (m^2)
C_p:	Specific heat capacity under constant pressure (kJ/kg K)
d:	Spacing of the channel (m)
D:	Tube diameter (m)
$D_{h:}$	Hydraulic diameter of a non-circular tube (m)
E:	Exergy rate (W)
g:	Acceleration due to gravity (m/s^2)
Gr:	Grashof number
G:	Solar Irradiance (W/m^2)
h:	Heat transfer coefficient (W/m^2 °C)
H:	System's height (m)
I:	Current (A)
k:	Thermal conductivity (W/mK)
L:	System's length (m)
m:	Mass flow rate (kg/s)
Nu:	Nusselt number
P:	Power output (W)
p:	Perimeter (m)
Pr:	Prandlt number
$\dot{Q}$:	Rate of heat transfer (W)
Ra:	Rayleigh number
Re:	Reynolds number
T:	Temperature (°C)
U, u:	Velocity (m/s)
V:	Voltage (V)

Greek Symbols:

α:	Thermal diffusivity (m^2/s)
β:	Volumetric thermal expansion coefficient (1/K)
η:	Efficiency

μ:	Dynamic viscosity (N s/m^2)
ρ:	Fluid density (kg/m^3)
v:	Kinematic viscosity (m^2/s)

Subscripts and superscripts:

amb:	Ambient
ave:	Average
b:	Bottom
c:	Convective
ch:	Channel
crit:	Critical
e:	Exit
en:	Energy or energetic
est:	Estimated
exp:	Experimental
ex:	Exergy or exergetic
f:	Fluid
h:	Hydraulic
i:	Inlet or inside
m:	Middle
meas:	Measured
mp:	Maximum power
o:	Outlet or outside
oc:	Open circuit
opt:	Optimum
s:	Surface
sc:	Short circuit current
surr:	Surroundings
t:	Top
th:	Thermal
w:	Wall

CHAPTER 1

1 Introduction

The population growth, the exclusive reliance on oil for the energy needs, the relatively high cost of electricity, the reasonable high level of technology and the population acceptance of renewable energy sources, make the renewable energy technologies extremely viable from a technical, social and economic point of view.

As the energy crisis escalates and the fossil fuel resources are being depleted, the price of gas and electricity will increase. Therefore, there is an inevitable shift to renewable energy and especially solar energy which can be considered to be a unique opportunity to create new clean energy economy.

1.1 Solar Energy

As Friedman (2008) said, “The Stone Age didn’t end because we ran out of stones”, likewise the age of the oil will not end because we will run out of oil; it will end because we have better alternatives.

It is well known that fossil fuel reserves are finite, it's only a matter of time when they run out, not if they will run out. There are however, others who believe that coal reserves are enough to cover the next hundreds of years without problem. The situation with oil and natural gas is worse as the available reserves with current rate of consumption will last about 55 years. The point is that, sooner or later, fossil fuels resources are going to either be depleted or become very limited and thus too expensive

to use. Consequently, people should start using alternative source of energy. Such a source could be any renewable source of energy like wind, sun, water etc. It is easy in theory to shift from fossil fuels to renewables but in reality, this is very complicated because humans rely so much on the infrastructure developed, which is entirely based on fossil fuels. It is not simple to just stop using fossil fuels when they become expensive. The shift to alternatives should be done in a planned manner.

Another reason to start using alternative sources of energy is the effect that conventional sources have on climate change. Again, scientists are separated to those who support the idea of the climate change and those who don't. However, it is mostly believed that the climate is changing and that fossil fuel emissions have a significant contribution to that change. In contrast, solar energy panels and wind turbines do not produce any emissions in the process of electricity generation. Nevertheless, the manufacturing process of the solar panels or wind turbines, is entirely reliant on fossil fuels. Therefore, society can benefit not only from shifting power generation to renewables, but it can also benefit from shifting the manufacturing systems to rely on renewables.

Solar energy was a main topic of interest in many articles published in the past. This means that it was known for many years that sun's energy must be exploited in order to have better future with clean environment and free energy. Thomas Edison in 1931 said "I'd put my money on the sun and solar energy. What a source of power! I hope we don't have to wait until oil and coal run out before we tackle that" (Famous Quotations, 2014).

Solar energy is an important input of almost every life process, if not all life processes. In the future, solar energy may be the primary form of energy. This could lead to a clean environment, a cheap energy source, and a healthier world.

Brown (2009) and Thomas (2001) wrote that just as the nineteenth century belonged to coal and the twentieth century to oil, the twenty-first century belongs to the sun, the wind and the energy within the earth.

1.2 Solar Energy Use in Buildings

Because of the increasing environmental awareness and the need to reduce the energy consumption, the demand for energy alternatives is growing. Additionally, the Renewable Energy Systems (RES) Framework Directive sets a 20% target for renewable energy utilization, 20% emissions reductions from 1990 levels, and 20% improvement in the EU's energy efficiency by 2020. These targets are known

as the "20-20-20" targets of the 2020 climate and energy package of the European Commission (European Commission, 2014a).

The motivation to improve the existing building's energy consumption lies in society's efforts towards sustainable development. The building sector has a considerable role to play in EU's energy consumption as it accounts approximately for 39% of the total energy consumption, and it is the biggest energy user, bigger than industry and road transport (Figure 1.1). Directive 2012/27/EU on energy efficiency (European Commission, 2014b) is a direct outcome of the 20-20-20 target, consequently the reduction of the energy consumed by buildings is of a great importance.

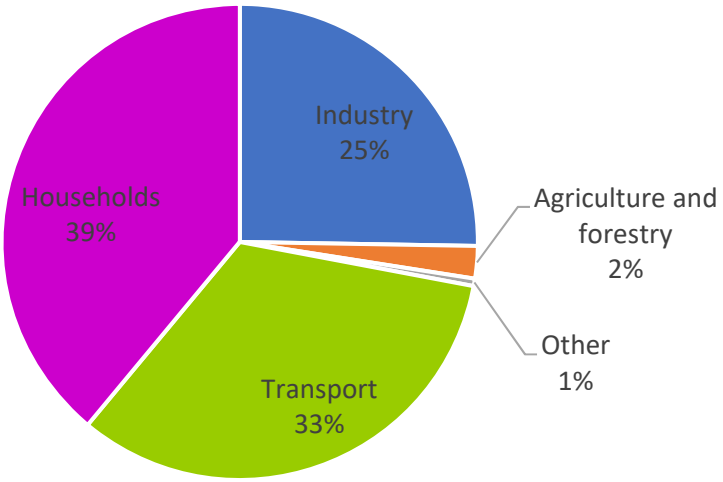

Figure 1.1. Final energy consumption, EU-28 in 2015 based on the % total on tonnes of oil equivalent (Eurostat, 2016).

Among the renewable energy sources, solar energy is the most essential and prerequisite resource of sustainable energy because of its abundance and sustainability. Especially, in the case of buildings, solar energy is the most used renewable energy rather than wind, biomass and hydropower. This is because in contrast with solar energy systems, the other energy sources cannot easily be part of the building's design, they require extra space in the building for installation and require maintenance. Solar energy systems in buildings can be added on the roof or near the building (Figure 1.2) or can be part of the building construction such as in the facades (walls, windows, roof) and other parts of the building (skylights, railing) (Figure 1.3).

Photovoltaics (PVs) and solar thermal collectors are the solar systems that are usually employed in buildings. Photovoltaic (PV) panels are used for on-site electricity production which can be sold to the grid, and solar thermal systems can supply thermal energy for space heating and provision of hot

water. Both systems can be installed on a building with brackets on a flat roof or on top of a sloping roof, or can be integrated on the building's envelope to replace conventional construction materials.

Figure 1.2. Photovoltaic panels on the roof of a building.

Figure 1.3. Photovoltaic panels on the building's facade.

1.3 PV Panels

PVs generate electricity from the sunlight and can be installed on the building or at the building, giving a new dimension to energy conscious design. PV systems have successfully been used in thousands of small scale and large scale applications. Electricity from PVs seems to be a viable and cost-effective option for many remote site applications where the cost of grid extension or maintenance of diesel engine power supply systems would be limited and expensive.

PVs are solid state devices that convert solar radiation to electricity with no moving parts, no fuel requirement and no emissions over their life cycle. In general, a PV module is an assembly of solar cells, connections, protective parts and supports. A PV cell is the basic element in the PV module that absorbs sunlight and converts it to direct current (DC) electricity. The electrical power output from a cell is very small, so multiple cells are connected and encapsulated to form a module/panel. The number of modules in series determines the system voltage while the current of the plant can be sized by parallel connection of module strings. The desired electrical power output of the system is the product of the system voltage and current. Consequently, a PV system consist of a number of PV modules which consist of PV cells connected in series or in parallel in virtually any number and combination.

Solar PV devices are made of various semiconductor materials including silicon, cadmium sulphide, cadmium telluride and gallium arsenide. The most common PV modules are silicon modules which are of the mono-crystalline silicon panels, poly-crystalline silicon panels and thin film silicon panels.

Monocrystalline silicon and polycrystalline silicon are the traditional technologies of PV panels that are used mostly in the market.

1.4 History of Photovoltaics

Humans have been harnessing the sun's power since the beginning of time. In 1767 the first solar oven was invented by the Swiss physicist Horace de Saussure.

The history of PVs starts in 1839 when the French physicist Antoine-Cesar Becquerel, who was only 19 years old, was experimenting in his father's laboratory and found that certain materials produced little amounts of voltage when exposed to light. Becquerel observed that he could produce electricity by shining sunlight on an electrolytic cell composed on an electrolyte and two electrodes (Haleakala Solar, 2014).

In 1870' professor William Grylls Adam and his student Richard Evans Day observed for the first time the generation of electrical current when selenium was exposed to light. Although it wasn't efficient enough to produce energy on its own (1-2% efficiency), it proved the phenomenon can occur naturally and could be reproduced without heat or moving parts (Haleakala Solar, 2014).

In 1880' Charles Fritts, an American inventor, made simple plans for solar cells based on selenium wafers. That was the first design of a Photovoltaic cell.

The development of PVs continued and in the 1950' David Chapin, Calvin Fuller and Gerald Pearson of Bell Laboratory patented the first solar cell capable of converting enough of the sun's energy into power to run every day electrical equipment (Haleakala Solar, 2014).

During 1960' and 1970' the cost of the PVs decreased dramatically because of the improved manufacturing processes that resulted in better quality and performance of PVs. This fact helped the PVs be of more use in low-power devices. PVs became a famous source of power for electronic devices such as radios, lanterns, calculators and other small battery-operated applications. During the energy crisis of the 70s, PV power systems began to be developed for residential and commercial uses and in the 80s the use of PVs increased for off grid house holders, telecommunications, water pumping etc., especially in remote areas where the extension of the grid is expensive (Luque and Hegedus, 2003).

In the 80s, the industry began to mature, as emphasis on manufacturing and costs grew. Manufacturing facilities for producing PV modules from Si wafer p-n junction solar cells were built in the USA, Japan, and Europe (Luque and Hegedus, 2003).

1.5 PV Energy principles

The phenomenon responsible for converting the light into electricity is the photovoltaic effect, which as indicated already was first observed by Edmund Becquerel in 1839. He observed that a voltage appeared when one of two identical electrodes in a weak conduct was illuminated. The photovoltaic effect can be described as the procedure that light, which as a form of energy, enters a PV cell and transfers enough energy to cause the movement of electrons. A built-in potential barrier in the PV cells acts on these electrons to produce voltage which can be used to circulate current through an electric circuit.

The process of light conversion to electricity, requires a material in which the absorption of light raises electrons to a higher energy state, and transfer the energy electron from the solar cell into an external circuit.

In practice, a PV cell consists of two or more thin layers of semiconducting material usually silicon in the form of p-n junction. The p-n junction occurs after doping the silicon layers with holes and electrons respectively to form the p-type and n-type layers. When the two layers are placed together, a p-n junction is created. To allow the flow of electrons, a front contact and a back contact are installed to the layers. A glass is installed at the top of it, to protect the layers from environmental damage (Figure 1.4).

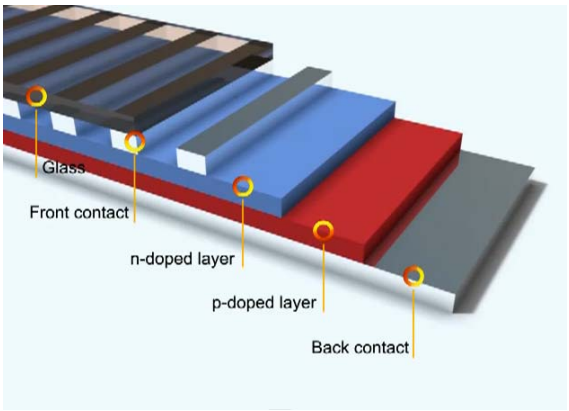

Figure 1.4. Layers of a PV cell.

In the n-type semiconductor there are electrons while in the p-type semiconductor there are positively charged electron holes (step 1 - Figure 1.5). When the two layers are in contact, the electrons from one layer finds their corresponding free hole from the other layer and an electrical field builds up. The holes from the p-type layer are then neutralized from electrons that came from the n-type layer. In this stage, electrons and holes cannot jump into the other layer again due to the electric field which is created from the positive and negative charges of the holes and electrons (step 2 - Figure 1.5).

When photons hit the silicon layers, electron-hole pairs are created and the electrons can move to the n doped layer and holes are moved to the p doped layer through the electric field. Then there is an excess of electrons in the n-doped layer and the corresponding holes are in the p-doped layer. These free electrons try to combine with the free holes but the electric field does not allow this condition (step 3- Figure 1.5).

If a wire is connected from the top layer to the other layer to form a circuit, electrons will travel through the cable to the free holes. This movement of the electrons causes the current flow (step 4- Figure 1.5).

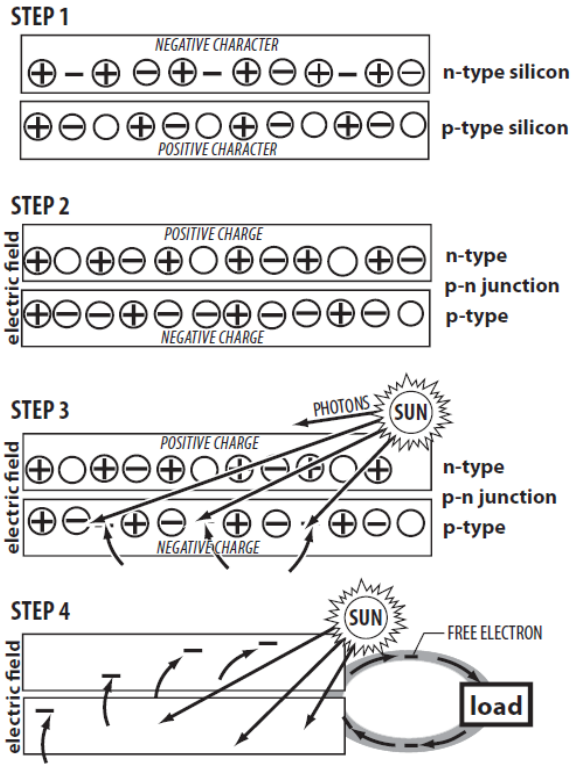

Figure 1.5.The photovoltaic effect in four steps and the current flow.

The voltage-current characteristic curve for the p-n junction diode (Figure 1.6) is described by the following Shockley diode equation (Kalogirou, 2014):

$$I_d = I_0 \left\{ exp\left(\frac{q\,V_d}{nkT}\right) - 1 \right\} \qquad 1.1$$

Where I_0 is the reverse (dark) saturation current (A), I_d is the diode current (A), V_d is the voltage across the diode terminals from the p side to the n side (V), q is the electron charge 1.602x10^{-19} Coulomb, k is the Boltzmann's constant 1.381x10^{-23} J/K, T is the junction temperature (K) and n is the ideality factor n=1 for ideal diode.

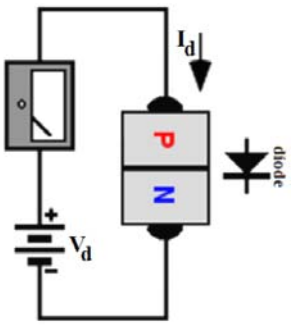

Figure 1.6. The p-n junction diode.

When light hits the solar cell, the energy of the photons generates free charge carriers (the hole electron pairs mentioned before). The power source produces the photo-electric current I_L which is proportional to the irradiance. In an ideal cell, the net circuit output I is equal to the difference between current I_L generated by the photoelectric effect and the diode current I_d according to the equation (Kalogirou, 2014):

$$I = I_L - I_d = I_L - I_0\left\{exp\left(\frac{q\,V}{nkT}\right) - 1\right\} \quad 1.2$$

For PV cells equivalent circuit, the current-voltage equation can be written as:

$$I = I_{SC} - I_d = I_{SC} - I_0\left\{exp\left(\frac{q\,V}{nkT}\right) - 1\right\} \quad 1.3$$

The open circuit voltage V_{OC} is the maximum voltage from a solar cell. The following equation shows that V_{OC} depends on the saturation current I_0 of the solar cell and the short circuit current I_{SC}:

$$V_{OC} = \frac{nkT}{q} ln\left[\frac{I_{SC}}{I_0} + 1\right] \quad 1.4$$

At cell temperature of 298 K, the current voltage equation becomes:

$$I = I_{SC} - I_0\{\exp(38.9\,V) - 1\} \quad 1.5$$

$$V_{OC} = 0.0257\; ln\left[\frac{I_{SC}}{I_0} + 1\right] \quad 1.6$$

1.6 Efficiency of PVs

As mentioned before, a PV panel is basically an assembly of solar cells, connections, protective parts and supports. The efficiency of the PV panels is mainly based on the PV cell characteristics as shown in Figure 1.7.

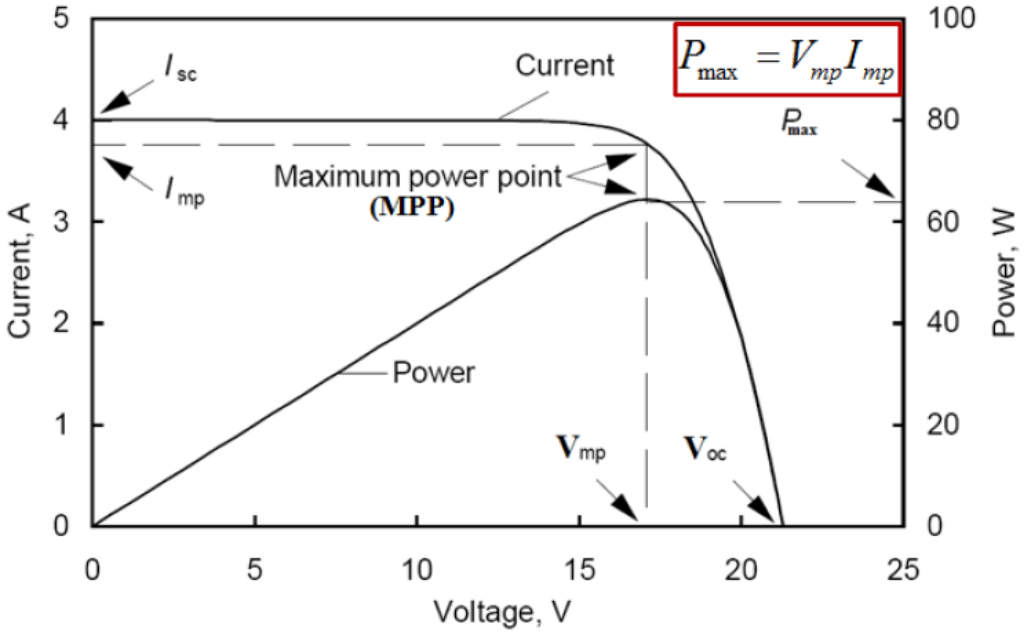

Figure 1.7. The I-V and P-V characteristics of a PV module.

In order to see the behaviour of a solar cell at certain irradiance at fixed cell temperature, the I-V characteristic curve should be obtained. The current of the PV cells depends on the external voltage applied and the amount of sunlight on the cell. When the cell is short circuited, the current is at maximum called short circuit current (I_{sc}) and the voltage across the cell is 0. When the PV cell circuit is open, with the leads not making a circuit, the voltage across the cell is at its maximum, called open circuit voltage (V_{oc}) and the current is 0. In both cases, the power output is 0 as it is defined by the Kirchhoff's law as $P = I \times V$. Between open circuit and short circuit, the power output is greater than 0.

The maximum power P_{max} *or* P_{MPP} passes from a maximum power point (MPP) at which point the load resistance is optimum and the power dissipated in the resistive load is maximum and given by $P_{max} = I_{mp} \times V_{mp}$.

The most important figure of merit of a solar cell is its power conversion efficiency given by Equation 1.7. The efficiency η is the ratio of the power delivered by the solar cell to the power of incident solar radiation or the fraction of incident power which is converted to electricity.

$$\eta = \frac{P_{MP}}{P_{in}} = \frac{FF \times V_{oc} \times I_{sc}}{A\ G} \qquad 1.7$$

Where FF is the fill factor that describes the quality of the solar cells, A is the PV surface area (m^2) and G is the solar irradiance (W/m^2).

The Fill Factor (FF) is a very important parameter of the PV performance, which describes how the I-V curve fills the rectangle that is defined by (V_{oc}) and (I_{sc}). It gives an indication of the quality of a cell's semiconductor junction and measures of how well a solar cell is able to collect the carriers generated by light. For good cells the FF value is greater than 0.7 but is always less than 1. Its value decreases as the cell temperature increases and differs from material to material. The FF can be calculated by:

$$Pmax = I_{sc} \times V_{OC} \times FF \qquad 1.8$$

Or

$$FF = \frac{P_{max}}{I_{sc} \times V_{OC}} = \frac{I_{max} \times V_{max}}{I_{sc} \times V_{OC}} \qquad 1.9$$

The maximum efficiency of the solar cells is another important parameter, which is the ratio between the maximum power and the incident light power given by:

$$\eta max = \frac{P_{max}}{P_{in}} = \frac{I_{max} \times V_{max}}{A \times G_t} \qquad 1.10$$

Efficiency is commonly reported for a PV cell temperature of 25°C and incident radiation of 1000 W/m^2 with a specified spectral distribution with an air mass of A.M=1.5. These are called Standard Test Conditions (STC) and the efficiency at the STC is given by:

$$\eta_{STC} = \frac{P_{max}}{A \times 1000 \frac{W}{m^2}} \qquad 1.11$$

The efficiency of a mono-crystalline silicon solar cell is around 14-15% and for the polycrystalline silicon solar cells the efficiency reaches 12-13%. A good knowledge of the PV systems is very important for their efficiency, correct product selection as well as for the accurate prediction of the electricity production.

1.7 Factors affecting output of PV modules

The efficiency is an important factor affecting the system design but it is also affected by many other factors. The power output of the PV systems depends on many factors such as (Thomas, 2001):

(a) Orientation, slope and elevation of the modules

PV panels deliver maximum power when they are placed to have their front surface perpendicular to the sun rays. This can be achieved in tracking systems but in most applications PVs are installed on fixed brackets because of the high cost of the trackers.

Apart from the tracking system that can ensure a perpendicular position of the panels to the sun, the slope of the panels is also very important. There are various studies carried out for many places in the world in order to obtain the optimum angle that the PVs should be placed in each country in order to collect the highest solar radiation through a year. Inclination should be 30^{o}-45^{o} from horizontal for an optimized output over the whole year but this depends on the location of the installation and the position of the sun.

Regarding the role of the orientation, the modules must be placed in an orientation that provide maximum sunlight for most time during a day. The optimum orientation is south, but a deviation of 10-15^{o} does not affect power output very much.

(b) Wiring and connection points losses

A PV system is mainly an assembly of solar cells, connections, protective parts, supports and wires.

It is observed that the maximum power output of the total PV array is always less than the sum of the maximum output of the individual panels. The power is lost due to resistance in the system wiring. These losses should be kept to a minimum but it is difficult to minimize them below 3%.

(c) Dirt and dust accumulation

It is expected that, as PVs are exposed to the environment in outdoor conditions, dirt and dust can accumulate on the solar module surface. The dust and dirt accumulation block some of the sunlight and thus reduce the power output of the modules. A study from Kalogirou et al. (2013) showed that there is an important decrease of the efficiency of the modules especially after dust episodes or after long time of natural weather conditions.

(d) Module Temperature

Module temperature is a very important parameter for the behaviour of a PV system as it affects the output energy of the system and thus the system's efficiency. The effects of the temperature on the PVs efficiency is a result of a special characteristic of Si cells based modules. Si modules tend to lose voltage when they operate in high temperatures and produce higher voltage as the temperature drops. Consequently, the module output power reduces as the module temperature increases.

With high temperature, the open circuit voltage decreases while the short circuit current increases only slightly. Thus, the power output decreases. For crystalline silicon, the reduction in the open circuit voltage for an individual module consisting of n_c cells connected in series is given by:

$$\frac{dV_{oc}}{dT} = \frac{V_{oc}\,(T_C) - V_{oc}(25°C)}{T_C - 25°C} = -2.3\,n_c \quad \left(\frac{mV}{°C}\right) \qquad 1.12$$

And thus

$$V_{oc}(T_C) = V_{oc}(25°C) - 2.3\,n_c(T_C - 25°C) \qquad (mV) \qquad 1.13$$

Where T_C is the cell temperature (°C). The cells in an illuminated module operate at a higher temperature than ambient temperature. NOCT (Nominal Operation Cell Temperature) is an indicator of this temperature difference and it is the cell temperature at Standard Operating Conditions of 20°C ambient temperature, 800 W/m^2 solar irradiance and 1 m/s wind speed. To evaluate the cell temperature for other ambient conditions, the following expression may be used:

$$T_C = T_{amb} + \left(\frac{NOCT - 20°C}{800\,W/m^2}\right) G \quad (°C) \qquad 1.14$$

The module efficiency decreases as the module temperature increases for monocrystalline and polycrystalline Si cells but not for the amorphous Si cells. Panels are tested under laboratory conditions in STC where the temperature is constant at 25°C which can be significantly different from the real outdoor situations.

PVs experience very high temperatures due to the heat input by that part of the absorbed solar radiation which is not converted into electricity. Temperatures of 70°C and more are observed, which when combined with a drop in the output, which may be 0.5% per °C rise, can significantly reduce the efficiency relative to that indicated by the panel rating determined at STC at operating temperature of 25°C (Brinkworth, 2000).

(e) Conversion losses

As mentioned earlier, the PVs produce Direct Current which must be converted to Alternative Current in order to be used in common households. For the conversion of the DC to AC an inverter is used. However, some power is lost in the conversion process and there are additional losses in the wires from the PV array to the inverter and to the building's panel.

Modern inverters have peak efficiencies of 92-96%, indicated by their manufacturers, but again these values are obtained under tests in well controlled factory conditions.

(f) Shading

Ideally solar panels should be located such that all the PV area will never be shaded. A shadow on even a small part of the panel can have a significant effect on its energy output and whole system's output.

Usually the cells within a panel are connected in series. Therefore, the shaded cells affect the current flow of the whole panel. Then if the affected panel is wired in series (in a string) with other panels, then the output of all those panels will be affected by the partial shading of one panel. In such a situation, an obvious solution is to avoid wiring lots of panels in series if possible.

However, there are some cases that the partial shading of the PVs cannot be avoided and thus the effects of partial shading should be considered during the planning phase.

1.8 Building Integrated Photovoltaics

Traditionally, the usual way to install a PV system on a building is to install PVs with brackets and connections on the roof of the building.

However, during the last few years, PV panels are increasingly being incorporated and integrated into the construction of buildings to provide electrical power. New technologies allow PV systems to be attached on the building's elements or even be a part of the building construction materials. The idea of integration of the PV panels and replacement of building elements, increases the prospects of the use of RES in buildings.

There are two ways of incorporating PV into the building envelope, BAPV (building applied PV) and BIPV (building integrated PV). In a BAPV system the PV modules are fixed onto the existing building façade but in a BIPV system, PV modules are part of the building envelope, forming the outer layer. According to Peng et al. (2011) these two classifications cannot be clearly defined in practice. From the definition given by the authors, the main difference between BIPV and BAPV is the extend of tightness in the integration of photovoltaic systems and buildings. In either BAPV or BIPV systems the PVs need to be cooled to prevent overheating and thus loss of their conversion efficiency.

In Building Integrated Photovoltaic (BIPV) systems, the PV modules are incorporated into the construction of the building and replace conventional construction materials and parts of the building envelope such as the roof, skylights and facades (Figure 1.8). They are specifically designed to blend in with the architecture of a building, combining the economic and sustainability benefits of distributed solar energy generation with the aesthetic appeal of a seamless integration into the overall building design.

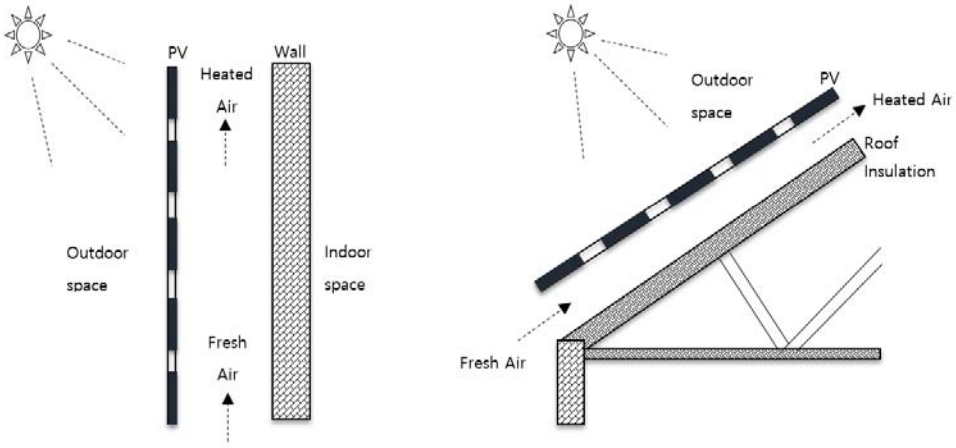

Figure 1.8. Schematic diagram of the BIPV system investigated, in vertical position (façade installation) and inclined position (roof installation).

According to the European Construction Product Directive CPD 89/106/EEC (European Commission, 2014c), PV modules are considered to be building integrated if the PV modules form a building component providing a function. Furthermore, the PV module should play an important role on the building's construction and must be necessary for the operation of the building. Consequently, in case that the PV module is uninstalled, this has to be replaced by a building component as appropriate.

The first installation of building integrated photovoltaics was realized in 1991 in Germany. The panels were integrated as a curtain wall façade with isolating glass. Benemann et al. (2001) describes the growth of the PV usage in buildings since then.

By simultaneously serving as building envelope material and power generator, BIPV systems can provide savings in materials and electricity costs, reduce use of fossil fuels and consequently the emission of ozone depleting gases, and add architectural enhancement to the building.

BIPV systems represent a promising solution for clean electricity combined with cooling or heating through the exploitation of natural ventilation or mechanical ventilation. BIPV systems should be applied to buildings where energy conscious design techniques have been employed, and equipment and systems have been carefully selected and specified. They should be viewed in terms of life-cycle cost, and not just initial first-cost because the overall cost may be reduced by the avoided costs of the building materials and labour they replace. Design considerations for BIPV systems must include the building's use and electrical loads, its location and orientation, the appropriate building and safety codes, and the relevant utility issues and costs.

Integration of the PVs can improve the cost effectiveness by supporting the PV panels in order to provide additional functions like shading (Figure 1.9), active solar heating (Figure 1.10) and day lighting (Figure 1.11).

Figure 1.9. BIPV typical applications for shading on buildings.

Figure 1.10. BIPV applications for solar heating.

Figure 1.11. BIPV applications for natural lighting in buildings.

Considering a PV module integrated on another surface, a very important issue appears. The efficiency of the PVs decreases with the increase of the temperature of their surface. This effect must be taken into account in the installation process, since its output drops by the temperature increase. Therefore,

from an energy yield point of view, it would be useful to create a rear-ventilation channel in order to keep the module temperature as low as possible.

The way of installation allows the application to be considered as double skin ventilated facade (DSVF) because there are two skins, the PV and the building's construction material separated by an air gap. Therefore, a wide duct is formed between the backside of the PV modules and the external wall of the building. This duct can be used to dissipate heat to provide adequate ventilation in order to cool the PV cells and keep their efficiency in standard levels. Double Skin Ventilated Facades have many forms and applications, described analytically by Fux (2006). The DSVFs are investigated by several researchers regarding their thermal properties, characteristics and their effectiveness as outlined in the next chapter of this thesis.

BIPV systems are usually employed in buildings to produce electricity. However, the heated air passing through the duct behind the hot PV panel, can be used for space heating or domestic hot water heating and in case of open loop air systems the heated air can also be used as fresh air for space ventilation or for drying clothes (Candanedo et al., 2010).

When active heat recovery is utilized with BIPV systems, either in a closed loop or in an open loop with forced air, they are known as Building Integrated Photovoltaic/Thermal systems (BIPV/T). BIPV/T systems can be readily integrated with building envelopes and with HVAC systems while producing both electricity and useful thermal energy. Apart from the electricity production and heat generation, BIPV/T systems reduce also the heating and cooling loads of the building compared to the conventional building envelope elements (Yang and Athienitis, 2014). Since high temperatures are harmful for the performance of PVs, the circulation of the air can be used to remove thermal energy from BIPV systems.

The ventilation of the cavity may be controlled by different factors such as the wind velocity, the air gap size, and the forced convection induced by fan or conventional air conditioning system. Accordingly, ventilation may be totally natural, fan supported or totally mechanical. Although mechanically ventilated systems are easier to be studied and thus their performance can be more easily predicted, the naturally ventilated systems have some very important advantages and many potentials. They do not require maintenance or extra cost for a fan, they can be easily installed in comparison with the mechanically ventilated systems, no noise of a fan and no extra cost of electricity to operate the fan.

There are plenty of reasons to integrate PVs on a building but there are also some drawbacks. First of all, the overall cost of the building may increase or decrease if PVs are integrated. This depends on the

difference between the cost of the construction material that will be replaced by the BIPVs and the cost of the BIPV. In the case that the cost of BIPV is bigger, the BIPV will pay back the initial expenditure in a few years. The major advantage is that the system does not require additional land because is integrated into the building envelope. In addition, electricity is produced on site and replaces power that would otherwise be purchased at commercial rates and reduce transmission losses. Moreover, the BIPV can be connected to the grid and this means that it avoids the high cost of storage (batteries). Furthermore, a well-integrated system is architecturally elegant and could increase the aesthetic appearance of a building.

Additionally, by 2020 according to the European Directive 2010/31/EU all new buildings will have to be Nearly Zero Energy Buildings (NZEB) which requires a building to produce almost all the energy that it needs on an annual basis. This might be a revolution for architecture and PVs sector as well. Consequently, BIPV systems have also a great prospect in the ZEB scenario thanks to their features and the decrease in PVs cost.

1.9 Problems/Drawbacks of the BIPV and DSF systems

New designs and applications of facade concepts are today more relevant than ever before. New designs of facades should allow for a comfortable indoor climate, sound protection, good lighting and at the same time minimize the demand for energy. During the last 15 years, double skin facades have become an increasing and important architectural element in buildings especially in combination with integrated PV panels. This is happening especially in commercial and office buildings which with integrated double skin facades can be energy efficient with lots of advantages. Double skin facades can provide a thermal buffer zone, solar preheating of ventilation air, energy saving, sound protection, wind and pollutants protection, night cooling and space for energy gaining devices like PV cells.

However, not all double skin facades installed during the last years performed well, while in most cases large air conditioning systems have to compensate for summer overheating problems and the energy consumption is very high. Therefore, despite of all research carried out on double skin facades technology, there is still a large area of research in order to exploit their advantages and use them more effectively.

As it is already pointed out, most of the absorbed solar radiation by the PV modules is converted to heat since the cell's conversion efficiencies are low and this heat increases the temperature of the module. The high temperatures have negative impact on the electrical output of the PV especially in the crystalline Si based cells. According to Fossa et al. (2008), this phenomenon is made significantly worse if the components are integrated as parts of the building envelope. Consequently, the BIPV

panels get warmer than the ones mounted in free air, thus lowering more their electrical power output. To solve this problem, new efficient ways to extract the heat by forced or natural fluid circulation have to be devised. Kaiser et al. (2014) mentioned that a cost-effective way to eliminate the high PV temperatures is to provide an open-air channel behind the integrated PVs. As will be shown in the next chapter, there are a lot of studies that tried to optimize the air gap between the PV modules back surface and the building element for air circulation, either by forced or natural flow, for cooling the PV arrays.

The raised temperature of the PV causes heat which is lost from the front face to the surroundings and from the rear face which goes into the air gap (cooling duct) by convection and radiation. The heat that goes to the air gap heats up the air, setting up buoyancy force which induces an upward flow so that the inwardly transmitted heat is removed to the surroundings, thus lowering the temperature of the PV and restoring some of its efficiency (Brinkworth and Sandberg, 2006). According to Gan (2009) it is important to provide an adequate gap behind the PV modules to facilitate ventilation cooling.

According to Zogou and Stapountzis (2012), the cooling effect maintains a high conversion efficiency of the PV panels and the heated air may be exploited by the HVAC system or water heating. If the system is a PV/T one with exploitation of the thermal energy generated, then the preheated air is channeled through proper ducting systems between building interior and outside. The natural air ventilation usually generates low air flow rates and in PV/T systems may not produce enough flow rate to cool the PVs satisfactorily and thus a small fan is usually employed.

As mentioned earlier, Double Skin Facades create building overheating problems. In a similar way for BIPV systems, apart from the effect of the heated air in the PVs efficiency, the high air temperature in the duct between the PV and the wall of the building, can result to increased cooling loads in warm climates. In case that this happens, the BIPV system is not effective anymore as it will require electricity to cover the high cooling loads created by itself.

One concern is usually if the BIPV systems work more effectively with a fan to drive the air, and if so, why it is not installed in all systems to solve the overheating problems. This is because the use of the fan means extra cost to the system for the fan's installation and operation, noise from the fan and often maintenance. The systems with buoyancy driven air do not have those problems as the air moves naturally under the right conditions. Consequently, it is important to understand the behaviour of the system in various conditions and make the system more effective with natural ventilation without the use of mechanical means to drive the air.

The overheating problems do not appear at the stage when the engineers design the system before the installation. This is apparently because the models in simulations do not take into account all the parameters playing a role in the system, like the importance of the air behavior in the duct. For example, in many studies, researchers consider the temperature of the two skins to be the same in all height, the convective heat transfer coefficients to be constant in all skins and in all the sections of the system whether the skin is facing outside or inside. Those assumptions are also used by the engineers who investigate the systems to install, to simplify the models and make a rough estimation of the performance of the systems. However, these assumptions seem to underestimate the importance of the air flow behind the PVs and this is the reason the systems at the end of the day (after the installation) do not work as efficiently as they were estimated to do. Consequently, more knowledge is needed not only for researchers who want to investigate these systems, but also for practicing engineers that undertake the engineering designs of these installations.

1.10 Subject & Aim of this Study

The main subject of this study is the thermal behaviour of a Double Skin Façade (DSF) system named Building Integrated Photovoltaic (BIPV) system since PV panels comprise one of the two skins of the façade. As previously discussed, DSF are very popular nowadays but despite their increased usage, some problems occur in the applications and the several approaches tested from many researchers to understand the physical effects and mechanisms of the systems, signify that these systems worth to be better investigated and solutions need to be found for some specific issues.

The investigation of the thermal behaviour of the BIPV/T systems is very important for engineers in order to find out the optimum way to install them and predict their performance. Various researchers from the past years studied the thermal conditions of DSVF and during the last years there are many studies concerning the thermal analysis and performance of the solar facades.

The aim is to understand the thermal behavior of a naturally ventilated BIPV system and prevent overheating and loss of the PV efficiency. Investigation of the natural convective flow which determines the thermal behavior of the PV modules in a double skin system is challenging because it is highly sensitive to external disturbances. This is maybe the reason why most researchers decide to investigate the forced convection mechanism in those systems. According to Mei et al. (2003), in order to achieve good heat transfer within the façade and the solar collectors and reduce also the operating temperatures of the PV modules, forced convection was found necessary since stack effect/buoyancy driven flow rates were too limited. On the other hand, there are some studies which tried to find

optimum configurations of the system in order to be efficient without mechanical means. All these will be discussed in next chapters.

Accordingly, the major objective is the thermal analysis of a naturally ventilated BIPV system and the ultimate goal is to estimate the convective heat transfer coefficients in all sections of a BIPV system and develop an equation that describes best the convective heat transfer coefficients in the air gap between the PV panel and the second skin of the building. This will allow better estimation of the system's performance and give the engineers a tool to estimate the correct coefficients for building energy analysis or for optimum system design and installation.

Optimized design of the BIPV or BIPV/T systems must be based on the understanding of the air flow and heat transfer inside the cavity behind the PV panels (Zogou and Stapountzis, 2012). Sandberg and Moshfegh (2002) pointed out that since the temperature distribution along the PVs is highly dependent on the flow and accordingly to the chimney effect, characteristics of the buoyancy induced flow as well as heat transfer, are of primary importance in order to be able to optimize the design.

In order to be able to assess the actual benefits of ventilated facades with integrated photovoltaics, there are various examination methods that can be combined. These methods are; the theoretical analysis, detailed simulation, and the last but most important is the experimental which can be combined with the previous ones to validate the results. This study is going to combine all the three methods in order to give a clear view of the thermal behaviour of the solar facades.

Since the ultimate objective of this study is to understand the thermal analysis of the BIPV systems with natural ventilation, the first aim was to collect all the available information on the heat transfer analyses of the DFVF and BIPV systems, analyze, discuss and compare them in order to understand the current state of knowledge on the topic.

The present study aims to the improvement of our knowledge on the BIPV systems thermal behaviour and this will be accomplished by the following steps:

- The collection of the current knowledge from other studies from the literature.
- The collection of Nu number correlations and convective heat transfer coefficient correlations from the literature relevant to the topic and find the one that represents the BIPV systems better.
- The selection of the Nu correlation that approaches a BIPV system in the best possible way.
- The design and setup of two testing devices to represent a double skin BIPV system. One apparatus for indoor experiments and one for outdoor.

- The indoor testing with the use of a large scale solar simulator to carry out thermal measurements on the experimental device under controlled environmental conditions, and the use of hot wire anemometer for measurements of buoyancy flow conditions.
- The outdoor testing of the system under real sun to record its temperature distribution.
- The Computational Fluid Dynamics (CFD) modeling of the system, and the validation of the model with the use of the experimental data. The use of the validated system for the investigation of more parameters of the system's design which are difficult to be investigated experimentally.
- The estimation of the energy and exergy efficiencies of the system.
- The development of a new correlation for the estimation of the Nu number in the air gap of the double skin BIPV systems for the estimation of the convective heat transfer coefficients, with the use of the experimental data.
- The application of the knowledge to carry out a building level energy simulation.
- The analysis of measured on site data of a real roof BIPV application in a demonstration site and the comparison of the measured data with those estimated from the simulation.

1.11 Thesis Outline

In this project, a naturally ventilated BIPV system is proposed and tested experimentally in outdoor environmental conditions and indoor controlled conditions, as well as with simulations with a 3D simulation model. The structure of this thesis is as follows (Figure 1.12).

The first chapter introduces the general characteristics of the PV modules and proposes the BIPV concept for investigation.

The second chapter presents the state of knowledge on the thermal analysis of Double Skin Facades (DSF) with integrated PV panels by discussing the most known studies from the literature, including both mechanically and naturally ventilated systems.

The third chapter presents an extensive experimental analysis carried out in outdoor environmental conditions and in indoor controlled conditions with the use of a solar simulator. Having a clear idea on the thermal behaviour of the system, an analysis of the natural convection is carried out using fundamental convection equations and as a result, two correlations for the estimation of the convective heat transfer coefficients (CHTC) are extracted.

Chapter 4 presents a 3D computational fluid dynamic (CFD) model which is built in COMSOL Multiphysics and it is validated with the experimental results. The general conclusion is that the

experimental results were in a good agreement with the simulation results. This chapter discusses the importance of the CHTC on the energy analysis of a building as well.

Subsequently, in Chapter 5, energy and exergy analyses are carried out and the correlations for the estimation of the energy and exergy efficiencies of the system are presented. The energy efficiency of the system is estimated to be up to 26.5-33.5% while the exergy efficiency is estimated to be between 13-16%.

The last chapter applies all the gained knowledge from the previous chapters to a real BIPV demonstration system in Belgium. The work presented in this chapter is carried out under an EU funded project. A building simulation model is carried out to predict the temperature of the PV panels and the energy production of the system for one year. Then the simulation data are compared with real data measured on-site from the monitoring procedure. A good agreement is observed between the calculated and measured data.

Finally, the conclusions obtained from this project are presented as well as recommendations for future work.

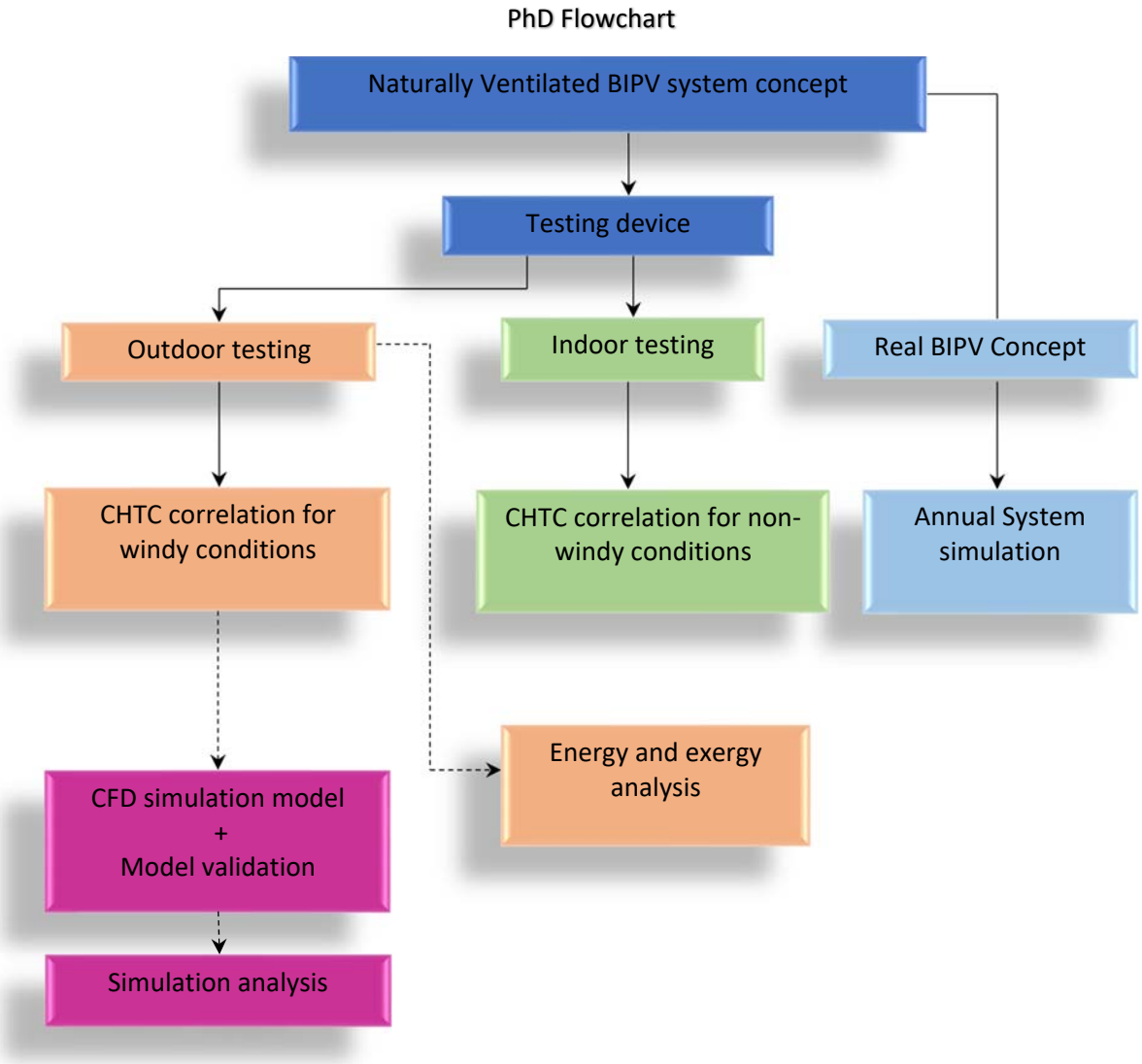

Figure 1.12. Flowchart of this thesis.

1.12 Novel Features of this study

- Provides a complete idea of the temperature distribution of the system: Combination of experiments, theory and simulations to understand the thermal behaviour of the naturally ventilated BIPV systemsunder windy and non-windy conditions
- Development of two new correlations for the estimation of the CHTC in the air gap of a double skin naturally ventilated BIPV system
- Provides researchers a Nusselt number correlation to be used when investigating NVBIPV systems
- Creates tool for engineers and installers
    - For more accurate estimation of the system's performance before the installation

- To provide an idea of the range of the temperature that the system will develop under different conditions and take measures to prevent overheating problems
- To use the correct range of CHTC when estimating the thermal resistances of the building's components

- Estimation of the energetic and exergetic efficiencies of naturally ventilated BIPV system

CHAPTER 2

2 Literature Review

This chapter[1] presents a comprehensive discussion of studies carried out on Double Skin Facades (DSF) and Building Integrated Photovoltaics (BIPV) collected from literature but firstly discusses the convection heat transfer principles. The purpose is to present the state of knowledge on the specific subject in terms of the most known or most used published studies.

In order to understand how to approach a DSF or a BIPV façade, it is important to understand the conditions of the system regarding the air flow, the openings, and the behaviour of the fluid, the temperature as well as the performance of the system. For this reason, this review is divided into six subsections. The first section presents the basic convection principles. The second section presents the most known studies investigated the double ventilated facades while the third one presents some of the studies carried out on double skin ventilated facades with integrated PV panels. In section four, a small discussion on the aspects of solar architecture is presented and in section five emphasis is given on the air flow in the PV facades which is examined in several studies thermo-graphically, experimentally or with simulations. The sixth section presents the relevant work published since today, based on the heat transfer analysis of BIPV facades and DSF. This last section presents also a discussion

[1] Part of this section is published as: Agathokleous, R.A., Kalogirou, S.A., (2016). Double skin facades (DSF) and building integrated photovoltaics (BIPV): A review of configurations and heat transfer characteristics. Renew. Energy 89, 743–756.

of the various heat transfer correlations from the literature for both naturally ventilated and mechanically ventilated facades (with the use of a fan), with emphasis to the convective heat transfer coefficients. The chapter closes by summarizing the most important information found in the literature and some conclusions on the state of knowledge of the subject.

2.1 Convection Heat Transfer Principles

Convection heat transfer can be classified according to the nature of the flow. There is forced convection when the flow is caused by external means (e.g. a fan), and free convection when the flow is created by buoyancy forces which arise from density differences created by the temperature variation in the fluid.

When no external work is applied, the energy for the steady flow of a fluid in a tube can be expressed as:

$$\dot{Q} = \dot{m}\, C_p\, (T_e - T_i) \qquad 2.1$$

Where:

$\dot{Q}$: Rate of heat transfer to or from the fluid (W)

$\dot{m}$: Fluid mass flow rate (kg/s)

C_p : Specific Heat capacity of the fluid at constant pressure (kJ/kg K)

T_e : Mean fluid temperature at the exit (ºC)

T_i : Mean fluid temperature at the inlet (ºC)

Since the air is the fluid involved in the heat transfer between the exterior and the interior skin, convection is the most important heat transfer mechanism of the system. The overall effect of convection between the PV and the air behind it, can be expressed by the use of the Newton's law of cooling from Equation (2.2), and it is related to the overall temperature difference between the wall and fluid, a surface area A and the convection heat transfer coefficient h:

$$\dot{Q} = h\, A\, (T_w - T_\infty) \qquad 2.2$$

Where:

h : Convective heat transfer coefficient (W/m^{2}K)

A : Cross sectional area of the duct (m^2)

T_w : Temperature of the wall (°C)

T_∞ : Temperature of the air (°C)

The rate of the heat transfer by convection can be found by Equation (2.2) and the heat transfer coefficient h, can be estimated by correlations of the Nusselt number depending on the type of the convection; natural or forced, the area of the flow, and the fluid properties.

The Nusselt number, is the ratio of the convective to conductive heat transfer across the boundary and is given by:

$$Nu = \frac{h\,L}{k} \qquad 2.3$$

L : Length of the surface of the flow (m)

k : Thermal conductivity (W/mK)

In case the flow is created by external means there is forced convection. Forced convection in BIPV systems and double skin facades is studied in a greater detail than the natural convection because of the simplicity of the known air flow as this can be set constant by a fan or other mechanical means.

The type of the flow laminar or turbulent, is defined from the Reynolds number and for each type there are empirical equations of the Nu number.

$$Re = \frac{U_\infty x}{v} \; or \; Re = \frac{U_\infty D}{v} \qquad 2.4$$

U_∞ : Free steam velocity (m/s)

x : Distance from leading edge (m)

$v=\mu/\rho$: Kinematic viscosity (m^2/s)

D : Diameter of the cylinder if there is internal flow in a cylindrical duct or the hydraulic diameter in other shapes.

In the case of the BIPV system where a fan is used to drive the air flow, the system can be considered to have internal flow in a duct with non-circular section. In this case the diameter D is replaced by the D_h, the hydraulic diameter, given by:

$$D_h = \frac{4\,A_c}{p} \qquad 2.5$$

A_c : Cross sectional area of the duct (m^2)

p : Perimeter of the flow area of the duct (m)

The same applies to natural convection when the duct is not circular and in the Rayleigh number, the characteristic length L is replaced by D_h

In case the flow is not driven by any external means, the air flow is determined from the buoyancy forces effect through the static pressure head from the density differences caused by the temperature variation in the fluid as:

$$\Delta P = H \cdot g \cdot (\rho_{air} - \rho_a) \qquad 2.6$$

ΔP : Pressure difference (Pa)

H : Total height of the column above the test area to the surface (m)

g : Acceleration due to gravity (m/s^2)

ρ_{air} : Mean density of the air in the duct (kg/m^3)

ρ_a : Ambient air density (kg/m^3)

The density difference gives rise to the buoyancy force and sustains flow. This is known as the Boussinesq approximation. Boussinesq approximation assumes that variations in density have no effect on the flow field, except that they give rise to buoyancy forces. Thus, the density variation is only important when is multiplied with the acceleration due to gravity, and can be neglected in the rest of the Navier-Stokes equations. The Navier-Stokes equations govern the motion of fluids and can be seen as Newton's second law of motion for fluids. In the case of a compressible Newtonian fluid the equation is as follows:

$$\rho\left(\frac{\theta u}{\theta t} + u\,\nabla u\right) = -\nabla P + \nabla\left(\mu(\nabla u + (\nabla u)^T) - \frac{2}{3}\mu(\nabla u)I\right) + F \qquad 2.7$$

Where u is the fluid velocity, P is the pressure, ρ is the fluid density, μ is the fluid's dynamic viscosity, I is the identity matrix and F includes the external forces to the fluid.

Considering natural convection over a vertical plate, the complete set of conservation equations solved with the Navier-Stokes equations, consists of the continuity equation, the momentum equation and the energy equation as shown below at the simplified mode:

$$\frac{\theta u}{\theta x} + \frac{\theta u}{\theta y} = 0 \qquad 2.8$$

$$u\frac{\theta u}{\theta x} + v\,\frac{\theta u}{\theta y} = v\,\frac{\theta^2 u}{\theta y^2} + g\beta(T - T_\infty) \qquad 2.9$$

$$u\frac{\theta T}{\theta x} + v\frac{\theta T}{\theta y} = \alpha\frac{\theta^2 T}{\theta y^2} \qquad 2.10$$

These equations must be solved in conjunction with their boundary conditions which are:

At $y = 0$: $\mathrm{u}(\mathrm{x}, 0) = 0, \mathrm{v}(\mathrm{x}, 0) = 0,\ \mathrm{T}(\mathrm{x}, 0) = \mathrm{T}_s$

At $y = \infty$: $\mathrm{u}(\mathrm{x}, \infty) = 0, \mathrm{v}(\mathrm{x}, \infty) = 0,\ \mathrm{T}(\mathrm{x}, \infty) = \mathrm{T}_\infty$

The convective heat transfer coefficient (CHTC) *h* to estimate the heat transfer rate by natural convection, can be estimated by Nu correlations as a function of the Grashof, Prandtl and Rayleigh numbers, i.e., Nu=*f*(Gr, Ra, Pr).

The role that the Reynolds number plays in forced convection is replaced by the Grashof number (Gr) in natural convection. The Grashof number provides the main criterion in determining whether the fluid flow is laminar or turbulent in natural convection. The critical Gr is 10^9. The flow can be considered turbulent for Gr>10^9. The Grashof number is given by the following expression:

$$Gr = \frac{g\beta\ (T_s - T_\infty)\ L^3}{v^2} \qquad 2.11$$

Where:

β	:	Volumetric thermal expansion coefficient (1/K)
v	:	Kinematic viscosity (m^2/s)
T_s	:	Temperature at the surface (°C)
T_∞	:	Temperature of the air (°C)
L	:	Characteristic length (m)

The Prandlt number is the ratio v/α named by the German scientist Ludwig Prandlt who introduced the concepts of boundary layer theory. The Pr number is dimensionless when a consistent set of units is used as shown below.

$$Pr = \frac{v}{a} = \frac{\mu/\rho}{k/\rho\ C_p} = \frac{C_p\ \mu}{k} \qquad 2.12$$

μ	:	Dynamic viscosity (N s/m^2)
C_p	:	Specific heat of the fluid (kJ/kg K)
k	:	Thermal conductivity (W/m K)

a : Thermal diffusivity (m^2/s)

The Rayleigh number is a dimensionless number formed by the product of the Grashof and Prandlt numbers, given by the following expression.

$$Ra = Gr\ Pr = \frac{g\beta\ \Delta T\ L^3}{v\ a} \qquad 2.13$$

All properties of the air are estimated at the mean fluid temperature $T_f = (T_s + T_\infty)/2$.

Initially, in cases with flow in ducts, at the entrance of the fluid in the duct, the flow is laminar, but at some critical distance from the leading edge, depending on the flow field and the fluid properties, small disturbances in the flow occurs and the flow belongs to the transition region which takes place until it becomes turbulent.

For forced convection, the criterion to determine whether the flow is laminar or turbulent is the Reynolds number, while for the natural convection, it is the Grashof number. For internal forced convection, the flow in a tube is considered to be laminar for Re<2300, fully turbulent for Re>10000 and transitional in between. However, in many cases, flow becomes fully turbulent when Re>4000. In natural convection, this criterion is $Gr>10^9$ for turbulent flow.

When gravity is perpendicular to the walls, the known Rayleigh-Bénard convection exists. Rayleigh-Bénard convection is defined as a thermally driven flow in a fluid layer between two infinitely horizontal plates, where constant temperatures are imposed on both fluid boundaries. As shown in Figure 2.1, the bottom plate is heated and the top one is cooled (Physics, 2014).

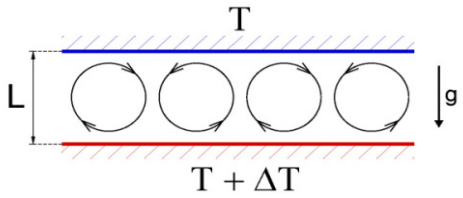

Figure 2.1.Schematic diagram of the Rayleigh-Bénard convection (Physics, 2014).

On the other hand, when the gravity is parallel to the walls (Figure 2.2), like the case of the vertical façade BIPV systems, a natural convection flow results when the walls are at different temperatures ($T_{w1} \neq T_{w2}$). For small temperature differences, the flow is laminar and after a critical value, the flow becomes turbulent. In contrast with the Rayleigh-Bénard convection, in the case that the two planes are vertical, a mean flow develops. This makes the situation more complex due to the additional effect of turbulence production by shear (Physics, 2014).

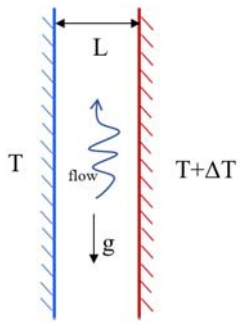

Figure 2.2. Schematic diagram of vertical parallel plates of different temperatures.

As mentioned earlier, the Ra number range defines the area of the flow and there is a different Nu number equation for every range. The Ra number as well as Nu number depend on the type of the convection; natural or forced, the area of the flow, and the fluid properties. Accordingly, the investigation of a BIPV system as a system with two parallel plates exposed to different thermal conditions, should take into account the different values of Ra that may occur at the various parts of the system. Although the wall of the system may be considered as isothermal plates, the PV cannot be isothermal because its temperature distribution is affected by the air openings of the duct formed between the wall and the PV as well as the incident solar radiation. Thus, it can be considered only isoflux and the situation remains complex as there is air flow at the front of an isothermal plate (wall) and at the back of an isoflux plate (PV).

2.2 Double Skin Ventilated Facades (DSVF)

A ventilated double facade can be defined as a traditional single facade doubled inside or outside by a second, essentially glazed façade (Figure 2.3). Each of these two facades is commonly called a skin. A ventilated cavity is located between these two skins. The width of the cavity can range from several centimeters at the narrowest to several meters for the widest accessible cavities. There exist facade concepts where the ventilation of the cavity is controllable, by fans and/or openings, and other façade concepts where this ventilation is not controllable.

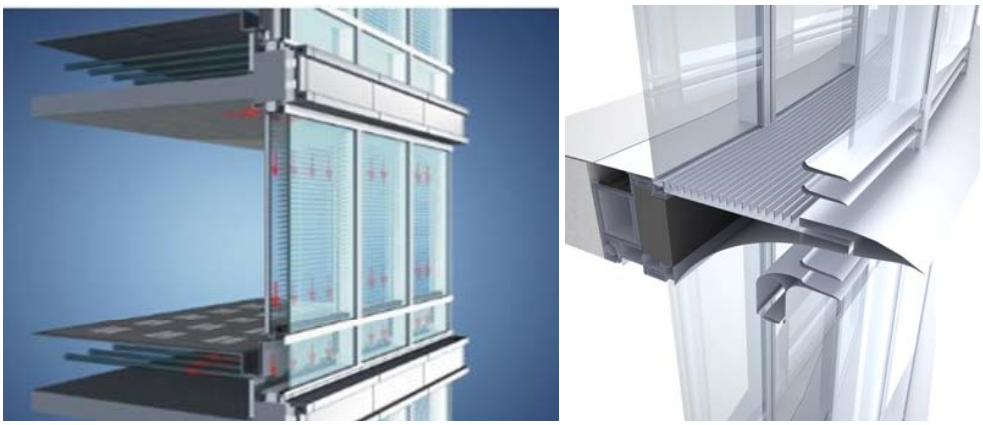

Figure 2.3. Double skin ventilated façade with glazing (Redchalksketch, 2011).

Streicher et al. (2004) made an analytical study on the double skin façade (DSF) concept and presented historical literature review on its definition and history. Different definitions are given through the years, by several researchers about the double skin facades.

According to the BBRI (Belgian Building Research Unit, 2002), "An active façade is a façade covering one or several storeys constructed with multiple glazed skins. The skins can be air tight or not. In this kind of façade, the air cavity situated between the skins is naturally or mechanically ventilated. The air cavity ventilation strategy may vary with the time. Devices and systems are generally integrated in order to improve the indoor climate with active or passive techniques. Most of the time such systems are managed in semi-automatic way via control systems".

Boake (2003) described the DSF system as "essentially a pair of glass ʹskinsʹ separated by an air corridor. The main layer of glass is usually insulating. The air space between the layers of glass acts as insulation against temperature extremes, winds, and sound. Sun-shading devices are often located between the two skins. All elements can be arranged differently into numbers of permutations and combinations of both solid and diaphanous membranes".

Arons and Glicksman (2001) define the DSF as "a façade that consists of two distinct planar elements that allows interior or exterior air to move through the system. This is sometimes referred to as a twin skin."

Uuttu (2001) defines the DSF as "a pair of glass skins separated by an air corridor (also called cavity or intermediate space) ranging in width from 20 cm to several meters. The glass skins may stretch over an entire structure or a portion of it. The main layer of glass, usually insulating, serves as part of a conventional structural wall or a curtain wall, while the additional layer, usually single glazing, is placed either in front of or behind the main glazing. The layers make the air space between them work to the building's advantage primarily as insulation against temperature extremes and sound".

Saelens (2002) describes the multiple – skin facade as “an envelope construction, which consists of two transparent surfaces separated by a cavity, which is used as an air channel. This definition includes three main elements: (1) the envelope construction, (2) the transparency of the bounding surfaces and (3) the cavity airflow”.

Compagno (2002) describes the DSF as “an arrangement with a glass skin in front of the actual building façade. Solar control devices are placed in the cavity between these two skins, which protects them from the influences of the weather and air pollution a factor of particular importance in high rise buildings or ones situated in the vincity of busy roads.”

Kragh (2000) describes the DSF as “a system that consists of an external screen, a ventilated cavity and an internal screen. Solar shading is positioned in the ventilated cavity. The external and internal screens can be single or double glazed units, the depth of the cavity and the type of ventilation depend on environmental conditions, the desired envelope performance and the overall design of the building including environmental systems”.

The history of DSFs is described in several books, reports and articles. In 1849 Jean-Baptiste Jobard director of the industrial museum in Brussels, described an early version of a mechanically ventilated multiple skin façade. He described the different conditions that should be taken into account separately for winter and summer. He mentioned that in winter the hot air should be circulated between the two glazings, while in summer cold fresh air should be circulated to avoid heat gains (Saelens, 2002).

According to Crespo (1999) the first instance of a Double Skin Curtain Wall appears in 1903 in the Steiff Factory in Giengen / Brenz near Ulm, Germany. In this case, the priorities were to maximize day lighting while taking into account the cold weather and the strong winds of the region. The solution was a three storey structure with a ground floor for storage space and two upper floors used for work areas. Later, two additions were built in 1904 and 1908 with the same Double Skin system, but using timber instead of steel in the structure for budget reasons.

Until the late 70’s, early 80’s little or no progress was made in double skin glass construction. During the 80’s this type of façades started gaining momentum. In the 90’s two factors strongly influenced the proliferation of double skin façades. The increasing environmental concerns start influencing architectural design both from a technical standpoint but also as a political influence that makes “green buildings” a good image for corporate architecture (Streicher et al.,2004).

Various terms are used to name these facades in the literature. Terms such as active facades, passive facades, double-skin facades, climatic facade or multiple-skin facades are often used. Most of the

classifications of the DSVFs are based on the geometry of the facades and their different working modes are not taken into account in most cases. For example as shown in Figure 2.4, Barbosa and Ip (2014) presented a classification of the DSFs according to the structure of the system or to the form in which the intermediated space is divided.

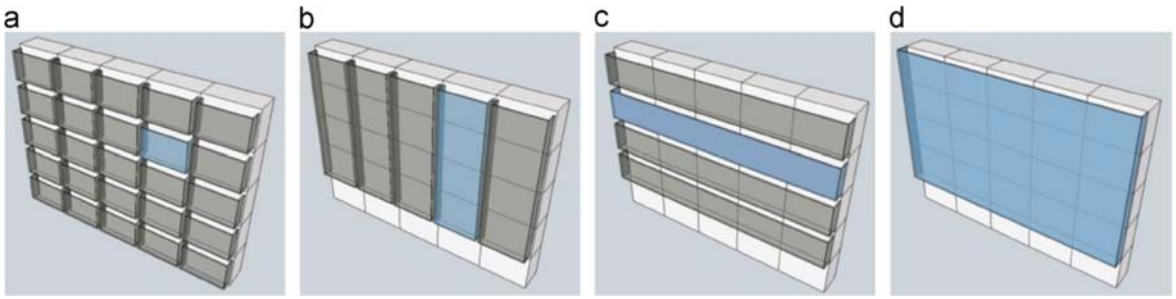

Figure 2.4. DSF classification: (a) Box Window, (b) Shaft-Box, (c) Corridor and (d) Multi-Storey double skin façade (Barbosa and Ip, 2014).

However, Loncour et al. (2004) introduced three criteria which are independent of one another for the double facades classification:

- The type of ventilation
    - Natural Ventilation
    - Mechanical Ventilation
    - Hybrid Ventilation
- The partitioning of the façade (how the cavity is situated between the two skins)
    - Ventilated double window
    - Ventilated double facade
- The modes of ventilation of the cavity
    - Outdoor air curtain: air enters from outside and rejected to outside
    - Indoor air curtain: air comes from the inside and return to inside
    - Air supply: ventilation is created from the outdoor air
    - Air exhaust: air comes from inside and exits towards the outside
    - Buffer zone: no ventilation of the cavity is possible

DSVFs are complex from a building's physics point of view because issues such as thermal and visual comfort, cooling load during summer time heat loss during wintertime, ventilation, acoustics, moisture and fire safety consideration. As buildings with this type of façade are usually highly glazed, they tend to overheat during summertime when peak outside air temperatures coincide with high solar gains. Although the suitability of this façade constructions for Central European weather conditions remains questionable, it is becoming more popular mainly for aesthetic reasons.

During the last years, there is an increasing demand for higher quality office buildings. Occupants and developers of office buildings ask for a healthy and stimulating working environment. DSVFs are appropriate when buildings are subject to great external noise and wind loads. There are lots of published works related to the double ventilated facades describing the several types they have. Some of the most popular published studies are presented below.

Fux (2006) mentioned that as a result of the increasing number of buildings with double facades, disadvantages such as the poor thermal comfort and high construction as well as operating costs have been observed. Fux (2006) presented several studies from Gertis (1999), Hausladen et al. (1998), Kornadt et al. (1999), Blum (1998), Jachan (2003) and Saelens et al. (2005) who investigated the advantages and disadvantages from these systems.

Saelens et al. (2005) examined different strategies to optimize the energy efficiency of multiple skin facades. The results were compared with the traditional cladding systems.

Lee et al. (2002) investigated the application of double glazed facades in high office buildings with large amount of glazing in extremely moderate climatic conditions. He described several actual façade constructions and examined theoretically with the use of TRNSYS (Transient System Simulation) program, different façade constructions and parameter variations. His results were very positive for some of the examined construction types.

Gratia and De Herde (2004) studied the thermal behaviour of a building with and without double-skin for one week. Simulations were carried out with Thermal Analysis Simulation (TAS) software and the case study analysis shows that for this specific building, the use of a double-skin façade decreases the heating loads and increases the cooling loads.

Hien et al. (2005) investigated the combined effects of double glazed façade with a ventilation system on the energy consumption, thermal comfort and condensation aspects for a typical office building in Singapore and compared them to single glazed façade system. TAS and CFD software was used to calculate energy consumption and thermal comfort for a single glazed façade building as well as a double glazed façade building. The simulation results showed that double glazed façade with natural ventilation was capable of minimizing energy consumption and provide thermal comfort.

Hamza (2008) in his study followed a quantitative analytical methodology to test and reconstruct the hypothesis on the efficiency of double skin façades as a façade technology suitable for reducing air-conditioning loads in hot arid climates. Transparent double skin façades were predicted to increase cooling loads in office buildings in hot areas in comparison with a single skin façade with reflective glazing. Nevertheless, such a disadvantage may be neglected if the double skin façades are to be used

in cases where protection from the environment is needed to preserve the front view of historic building.

Høseggen et al. (2008) carried out a study based on a planned office building in the city-centre of Trondheim, Norway. The building was modelled both with and without a double-skin façade with the building energy simulation program ESP-r. In contrary to some other studies on this subject, this study shows that an application of a double-skin façade can decrease the heating energy demand of a building, without increasing significantly the number of hours with excessive temperatures.

Manz (2003) investigated the heat transfer by natural convection of air layers within vertical rectangular cavities with aspect ratios A=H/L of 20, 40 and 80 using a CFD code. The objective of this work was to compare the results obtained by CFD code with empirical correlations derived from experiments from the literature including laminar and turbulent flow. The study focuses on tall vertical cavities like DSVF, BIPV systems, building integrated solar collectors etc. The average Nu numbers were calculated as a function of Ra numbers and compared with five correlations from the literature which are based on experimental data. The boundary conditions for the CFD were assumed to be isothermal hot and cold wall and zero heat flux at bottom and top cavity surfaces. Ra number was from 10^3 to 10^6 to represent tall ducts. The classification of the flow regimes which depend on Ra and A, was made through the study of Yin et al. (1978). The correlation of Yin et al. (1978) was one of the five compared with the CFD. The other four equations are from ElSherbiny et al. (1982), Wright (1996), Zhao et al. (1997) and the European Standard EN 673 (1997). As shown in the graphs of Nu=*f*(Ra,A) presented in the paper, with exception of correlation of Yin et al. (1978), the calculated Nu numbers do not deviate more than 20% from analytical correlations. In fact, the deviations are less than 10% for A=20.

A similar study is carried out two years later by Xamán et al. (2005) which is comparative with the results obtained from Manz (2003). Xamán et al. (2005), presented a detailed bi-dimensional steady state theoretical study of a fluid flow and heat transfer by natural convection in a tall cavity using a laminar model for Rayleigh numbers from 10^2 to 10^6 and a turbulent model for Rayleigh numbers from 10^4 to 10^8. Aspect ratios of 20, 40, 80 and Ra from 10^2-10^8 were examined. The average Nu number as function of the Ra number, are compared with the five correlations presented in the study of Manz (2003). The results found by Xamán et al. (2005) are compared with the results presented by Manz (2003) also. It is observed, that for aspect ratios 20, 40, 80, the convective Nu for laminar flow model fitted very closely to the experimental results obtained by Yin et al. (1978) in almost all the range, in contrast to the results obtained from Manz (2003) where the Nu reported were very far from the experimental results of Yin et al. (1978) in the range of Ra 10^3 - 10^5. Additionally, it is found that the

convective Nu for turbulent range, increases with the increase of the aspect ratio while the convective Nu for laminar range, decreases as the aspect ratio increases.

Manz and Frank (2005) presented a method based on the coupling of three different types of simulation models on double skin facades that is economical in terms of computing time and thereby suitable for design purposes. The models are spectral optical model, computational fluid dynamics models and building energy simulation model. The authors stated that the thermal design of buildings with this type of envelope remains a challenging task as there is no single software tool that can accommodate all of the three modeling levels. The physical phenomena involved are complex and numerous parameters are important in such energy system. The authors concluded that compared with the simple nodal models used in building's design by that time, the proposed method enhances reliability of prediction.

2.3 Double Skin Facades with Integrated PV Panels

As mentioned earlier, the double skin ventilated façade system that have PVs as the outer skin of the façade is called BIPV system. The first installation of BIPV was realized in 1991 in Germany where the PV elements were integrated into a curtain wall façade with isolated glass. The first production line for PV modules specialized for BIPV with a capacity of 5000 m^2 per year was established in 1993 in Germany. Since then the production increases significantly to a capacity around 50000 m^2 per year at the end of 1999, and since 2000 the building integration is one of the fastest growing market segments in PVs (Benemann et al., 2001).

As indicated by the term "double-skin", such a façade is intended to mean a system in which two "skins" are separated by a significant amount of air space. In the case of a PV façade, the second skin is a PV module placed in front of the first skin which is the wall of the building. These two skins act as an insulation between the outside and inside enabling the air to circulate between the cavity of the two skins providing good air circulation, thermal and acoustic performance (see Figure 2.5).

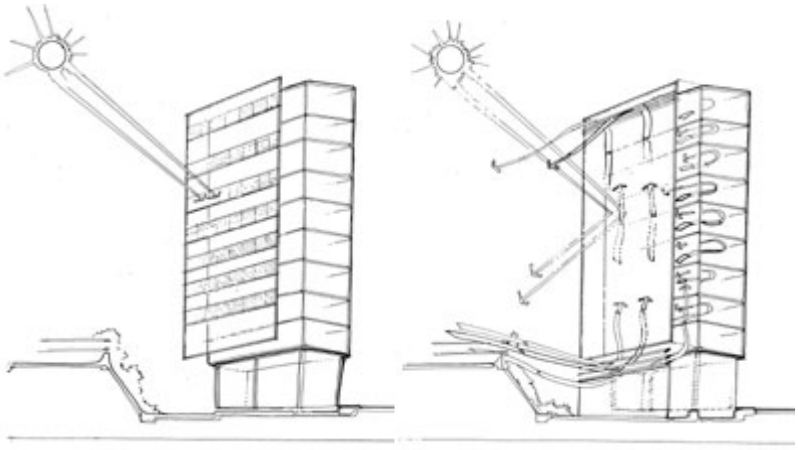

Figure 2.5. Building integrated photovoltaics and air circulation sketch (Single Aspects, 2014).

Considering that the efficiency of the PV cells drop with increasing temperatures, the fact that BIPV systems allow the air to flow behind the PVs helps to keep the PV at low temperature. Thus, a BIPV facade can be considered as a system with two vertical parallel plates, and the type of flow can be natural as shown in Figure 2.6 or forced as shown in Figure 2.7.

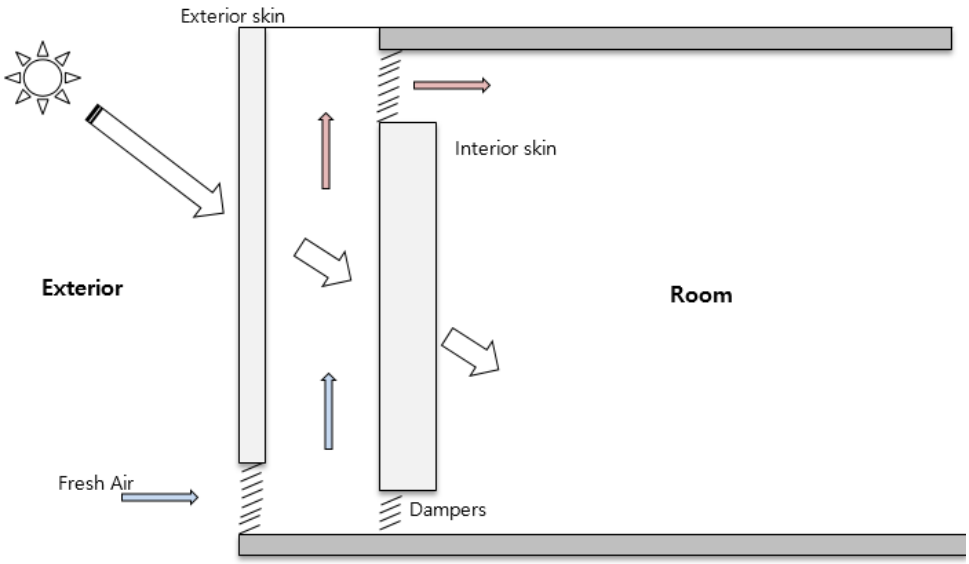

Figure 2.6. Schematic diagram of naturally ventilated façade (NVF).

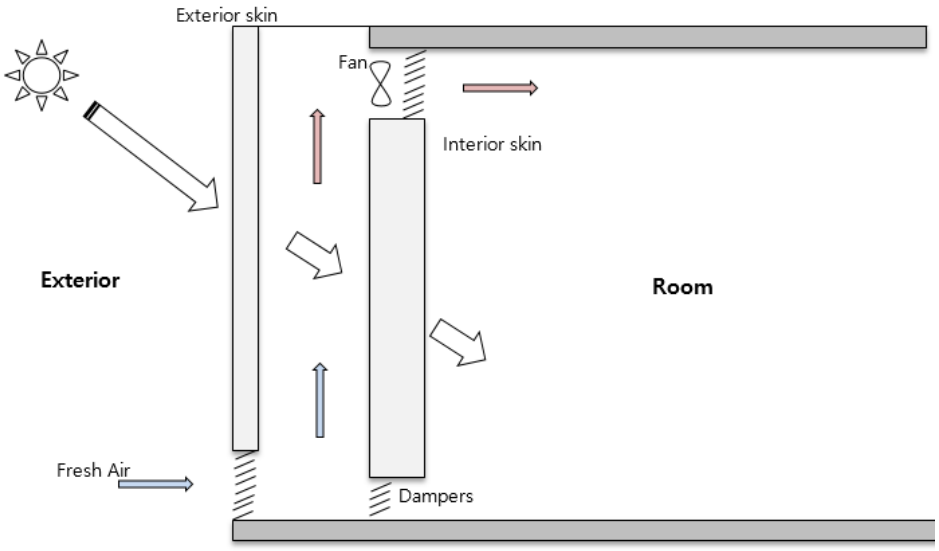

Figure 2.7. Schematic diagram of mechanically ventilated façade (MVF).

As mentioned before, the cavity in DSF and BIPV systems is either naturally or mechanically ventilated. Natural ventilation provides an environmental friendly atmosphere and reduce the requirement for mechanical ventilation but on the other hand mechanical ventilation provides stability and flexibility to the system.

For the naturally ventilated facades, the air is brought into the duct and exhausted by two means: wind pressure and stuck effect. Wind pressure dominates the air flow rate and if the system is properly designed, wind flows over the façade and create pressure differences between the inlet and outlet and as a result there is air movement upwards. Without wind, the duct can still be ventilated due to the stack effect. As air flows into the lower inlet of the duct, and is being heated due to the outer hot surface of the façade, it becomes less dense and thermally buoyant. As a result, air flows into the inlet and outlet while removing heat from the duct. However, there is the potential for wind pressure and stack effect to neutralize. For this reason, the air path and the openings to the exterior need to be correctly sized to ensure the stack effect pressures and the wind pressures, otherwise the airflow in the duct will tend to radiate to the interior and create overheating into the building.

For the mechanically ventilated facades, fresh air is forced with constant velocity into the cavity by mechanical means. The air rises and removes heat from the cavity and continues upwards to be ejected back to the atmosphere or be recirculated. With mechanically ventilated facades, the mechanical means can be a fan, which can be installed either at the inlet or the outlet of the duct. In most cases, it is placed in the outlet in order to drive the heated air into the building to provide space heating in winter.

BIPV system can be installed either to produce electricity only, or to provide both electricity and space heating. The last one can be done if the heated air into the duct behind the PV, is diverted inside the building with mechanical means to provide space heating. As already mentioned earlier, such a system is named BIPV/T. Most of the systems installed are of this type and always utilises the heated air for indoor space heating. These systems require a fan to drive a controlled amount of air into the building instead of leaving it to go naturally to the environment. Without a fan, the air can also be driven into the building through a specific duct, but due to the small air velocities that are developed naturally by the buoyancy effect from pressure differences across the duct, only areas close to the external wall can be heated. This is usually adequate, depending on the building. The BIPV systems that are used for electricity production only, do not require mechanical means to drive the air, as it is naturally driven to the environment.

In addition, the natural ventilation of the BIPV system does not require technical means e.g. a fan to move the air and cause the flow, and the overall cost of the system is lower than for a system with forced ventilation.

Under those circumstances, it is believed that before each installation, a study should be carried out in order to choose the best system for each situation. Consequently, the type of ventilation in BIPV double facades can be either forced or natural. This depends on the use of the system whether the heated air is to be used to heat the building or not, and the climatic conditions (hot or cold climates). In climates with hot summers and cold winters, in summertime the temperature of the air in the gap between the PV and building's wall will get very high, the heat energy must be dissipated as much as possible by forced ventilation, but can be driven directly into the building during winter time.

The high power consumption of the ventilation systems makes the construction unprofitable if the ventilator is used only for the facade. The main argument for PV facades exists because of standard forced ventilation systems that are present in large office buildings. For an already existing mechanical ventilation system, only the increased energy consumption corresponding to the additional pressure drop through the facade must be considered. The PV façade can be considered as an architectural design concept suited to prestige buildings. Compared to other façade types the price is within the same range. Fux (2006) wrote that according to Aurer (1998) in comparison to a representative granite façade, the PV façade is more economical.

2.4 Solar Architecture

As BIPV systems and PVs on buildings are part of the solar architecture in general, it is interesting to see how solar architecture began. In the early stages of solar architecture, orientation to the sun was

seen as an unalterable law. In cold places, people tried to have solar gain on their buildings, but in hot regions the protection from the sun was an important factor to the people's thermal comfort and the needs for cooling (Schittich, 2003). The first applications of solar architecture were in ancient Egypt. The design of the temples in Egypt, was based on the orientation of the sun. However, the first construction that characterized to be solar architecture design is the Socrates Megaron House in ancient Greece. The building is orientated south where it was open. The trapezoidal plan leads the sunlight into the building in winter where the sun is lower. On the other hand, the summer where the sun is higher, the portico creates cold and shady interior conditions (Schittich, 2003). As solar architecture was developing, a new opportunity opened for manufacturers and engineers. In 19th century the new way to manufacture glass had started and the price of the glass dropped dramatically. This opportunity helped the solar architecture and allowed architects to create large openings for solar gain without the problems of expensive glass (Schittich, 2003).

PV facades is more than a simply new style of building facades. Integrating the technical and functional requirements of the solar architecture into an aesthetically satisfying comprehensive concept presents both a challenge and an opportunity for architecture.

The fact that BIPV is used on the external envelope of the building opens many opportunities for creative and interesting building designs rather than boring and repeated facades.

PV façade technology is a challenge for architects and engineers. Studies from Luque and Hegedus (2003) and Probst (2008), discuss the position of architecture on the PV facades, the ways of application and the types of PV cells that are preferable in terms of the aesthetics. In general view, it can be said that the opinion of architects in this topic is divided to those who support the PV facades and use it as part of their design and those who believe that PV façade eliminates their creativity.

Scognamiglio and Røstvik (2012) stated that engineers and architects should try to create a bridge over scientific knowledge and architecture's practice. From 1990 up to now, in many buildings PVs has been used in a very successful way from the architectural point of view both in new and existing buildings. The most important reason that these systems should be used in buildings is the Zero Energy Buildings (ZEB) scenario described by the directive ED2010/31 EU. The directive states that from 2020 all new buildings will have to be of nearly zero energy consumption. This might be a revolution for architecture and photovoltaics, but there are both cultural and technical difficulties to defeat, for example the way buildings are designed and the way PVs are designed in buildings. In the future, design of the buildings has to consider not only the space people use directly but also the space required to be provided so as to produce adequate quantities of electrical and thermal energy from RES.

It is repeatedly discussed all these years that in the past the engineers used to take into account only the energy aspects in order to ensure the diffusion of the zero energy buildings. The most important point, is that the role of the PVs usage on buildings will be undertaken by architects and engineers who are amongst the main actors of this revolutionary change. To increase the usage of BIPV, architects and engineers should cooperate to discuss what is the architectural needs and in which sectors the engineers should focus for more development.

According to Cerón et al. (2013), from architect's point of view the formal aspects of the materials are as important as the physical and functional integration. Thus, PV sector and construction industry must work together with architects and join their experiences and knowledge in order to develop innovative elements to satisfy all related sectors and comply with all regulations.

Probst and Roecker (2012) give an explanation of the important formal aspects that architects take into account for their design. These formal aspects are called 'aesthetics' and deal with all the system's characteristics that affect the building's appearance. Firstly, the position and the dimension of the collector fields must be united with the architectural composition of the whole building and not only with the related façade. Secondly, the visible materials, textures and colours should be adaptable with the other materials of the building. Thirdly, the module size and shape have to be compatible with the grid composition of the building and the dimensions of the other facades. Finally, the jointing types have to be carefully considered for the product choice, as they may underline differently the modular grid of the system in relation to the building.

The BIPVs are divided into five main categories according to how the BIPVs appears on the building and how BIPVs affect the overall design of the building (Luque and Hegedus, 2003):

1. Invisible integration: To achieve that, usually thin-film PV elements are integrated at roofs. Often, invisible integration happens on historical buildings and on traditional, existing or new buildings where the PVs are not to be visible.
2. PVs added to the building's design: This means that PVs are added to the building when the design phase is finished and even when the constructions of a building is finished. In this case, the PV system is not really integrated but the architectural appearance of the PVs is still good.
3. The PVs add to the architectural appearance: This happens, when PVs are integrated on a building without changing the whole architectural appearance and image of the building. Therefore, it is a good PV integration on the context of the building.
4. The PVs determine the architectural appearance: In this case, a building is designed according to the PV system's needs and it plays a significant role in the architectural appearance. This factor does not necessarily mean that the architectural quality of the building is limited.

5. BIPVs lead to a new architectural style: BIPVs alone and possibly in combination with other solar strategies like Building Integrated Solar Thermal Systems (BISTS) and other environmental strategies can develop a new architectural design and style.

2.5 Air flow in BIPV systems

During the last years, the idea of exploiting the rejected heat of the PV modules is gaining attention. Various studies show that many researchers tried to understand the air flow between the PV and the construction material in several ways. The following sections will present studies carried out for this purpose either by experimental procedures or simulations.

2.5.1 Simulation based studies

According to Wang et al. (2006) BIPV has significant influence on the heat transfer through the building envelope because of the change of the thermal resistance by the various building elements. They used four different roof designs to assess the impacts of BIPV on a building's heating and cooling loads in China. The performance comparisons for the different BIPV roofs have been made based on the one-dimensional transient model for Tianjin, China. It was concluded that PV roof with ventilated air gap is suitable in summer because the integration leads to the low cooling load and high PV conversion efficiency. On the other hand, a PV roof without ventilated air gap is suitable for winter due to the combination of the low heating load through the PV roof and high PV power output.

Sanjuan et al. (2011c) carried out a study about the energy performance of an open joint ventilated façade (OJVF) compared with a conventional sealed cavity façade. The OJVF is shown in Figure 2.8. The term 'open-joint ventilated facades' refers to a building system in which coating material like metallic, ceramic or stone is hanged by means of a metallic frame structure to the exterior face of the wall creating an air cavity between wall and slabs. The OJVF is usually classified among the light weight or advanced integrated facades.

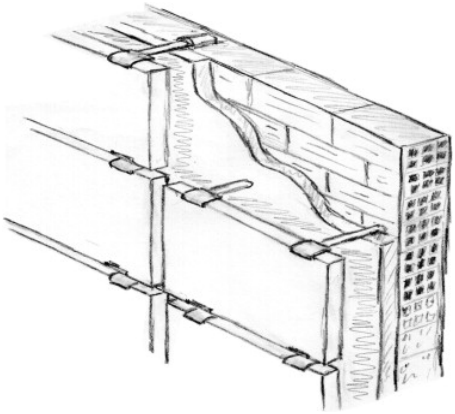

Figure 2.8. The Open Joint Ventilated Façade (Sanjuan et al., 2011b).

As stated by the authors, the main difference between the OJVF and other advanced façades is that, as a rule, the ventilated air chamber is only open to the exterior at the top and at the bottom while, in the OJVF, the exterior coating is placed in an arrangement of tiles or slabs and a series of thin gaps (joints) are shaped from slab to slab, enabling the exterior air to enter and leave the cavity all along the wall. A typical cross section of a conventional cavity façade and an OJVF is shown in Figure 2.9.

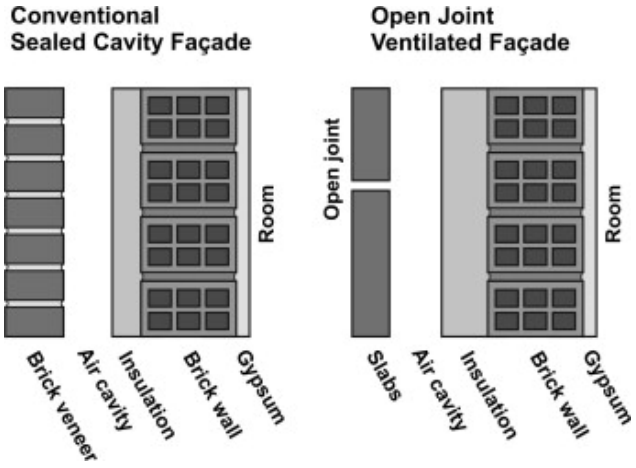

Figure 2.9. A typical cross section of a conventional cavity façade and an OJVF (Sanjuan et al., 2011b).

The objective of their work was to investigate the thermal and fluid dynamic phenomena taking place in OJVF under solar radiation and to establish a methodology to quantify the energy savings produced by an OJVF in comparison with a conventional façade. The thermo fluid-dynamic behaviour of both systems has been analyzed with computational fluid dynamics (CFD) techniques using FLUENT 6.3 and the results of the 3D simulations conclude that OJVF can help to achieve important energy savings in climates with hot summers and mild winters.

Although the work done by Sanjuan et al. (2011c) was not based on BIPV facades specifically but generally for Double Skin Ventilated Facades, the idea of the open joints between the panels might be a good solution for the PV integration in order to reject the excess heat in the air gap.

Mei et al. (2003) presented a dynamic thermal model based on TRNSYS, for a building with a ventilated PV façade with solar collector system. They used the model from an earlier work by Eicker et al. (1999) where a dynamic general finite element thermal model for ventilated PV facades was developed. Based on this and TRNSYS software, a completed thermal model was designed for this study. From the results, it was concluded that the cooling loads were higher with the PV façade for all locations considered, while heating loads were depended on location.

Gan (2009) used a CFD method to assess the effect of the air gap between PV modules and the building envelope on the performance of the system in terms of the cell temperature for a range of roof pitches and panel lengths and to determine the minimum air gap that is required to minimize the PV overheating. Initially, the air flow patterns and the images of the temperature distribution around the module, shows that while the roof inclination increases, the velocity of the air increases but the PV temperature decreases. Additionally, it has been found that the mean velocity in the air gap behind PV modules increases with size of air gap, length of panel and the angle of pitch for roof-mounted modules. The mean and maximum PV temperatures decrease with the increase in the air gap and roof pitch. The mean PV temperature also decreases with increasing panel length for air gaps larger than 8 cm. The maximum PV temperature associated with hot spots generally increases with panel length but for roof-mounted modules it decreases when the panel length increases from two modules to three modules and the air gap is about 0.1–0.11 m. For single module installation, the air gap should be between 0.14 m and 0.16 m in order to minimise the mean temperature.

2.5.2 Experimental based studies

Straight to the problem of PV overheating, Kaiser et al. (2014) performed an experimental study of cooling BIPV modules by forced convection in the air channel. The aim of the study was to investigate the influence of the air gap size and the forced ventilation on the cell temperature and consequently on the electrical efficiency of the PV module. Experiments took place on a BIPV configuration for different values of solar radiation, ambient temperature, aspect ratios, and for several forced ventilation conditions. The results presented showed that a critical aspect ratio close to 0.11 can be considered to minimize overheating of PVs. It is also concluded that the forced ventilation conditions (v=6 m/s) resulted to bigger power output increase than the natural ventilation cases (v=0.5 m/s).

It is noteworthy to mention that as years pass the outcomes and opinions of the researchers change. This can be seen when comparing the study of Kaiser et al. (2014) and Mei et al. (2003) where the second one stated that forced convection is necessary in order to cool the PV surface and that natural convection is not able to do this. Eleven years later Kaiser et al. (2014) stated that forced ventilation increases power output by 19% in comparison with natural ventilation. This means that natural convection can circulate the air but not so good as the forced ventilation does. There are also many studies investigating various configurations to improve the systems with natural ventilation because the cost of the energy needed by the mechanical means to drive the air is high.

However, regarding the study by Kaiser et al. (2014) it is important to mention that although 19% power increase was observed in forced ventilation conditions, the authors did not take into account the energy spent by the fan to cool the PVs which may overcome the energy gained by the PVs due to the cooling.

Brinkworth et al. (1997) found that a reduction up to 20 K can be obtained on the PV due to an air flow in a duct behind the PV component. That leads to significant increase in the electrical output and reduction of heat gain into the building. Measured losses of peak output power of around 0.5% per K temperature rise have been reported for monocrystalline silicon cell arrays. Additionally, the air velocity in free flow duct have been shown to vary across the duct as well as in the flow direction with small numerical values. They noted also from previous work that low value induced air velocity is expected and they suggested to use Laser Doppler Anemometry for reliable and accurate results instead of hot wire anemometer. This observation is reported also in other studies (Tonui and Tripanagnostopoulos, 2008).

Brinkworth (2000) set out a practical procedure to determine the flow and convective heat transfer in inclined cooling ducts as used in PV installations. The procedure covers the case of free convection by buoyancy due to heat input into the duct, when temperatures are high, the case of forced convection induced by wind pressure differences between the duct ends, and the case of mixed flow conditions when both influences occur together. For all cases, the flow regime was either laminar or turbulent. As mentioned by the author, the main objective was to generate a set of heat transfer coefficients at the duct walls for incorporation into the overall thermal model of the PV installation. A good explanation of the solution method has been given describing the driving forces and the resistance to flow. The case selected is one of the standard forms which is probably the closest to situations found in practice. This is the flat duct formed between parallel plates with a uniform heat flux into the fluid on the one side and adiabatic wall on the other. This is considered as a fair approximation to real situation where the ongoing heat flow is much lower when a cooling duct is used than without it.

Generalized solutions have been given for the representative case to illustrate the effects of the principal variables showing for example the conditions in which wind driven flow is likely to dominate free convection due to heat input.

Brinkworth et al. (2000) developed a simplified method to estimate the flow rate in naturally ventilated PV cladding for buildings. The method is based on one dimensional loop analysis where the buoyancy forces are balanced by the pressure drop from friction. The hypothesis tested is that the form and values for the friction factors and internal heat transfer coefficients for the buoyancy driven cases are the same as those for forced convection in ducts.

The single loop theory used for this study considers a PV cell array attached to the exterior of a channel which may be tilted from horizontal. The usual approximation for operation in real conditions, is that the system is considered to move through a sequence of quasi steady states. Therefore, the mass flow rate will be constant everywhere in the loop flow path (thin line in Figure 2.10). However, this cannot represent the real conditions for outdoor performance of the system unless a fan is employed to control the steady flow.

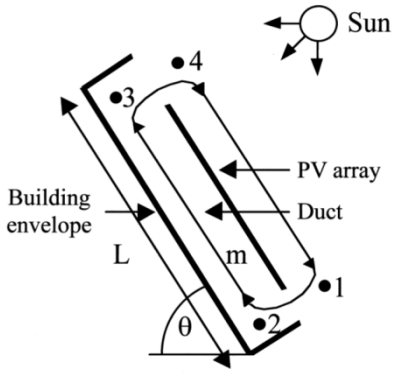

Figure 2.10. Schematic cross section of PV cladding (Brinkworth et al., 2000).

The authors concluded that excellent agreement was observed between the modelled and measured mass flow rate; and consequently, the hypothesis proved valid. The determination of two parameters for an equivalent Nusselt-Reynolds number relationship was also successful. The model developed in this study is simple enough to use in a spreadsheet both to analyze existing experimental data and to be used as a preliminary prediction design tool for PV cladding on buildings.

According to Brinkworth and Sandberg (2006), the most important variable to be fixed in the design of a PV cooling duct is the depth, and hence the hydraulic diameter of its cross section (D_h). A series of measurements with full scale test rig have been carried out to validate the flow and heat transfer in the duct under still air conditions when the temperature rise is greatest. The results shown that there

is an optimum value of the design variable, such that for an array of length L the minimum temperature of the PV occurs when the ratio L/D_h is about 20. As shown, the optimum value is not affected considerably by other quantities, including the slope of the array. In addition, it is shown that the array temperatures are strongly reduced by wind effects which increase both the heat lost from the front surface of the array and by enhancement of the flow in the duct. The measurements made on the full-scale test rig agree with the theoretical estimations of the temperature of the heated wall on the PV side.

Brinkworth (2006) continued the work done earlier by Brinkworth and Sandberg (2006) and carried out a theoretical foundation for the geometry of the PV cooling ducts. He confirmed that the temperature rise on the face of the duct near its exit and the PV array's temperature is minimized when the ratio L/D_h of the duct length to its hydraulic diameter is around 20. This ratio minimizes the loss of efficiency of the PV cells because of the higher operating temperature. It is also proved that this ratio is independent from the array slope as mentioned earlier.

Li and Karava (2012) performed 3-dimensional steady state Reynolds Averaged Navier-Stokes (RANS) CFD simulations and evaluated the performance of five turbulence closure models, potentially suitable for modelling UTCs (Unglazed Transpired Solar Collectors) in terms of accuracy and computing cost. The predicted air velocity, air temperature and turbulent kinetic energy were compared against experimental data from the literature and those obtained from the experimental procedure carried out with a solar simulator. The results show that although the Reynolds Stress Model can provide more detailed features of flow in comparison with other models, it does not result necessarily in better performance. The analysis of a BIPV/T system with two types of PV panel arrangement, revealed that under 3 m/s wind speed, the integrated system with UTC can provide up to 1.2% higher electrical efficiency which canl increase for higher suction velocity. Additionally, it was shown that the small PV modules can provide slightly higher overall efficiency compared to a system with larger PV modules covering the same area.

Sanjuan et al. (2011a) carried out a study to present a Particle Image Velocimetry (PIV) technique to measure the velocity field inside the air cavity of an OJVF model in laboratory conditions. The study focuses on a generic geometry and investigates the turbulent natural convection inside the ventilated cavity under radiation conditions. They have performed measurements in the vertical central plane of the cavity for three heating conditions corresponding to $Ra= 5.92 \times 10^8$, $Ra= 9.19 \times 10^8$, and $Ra= 1.35 \times 10^9$, where Ra is the Rayleigh dimensionless number based on the channel height. A total of 8 vertical runs were necessary to analyze the whole length of the air cavity during the experiments. For each run, a total number of 300 snapshots were recorded with a frequency of 7 Hz. The velocity vectors

inside the cavity show the importance of the number of joints in the behaviour of the façade. As can be seen in Figure 2.11, the air enters through the first and second open joints and leaves the cavity through the fourth and fifth open joints.

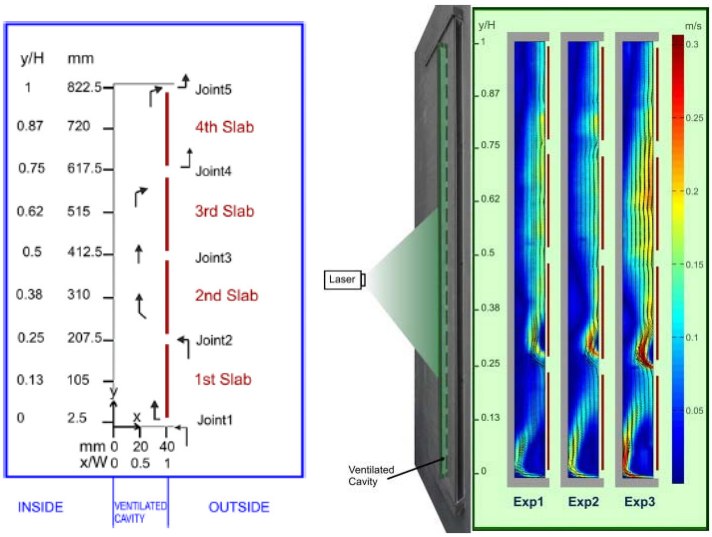

Figure 2.11. Velocity vectors measured in experiments for the three experiments with three values of Ra (Sanjuan et al., 2011a).

Due to the pressure equilibrium created inside the air cavity, the exterior air does not enter or leave the cavity through the third open joint. This behaviour of the flow shows that the total height of the cavity as well as the number, size and distribution of the horizontal joints are fundamental parameters that determine the fluid pattern inside the OJVF.

As shown in the study of Sanjuan et al. (2011a) complex air flows generated inside the naturally ventilated cavity by the existence of open joints. For this reason, the use of advanced fluid measurements and simulation techniques are necessary. Accordingly the authors in Sanjuan et al. (2011b) have tested different turbulence and radiation models available in commercial computational fluid dynamic codes, on a three-dimensional model, and the results have been compared to those of the PIV measurements. The simulations have been carried out on a 3D model with the same geometry, materials and boundary conditions as the experimental unit of Sanjuan et al. (2011a). The results show that the ventilation produced by buoyancy is enhanced by the cavity height and incident radiation. Despite the number of the open joints, the flow enters from the low slabs and leaved the cavity from the upper ones.

Sanjuan et al. (2012) investigated the thermal and energy behaviour of the OJVFs. The model used was the one presented earlier in Sanjuan et al. (2011b) and the investigation was carried out by 2D PIV techniques with laboratory measurements. Instantaneous and time averaged velocity fields along the

cavity were obtained for five different radiation conditions. The results gave a good description of the flow structures in the cavity. It was shown that under radiation conditions, the natural thermal convection produces a chimney effect that forces external air to circulate along the air cavity. Accordingly, a part of the heat is removed from the façade and as a result the heat transferred to the building is reduced.

Yang and Athienitis (2014) carried out a series of experiments on a prototype open loop air based BIPV/T system with single inlet. The experiments were performed with a large scale solar simulator in Concordia University (Figure 2.12). Based on the experimental results, a numerical control volume model is developed and validated. Additionally, improved designs with multiple inlets and other means of heat transfer enhancement are studied through simulations.

Figure 2.12. BIPV/T air collector tested horizontally and in 45° slope, in the solar simulator and air collector testing platform (Yang and Athienitis, 2014).

Different radiation levels were considered for the experiments using the solar simulator, while the flow rate in the channel is controlled with Re from 1200 to 10000. The artificial winds were parallel to the collector with a controlled speed ranging from 1.6 to 3.5 m/s. As expected, with increasing wind speed, the thermal efficiency is reduced.

It was concluded that the peak PV temperature in the 2-inlet system is lower than in the 1-inlet system, which means that the PV degradation with high temperature is reduced in the two-inlet system and by extension in a multi-inlet system. Simulations show that the application of 2-inlets on a BIPV/T collector, increases its thermal efficiency by 5%. The addition of a solar air heater increases the thermal efficiency by about 8% with a smooth air channel and by 10% with a wire mesh packed air cavity.

Zogou and Stapountzis (2011a) examined an improved concept of incorporating PV modules to the south facades of an office building exploiting both the electricity produced and the heat rejected from

the module to increase building energy efficiency. The PV modules were integrated to the building in a form of double façade which employs a duct for ventilation purposes. The configuration of the specific building integration is presented in Figure 2.13.

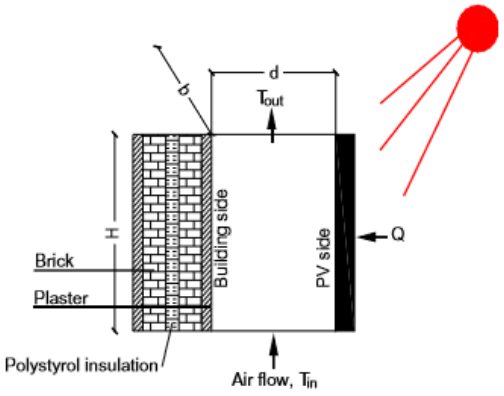

Figure 2.13. Heat transfer in the duct behind the PVs at the considered building integration concept (Zogou and Stapountzis, 2011a).

The heated air from the duct was employed to cover the ventilation needs of the building as well as a part of the heating loads. In order to investigate the buildings energy performance after these modifications on its envelope, simulations for typical winter and summer weather conditions were carried out. Three special cases were examined for the fluid convection correlations; no flow through the channel, laminar flow through the channel and turbulent flow through the channel. Additionally, three alternative cases (apart from the reference case without PV façade) were tested regarding the PV façade; 1) PV panels in contact with the outer wall of the building, 2) PV panels with 0.15 m air gap between the panels and the wall with the heated air to flow at a rate of 400 kg/h, and 3) the panels again in a distance 0.15 m from the wall but the flow rate is limited to 133 kg/h. The reference building is located at Volos, Greece and the relevant Typical Meteorological Year (TMY) file is employed for the simulations using TRNSYS software. The results indicate that the selection of the flow rate and duct dimensions are critical to the performance of the PV façade. Additionally, different design of the system must be adapted to different climatic conditions and building orientations.

In another study Zogou and Stapountzis (2011b) stated that, in principle, a steady state free or forced convection coefficient could be estimated by a typical Nu=*f*(Gr, Pr) or Nu=*f*(Re, Pr) relationship respectively. However, in real world, the duct is quite complex due to the important role of radiation and the transient phenomena involved require an experimental approach. They investigated experimentally in real insolation conditions the transient thermal behaviour of the basic structural module of a double skin photovoltaic façade. A testing device was designed to test the transient

thermal and electrical behaviour of the basic building element of the concept and it was tested outdoors in real insolation conditions at Volos, Greece. The device is shown in Figure 2.14.

Figure 2.14. Front and back side of the test device representing a double façade with PV integration (Zogou and Stapountzis, 2011b).

The panels could be oriented south or west in three operation modes; natural convection without fan and forced convection cooling by means of two different capacity axial fans with 110 and 190 m^3/h nominal flow rate with 20 and 22 W power consumption respectively. Five temperatures were measured using thermocouples (inlet and outlet positions and three surface temperatures at the back of the PV) and the solar radiation with the use of a pyranometer placed vertically at the upper left corner of the PV panel. The use of fan resulted to a decrease of the mean panel temperature and a respective increase in cell efficiency, especially for the higher capacity fan. The results point to the complex character of the air flow field in the cavity and the requirement to further investigate it by hot wire anemometry.

A year later Zogou and Stapountzis (2012) presented a study showing the results from flow visualization and hot wire anemometry measurements performed on the basic structural module of a double skin photovoltaic façade presented previously in Figure 2.14 from the same authors. The air gap width was set to 150 mm and at the top of the duct there was a circular outlet with a diameter of 125 mm. As a first step to understand the air flow in the duct, flow visualization was performed in steady state indoor conditions as shown in Figure 2.15.

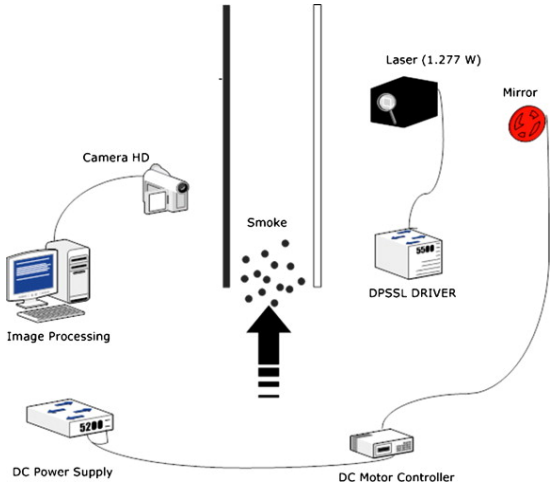

Figure 2.15. Schematic representation of the flow visualisation layout (Zogou and Stapountzis, 2012).

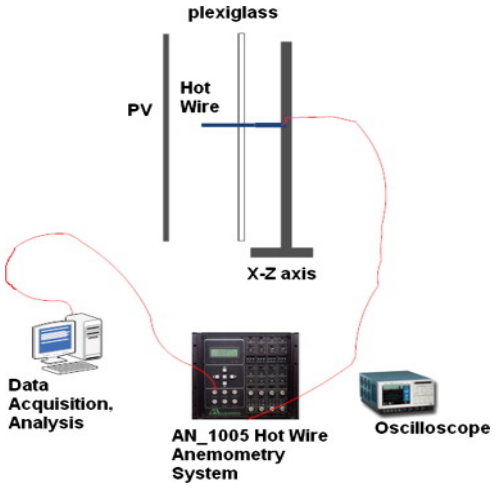

Figure 2.16. Schematic representation of the hot wire anemometry measurements (Zogou and Stapountzis, 2012).

Three operation modes were studied; constant temperature air flow with low capacity fan, constant temperature air flow with high capacity fan and air flow field with buoyancy flow produced by the heating of the PV panel to its typical operation temperature. The flow visualization experiments indicate that the flow was in the transitional flow regime. The next step was to perform hot wire anemometry measurements (Figure 2.16). The measurements were taken at 4 vertical positions along centreline of the device. The results were combined with CFD computations to calculate heat transfer coefficients and help to understand the specific PV/T concept. The results of this study show that the selection of the flow rate and the heat transfer characteristics on the back sheet are critical to the performance of the PV façade. At this point it is worth mentioning that in the buoyancy flow the maximum air velocity recorded was around 0.12 m/s which is very low in comparison with the 0.5 m/s assumed by Kaiser et al. (2014) to represent the natural ventilation.

Bazilian et al. (2002) investigated thermographically a large scale residential BIPV system in Sydney, Australia. The thermographic analysis gave both quantitative results and qualitative results. The quantitative results were in good agreement with the experimental data of operating temperatures in various parts of the system. The qualitative results give good insight into the nature of the BIPV installations in attic spaces. The system is being used to test the feasibility of a heat recovery unit that will utilize the waste heat from the backside of the PVs while cooling the panels. From the infrared (IR) thermographic analysis the interior of the BIPV array was found to be distinctly hotter than the surrounding roofing on a clear sunny day.

An extensive study on the air cooling of a PV/T commercial air collector by natural flow has been carried out by Tonui and Tripanagnostopoulos (2008). The experimental tests were carried out on a small prototype

PV/T air system and the rectangular air duct box behind the PV was designed with channel depth of 0.15 m. The built system was mounted at a tilt angle of 40°. As explained by the authors, the buoyancy force is the driving force in natural flow systems and controls the induced flow rate through the air channel. The buoyancy force is a complex function of the design and operating parameters of the system. Higher buoyancy forces are created when the temperature of the air rises and this cause larger air flow rate through the collector. The opposing forces are the frictional forces between duct walls and airflow as well as pressure gradients at the entrance and exit of the flow channel. At steady state, the buoyancy forces and the opposing forces are balanced and control the induced air flow rate in the channel. The latter is the basis to derive the flow rate in the analysis carried out by the authors. They also investigated the effect of the incident radiation, the effect of the channel's depth, the effect of the collector's length and the effect of the exit vent. Regarding the incident radiation, it was observed that the induced mass flow rate increases with increasing the solar radiation due to the increased radiation intercepted by the collector. Regarding the channel's depth, the results show that there is an optimum depth at which the induced mass flow rate is maximum, which occurs at 5-10 cm. As shown in the test to examine the effect of the collector's length, the thermal efficiency increases with the collector's length increase while the electrical efficiency decreases when the collector's length increases. The outcomes of this study gave the optimal, configurations for the PV/T solar systems.

Sanvicente et al. (2013) carried out an experimental study on natural convection flows in differentially heated open channel configurations. The test rig was consisted of two walls, one heated uniformly and the other not heated at all. Emphasis is given in the kinematic characteristics of the flow using PIV system which allows to investigate the mean velocity field and velocity fluctuations at different heights in the channel. The results showed that due to the repeatability of the results the measured thermal characteristics was done with a good accuracy, but for the flow kinematic results the agreement was not very good. The experimental data showed that the flow is not fully turbulent but also not really laminar for the range of Rayleigh number considered.

2.6 Heat Transfer Analysis of BIPV systems and DSF

The DSVF systems as well as the BIPV façade systems can be analyzed by considering two vertical parallel plates with different surface temperatures, as well as different indoor and outdoor conditions temperatures. Considering the front surface to be a PV panel facing towards the sun and the back surface to be a building's wall, the two parallel surfaces have different temperatures that are responsible for the heat transfer and the fluid flow in the air gap between them.

A BIPV system considered as a double skin solar façade with two vertical plates is very complex to be investigated in terms of its thermal behaviour, because of the difficulty to observe the flow in the duct while different heat transfer mechanisms coexist. However, the fluid mechanical conditions and heat transfer conditions are of a great importance when evaluating the thermal situation within the façade air gap.

After a research carried out to find previous studies on the heat transfer analysis of DSVF and BIPV facades, it is pointed out that there are many studies carried out on the heat transfer analysis of the DSVFs, but very few were carried out on the BIPV facades and especially to those that are based on the natural convection. The ventilation of the solar facades with natural convection is very little investigated in comparison with the forced circulation systems. Regarding particularly the theoretical and numerical heat transfer analysis considering the natural convection coefficients, there are no studies regarding the BIPV systems. Most studies regarding natural convection of BIPV systems, investigated the air flow behaviour in the air duct or the thermal analysis of the system thermographically.

This is mainly because of two reasons; the complexity of the natural flow of air in the duct between two plates exposed to different conditions each one, and the doubt if the natural ventilation is adequate to cool the system. Most researchers found the mechanically ventilated facades worthier to be investigated because of the flexibility of the system. A system with mechanical means to drive the air can be customized in order to operate in different conditions for different applications. This is not the same for the systems with natural ventilation because the natural flow may not be adequate to cool the PVs or drive naturally the air indoors for space heating and control the flow. Moreover, the investigation of the heat transfer behavior of a fluid with controlled flow has more known parameters to enable one to reach reasonable conclusions. On the contrary, the investigation of the heat transfer of a fluid that flows naturally without any known parameters and conditions makes the study more complex and the results might not be so realistic because of the way all the parameters are measured, the rationale of the results, the conditions under the experiments, the assumptions made etc.

Therefore, the existing knowledge on BIPV naturally ventilated facades is very limited. Considering that the published correlations of the heat transfer coefficients between two vertical isothermal plates with natural convection are empirical, in case that one of the assumed parameters is not applicable, the whole situation changes and new conditions should be applied. In the case of a BIPV system, the problem is complex because the two vertical plates cannot be isothermal because the integrated PV usually is colder at the bottom side where the air enters the duct and hotter at the top where the air moves through the duct. This is the same for the BIPV systems with natural air flow as well as for the systems with mechanical means to drive the air. The difference in the systems with forced convection is that the air flow rate and air velocity

are known values because they are adjusted by technical means like fans, and this makes the investigation easier.

Accordingly, the studies on this topic are mainly classified based on the type of the flow and convection type. These categories are mainly the free convection, the forced and mixed convection and convection between vertical plates in enclosures. An extensive discussion on the three categories has been made by Fux (2006). Additionally, Quesada et al. (2012) presented a comprehensive review of solar facades and referred to transparent and translucent active and passive solar facades studies. In their paper, they highlight the categories of ventilated facades and semi-transparent building integrated photovoltaic facades.

The following section presents studies of the BIPV systems based on the heat transfer analysis. Some of them are mainly focused on the development of Nu number correlations and convective heat transfer coefficient correlations. The section is divided in two parts, to the studies deal with the natural convection and the studies based on forced convection in solar facades or roofs. As said earlier, there are not many studies of the natural convection in BIPV systems and thus the first part presents some of the most known studies carried out in similar aspects such as DSF, PV applications, air ducts and air channels. The analysis of those systems is helpful to understand the thermal behaviour of the BIPV systems with natural convection.

2.6.1 Natural Convection in BIPV systems

Various studies in the literature refer to the natural ventilation in the air gap of the BIPV facades but not all of them are based only on the natural convection mechanism. Some of the authors studied the natural convection in double skin facades and PV facades have already been presented in previous sections such as Brinkworth (2000); Sanjuan et al. (2011a; 2011b); Tonui and Tripanagnostopoulos (2008); Zogou and Stapountzis (2011b).

Fossa et al. (2008) made an experimental study on natural convection in an open channel in order to investigate the effect of the geometrical configuration of heat sources on the heat transfer behaviour. Accordingly, a series of vertical heaters are cooled by natural convection of air flowing between two parallel walls. The experimental device used for this investigation is a simplified small-scale representation of a building double façade with PV modules on the external side, eventually separated by glass partitions. A series of tests have been carried out by changing the values of the panel distance, the voltage supply per heater series and the heating configurations. The experimental results show that the effect of the air gap and heating configuration noticeably change the heat transfer conditions at the overall heat flux and suggests the best possible configurations of the BIPV modules in building applications. In terms of wall

temperatures, the results show that the effect of increasing the channel spacing is that the working temperatures for all the modes investigated were reduced. Additionally, new local and wall average Nu numbers correlations were obtained with respect to proper Ra number and finally they were compared with correlations from the literature.

The Nusselt numbers are based on the temperature difference between the wall and the fluid inlet temperature, either on a local (Equation 2.14) or average basis (Equation 2.15).

$$Nu_{\mathrm{y}} = \frac{\dot{Q}\, y}{(T_w - T_\infty)k} \qquad 2.14$$

$$Nu_{\mathrm{d}} = \frac{h_{ave} d}{k} \qquad 2.15$$

Where:

$\dot{Q}$: local convective heat flux (W/m^2)

y : Generic vertical coordinate (m)

T_w : Temperature at the heated side (K)

T_∞ : Temperature at the conditions of inlet air (K)

k : Thermal conductivity (W/m K)

The wall average heat transfer coefficient is calculated as an integration of local values of heat flux and wall temperatures as shown in Equation (2.16). The thermophysical properties of the air are evaluated at the reference temperature $(T_w - T_\infty)/2$.

$$h_{ave} = \frac{1}{H}\int_0^H h_z dz = \frac{1}{H}\int_0^H \frac{\dot{Q}}{T_w - T_\infty} dz \qquad 2.16$$

Where

H : Heated surface overall height (m)

z : Vertical coordinate from heated section leading edge (m)

h : Heat transfer coefficient (W/m^{2}K)

La Pica et al. (1993) studied the free convection of air in vertical channel. The experimental procedure was carried out with a 2.6 m height model with rectangular cross section with variable channel width. One of the channel walls was heated with a uniform flux and the tests made with different values of channel gap and heating power. Since one wall was subjected to heat flux, the study can be correlated with a case of PVs which are exposed to solar radiation.

As a result, two empirical formulas were found, giving Nu and Re numbers as functions of Ra number and the geometrical parameters s/H where 's' is the width and 'H' is the height of the model. The two formulas are shown in Equations 2.17 and 2.18 respectively. In all cases studied, the convective coefficient h ranges between 5.1 and 4.8 W/m^{2}K with a slight tendency to increase when heat flux increases.

$$Nu = \frac{h\,s}{k} = 0.9282\,Ra^{0.2035}\left(\frac{s}{H}\right)^{0.8972} \qquad 2.17$$

$$Re = 0.5014\,Ra^{0.3148}\left(\frac{s}{H}\right)^{0.418} \qquad 2.18$$

s : Width of the model (m)

H : Height of the model (m)

As mentioned previously, Manz (2003) and Xamán et al. (2005) considered the double skin façade concept as a rectangular cavity with air. The first carried out a numerical simulations of heat transfer by natural convection in cavities of façade elements. The objective of this work was to compare the results obtained by CFD code with empirical correlations derived from experiments from the literature including laminar and turbulent flow. The results from the CFD and the correlations from literature are plotted as shown in Figure 2.17. As can be seen from the graphs of Nu=*f*(Ra, A), with exception of correlation of Yin et al. (1978) the calculated Nu numbers do not deviate more than 20% from analytical correlations. In fact, the deviations are less than 10% for A=20. Xamán et al. (2005), carried out a numerical study of heat transfer by laminar and turbulent natural convection in tall cavities of façade elements and compared their results with the ones obtained from Manz (2003).

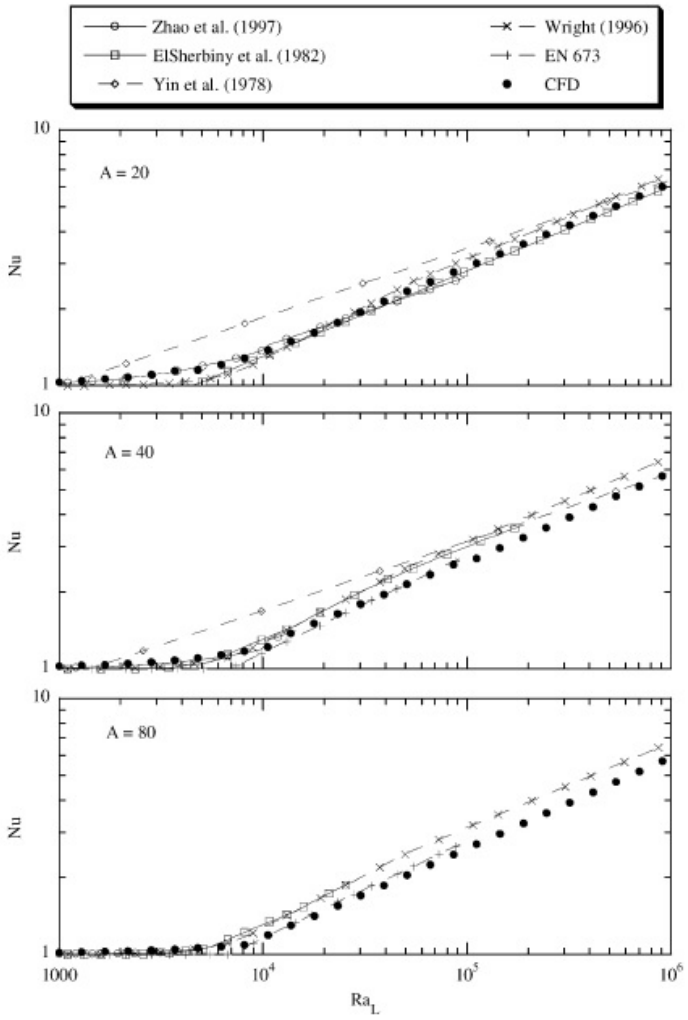

Figure 2.17. Comparison of Nu=f(Ra, A) of the correlations from literature and CFD (Manz, 2003).

Hollands et al. (1976) presented experimental measurements on free convective heat transfer rates for inclined air layers heated from below. The range of inclination angle tested was from 0° to 70° and the Ra number from subcritical to 10^5.

If Ra number is less than a critical value, of $Ra_{L,crit}$=1000, then the buoyancy force is insufficient to overcome the viscous force and the fluid remains stagnant. In this limit, the free convection problem reduces to a conduction problem.

Above the critical Ra number, Hollands et al. (1976) correlated the Nu number as shown in Equation (2.19), for inclination angles $\varphi \leq 60°$.

$$Nu = 1 + 1.44\left[1 - \frac{1708}{Ra\,cos\varphi}\right]\left(1 - \frac{(\sin 1.8\varphi)^{1.6}1708}{Ra\,cos\varphi}\right) + \left[\left(\frac{Ra\,cos\varphi}{5830}\right)^{1/3} - 1\right] \qquad 2.19$$

At a tilt angle between 75° and 90°, Ayyaswamy and Catton (1973) proposed the following relationship:

$$Nu = Nu_{L,a=\frac{\pi}{2}}[\sin a]^{0.25} \quad 2.20$$

Catton (1978) presented the following equations for vertical enclosures:

$$Nu = A\left(\frac{Pr}{0.2+Pr}\,Ra_L\right)^{n1}\left(\frac{H}{L}\right)^{n2} \quad 2.21$$

Where H/L is the Aspect ratio and for 1<H/L<2, A=0.18, n_1=0.28 and n_2=0. These values apply for most fluids with 10^{-3}<Pr<10^5 and for Ra Pr/ (0.2+ Pr) >1000. For larger wall separation where 2<H/L/10, A=0.22, n_1=0.29 and n_2=-1/4. These values are applied for Pr<10^5 and for Ra<10^{10}.

Bar-Cohen and Rohsenow (1984) carried out a study in order to find the optimum spacing of vertical parallel plates cooled with natural convection. They focused on the mathematical development and verification of composite relations and the formulation and solution of the optimizing equations for various boundary conditions. Equations for the Nu were extracted and optimum spacing (b_{opt}) for determining the channel width or spacing between surfaces forming a two-dimensional channel appropriate to various thermal constraints for symmetric and asymmetric, isothermal and isoflux boundary conditions. The symmetric characterisation represents two plates under the same conditions, isoflux or isothermal, and the asymmetric characterisation considers one of the two plates to be insulated while the other may be isothermal or isoflux. The relations of this study are presented below. The more representative case for BIPV is the last one as the PV receives a constant heat flux from the sun (isoflux) whereas due to its thickness, the wall at the building can be considered as adiabatic.

Isothermal plates, Symmetric

Nusselt number:

$$Nu_O = \left[\frac{576}{(Ra')^2} + \frac{2.873}{\sqrt{Ra'}}\right]^{-0.5} \quad 2.22$$

Optimum Spacing:

$$d_{opt} = 2.714P^{-0.25} \quad 2.23$$

Optimum Nu:

$$(Nu_O)_{opt} = 1.31 \quad 2.24$$

Isothermal plates, Asymmetric

Nusselt number:

$$Nu_O = \left[\frac{144}{(Ra')^2} + \frac{2.873}{\sqrt{Ra'}}\right]^{-0.5} \quad 2.25$$

Optimum Spacing:

$$d_{opt} = 2.154P^{-0.25} \quad 2.26$$

Optimum Nu: $$(Nu_O)_{opt} = 1.04$$ *2.27*

Isoflux plates, Symmetric

Nusselt number: $$Nu_{O,L/2} = \left[\frac{12}{Ra''} + \frac{1.88}{(Ra'')^{0.4}}\right]^{-0.5}$$ *2.28*

Optimum Spacing: $$d_{opt} = 1.472R^{-0.2}$$ *2.29*

Optimum Nu: $$(Nu_{O,L/2})_{opt} = 0.62$$ *2.30*

Isoflux plates, Asymmetric

Nusselt number: $$Nu_{O,L/2} = \left[\frac{6}{Ra''} + \frac{1.88}{(Ra'')^{0.4}}\right]^{-0.5}$$ *2.31*

Optimum Spacing: $$d_{opt} = 1.169R^{-0.2}$$ *2.32*

Optimum Nu: $$(Nu_{O,L/2})_{opt} = 0.49$$ *2.33*

Rohsenow et al. (1998) recommended a new formula for the Nu number calculation with the parameter C1 related to the Pr number. The correlations are:

$$Nu = ({Nu_{fd}}^{-1.9} + {Nu_{plate}}^{-1.9})^{-1/1.9}$$ *2.34*

Where

$$Nu_{fd} = \frac{Ra}{24}$$ *2.35*

$$Nu_{plate} = 1.32\ C1\ Ra^{1/4}$$ *2.36*

$$C1 = \frac{0.671}{\left(1 + \left(\frac{0.492}{Pr}\right)^{9/16}\right)^{4/9}}$$ *2.37*

Sparrow and Azevedo (1985) studied the effect of plate spacing on natural convection in an open ended vertical channel bounded by an isothermal and unheated wall experimentally and computationally. They analysed data which were based on the heat flux of two parallel walls the one heated and the other one adiabatic. The data were between Ra=200 and 80000 and found to the following expression:

$$Nu = 0.667\ Ra^{0.229}$$ *2.38*

Tiwari (2002) proposed a Nu correlation to calculate the heat transfer coefficient between the absorber plate and the air flow inside an air collector. The empirical correlation proposed by Tiwari (2002) becomes complicated for inclined plates with heated surface facing upwards for angles between 15° and 75° from the horizontal. The empirical equation proposed by Tiwari (2002) is shown in Equation (2.39) where the Ra_c is the critical Rayleigh number, equal to 1708 inside a rectangular cavity.

$$Nu_c = 0.14\left[Ra^{\frac{1}{3}} - Ra_c^{\frac{1}{3}}\right] + 0.56\,(Ra * \cos\theta)^{1/4} \qquad 2.39$$

Although the investigations done by Ayyaswamy and Catton (1973); Catton (1978); ElSherbiny et al. (1982); European Standard EN 673 (1997); Hollands et al. (1976); La Pica et al. (1993); Manz (2003); Wright (1996); Xamán et al. (2005); Yin et al. (1978); Zhao et al. (1997); Tiwari (2002) are very popular and the correlations (especially the one from Hollands et al. (1976)) are widely known from various heat transfer books and used by many researchers, these studies considered the DSF as a case with air in a cavity/enclosure. It should be noted however, that the heat transfer analysis of a BIPV system cannot be considered as a cavity/enclosure, because the space between the PV and the wall is not a closed cavity and the application of a correlation under these conditions will be incorrect. It can only be conducted as a duct with fluid flow in and out. Therefore, a different analysis from the cavities should be adopted for the analysis of such systems because air enters and exits continuously through the duct. This is in agreement with a recent study done by Al-Kayiem and Yassen (2015) where they state that the use of the Hollands equation by many researchers for air collectors is incorrect because this correlation was developed for a closed cavity. Such a condition cannot be correct for air collectors investigation or a BIPV system investigation.

Al-Kayiem and Yassen (2015) carried out an analysis of the natural convection heat transfer in a rectangular passage solar air heater. They presented and discussed experimental measurements versus the results from commonly used Nu number correlations from Hollands et al. (1976), Bar-Cohen and Rohsenow (1984) and Tiwari (2002). The three correlations refer to free convection heat transfer between two surfaces and flowing air. The experimental measurements were carried out using a rectangular duct formed as a solar air heater, in inclination angles of 30°, 50°, and 70° in order to determine the optimum angle of the free convection mechanism of the solar air heater. Regarding the optimum angle, it is shown that the 50° slope of the system achieve best collector performance. In the comparison of the experimental results with the three equations, for the tested Ra number range, the Tiwari correlation overestimates the Nu number while the Bar Cohen equation and Hollands equation underestimate the Nu number.

An interesting investigation in terms of the understanding of the physical mechanisms found in BIPV applications for facades and roof, was carried out by Lau et al. (2012a). Flow and heat transfer of natural convection in vertical and inclined BIPV systems were investigated, through numerical simulations and experimental geometry of two parallel smooth walls. A uniform heat flux was applied in the front skin of the application and the second skin was assumed to be adiabatic. The effect of varying inclination angle on the velocity and temperature fields was explored, and a comparison between experimental and modelling results was done. In the apparatus used in the laboratory, heat loss from the rear of each skin of the channel, were reduced by placing a 50 mm thick polystyrene block. Eight cases with different magnitudes of q_{conv} and ϑ were studied both experimentally and computationally. The results demonstrated that the biggest the inclination angle, the lower the temperature distribution along the PVs. In addition, it was stated that the air velocity and the thus the temperature fluctuations increase when system is in vertical position. Subsequently, Lau et al. (2012b) performed a numerical investigation of natural convection flow and heat transfer in vertical channels which are relevant to the passive cooling of BIPV systems. The results obtained are compared with the experimental data from literature. The numerical results were then used to determine the Nu number correlation for turbulent natural convection in vertical channel, based on the channel width (W). From the specific study, the results obtained from the numerical study has resulted in the following equation with values of A=0.8544 and B=0.2374.

$$Nu_W = A\,[Ra_W(H/W)]^B \qquad 2.40$$

2.6.2 Forced & Mixed Convection in BIPV systems

Candanedo et al. (2010) presented a study with transient and steady state models for open loop air based BIPV/T systems. The model presented, could be readily adapted as a design tool for air-based open loop BIPV/T systems in cold climates. With the relevant meteorological data, this model could be used as a decision-making tool for pre-feasibility studies. The experimental facility consists of an amorphous silicon PV panel with 4 cm air gap between the PV and the board, tilted at 45°. Two models were developed; a steady state (SS) model that does not consider the PV thermal capacitance, and a transient (TR) model that takes into account the capacitance of the PV. Both models were analyzed numerically in Matlab.

The interior heat transfer coefficients for the bottom and top surfaces (hc_b and hc_t), were calculated as average values for the entire channel according to correlations developed for this case as function of the air speed inside the channel. The asymmetric conditions inside the channel, cause hc_b to be

much larger than hc_t with the consequence that the average air temperature is closer to T_{board} than to T_{PV} at the bottom side. The two correlations are shown in Equations (2.41) and (2.42) below.

$$h_{ct} = 8.38\, V_{ch} + 1.76 \qquad 2.41$$

$$h_{cb} = 13.2\, e^{1.73 V_{ch}} \qquad 2.42$$

h_{ct} : Heat transfer coefficient at the top interior surface (W/m^{2}K)

h_{cb} : Heat transfer coefficient at the bottom interior surface (W/m^{2}K)

V_{ch} : Air speed inside the channel (m/s)

The exterior convective heat transfer correlations are obtained using different correlations to compare their effects into the results. Equation (2.43) obtained from Test et al. (1981), Equation (2.44) by Sharples and Charlesworth (1998) and McAdams Equation (2.45) from Duffie and Beckman (1980). From plots presented in Candanedo et al. (2010), it is stated that Equation (2.44) gives the highest values of h_o for a specific range of wind speed, while Equation (2.45) the lowest. However, it is pointed out that Equations (2.44) and (2.45) give better estimations to the average PV bottom surface temperature.

$$h_o = 8.55 + 2.56 V_{wind} \qquad 2.43$$

$$h_o = 11.9 + 2.2 V_{wind} \qquad 2.44$$

$$h_o = 5.7 + 3.8\, V_{wind} \qquad 2.45$$

V_{wind} : Air speed outside the channel (m/s)

h_o : Heat transfer coefficient at the exterior (W/m^{2}K)

Authors concluded that there is a good agreement between both models and experimental results. At the end of their work, they proposed some improvements for the models, based on the method used.

Candanedo et al. (2011) presented an experimental study for the development of heat transfer correlations for an open loop air based BIPV/T system with outdoor air as the cooling fluid. Correlations for the average Nusselt number as function of the Reynolds number were presented, for BIPV/T system design where forced convection dominates. It is mentioned that natural convection is not investigated and their work is only based on forced convection. The authors also presented a table showing the Nu number correlations for flow in a cavity or a duct from previous literature and made a critical comparison of the new correlation with others.

The system considered for investigation in this study includes a variable speed fan that controls the airflow to produce an air outlet temperature to be used for heating. Their work focused on the determination of the internal convective coefficients for a BIPV/T system with outdoor air as the cooling fluid. An amorphous PV panel is used, mounted on a metal roof sheet as shown in Figure 2.18.

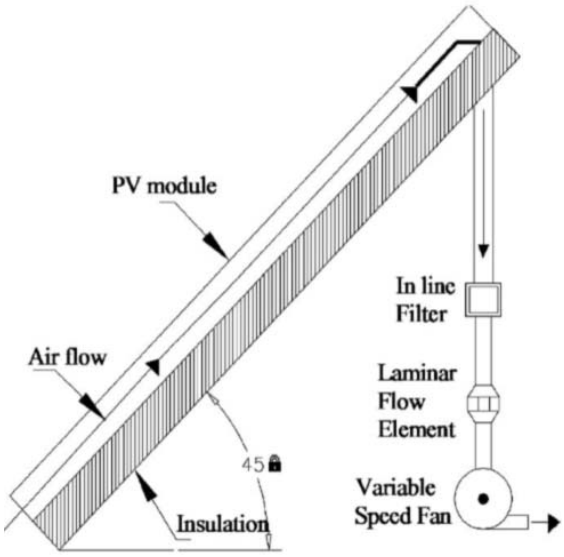

Figure 2.18. Roof mounted BIPV/T (Candanedo et al., 2011).

Because of asymmetry of the system, two Nu number correlations (Equation 2.46 and 2.47) are recommended; one for the top and one for the bottom surface at different Re ranges. The correlations developed, are recommended by the authors for the determination of the average Nu number for open loop BIPV/T systems and solar air heaters for tilt angles 30°-45°.

$$Nu_{top} = 0.052\ Re^{0.78} Pr^{0.4}\ for\ 250 \leq Re \leq 7500 \qquad 2.46$$

$$Nu_{bottom} = 1.017\ Re^{0.471} Pr^{0.4}\ for\ 800 \leq Re \leq 7100 \qquad 2.47$$

Both correlations with the uncertainty of the data are plotted as shown in Figure 2.19 and Figure 2.20.

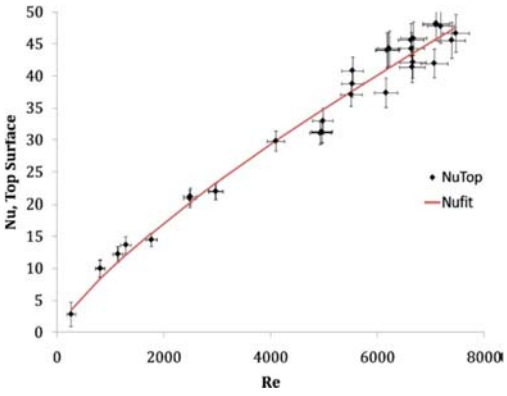

Figure 2.19. Nusselt numbers for the top surface versus Reynolds number (Candanedo et al., 2011).

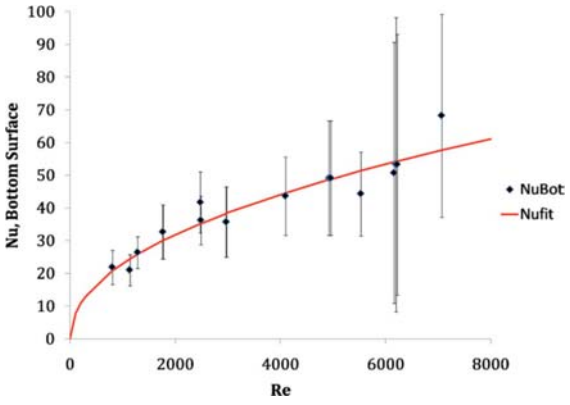

Figure 2.20. Nusselt numbers for the bottom surface versus Reynolds number (Candanedo et al., 2011).

Zöllner et al. (2002) described experiments performed in an outdoor double-skin façade. In their conclusions, the authors stated that solar radiation induced mixed convection fluid flow in double skin façades, depends strongly on the height of the channel, the distance between external and internal façade and the height of the air inlet and outlet. On the same issues, Selkowitz (1978) suggests that for a single air space, the minimum conductance is typically reached with an air space thickness of 0.6 to 0.2 cm. Once the boundary layer regime has been reached, further increases in air space thickness show little or no decrease in air space conductance.

Dittus and Boelter (1930) recommended a simple Nu number equation for fully developed turbulent flow in smooth pipes for Re ≥10.000, L/D ≥ 10, and 0.7< <Pr <160. The Dittus-Boelter equation (Equation 2.48) is the most widely used single-phase correlation for a pipe or duct, and describes an average Nu number for forced convection and symmetrical heating. In the estimation of Re for a duct, the hydraulic diameter D_h is used.

$$Nu = 0.023 Re^{0.8} Pr^{0.4} \qquad 2.48$$

Another average Nu number correlation for forced convection and symmetrical heating is given by the Gnielinski (1976) correlation. This correlation is for smooth tubes for 3000< Re <5x10^6 and 0.2< Pr <2000:

$$Nu = \frac{(Re - 1000) Pr \frac{f}{8}}{1 + 12.7 \sqrt{\frac{f}{8}} (Pr^{\frac{2}{3}} - 1)} \qquad 2.49$$

The Nu number for fully developed turbulent flow is provided by Gnielinski, who modified the Petukhov correlation to obtain values that agree with data for smaller Re number. Equation (2.50)

gives an average Nu for forced convection and symmetrical heating and it is valid for short channel lengths and pipes.

$$Nu = \frac{(Re - 1000)Pr\frac{f}{8}}{1 + 12.7\sqrt{\frac{f}{8}}(Pr^{\frac{2}{3}} - 1)}\left(1 + \left(\frac{D_h}{L}\right)^{2/3}\right) \quad 2.50$$

Where: f = (0.79 ln (Re)-1.64)-2 and Re≥3000. *2.51*

Tan and Charters (1970) carried out an experimental investigation of forced convective heat transfer coefficients for fully developed turbulent flow in a rectangular duct with asymmetric heating. They developed a Nu number correlation for average Nu for forced convection and asymmetrical heating in a horizontal duct with Re>9500:

$$Nu = 0.0158\,Re^{0.8} + (0.00181\,Re + 2.92)e^{(-0.03795\,L_{c/D_h})} \quad 2.52$$

For the case of parallel plates with constant temperature on one side and insulated on the other side, Mercer et al. (1967) obtained the average Nu number in the form of equation for 0.1< Pr<10, Re<2300, for forced laminar convection and asymmetrical heating:

$$Nu = 4.9 + \frac{0.0606\left(\frac{Re\,\mathrm{Pr}\,D_h}{L}\right)^{1.2}}{1 + 0.0909\left(\frac{Re\,\mathrm{Pr}\,D_h}{L}\right)^{0.7} Pr^{0.17}} \quad 2.53$$

2.6.3 Comparison of the mostly used equations

In order to make the analysis clearer, the most used Nu correlations from the studies presented in this chapter will be compared in this section.

The most known Nu number equations based on the heat transfer with natural and forced convection on DSVFs and BIPV systems are selected, as well as equations of Nu number for air flow between parallel plates. Ten Nu number correlations are selected as shown in Table 2.1, which were already presented in previous sections.

The selection of the specific equations was made in accordance to the fact that are the mostly used equations. Then it was decided to select equations that refer to various cases in order to see the Nu number ranges for different cases. Equation (2.19) although it applies for closed ducts, it is included as it is used by many researchers for air collector and DSF investigations.

Table 2.1 Nu number correlations from literature presented previously, selected for discussion.

Study	***Convection***	***Air between plates***	
Hollands et al. (1976)	Natural	Inclined layers 70º slope	Equation 2.19
Bar-Cohen and Rohsenow (1984)	Natural	2 isothermal plates	Equation 2.22
Bar-Cohen and Rohsenow (1984)	Natural	1 isothermal, 1 insulated	Equation 2.25
Bar-Cohen and Rohsenow (1984)	Natural	2 isoflux plates	Equation 2.28
Bar-Cohen and Rohsenow (1984)	Natural	1 isoflux, 1 insulated	Equation 2.31
Sparrow and Azevedo (1985)	Natural	1 isothermal, 1 unheated	Equation 2.38
Candanedo et al. (2011)	Forced	BIPV/T, top side	Equation 2.46
Candanedo et al. (2011)	Forced	BIPV/T, bottom side	Equation 2.47
Tan and Charters (1970)	Forced	Rect. duct, asymmetric heating	Equation 2.52
Mercer et al. (1967)	Forced	Rect. duct, asymmetric heating	Equation 2.53

Initially, the six equations for natural convection are plotted in Figure 2.21, Figure 2.22, and Figure 2.23 and then four equations for forced convection approaches are plotted in Figure 2.24 and Figure 2.25.

As shown in Table 2.1, the Equations (2.22), (2.25) and (2.38) refer to isothermal plates, Equations (2.28) and (2.31) to isoflux plates and Equation (2.19) refers to inclined layers considered as enclosures.

As can be seen from Figure 2.21, Equations (2.22), (2.25) and (2.38) give similar results of Nu number for the same range of Ra. The same applies for Equations (2.28) and (2.31) as shown in Figure 2.22.

It is observed that for the cases with isothermal plates the Nu ranges between 1 and 11 (Figure 2.21), while for the isoflux plates the Nu ranges between 0.2 to 2.7 (Figure 2.22). Therefore, the heat transfer coefficients '*h*' that can be derived from Equations (2.22), (2.25) and (2.38) are expected to be similar, and the same is expected to happen for the coefficients from Equations (2.28) and (2.31).

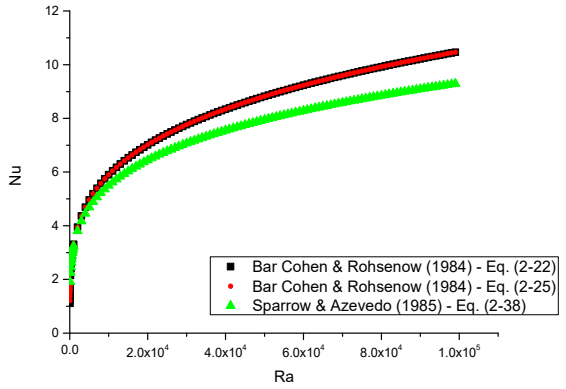

Figure 2.21. Nu number correlations for isothermal plates.

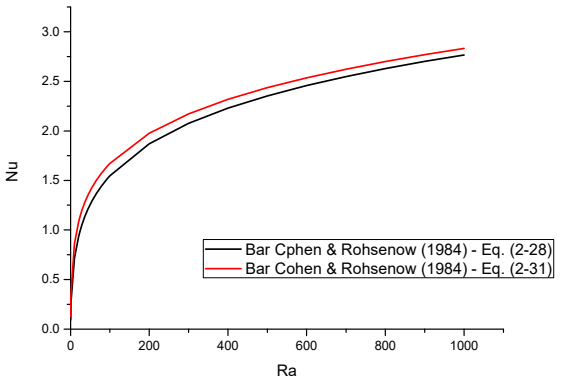

Figure 2.22. Nu number correlations for isoflux plates.

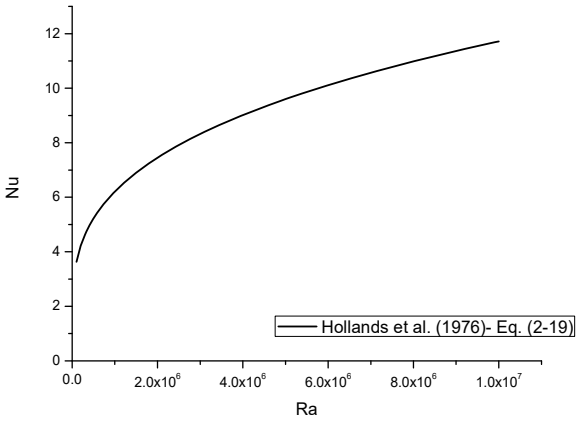

Figure 2.23. Nu number for natural convection between inclined layers from Nu correlation Hollands et al. (1976).

Comparing Equation (2.19) which applies for inclined layers in 70º, with the Equations (2.22), (2.25) and (2.38), it can be seen that the resulting Nu number values are in the same range. This was expected because they all refer to heat transfer through isothermal plates, although they do not all refer to the same range of Ra number. This is maybe the reason why although Equation (2.19) refers to a cavity/enclosure and not an open channel it is used by many researchers that designed sloped DSF and air collectors. Regarding particularly the case for heat transfer between an isothermal and an unheated plate, Equation (2.25) and Equation (2.38), were expected to give similar results regarding the Nu number range (as both are isothermal). As can be seen from Figure 2.21, the two correlations give very similar Nu and accordingly will provide the same ranges for heat transfer coefficients h, for the same range or Ra number.

Figure 2.24 and Figure 2.25 show the plots of the Equations (2.46), (2.47), (2.52) and (2.53) from the studies that investigated forced convection and fluid flow through ducts. As can be observed from Figure 2.24, Equation (2.52) for turbulent flow gives much higher Nu number than the Equation (2.53) for laminar flow while both of them consider forced flow in a rectangular duct with asymmetric heating. As it was expected, the turbulent flow results to higher Nu and thus will lead to higher convective heat transfer coefficient *h*.

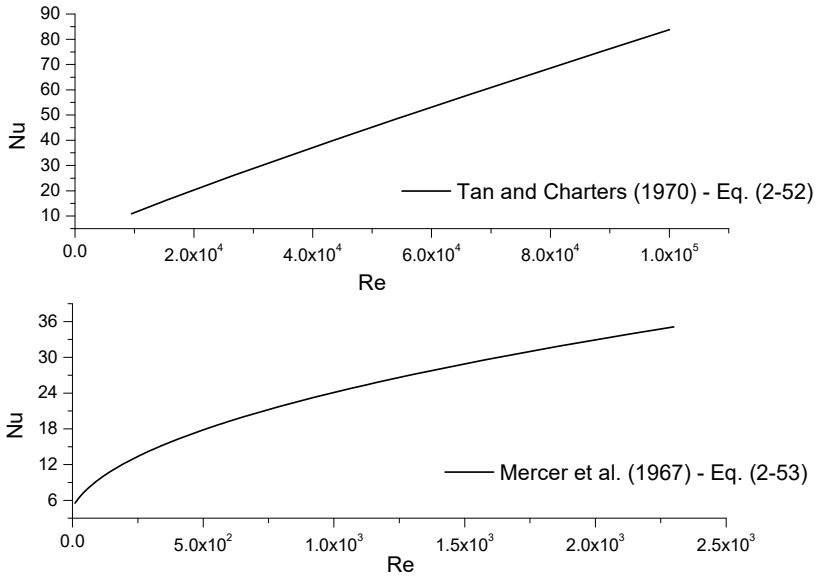

Figure 2.24. Nu number correlations from Mercer et al. (1967); Tan and Charters (1970) for turbulent and laminar flow in a rectangular duct with asymmetric heating.

From Figure 2.25 it is clearly seen that although Equations (2.46) and (2.47) refer to the same system for the same range of Reynolds number, they give much different Nu number. At the top side of the BIPV/T system the Nu number ranges from 3 to 52 while at the bottom side of the system it ranges in higher levels. Equation (2.46) refers to the top of the duct of the BIPV/T system and Equation (2.47) refers to the bottom side. Thus, the entrance of the air at the bottom side of the system gives higher Nu number and thus higher convective heat transfer coefficients.

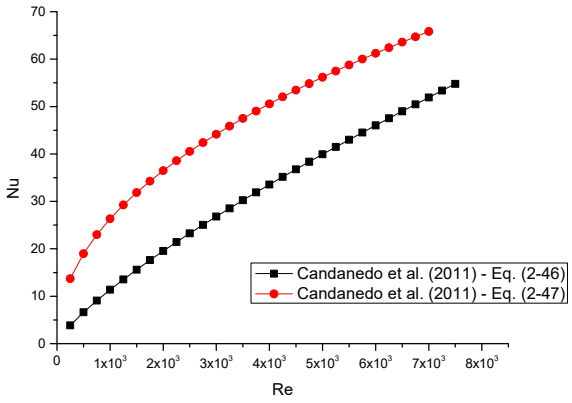

Figure 2.25. Nu number correlations from Candanedo et al. (2011) for the bottom and top sides of a BIPV/T system.

Comparing generally the forced convection with the natural convection, it can be stated that the Nu number and thus the coefficient *h* are much higher during forced convection than in natural

convection. This also happens where the flow is turbulent or laminar. For turbulent flow, the Nu is much higher than in laminar flow.

2.7 Discussion & Conclusion

Despite all the research carried out in both DSVF and BIPV systems regarding the heat transfer analysis there is still a need for research in order to find solutions for better operation. It is observed that most of the studies approached the investigation of the systems experimentally or with simulations because of the complex characteristics of the flow and the different conditions of the two plates comprising the systems. The best way to understand the system is to combine all the knowledge from experiments, theory and simulations and this is the aim of this study in general.

After the literature review carried out to find published studies on the heat transfer analysis of DSVF and BIPV facades, it is pointed out that there are many studies carried out on the heat transfer analysis of the DSVFs, but very few carried out on the BIPV facades and especially to those that are based on the natural convection. The ventilation of the solar facades with natural convection is insufficiently investigated in comparison with the forced circulation systems. Regarding particularly the heat transfer analysis on natural convection coefficients, there are no studies on the BIPV systems. In order to approach the BIPV systems in terms of heat transfer analysis, relevant studies were presented based on double skin facades or parallel plates exposed to different conditions forming a duct. However, the assumptions and approximations considered cannot be the same for the BIPV systems. Consequently, the correlations and values obtained from other studies, based on natural convection in enclosures, cannot be considered correct for ventilated solar facades and subsequently the values for *h* and *Nu* obtained are not representative for the BIPV case. In the following chapters a heat transfer analysis will be carried out based on experimental data of a BIPV system and new correlations for the estimation of the convective heat transfer coefficients will be presented.

Researchers seem to agree that the optimum air gap between the PVs and the building façade ranges between 10 and 15 cm in order to keep the PVs temperature at low levels. Additionally, various studies have tested the effect of the temperature increase or the air gap increase to the Ra number and subsequently to the Nu number and thus the convection coefficient *h*. Regarding the value of the convective heat transfer coefficient *h* in each case, this is dependent on the length of the duct, the type of the flow, as well as on the Rayleigh and Reynolds numbers range. From a rough estimation in accordance with the Nu number correlations discussed earlier in Section 2.6, the expected *h* values for a naturally ventilated BIPV system are in range from 1 to 15 W/m^2K for the natural convection

and 10-50 W/m^{2}K for the forced convection regarding the BIPV systems. The ranges are estimated having in mind that the values are always dependent on other parameters such as the air gap size, the inclination of the PV and the developed temperatures.

As a conclusion it can be said that the choice whether the heated air is needed for space heating or not, depends on the location of the installation, the weather conditions and on the heating and cooling loads of the building. When the heated air is needed for space heating, technical means like a fan are usually necessary to drive the air through the duct and dumpers to direct the air into the building space (BIPV/T system). On the other hand, when the heated air is not needed for space heating, it should be allowed to exit the duct naturally or with mechanical means while cooling the PVs (BIPV system). Considering the study of Sanjuan et al. (2011c) based on the OJVFs, the open joints help to achieve important energy savings in climates with hot summers and mild winters. So, the open joints may be the solution for such climates and this will enable the building to operate as a Nearly Zero Energy Building (NZEB). Another proof that the BIPV systems need to be modified in accordance with the location of installation, are the outcomes of the study made by Mei et al. (2003). Zogou and Stapountzis (2011a) concluded that different design of the system must be adapted to different climatic conditions and building orientations.

However, these solutions would eliminate the use of electrical power for space heating in winter and reduce the cooling loads in summer. A good approach is to give the homeowner the option whether to use technical means to drive the air indoors or leave it to move naturally to the ambient according to the season, weather conditions and heating requirements. Therefore, maybe a combination of the two systems would be optimal. In order to make those systems more viable and support the ZEB scenarios, both systems with mechanically and naturally ventilation should be incorporated for a viable and sustainable operation. A system should be able to operate with both functions or be able to change from one to other easily, cheaply and effectively. It is however recognized that such a combination would be very costly and non-viable for most cases. This supports the idea to investigate the naturally ventilated systems more, in order to show the system's advantages and increase their efficiency and henceforth their usage to maximum.

As indicated before, it is noted that most researchers studied the systems with mechanical ventilation rather than the systems with natural ventilation. This is because the latter are more complex in terms of the air flow behaviour in the air duct. However, researchers agree that there is a need to understand the natural ventilation also.

Consequently, here is the innovative idea of this study. It is considered that the naturally ventilated systems have many potentials to make the system more effective and thus more usable. It is believed

that the investigation of the systems with natural flow should be taken into consideration, although the natural flow is more complex. The knowledge on the heat transfer aspects of the BIPV systems will improve the engineering installations, applications and studies because it will give new estimation method for the heat transfer coefficients that represent the real system.

CHAPTER 3

3 Experimental Investigation

The experimental procedures to investigate the temperature distribution of the various parts of a naturally ventilated BIPV system were carried out in Limassol, Cyprus (34.70^{o}N, 33.02^{o}E). Both outdoor and indoor experiments were carried out, to examine the thermal behaviour of a BIPV system, under various configurations, different orientations, solar radiation, slope, air gap size etc. The basic schematic representation of the tested BIPV system is shown in Figure 3.1. The duct is naturally ventilated without the use of a fan to circulate the air.

The outdoor experiments were performed in real sun conditions where wind, clouds, dust and all other natural weather and environmental parameters were present. Indoor experiments were performed in a laboratory with controlled conditions with the use of a solar simulator. The aim of the indoor experiments was to test the system under uniform and constant amount of solar radiation for a certain amount of time without the external disturbances mentioned before for the outdoor experiments.

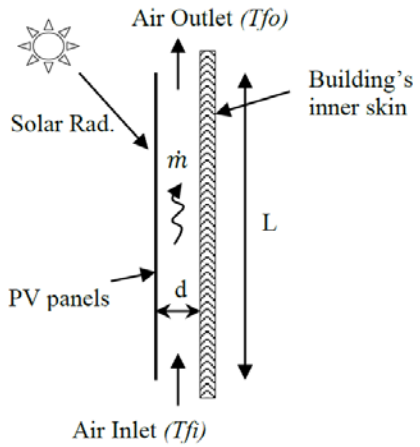

Figure 3.1. Schematic representation of the BIPV system tested.

During the experiments, various parameters were monitored, which are, the temperature of the various parts of the system (PV, air, wall), the air velocity in the air gap, the electrical characteristics of the PV panel, the weather conditions such as solar radiation, ambient temperature and wind speed.

The experimental measured data are used to determine the temperature distribution on the various parts of the system, to observe the natural air flow in the air gap, so as to carry out a heat transfer analysis in order to estimate the convective heat transfer coefficients of the system. Additionally, the experimental data are used to validate the simulation model that will be presented in Chapter 4.

3.1 Methodology – Basic Test Rig

For the experimental procedures, two custom made experimental apparatuses are designed and built, one for outdoor and one for indoor experiments. Both apparatuses represent a single PV panel BIPV system with air gap between the PV panel and a second skin, forming an open-ended duct.

The two experimental apparatuses for indoor and outdoor experiments are shown in Figure 3.2 and Figure 3.3 respectively. Each apparatus consists of a polycrystalline PV panel with dimensions 1640 x 992 x 4 mm (40 mm with the frame), a wooden back side with dimensions 2000 x 1020 x 100 mm, and two plexiglass plates with dimensions 2000 x 100 x 20 mm. The only difference between the two apparatuses is the back wall where in the indoor experimental apparatus is made from wood, but in the outdoor experimental apparatus it is represented with a real brick wall with dimensions 2000 x 1020 x 200 mm. The two plexiglass plates define the air gap size in this study set as 100 mm which is in agreement with published literature from Gan (2009); Lau et al. (2012a) and Tonui and Tripanagnostopoulos (2008). Two openings are left at the top and the bottom of the duct formed between the PV, the wall and the plexiglass sides.

Additionally, the experimental apparatus for indoor experiments can change its slope from 0^{o} horizontal to 90^{o} while the outdoor experimental apparatus is tested only in vertical position. Thus, any test rig placed on the testing metallic base, can be tested in different inclination angles, perpendicular to the light from the solar simulator or in another slope.

Figure 3.2. Indoor experimental test rig.

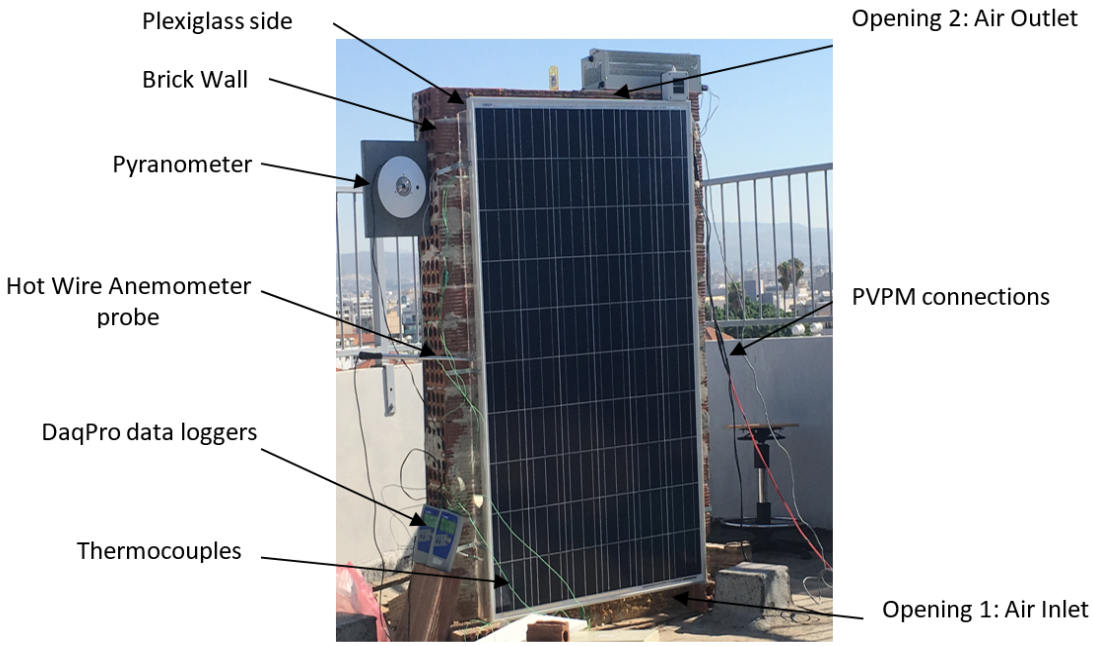

Figure 3.3. Outdoor experimental test rig.

Figure 3.2 and Figure 3.3 show the instruments used for the various measurements as well, and Figure 3.4 shows the experimental set up and the position of the thermocouples on the tested systems.

Nine thermocouples were placed at the back side of the PV panel; three at the top, three in the middle and three at the bottom, 6 thermocouples in the air gap in two positions 10 cm from the bottom opening and 10 cm from the upper opening, and 3 thermocouples on the wall, at the top, bottom and middle of its height.

All the thermocouples were connected to DaqPro data logger devices to record the temperature at every point during the experiment with 1-minute time interval. A pyranometer is also connected to a data logger in order to measure the solar radiation in the form of voltage (mV). A PVPM (Peak Power Measuring Device and Curve Tracer for Photovoltaic Modules) device is connected to the PV panel to measure the electrical characteristics of the PV in the form of the Current-Voltage (I-V) curve. For the velocity of the air in the duct, a hot wire anemometer probe is placed in the middle of the air gap. At the end of the experiments, all data are downloaded to a computer for analysis through MATLAB and OriginLab softwares.

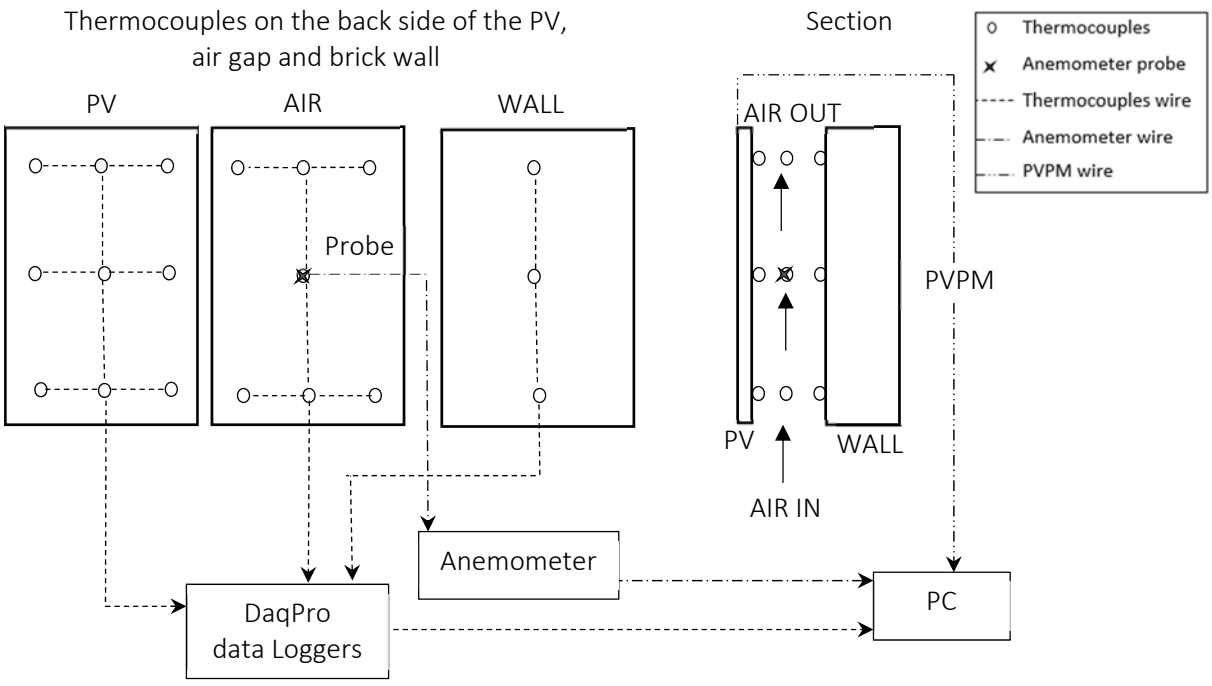

Figure 3.4. The experimental set up, showing the place of the thermocouples and other instruments, on the three parts of the system, PV panel, air gap and brick wall.

3.2 Equipment

3.2.1 Photovoltaic Panels

A Luxor 230 W polycrystalline PV panel is used for the experiments. The panel's dimensions are shown in Figure 3.5 and the total weight of the panel is 18.3 kg. More specifications of the panel are shown in Table 3.1.

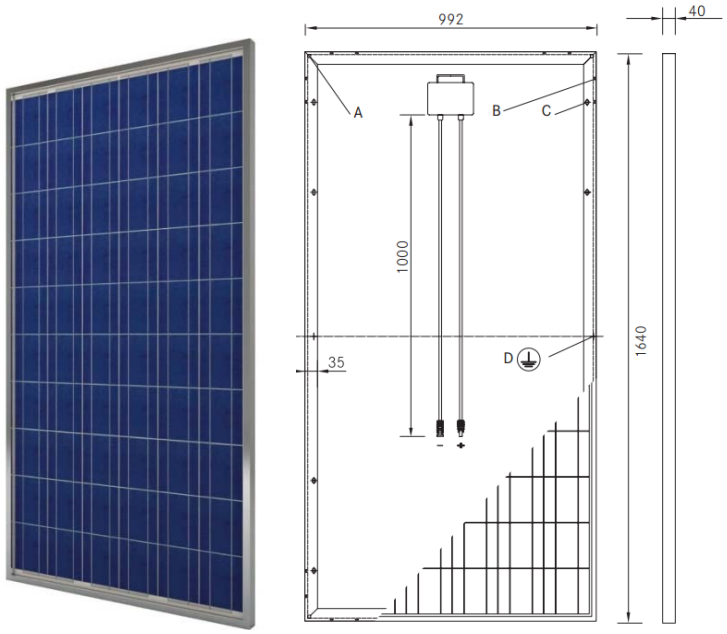

Figure 3.5. The Luxor 250 W Photovoltaic panel's dimensions, used for the experiments.

Table 3.1. Technical data of the PV panel.

Parameter	Units	Value
Cells technology	[-]	Polycrystalline
Cells size	[mm]	156 x 156
No of cells	-	6 x 10
Length	[mm]	1640
Width	[mm]	992
Thickness	[mm]	40
Weight	[kg]	18.3
Maximum power	[W]	250 W
Current at maximum power point I_{mpp}	[A]	8.16
Voltage at maximum power point V_{mpp}	[V]	30.83
Short circuit current I_{sc}	[A]	8.61
Open circuit voltage V_{oc}	[V]	37.41
NOCT	-	47 ± 2°C
Efficiency at STC	-	15.46 %
Temperature coefficient of V_{oc}	%/°C	-0.32
Temperature coefficient of I_{sc}	%/°C	0.05
Temperature coefficient of Max. Power	%/°C	-0.45

3.2.2 Thermocouples, Data Loggers

A number of K-type thermocouples with 0.13 mm wire diameter were used to measure the temperature of the system at various points.

The signals from the thermocouples were recorded by DaqPro thermometry devices and data loggers of 8 input channels. The devices used are DaqPro with fast Analog to Digital converters which can display measured values and analyze them in real time on graphical interface and minimize the need to download directly the collected data to a computer for further analysis (Figure 3.6). However, these can be downloaded subsequently to a computer for further processing.

The DaqPro devices can perform measurements of current, voltage, temperature from various thermocouple types, pulse, frequency and power. In our case, they are used to measure voltage from the pynanometer and temperature from the K-type thermocouples. The specifications of these two parameters are shown in Table 3.2.

Figure 3.6. The DaqPro data logger.

Table 3.2. Technical data of the DaqPro thermometry devices and data loggers.

Thermocouples: K- type		**Voltage 0-50 Mv**	
Range	-250°C to 1200°C	Range	0 to 50 mV
Accuracy	±0.5°C	Accuracy	±0.5 %
Resolution	0.1°C (1 µV)	Resolution	3 µV
Accuracy	-250 to 1200°C: ±0.5 %		

3.2.3 Hot wire anemometer

A hot wire anemometer is used to measure the air velocity in various places in the air duct to observe how the movement of air from the stuck effect affects the temperature distribution on the various parts of the system and also estimate the flow rate of the air produced from the stuck effect.

The hot wire anemometer is the most well-known air velocity measurement device which measures air velocity by noting the heat which is transferred by the air. The core of the anemometer is an exposed hot wire on the probe, either heated up by a constant current or maintained at a constant temperature. Hence there are two types of anemometers, those who work based on the constant current and those based on the constant temperature. In both cases, the fluid velocity measurement is done by the estimation of the heat loss of the hot wire to the fluid by convection. By measuring the temperature change of the hot wire under constant current anemometers, the heat lost can be obtained and then converted to a fluid velocity by convection theory. Likewise, for the anemometers with constant temperature operation, by measuring the current required to maintain a constant wire temperature, the heat loss can be estimated and then converted to the fluid velocity by convection theory.

Hot wire anemometers use a very fine wire electrically heated up to some temperature above the ambient. The wire is installed on the probe which can be inserted in the air stream and the air flow which passes over the wire has a cooling effect on the wire. The relationship between the resistance of the wire and the flow speed can be obtained, as the electrical resistance of the most metals is dependent on the temperature of the metal.

For this study the HD 2303.0 hot wire anemometer from Delta Ohm is used and the probe AP 471 S2 as shown in Figure 3.7. The HD 2303.0 is a portable instrument with an LCD display. It is designed for use in the fields of air conditioning, heating, ventilation and environmental comfort. It uses hot wire or vane probes to measure air speed, flow rate, and temperature inside pipelines and vents. The AP 471 S2 probe can adjust its length with fully telescopic shaft to1800 mm and this gives us the ability to measure at any depth in the air gap. The probe diameter on the measurement area is 8 mm. Table 3.3 shows the technical data of the hot wire anemometer.

Figure 3.7. The HD 2303.0 anemometer used in the experiments to measure fluid velocity.

Table 3.3 Technical data of the HD 2303.0 Delta Ohm hot wire anemometer and the probe AP471S2 from Delta Ohm.

Parameter	**Value**
Type of measurements	Air speed, flow rate, air temp.
Cable length	~2 m
Speed Range	0.1 to 5 m/s
Speed Resolution	0.01 m/s
Speed Measurement accuracy	±0.3 m/s (1…5 m/s)
Temperature Range	0 to 80°C
Temperature Resolution	0.1°C
Temperature Measurement accuracy	±0.8°C (-10…80 °C)

For the needs of this study, the probe of the hot wire anemometer was inserted in the air gap through drilled holes on the plexiglass sides of the experimental apparatus as shown in Figure 3.8. Various holes are drilled at different heights on the plexiglass in order to insert the anemometer´s probe and record the air velocity at various points on the system. While measurements are taking place in one hole, the other holes are kept closed to avoid external disturbances.

Figure 3.8. Hot wire anemometer probe inserted to a drilled hole on the plexiglass side of the experimental apparatus to measure the air velocity in the duct.

3.2.4 Pyranometer

A pyranometer is used to measure the total irradiance on the experimental surface. The pyranometer is always installed at the same angle as the experimental apparatus and connected to the DaqPro data loggers to perform measurement of radiation every minute.

For this study, an Eppley Precision Spectral Pyranometer (PSP) is used (Figure 3.9). This device measures sun and sky irradiance in the range of wavelengths 0.285 to 2.8 microns, including most of the solar spectrum. It has a "hemispheric receiver" intended to approximate the cosine response for oblique rays.

Figure 3.9. The Eppley Precision Spectral Pyranometer.

This radiometer has sensitivity approximately 9 microvolts per W/m^2. Thus, an irradiance of 1000 W/m^2 will produce a DC potential of 9 millivolts. More specifications are shown in Table 3.4.

*Table 3.4. Technical data of the Eppley Precision Spectral Pyranometer (*The Eppley Laboratory, 2017*).*

Parameter	**Value**
Spectral Range	285 - 2800 nm
Output	0-10 mV analog
95% Response time	5 seconds

Oper. Temperature	-50°C to 80°C
Temperature Response	0.5% (-30°C to 50°C)
Tilt Response	0.5%

3.2.5 PVPM

In order to circulate the produced current from the PV panels during the experiments and measure the electrical characteristics of the PV panels, a Peak Power Measuring Device and Curve Tracer for Photovoltaic Modules is used. In the current study, the PVPM 2540C device is used (Figure 3.10). This device enables the measurement of the I-V curve of PV modules as well as of strings or arrays and can also measure and calculate the peak power of the PV system. Regarding the I-V curve, a total of 100 points are measured to represent the curve, and all data are available in the form of a curve and list of measured data as well.

Figure 3.10. The PVPM 2540C device.

The PVPM is a mobile measuring device with integrated battery supply and charge controller in a durable metal housing. The device has its own industrial miniature PC and a high contrast LCD display and thus its function is independent of other devices. However, it can be connected to a computer for data transfer and further analysis of the measured values over a standard interface. The specifications of the device are shown in Table 3.5.

*Table 3.5. Technical data of the PVPM 2540C device (*pve photovoltaik engineering, 2017*).*

Parameter	**Value**
Resolution	0.01V-0.25V, 0.005A – 0.01A
Voltage Range	25V / 50V / 100V / 250V
Current Range	2A / 5A / 10A / 40A
Single Measurement	20 ms up to 2 s
Irradiance Range	0 – 1300 W/m^2
Temperature Range	-40°C to +120°C

3.2.6 The Solar Simulator

For the implementation of the indoor experiments, a large scale solar simulator (SS) [2] is used to imitate in an indoor controlled environment the radiation of the sun. A SS is a device that provides illumination approximating natural light (Figure 3.11). The purpose of the solar simulator device is to provide a controllable indoor test facility under controlled laboratory conditions used for the testing of solar cells and other systems. The light from the solar simulator is controlled in three dimensions: spectral content, spatial uniformity and temporal stability.

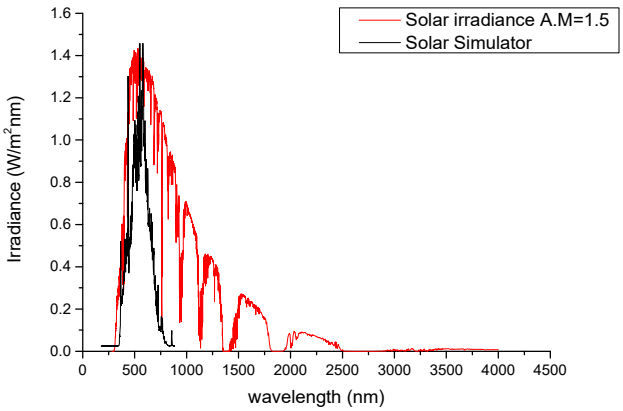

Figure 3.11. The spectrum of the solar simulator.

The solar simulator used for this study is located at the laboratories of the Department of Mechanical Engineering, Cyprus University of Technology in Limassol, Cyprus (Figure 3.12).

[2] Part of this section is published as: Kalogirou, S.A., Agathokleous, R., Panayiotou, G.P., (2014). Indoor Testing of Solar Systems: A Solar Simulator for Multidisciplinary Research on Solar Technologies. In: Proceedings of the 17th Conference Process Integration, Modelling and Optimisation for Energy Saving and Pollution Reduction. Prague, Czech Republic.

Figure 3.12.The solar simulator at CUT laboratories.

The solar simulator consists of a lamp array to produce simulated light, a large frame to provide support and operational flexibility and the control unit for operating the lamp array. The 2.24 m x 1.88 m x 0.35 m (length x width x depth) lamp frame consists of 20 (575 W) metal halide lamps arranged in 5 rows of 4 lamps with a maximum intensity of 1200 W/m^2. The intensity of the light on the test target can be controlled manually or automatically through the control unit.

The design of the simulator, allows to obtain uniform intensity of light on vertical, horizontal and inclined surfaces. Additionally, the design enables automated height adjustment and tilt adjustment and it is also able to move along the laboratory floor allowing testing in a variety of arrangements. Some general technical data of the solar simulator are shown in Table 3.6.

Table 3.6. Technical data of the Solar Simulator in Cyprus University of Technology.

Movements	
Vertical	Up and down in low speed
Inclination	0-90^o fast rotation, accuracy 1^o
Unit	Manual movement on wheels
Control	Manual Software control through PLC
Light Control	
Lamp type	Metal halide 575 W each
Minimum illuminated area	2.2 m x 1.5 m
Wavelength range	Spectral output matching the AM 1.5
Lamps number	20 lamps, in 5 rows of four lamps
Lamps lifetime	~1000 hours
Maximum intensity of light	Up to 1200 W/m^2
Dimming control	Individual control of each lamp

Display	
Height	With an accuracy of 1 mm
Angle of inclination	With an accuracy of 1 degree
Irradiance on the test sample	In W/m^2
Distance from the test rig	With an accuracy of 1mm

A unique dimming arrangement of each row of lamps allows the simulator to provide uniform intensity light under normal and non-normal incidence angle conditions. To cool the lamps during solar simulator's operation there are two ducts at the ends of the aluminium housing which contain fans that force ambient air temperature to pass through the lamp holders. Additionally, the simulator is equipped with an external control unit which includes safety features to protect the system from power failure and overheating. Any fault in the system will be displayed on the simulator control panel.

Special designed lenses at the aperture of the paraboloidal reflectors modify the angular distribution of the light to achieve the required overlapping between neighboring lamps. The lenses of the lamps on the SS, were turned to 45° according to the decision made through a study from Kalogirou et al. (2013) for which the light intensity contour plots showed the biggest area of uniform intensity.

A series of tests were carried out to calibrate the simulator including uniformity measurements of light intensity distribution and degree of light collimation. The measurements have been carried out on an area of normal incidence with dimensions 2.2 m x 3.2 m (Figure 3.13). The solar simulator's light intensity contour map is presented in Figure 3.14.

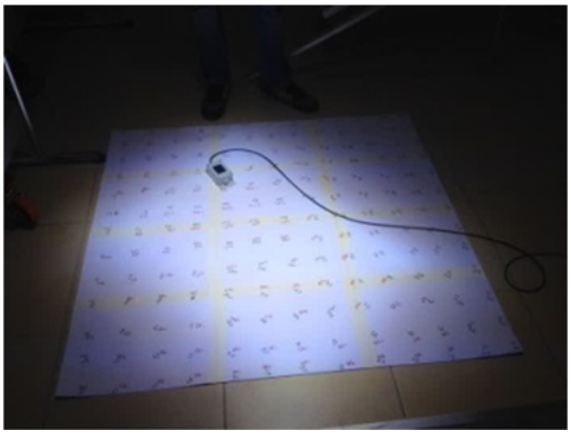

Figure 3.13. Area for light uniformity mapping.

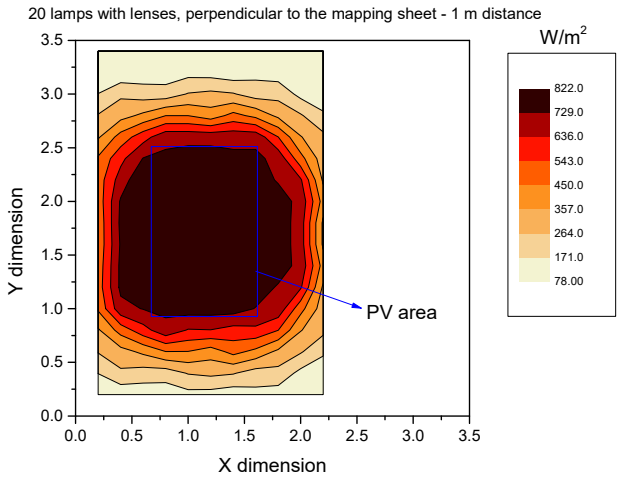

Figure 3.14. Light uniformity map in terms of solar radiation amount on the mapping area.

Another experiment concerns the generation of the performance characteristic curve of a polycrystalline PV panel with dimensions 1.30 m x 0.86 m as shown in Figure 3.15. This panel is initially tested outdoors recording also the solar intensity and incidence angle, and afterwards these conditions have been reproduced indoors with the solar simulator and a new performance curve is obtained which is compared to the outdoor one.

Figure 3.15. Experiment to obtain the characteristic curve of a PV indoors.

The comparison between the indoor and outdoor Power-Voltage curve of the PV panel is shown in Figure 3.16. The difference between the maximum power from the outdoor P-V curve and the indoor P-V curve is only 2.2 %. This shows that both tests were carried out at the same intensity and spectrum characteristics of the input light.

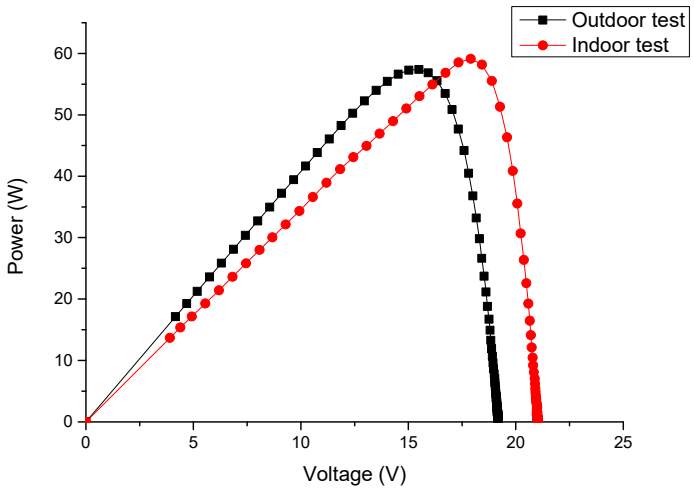

Figure 3.16.P-V curve of the panel of the indoor and outdoor tests.

3.3 Uncertainty of measurements

Considering the errors that occur due to the connection of the various devices, the experimental conditions, the uncertainty of every instrument, for all the experimental data, an error analysis is carried out to reflect the accuracy of the measured parameters.

The standard deviation of every set of data is estimated by the following equation:

$$\sigma_x = \sqrt{\frac{\sum_{i=1}^{n}(x_i - \bar{x})^2}{n-1}} \qquad 3.1$$

Where n is the number of data points

$\bar{x}$ is the mean value of all data points

x_i is each value of the data

Using the standard deviation data, the standard error (SE) is estimated using the following formula:

$$SE_x = \frac{\sigma}{\sqrt{n}} \qquad 3.2$$

3.4 The effect of slope and air gap size

The slope of the system and the size of the air gap are of the most important parameters that need to be examined. Thus, before the main experiments to investigate the temperature distribution of the experimental apparatuses, a series of experimental procedures were carried out in the laboratory to test the system's temperature distribution in different angles and different air gap sizes.

The indoor experimental apparatus described earlier can adjust its slope from 0º horizontal to 90º vertical, and thus three angles were tested 30º, 45º and 90º. According to the studies from the literature presented earlier, the most used air gap widths are 10 and 15 cm so these two values are tested. All configurations are tested with 800 W/m^2 uniform and constant solar radiation from the solar simulator. Each experimental procedure lasted for two hours, and each experiment was repeated several times to ensure the accuracy of the results. The list of experiments carried out are shown in Table 3.7.

Table 3.7. List of experiments carried out to investigate the effect of slope and air gap size on the temperature distribution of the system.

Exp. Number	BIPV slope	SS slope	Air Gap width	Incident radiation
1	90°	90°	15 cm	800 W/m^2
2	30°	30°	15 cm	800 W/m^2
3	45°	45°	15 cm	800 W/m^2
4	30°	30°	10 cm	800 W/m^2
5	45°	45°	10 cm	800 W/m^2
6	90°	90°	10 cm	800 W/m^2

Figure 3.17 and Figure 3.18 show the maximum temperature values measured during the experiments, for 10 cm and 15 cm air gap widths respectively. As shown, lower temperatures of the various parts of the system are observed for air gap of 15 cm and for inclination angle of 90º.

The system in vertical position develops lower temperatures in all measurement points and in 30º the system develops the highest temperatures. This is because for inclination of 90º the air particles are moving up with low resistance and the residence time of the particles in the conduit is less. This increases the air velocity and thus reduces the heat transfer from the PV to the working fluid. For 30º angle, the particles move up and hit the cover which reduces the kinetic energy of the working fluid and reduce the resulted mass flow rate in the system.

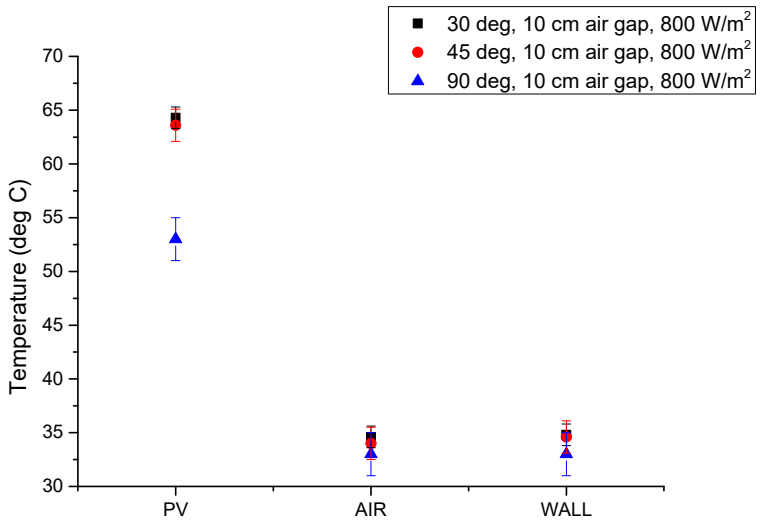

Figure 3.17. Comparison of the temperature distribution of the system with 10 cm air gap tested in all tested slopes under 800W/m^2 radiation.

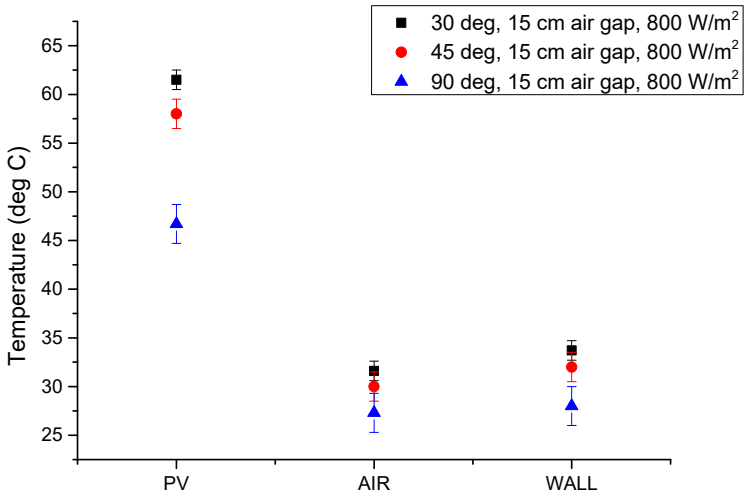

Figure 3.18 Comparison of the temperature distribution of the system with 15 cm air gap tested in all tested slopes under 800W/m^2 radiation.

Figure 3.19 shows three contour plots of the PV temperature distribution for the BIPV in 30^o, 45^o and 90^o angles with 15 cm air gap. As can be seen, the plot which shows the PV temperature distribution in 30^o has the highest temperature at the top of the PV (62°C) and then the 45^o (57°C), while the lower temperature is observed at the system in vertical position (47°C). It is important to see the high temperature difference between the top and bottom sides of the PV panel in all cases.

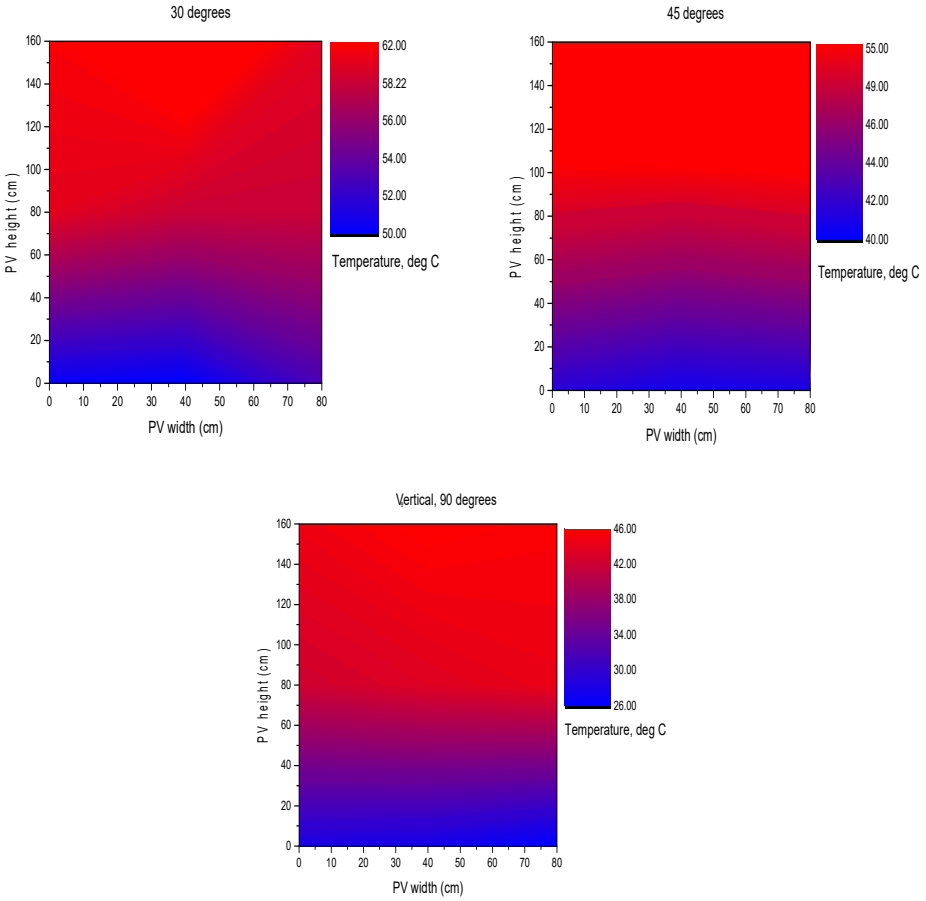

Figure 3.19. Contour plots of the PV's temperature of three experiments with 15 cm air gap, in different angles of 30°, 45° and 90°.

3.5 Indoor measurements with Solar Simulator

Subsequently, the vertical system is selected for further investigation because vertical façade systems are very common for BIPV applications and additionally from the previous experiments it is shown that the vertical system performs better in terms of lower PV temperature.

Regarding the size of the air gap, although the air gap of 15 cm showed lower temperature at the PV panel, the difference from the 10 cm is low and it is concluded that it is adequate to create enough flow to keep the temperature of the PV panel below 65°C in hot climates. Furthermore, an air gap of 10 cm is easier for installation of the PVs as the overall wall thickness is not increased a lot.

In this section, the indoor experiments carried out for the thermal investigation of the BIPV experimental apparatus described in section 3.1 are presented. The experiments are carried out with the use of a solar simulator, in controlled environmental conditions. There is no wind to affect the air pass through the air gap of the system and no mechanical means are used to circulate the air. The cold air enters the duct from the bottom opening and due to the heat from the hot front skin of the façade

(PV), it becomes less dense and moves to the top where it exits the duct. This is the stack effect mentioned earlier in this study.

Various experiments were carried out using the equipment described earlier in section 3.2. The indoor experimental apparatus is placed in vertical position in front of the solar simulator parallel with the simulator's lamp array. In this position, all the BIPV apparatus surface was exposed to uniform artificial radiation. Experiments were carried out for different solar radiation amounts considering constant radiation and a variable profile radiation. Additionally, different air gap configurations were examined, considering the closure of one of the two openings of the air duct or both. The aim of these experiments was to observe the differences in the temperature of the PV panel, the heated air in the duct and the air velocity in the duct which is created naturally due to buoyancy effect in all cases tested.

As mentioned before, the thermocouples from the PV, air and wall were connected to data loggers for recording the measurements at a time interval of 1 minute. At this point, it should be noted that the measurements began before the SS was turned on and were terminated after the SS was turned off, to record the thermal response of the PV panels as well.

3.5.1 Constant radiation

In this section, the results from the experiments carried out under constant artificial solar radiation are presented, for:

- 800 W/m^2 uniform constant solar radiation
- 1000 W/m^2 uniform constant solar radiation

Figure 3.20 shows the temperature recorded from the thermocouples installed on the top side of the PV panel and the bottom, for an experiment with a duration of 160 minutes where the BIPV apparatus was exposed under 800 W/m^2 of uniform and constant solar radiation. After minute 160 the solar simulator was turned off and the system was let to cool down.

As expected, while the whole PV surface is subjected to uniform radiation, the PV panel is cooler at the bottom side. This is because fresh air enters the duct from the bottom. The bottom side *(Tpv_b)* of the PV panel remains at stable temperature of 60^{o}C during the experiment, while the top side *(Tpv_t)* of the PV remains at 66.5^{o}C. The standard error of those measurements regarding the temperature at the top and bottom is less than 0.2 so it is not shown in the graph to simplify the plot.

From Figure 3.20, it is also observed that about 45 minutes after the beginning of the experiment, all the temperatures were almost stable until the end of the experiment. This means that the PV reaches a thermal balance after 45 minutes exposure in constant radiation.

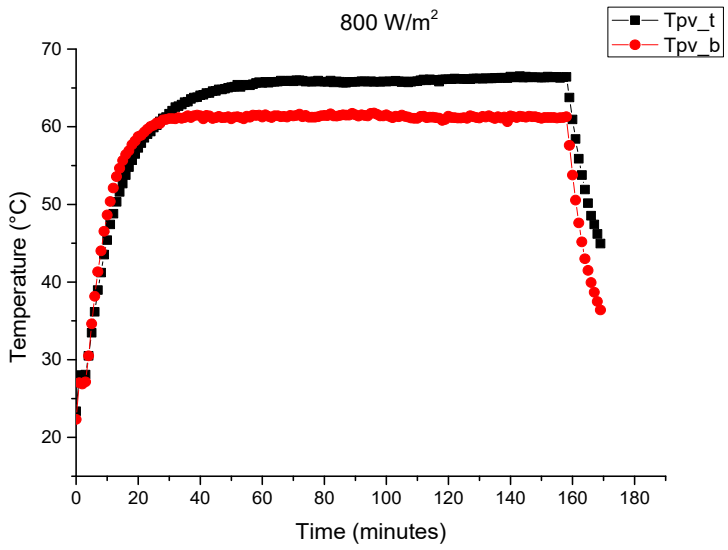

Figure 3.20. The temperature of the top and bottom side of the PV panel exposed to 800 W/m^2 constant radiation for 160 minutes.

As mentioned earlier in this study, the air gap has the main role on the thermal response and temperature distribution of the BIPV system. As shown in Figure 3.20, the bottom side of the PV panel is cooler due to the air inlet from the bottom opening of the air duct between the PV panel and the back wall. Figure 3.21 shows the temperature of the air near the inlet *(Tair_b)* and outlet *(Tair_t)* of the duct, as well as the ambient temperature of the laboratory during the experiment.

At this point it is important to state that the temperature of the air exactly at the inlet is equal to the ambient temperature. The temperature *Tair_b* shown in the figures refers to the temperature measured from the thermocouples installed at the bottom side of the air gap 10 cm from the inlet. Thus, the temperature of the air at this point is higher than the ambient temperature.

From Figure 3.21 it can be also observed that the air enters the duct at ambient temperature of 27.2^{o}C, travels through the duct for 10 cm and gets hotter up to 30 ^{o}C and until the exit its temperature reaches 36.5^{o}C. The difference between ambient and the air in the outlet is 9.3^{o}C.

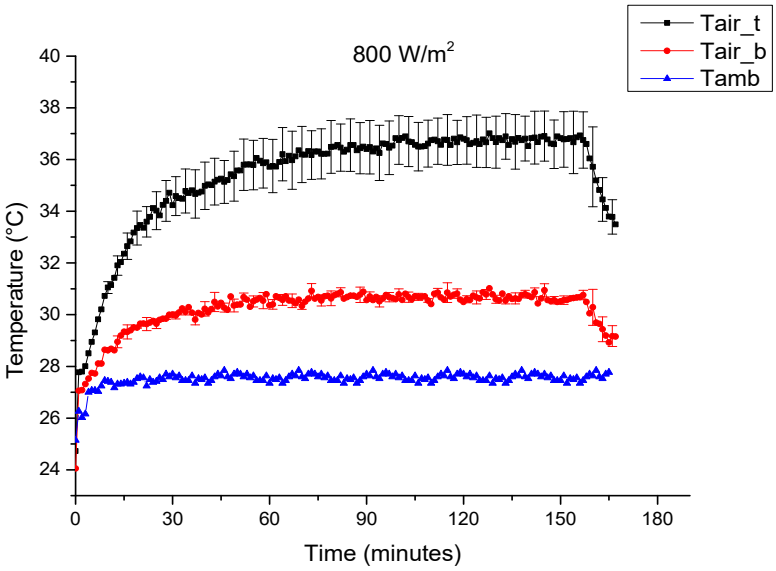

Figure 3.21. The temperature of the ambient air during the experiment of constant radiation of 800 W/m^2 with the temperature of the air in the top and bottom side of the duct.

Figure 3.22 shows the velocity of the air in the middle of the air gap, measured by inserting the probe of the hot wire anemometer in the air duct through a hole in the plexiglass side of the apparatus. The first observation is that there is flow. The tested system was able to develop air flow without any mechanical means or disturbances to circulate the air or create forced air flow. As can be seen, after about 45 minutes of experimental time, where the temperature of the system was almost stable, the air velocity varies between 0.25-0.34 m/s.

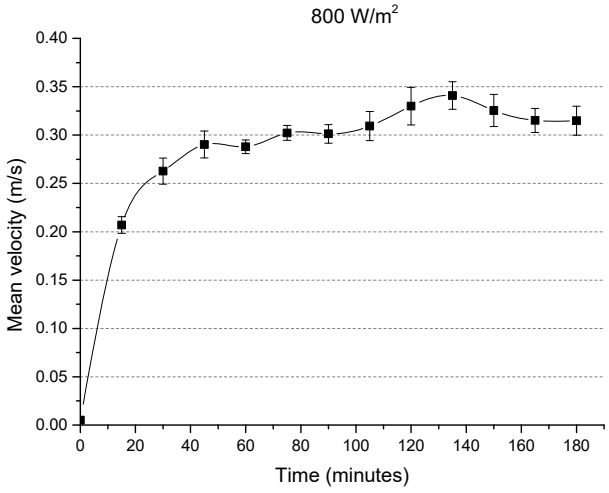

Figure 3.22. The air velocity in the middle of the air gap during the experiment of constant radiation of 800 W/m^2.

The next four figures show the results of an experiment carried out where the BIPV apparatus was exposed under 1000 W/m^2 of uniform and constant solar radiation for 180 minutes. After minute 180 the solar simulator was turned off and the system was left to cool down.

Figure 3.23 shows the temperature of the PV panel at the top and bottom sides as well as its temperature at L/2, the middle of the PV (L is the height of the PV). Comparing this figure with Figure 3.20, here we can see higher temperatures. The top side of the PV panel *(Tpv_t)* reaches 71.8ºC, the middle *(Tpv_m)* 65.5 ºC and the bottom *(Tpv_b)* 56.5ºC. There is a difference of 15.3ºC between the top and bottom sides of the PV panel.

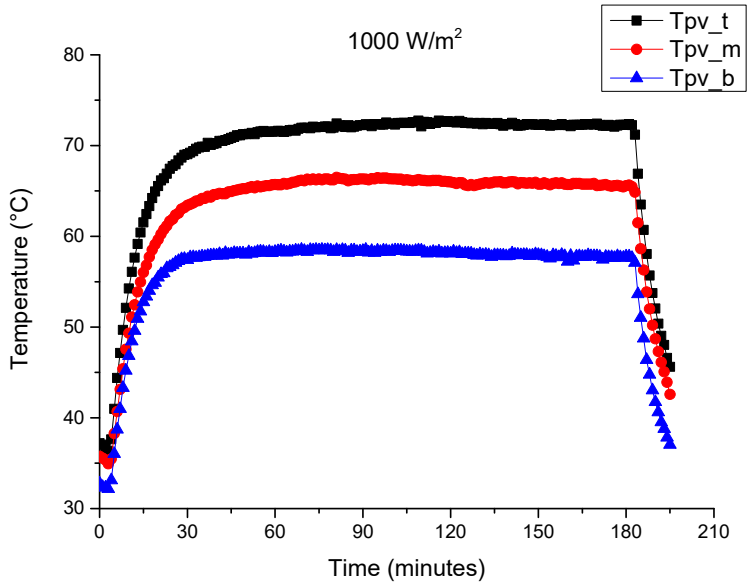

Figure 3.23. The temperature at the top, center and bottom of the PV panel exposed to 1000 W/m^2 constant radiation for 180 minutes.

Figure 3.24 shows the temperature of the air near the inlet *(Tair_b)* and outlet *(Tair_t)* of the duct, as well as the ambient temperature of the laboratory during the experiment. The air enters the duct at ambient temperature of 28-30ºC, travels through the duct for 10 cm and gets hotter up to 33.5ºC and until the exit its temperature reaches 38.5ºC.

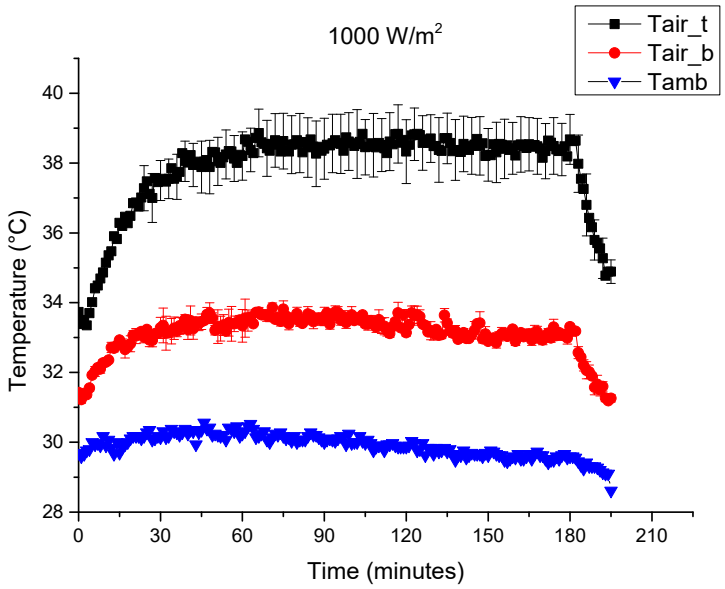

Figure 3.24. The temperature of the ambient air during the experiment of constant radiation of 1000 W/m^2 with the temperature of the air in the top and bottom side of the duct.

Figure 3.25 shows the velocity of the air in the middle of the air gap at L/2. As can be seen, after 30 minutes of experimental time, where the temperature of the system was almost stable, the air velocity varies between 0.30-0.35 m/s which is slightly higher than the experiment with 800 W/m^2 radiation as expected.

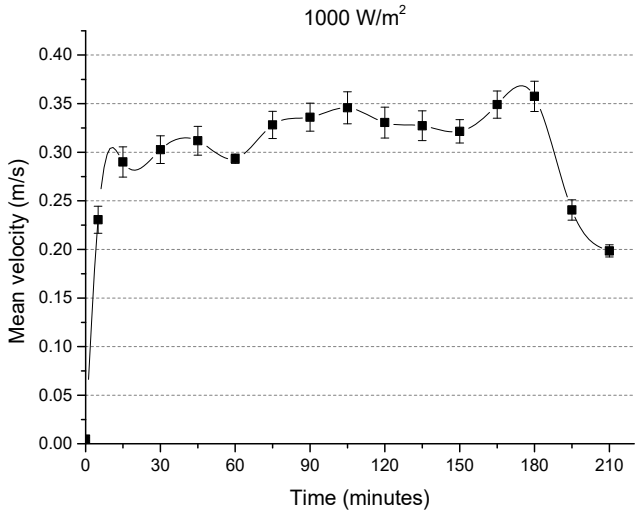

Figure 3.25. The air velocity in the middle of the air gap during the experiment of constant radiation of 1000 W/m^2.

Figure 3.26 shows the average temperature of the PV panel 30 minutes from the beginning of the experiments of 800 W/m^2 and 1000 W/m^2 radiation and one additional experiment at lower radiation of 400 W/m^2. As expected, the higher the solar radiation, the higher is the temperature of the PV panel.

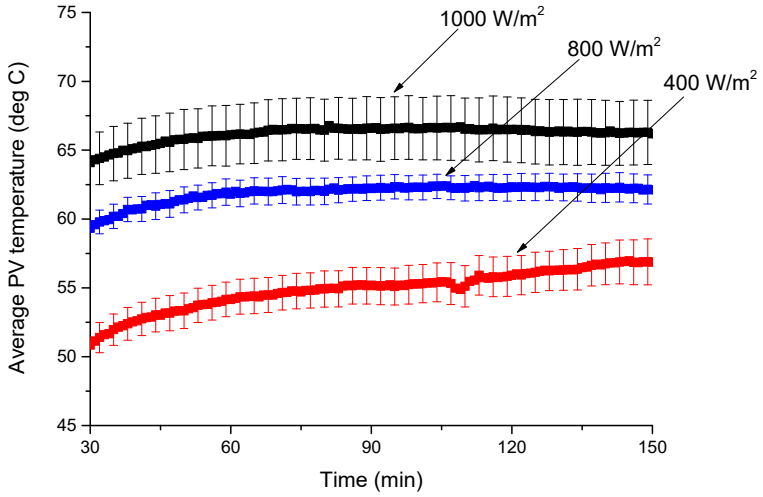

Figure 3.26. The average temperature of the PV panel exposed under 400 W/m^2, 800 W/m^2 and 1000 W/m^{2}solar radiation, with the standard error bars.

3.5.2 Variable radiation

This section presents the results obtained when the BIPV apparatus was exposed to a variable profile of solar radiation for 7 hours and 40 minutes. The total duration of the experiment was 8 hours including the cool down period after the solar simulator was turned off.

The radiation profile recorded from the pyranometer as well as the ambient air temperature of the laboratory during the experiment are shown in Figure 3.27.

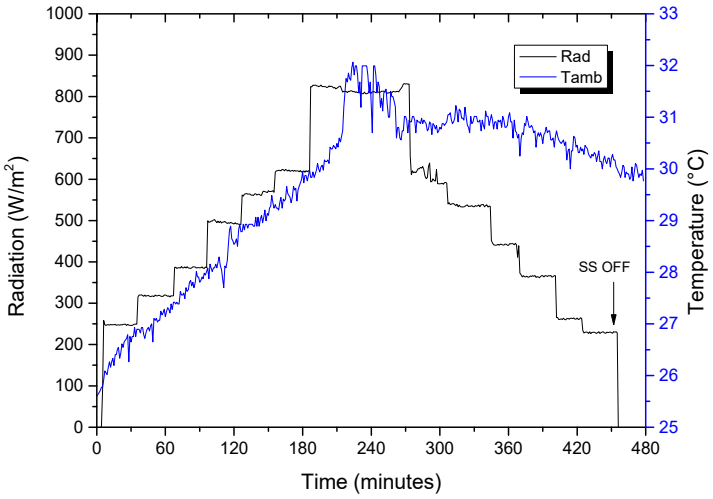

Figure 3.27. A variable radiation profile from the solar simulator for indoor experiment, and the ambient temperature of the laboratory.

Figure 3.28 shows the temperature at the top *(Tpv_t)* and bottom *(Tpv_b)* sides of the PV panel, reaching maximum at the time where the radiation was at maximum and constant. It can be said that the trend of the two lines showing the temperature of the panel follow the radiation's trend.

Figure 3.29 shows the temperature of the air near the inlet *(Tair_b)* and outlet *(Tair_t)* of the air gap and the ambient temperature of the laboratory as well. It is again ensured that the air exits the air gap hotter than it enters at about 8°C.

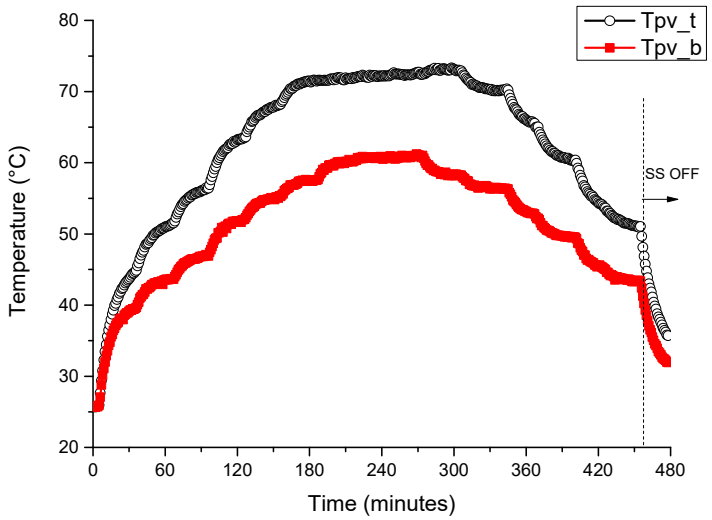

Figure 3.28. The temperature of the top and bottom side of the PV panel exposed to variable radiation for 7 hours and 40 minutes.

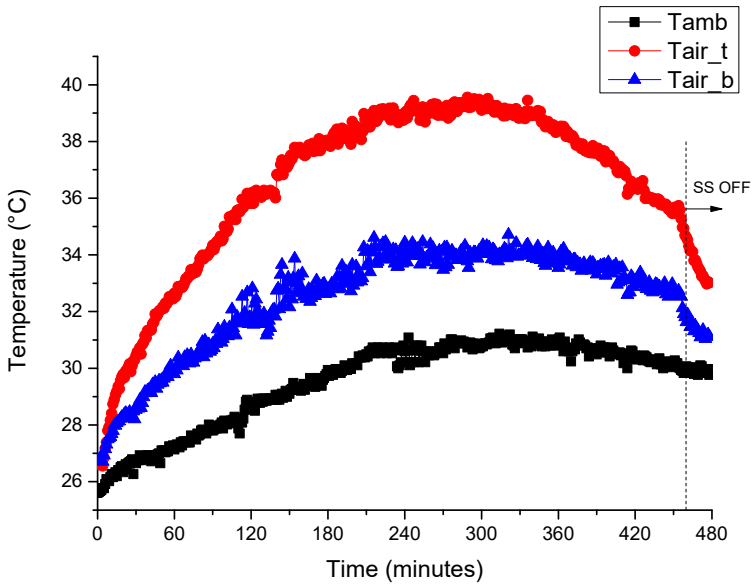

Figure 3.29. The ambient temperature in the laboratory during the experiment of variable radiation with the temperature of the air in the top and bottom side of the duct.

3.5.3 Duct Opening configurations

This section presents the temperature distribution of the various parts of the system and the air velocity in the air duct for experimental procedures carried out for different air gap configurations under constant radiation of 800 W/m^2. These were investigated to show the importance of the openings.

Figure 3.30 shows the temperature at the top and bottom of the PV panel when the bottom opening of the air duct was closed during the experiment of duration 180 minutes. Comparing this graph with Figure 3.20 where both openings were open, it can be seen that the overall temperature of the PV is higher when the bottom opening was closed. Additionally, the difference between the temperature at the bottom side of the panel and the top is smaller because no air flows from the bottom. The temperature at the tops reaches a maximum of 68^{o}C and at the bottom 64.8^{o}C.

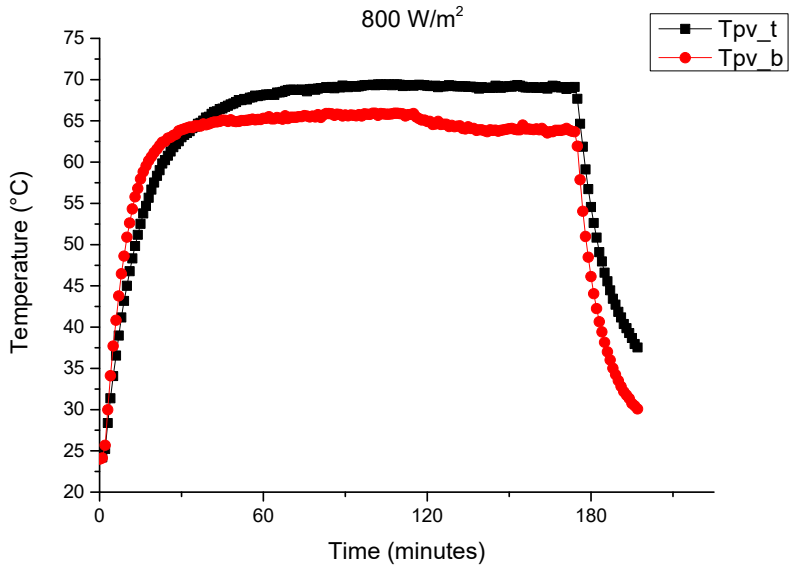

Figure 3.30. The temperature of the top and bottom side of the PV panel exposed to 800 W/m^2 constant radiation for 180 minutes – closed bottom opening of the duct.

Figure 3.31 shows the temperature of the air near the bottom opening *(Tair_b)* and near the top opening *(Tair_t)* of the duct, as well as the ambient temperature *(Tamb)* of the laboratory during the experiment. The temperature of air at the bottom side of the duct is 32.5^{o}C and at the top is 49^{o}C, i.e., there is a difference of 16.5^{o}C. Comparing this difference to the air temperatures of the system tested under 800 W/m^2 radiation when both openings were open (shown in Figure 3.21), it can be seen that both air temperatures (top and bottom) are much higher in this case. In this experiment it is the first time that a temperature difference of 7.5^{o}C exists between the ambient air and the air at the bottom of the duct. The air at the bottom side is much hotter than the ambient in this case because the bottom opening is closed and there is no flow of fresh air. Accordingly, the bottom side of the PV gets hot as well, but only 3.2°C cooler than the top side as shown previously in Figure 3.30. In the previous experiments this difference was bigger.

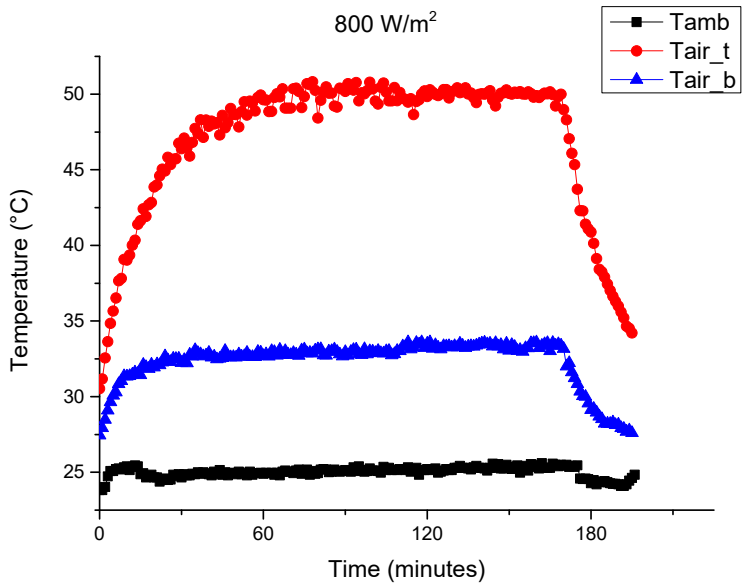

Figure 3.31. The ambient temperature of the laboratory during the experiment of 800 W/m^2 constant radiation with the temperature of the air in the top and bottom side of the duct – closed bottom opening of the duct.

The next experiment shows the resulting temperatures of the system when the top opening of the duct was closed for 180 minutes and then opened to see the effect on the system's temperature. The temperatures of the top and bottom sides of the PV panel are shown in Figure 3.32. Until minute 180 the temperatures are only slightly higher than the ones seen in Figure 3.20 where both openings were open. After minute 180, both openings were closed and no air was circulating in the air gap. The effect on the temperature of the PV panel is obvious since it increases immediately.

The increase of the temperature of the air in the duct is also obvious. Figure 3.33 shows the temperature of the air near the bottom opening of the duct *(Tair_b)* and near the top opening *(Tair_t)*. As can be seen, immediately after minute 180 when both openings were closed, the temperature near the top rises from 31.5^{o}C to 55^{o}C and near the bottom from 31.5^{o}C to 40^{o}C.

Another important fact to discuss from this experiment is the air velocity in the middle of the air duct (Figure 3.34). The velocity was very low between 0.09-0.125 m/s since minute 180 where only the top opening was closed. After minute 180 that both openings were closed, the velocity values are between 0.04-0.07 m/s which means almost no flow. From this graph, we can conclude that in order to cause flow, both openings are needed, exactly like the chimney effect in building applications.

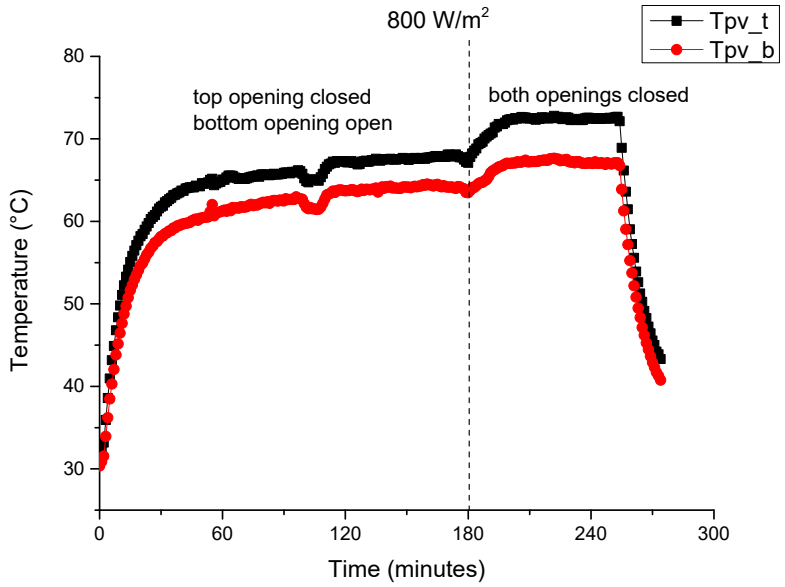

Figure 3.32. The temperature of the top and bottom side of the PV panel exposed to 800 W/m^2 constant radiation– closed top opening and closed both openings.

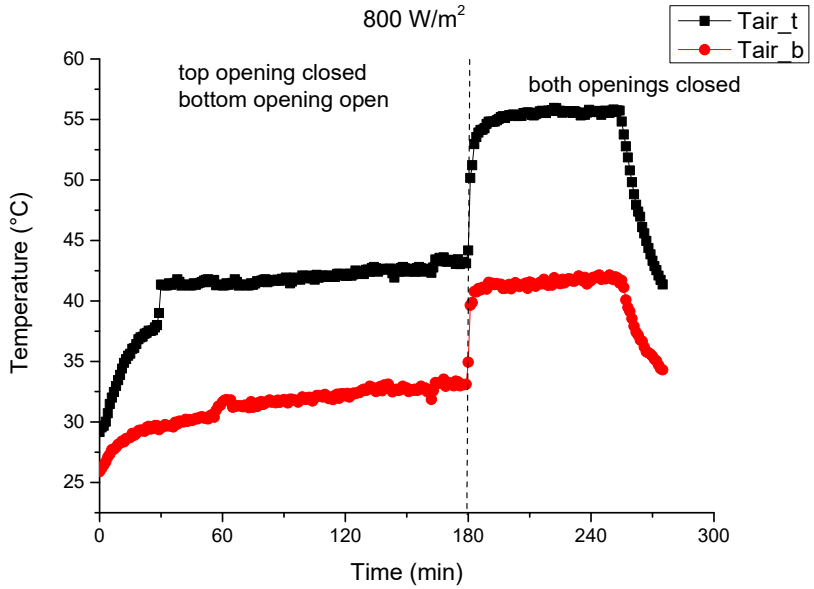

Figure 3.33. The temperature of the air in the top and bottom side of the duct for experiment with 800 W/m^2 constant radiation – closed top opening and closed both openings.

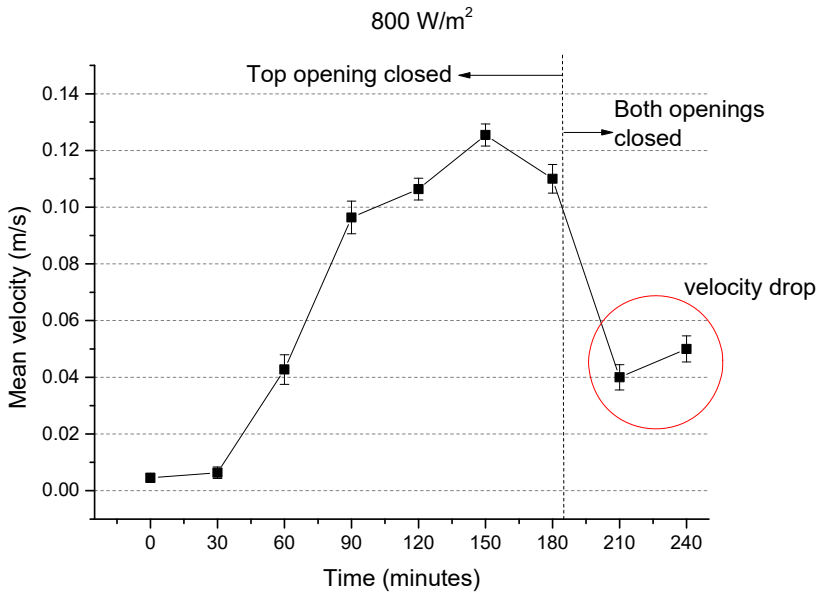

Figure 3.34.The air velocity in the duct during the experiment of 800 W/m² constant radiation– closed top opening and closed both openings.

Figure 3.35 below shows the temperature of the PV panel measured during an experiment where both openings of the air gap were closed. As can be seen the temperature at the top side of the PV panel reaches 77°C which is high enough to affect its efficiency. The temperatures of this figure are higher than the other experiments and here we can see how important are the openings in the naturally ventilated BIPV systems, to keep the temperature of the PV panels in low and efficient levels.

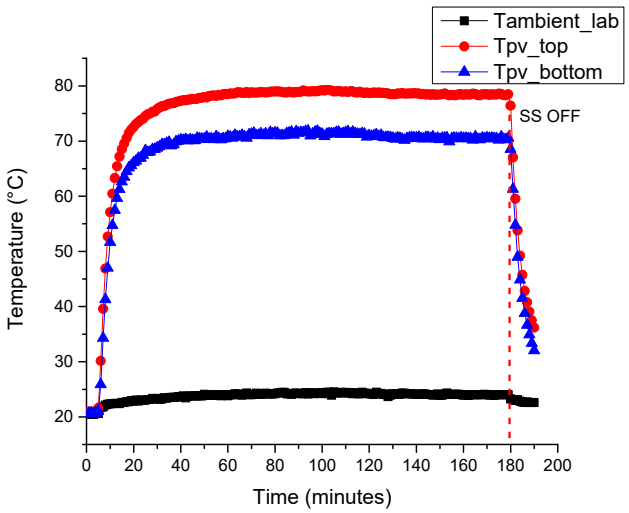

Figure 3.35. The temperature of the top and bottom side of the PV panel exposed to 800 W/m² constant radiation–both openings closed.

3.5.4 Air gap velocity measurements

So far it is proved that air flow in the duct has the most important role on the thermal behavior of the system. This section discusses the air velocity measured at experiments with different air gap openings configurations.

To present data in a representative way, box charts are used which display variation of the statistical population of data. The spacings between the different parts of the box indicate the degree of spread in the data. The lines extending vertically from the boxes indicate the variability outside the upper and lower quartiles.

Figure 3.36, Figure 3.37 and Figure 3.38, show the air velocity measured in the middle of the air gap for three cases; when the bottom opening was closed, when the top opening was closed and when both openings were closed respectively. These experiments were carried out under constant solar radiation of 800 W/m^2 as before. It is ensured that when both openings are closed almost zero air flow occurs (Figure 3.38). And additionally, when one of the two openings are closed the air flow is very small and as shown earlier this causes an increase of the PV module temperature. It should be noted that in all these plots, around 40 readings are taken for each box.

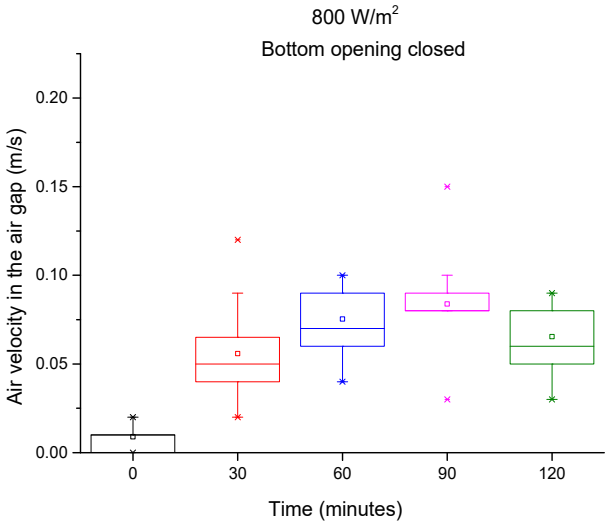

Figure 3.36. The air velocity in the middle of the air duct when bottom opening is closed - Experiment with 800 W/m^2 constant radiation.

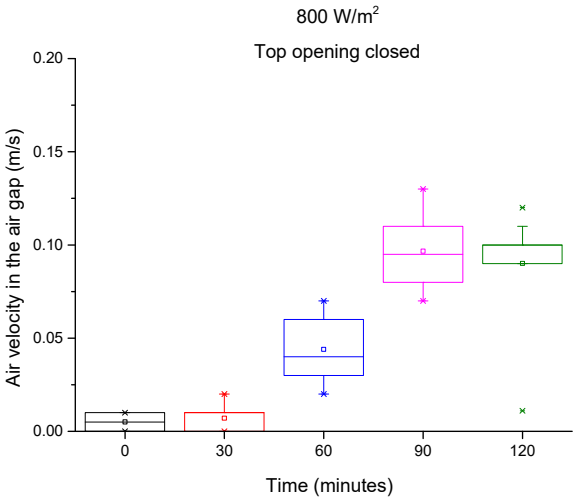

Figure 3.37. The air velocity in the middle of the air duct when top opening is closed - Experiment with 800 W/m^2 constant radiation.

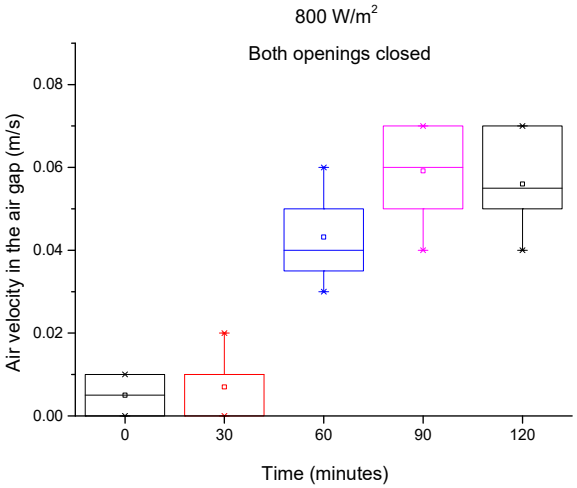

Figure 3.38. The air velocity in the middle of the air duct when both openings of the duct are closed - Experiment with 800 W/m^2 constant radiation.

Figure 3.39 shows the air velocity measured in the middle of the air duct during an experiment with 800 W/m^2 constant radiation, and both openings closed for 3 hours. After 3 hours, the top opening opened and the air velocity increased significantly from 0.05 m/s on average, to 0.4 m/s.

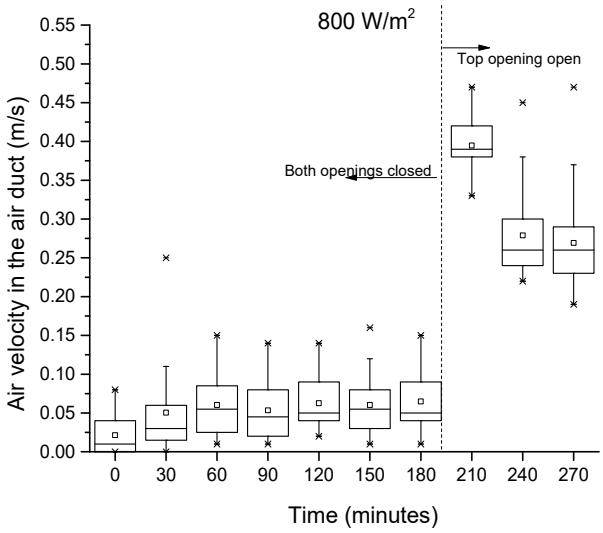

Figure 3.39. The air velocity in the middle of the air duct when both openings are closed and then the top opening is open - Experiment with 800 W/m^2 constant radiation.

Up to now, the air velocity values presented were measured in the middle of the air gap width and in the mid-height at L/2. The next figures show measured air velocity in the air gap measured in the mid-width but at different heights, near the bottom opening, in the middle and near the top opening.

Figure 3.40, Figure 3.41 and Figure 3.42 show the measured air velocity at the bottom, middle and top side of the air gap during the experiment of constant radiation of 800 W/m^2. Higher velocity is observed at the bottom side of the duct near the bottom opening where fresh air enters the duct. It is also observed that near the top opening the air velocity is slightly higher than the one measured in the middle of the air gap. The temperature difference between the outlet air and the ambient air creates higher air flow near the openings.

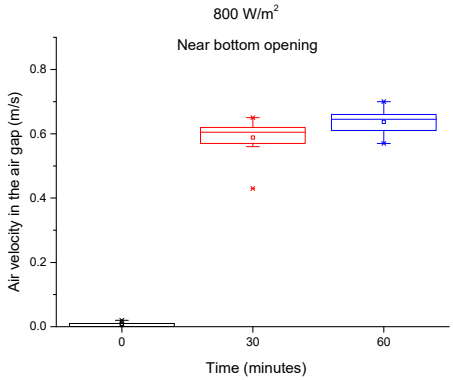

Figure 3.40. The air velocity measured near the bottom opening of the air duct – Experiment with 800 W/m^2 constant radiation.

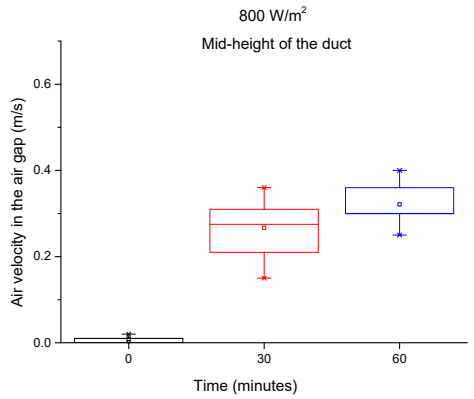

Figure 3.41. The air velocity measured in the middle of the air duct – Experiment with 800 W/m^2 constant radiation.

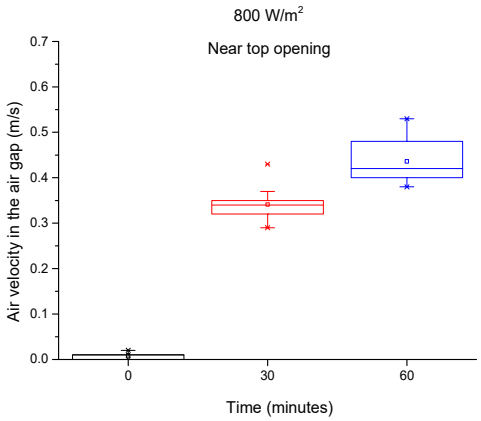

Figure 3.42. The air velocity measured near the top opening of the air duct – Experiment with 800 W/m^2 constant radiation.

3.5.5 Measured PV Electrical Characteristics

As mentioned in the introduction of this study, high temperature of the PV cells affects mainly the open circuit voltage. With high temperature, the open circuit voltage decreases while the short circuit current increases. This is shown in Figure 3.43.

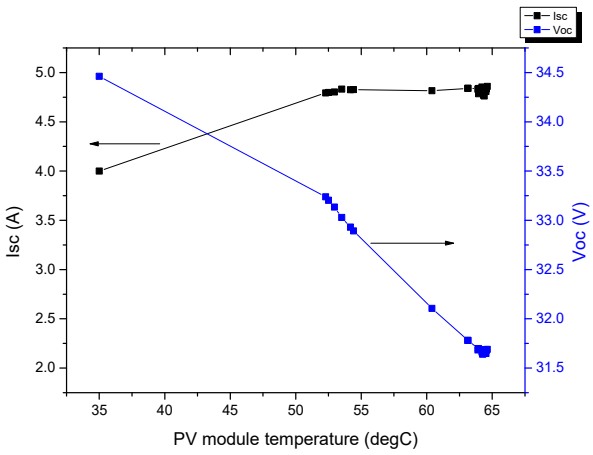

Figure 3.43. The effect of high temperature of the PV panel on the short circuit current and open circuit voltage.

The I-V and P-V curves of the PV panel are shown for three temperatures in Figure 3.44 and Figure 3.45 respectively. The drop of the open circuit voltage is obvious as well as the drop of the power. From 36°C to 69°C there is 12.8% drop in power. This is 0.4%/°C which agrees to the temperature coefficient of maximum power 0.45%/°C given by the manufacturer as shown previously in Table 3.1Table 3.1. Technical data of the PV panel..

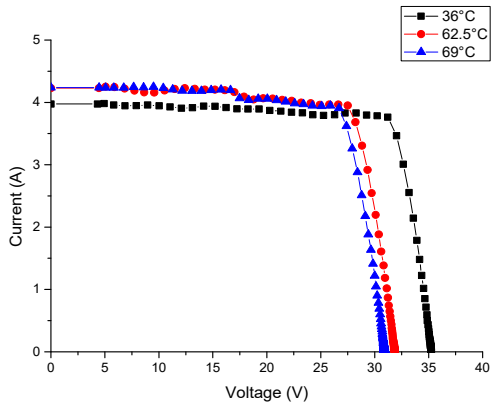

Figure 3.44. I V curves.

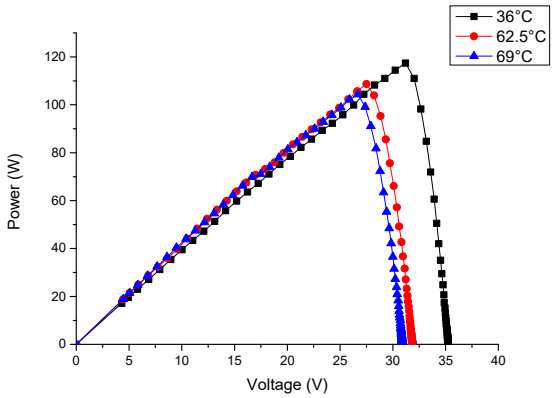

Figure 3.45. P-V curves.

Figure 3.46 shows the electrical efficiency of the PV panel estimated for various temperatures of the PV panel estimated considering the nominal efficiency and the temperature coefficient given by the manufacturer. It is observed that there is a 2.3% drop of efficiency between 35 and 70°C.

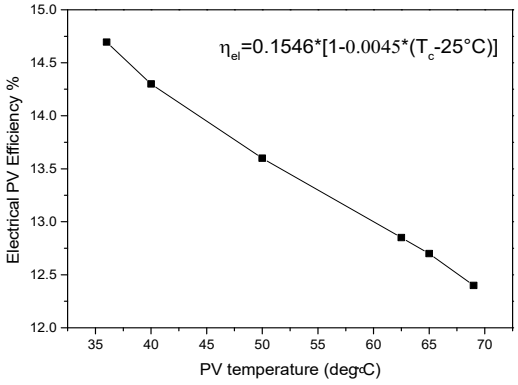

Figure 3.46. The electrical efficiency of the tested PV panel for different temperatures of the PV.

3.5.6 Air Gap Heat Transfer Analysis - Convective Heat Transfer Coefficients CHTC

The experimental data presented in the previous sections are used together with the theoretical equations to carry out a heat transfer analysis of the system. One of the most important goals of this study is the estimation of the convective heat transfer coefficients in the air gap which is the part of the system which is responsible for its thermal behaviour. The coefficients are also important for the energy level investigation.

For the estimation of the convective heat transfer coefficients (CHTC) in the air gap, the following the equations are used:

$$\dot{Q} = \dot{m}\, C_p\, (T_o - T_i) \qquad 3.3$$

$$\dot{Q} = h_{air}\, A_{ch}\left(T_{PV} - T_{m,a}\right) \qquad 3.4$$

$$h_{air} = \frac{\dot{Q}}{A_{ch}\left(T_{PV} - T_{m,a}\right)} \qquad 3.5$$

$$Nu = \frac{h_{air}\, d}{k_{air}} \qquad 3.6$$

Where $\dot{m}$ is the mass flow rate (kg/s)

C_p is the specific heat of air at constant pressure (kJ/kg K)

T_o is the temperature of the air at the duct's outlet (°C)

T_i is the temperature of the air at the duct's inlet (°C)

h_{air} is the CHTC in the air gap between the PV and the wall (W/m^{2}K)

A_{ch} is the cross section area of the duct (m^2)

$T_{m,a}$ is the mean temperature of the air in the air gap (°C)

d is the width of the air gap (m)

k_{air} is the thermal conductivity of air (W/m K)

The experimental CHTC and the Nusselt number for the air gap during the experimental procedures of 800 W/m^2 and 1000 W/m^2 constant radiation and variable profile radiation, are shown in Figure 3.47 and Figure 3.48 respectively. The CHTC in the air duct between the PV panel and the back of the wall, is slightly higher for the experimental procedure of 1000 W/m^2 constant radiation, due to the higher resulting temperature of the BIPV various parts. The same observation goes for the Nusselt number since the two parameters are related.

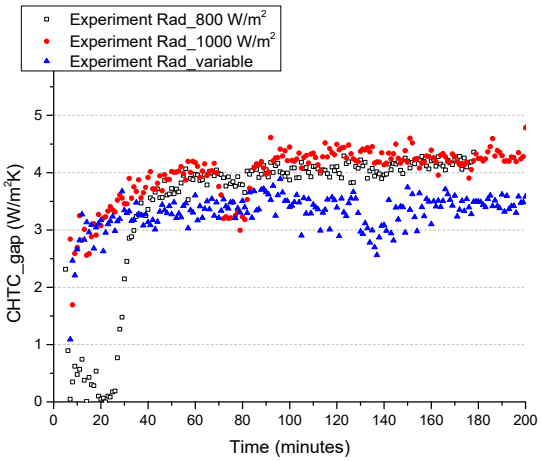

Figure 3.47. The experimental CHTC values of three experiments.

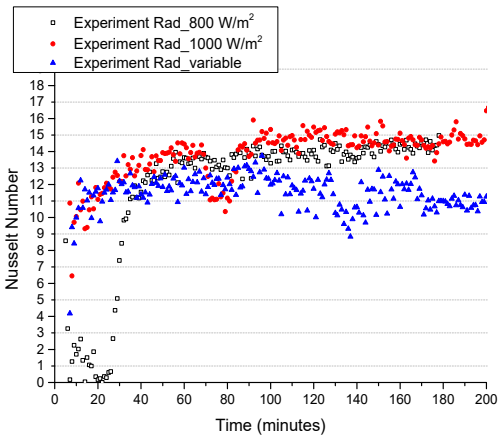

Figure 3.48. The experimental Nusselt Number values of three experiments.

As concluded from the literature review (Chapter 2) of this study, the most appropriate equation found on literature for the estimation of the CHTC in naturally ventilated BIPV systems, is the one given by

Bar-Cohen and Rohsenow (1984) for asymmetric heating tetween two plates considering the one isoflux surface and the other adiabatic:

$$Nu_{O,L} = \left[\frac{6}{Ra''} + \frac{1.88}{(Ra'')^{0.4}}\right]^{-0.5} \qquad 3.7$$

Where the Rayleigh number Ra'' is given by the following correlation:

$$Ra'' = \frac{\rho^2\ g\ \beta\ C_p\ d^5\ \dot{q}}{\mu\ L\ {k_{air}}^2} \qquad 3.8$$

Where ρ is the density of air (kg/m^3)

g is the gravitational acceleration (m/s^2)

β is the volumetric coefficient of thermal expansion (1/K)

C_p is the specific heat of air at constant pressure (J/kg K)

$\dot{q}$ is the heat flux (W/m^2)

μ is the dynamic viscosity of air (kg/m s)

L is the length of the channel (m)

d is the distance between the two plates (m)

In Figure 3.49, Figure 3.50 and Figure 3.51 the experimental Nu number is compared with the one given by the correlation of Bar-Cohen and Rohsenow (1984) for the three experiments of 800 W/m^2 radiation, 1000 W/m^2 radiation and variable profile radiation respectively.

The equation proposed by Bar-Cohen and Rohsenow (1984) represents the trend of the experimental Nusselt number well but it underestimates most of the experimental data.

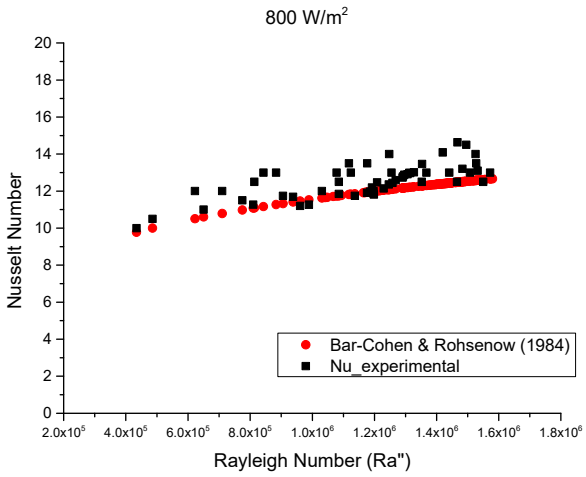

Figure 3.49. Experimental Nu number Vs estimated Nu from Bar-Cohen and Rohsenow (1984) - *Experiment with 800 W/m^2 constant radiation.*

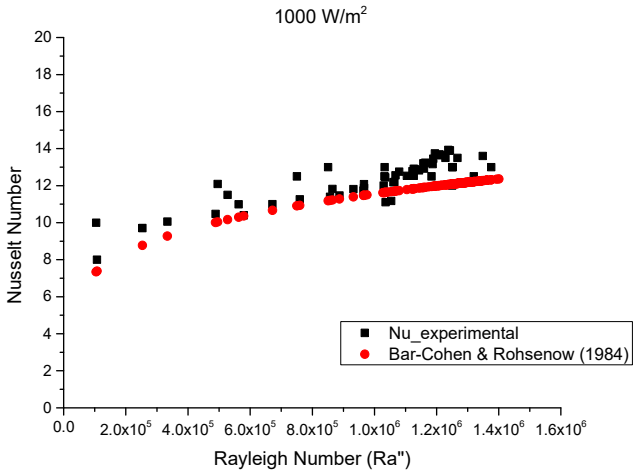

Figure 3.50. Experimental Nu number Vs estimated Nu from Bar-Cohen and Rohsenow (1984) - *Experiment with 1000 W/m^2 constant radiation.*

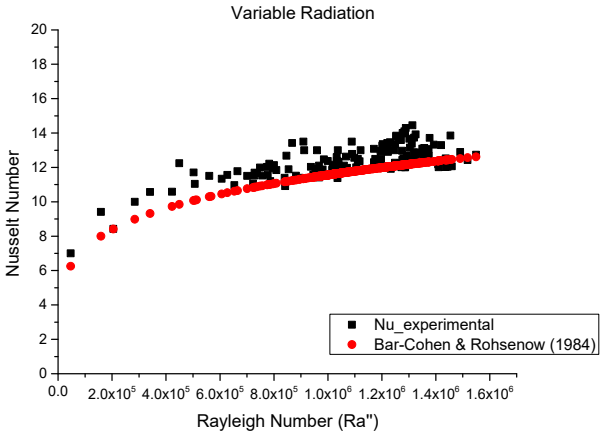

Figure 3.51. Experimental Nu number Vs estimated Nu from Bar-Cohen and Rohsenow (1984) - *Experiment with variable radiation.*

The differences between the predicted and the measured Nu number values are estimated by the percentage of the relative error (PRE) as:

$$PRE(\%) = \frac{Nu_{exp} - Nu_{est}}{Nu_{exp}} \times 100 \qquad 3.9$$

For $2x10^5$<Ra''<$1.2x10^6$ the PRE between the experimental Nu and the Nu estimated from the correlation from Bar-Cohen and Rohsenow (1984) is less than 18% while for bigger values of Ra'' the PRE reaches 43%. This is due to the relatively small values of Nu.

In order to give more emphasis on the size of the air gap *(d)* and the length of the system *(L)* on the estimation of the Nusselt number, a modified Rayleigh number Ra* is proposed:

$$Ra^* = \frac{g\ \beta\ d^4 \dot{q}\ \rho\ C_p}{v\ k^2} \qquad 3.10$$

Where ρ is the density of air (kg/m^3)

g is the gravitational acceleration (m/s^2)

β is the volumetric coefficient of thermal expansion (1/K)

C_p is the specific heat of air at constant pressure (J/kg K)

$\dot{q}$ is the heat flux (W/m^2)

v is the kinematic viscosity of air (m^2/s)

k is the thermal conductivity of air (W/mK)

d is the air gap width (m)

The experimental average Nu number data are plotted and fitted with power functions in terms of the modified Rayleigh number *Ra** and the aspect ratio *(d/L)* in the form of:

$$Nu = a\ (Ra^*\ (d/L))^b \qquad 3.11$$

where d is the width of the air gap (m) and L is the length of the air duct (m). Constants a and b are calculated in every case in every time step with the use of the experimental data.

Analysing all data from the fitted curves, the following correlation is obtained:

$$Nu = 1.23\ (Ra^*(d/L))^{0.168} \qquad 3.12$$

Consequently, Equation 3.12 is the proposed equation for the estimation of the CHTC in the air gap of a naturally ventilated BIPV system in non-windy conditions.

The estimated Nu from the proposed correlation compared to the experimental Nu for the experiments with constant radiation and variable radiation is shown in Figure 3.52 and Figure 3.53 respectively. The PRE between the experimental Nu and the Nu estimated from the proposed correlation is less than 15%.

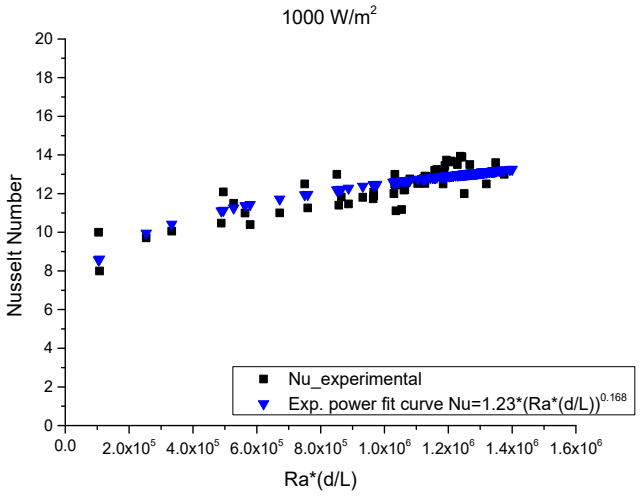

Figure 3.52. The Nu number from the proposed correlation in relation with the experimental Nu number for experiment with constant radiation.

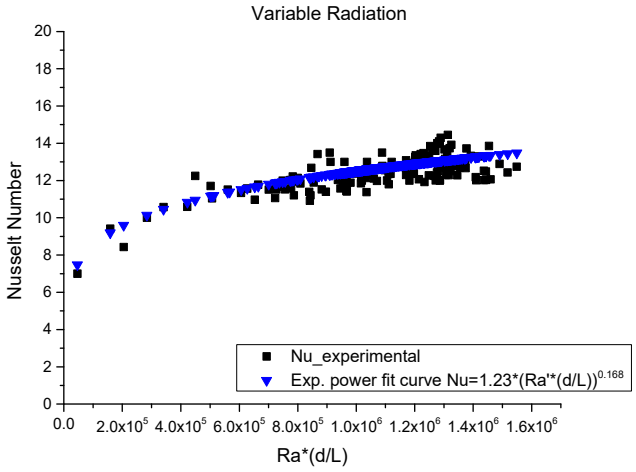

Figure 3.53. The Nu number from the proposed correlation in relation with the experimental Nu number for experiment with variable radiation.

Figure 3.54 shows a comparison between the experimental Nusselt number, and the Nu estimated from Bar-Cohen and Rohsenow (1984) and Lau et al. (2012a). The experimental Nu is close to the values obtained with the correlations from Bar-Cohen and Rohsenow (1984).

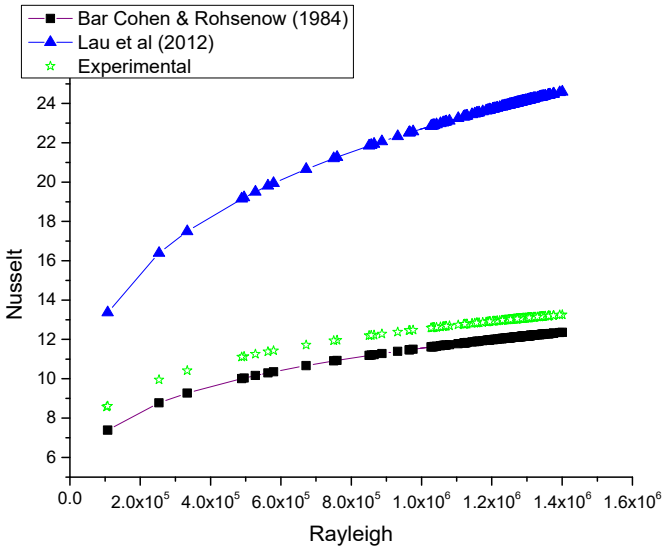

Figure 3.54. Nusselt Number from correlations from the literature and the estimated Nusselt number.

3.6 Outdoor measurements in real sun

In this chapter, the outdoor experiments carried out for the thermal investigation of the BIPV experimental apparatus described in section 3.1 are presented. The experiments are carried out in real environmental conditions with variable radiation, clouds, wind and air dust.

As mentioned before, only naturally ventilated systems are investigated. The cold air enters the duct from the bottom opening and due to the heat from the hot front skin of the façade it becomes less dense and moves to the top where it exits the duct. This is the stuck effect mentioned earlier in this study. However, this procedure is now affected by the wind speed which occurs in outdoor conditions. Although no mechanical means are used to drive the air in the duct, wind speed affects the flow in the duct and the temperature distribution of the system.

3.6.1 Solar Radiation Measurements

The measurement of incoming solar radiation is done on the vertical surface of the testing system. The pyranometer is placed vertically in the upper left corner of the BIPV apparatus (see Figure 3.3).

Recordings of the of solar radiation measured on the south and east orientations for several days during July, August and September 2016 in Limassol, Cyprus (34.70°N, 33.02°E) are shown in Figure 3.55.

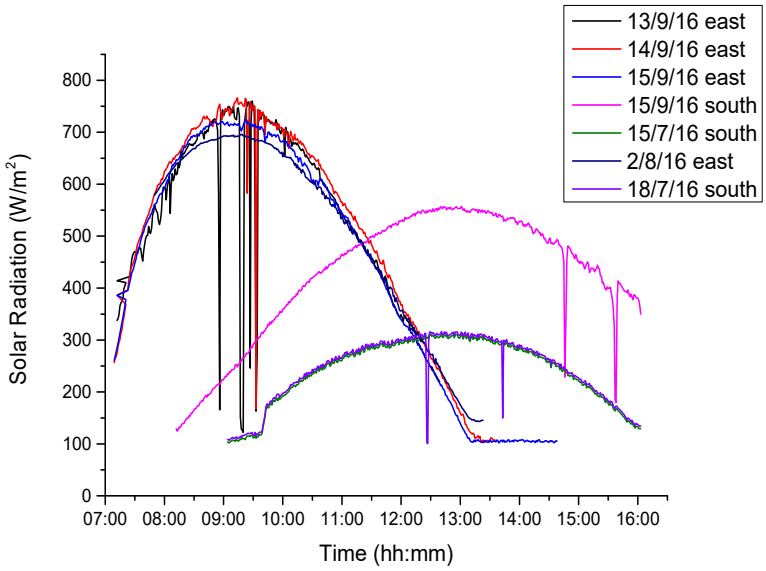

Figure 3.55. Variation of total radiation falling on the vertical south and east facing surfaces during several days in summer 2016 in Limassol, Cyprus.

Higher radiation is observed in the measurements of east orientation. This is due to the position of the sun in the morning hours in east orientation, which is almost perpendicular on a vertical surface facing east. Accordingly, east orientation is selected for analysis and the measurements in east orientation are performed during the effective hours of the east orientation which are from 7:00 am to 12:00 noon.

3.6.2 Thermal behavior of BIPV

Figure 3.56 shows the measured temperature of the top side of the PV panel for different experimental days. As can be observed the data measured for the days between 13-15 September 2016 are very close but those measured during July in south orientation are different due to the different solar radiation amount as shown in the previous figure.

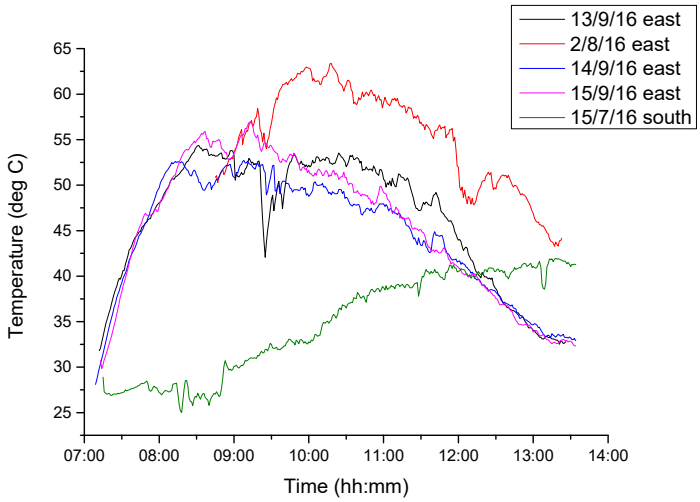

Figure 3.56. Measured temperature of the top side of the PV panel on various days of experiments.

For further analysis of the measurements, to avoid disturbances from clouds, the measurements of September 15th where the sky was clear are selected to be presented. However, the analysis is done for all the experimental procedures and the outcomes are based on all the experiments. The solar radiation and the ambient temperature measured on September 15th are shown in Figure 3.57.

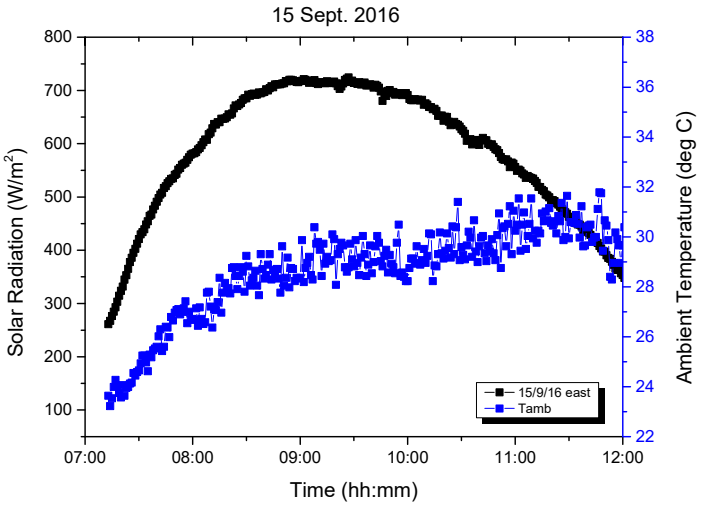

Figure 3.57. The measured solar radiation and ambient temperature on 15/9/2016.

Figure 3.58 shows the temperature recorded from the thermocouples installed at the top, center and bottom side of the PV panel. As can be observed the higher temperatures are observed at the time where the solar radiation is higher.

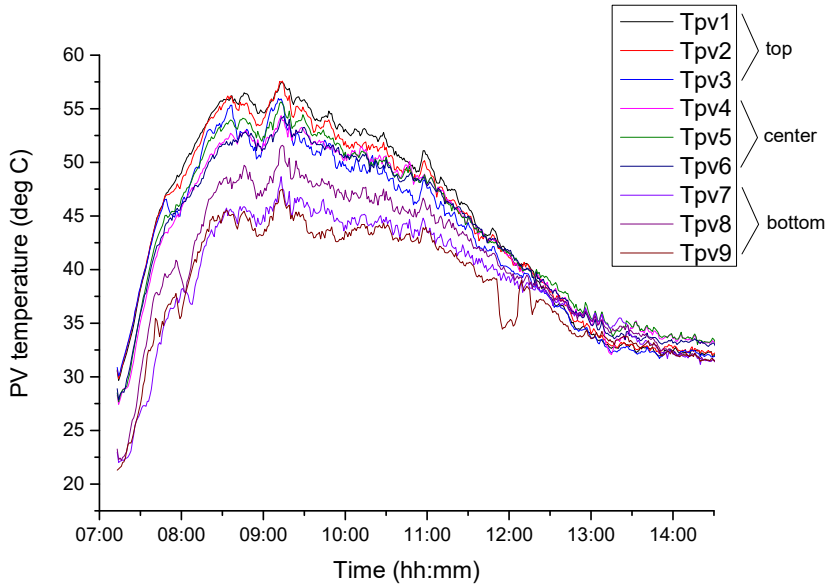

Figure 3.58. The temperature measured from the 9 thermocouples installed on the back side of the PV panel on the experiment carried out on September 15th 2016.

From the average values of the three thermocouples for the three heights of the PV panel, an average temperature is derived to represent the temperature at the top side of the PV, center and bottom. This is shown in Figure 3.59, where the bottom side *(Tpv_b)* reaches a maximum temperature of 47.5°C during the experiment, while the top side *(Tpv_t)* reaches 56.9°C. The standard error of those measurements is also shown in Figure 3.59 together with an infrared photograph of the PV panel taken from a thermal camera on specific time.

Figure 3.60 shows the average temperature of the PV panel with the calculated standard error. Having a difference from 2 to 8°C between the top and bottom sides of the PV panel, it is normal to have variable standard error during the measurement time.

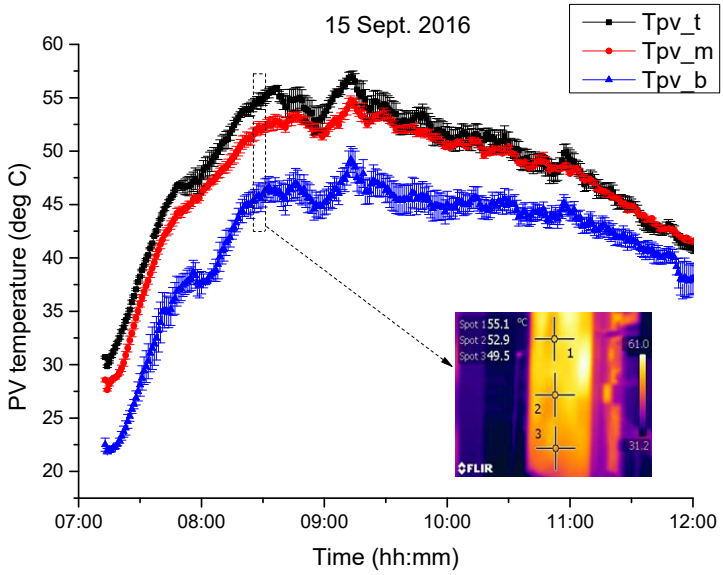

Figure 3.59. The temperature of the PV panel at the top, centre and bottom sides on 15/9/16 and infrared picture of the PV panel.

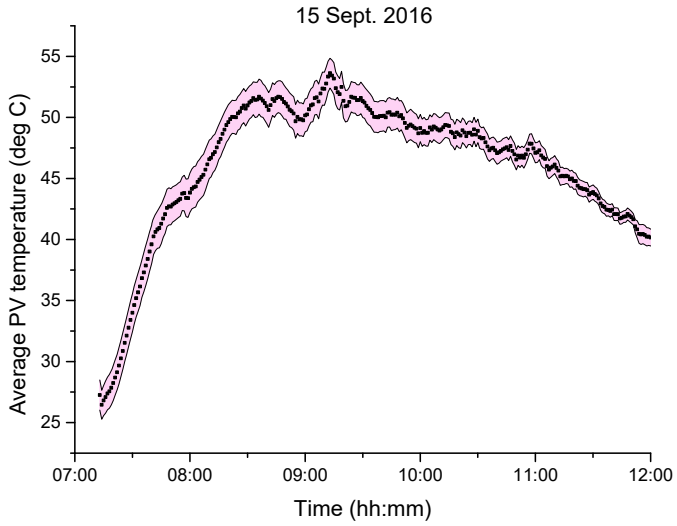

Figure 3.60. The average temperature of the PV panel on 15/9/16.

As mentioned before, the air gap has the main role on the thermal response and temperature distribution of the BIPV system. As shown in Figure 3.59, the bottom side of the PV panel is cooler due to the air inlet from the bottom opening of the air duct between the PV panel and the back wall. Figure 3.61 shows the temperature of the air near the inlet *(Tair_b)* and outlet *(Tair_t)* of the duct, as well as the ambient temperature of the air on September 15th, 2016.

Again, the temperature *Tair_b* refers to the temperature measured from the thermocouples installed at the bottom side of the air gap 10 cm from the inlet. Thus, the temperature of the air at this point is higher than the ambient temperature.

From Figure 3.61 it can be also observed that the air enters the duct at ambient temperature of 27.2°C, travels through the duct for 10 cm and gets hotter up to 33 °C and until the exit its temperature reaches 35°C. The difference between ambient air and the air at the outlet is smaller than that observed in the indoor experiments. This is because of the higher air flow in the duct due to the wind. Wind forces air to pass faster through the air gap and thus air doesn't have enough time to be heated more from the bottom to the top.

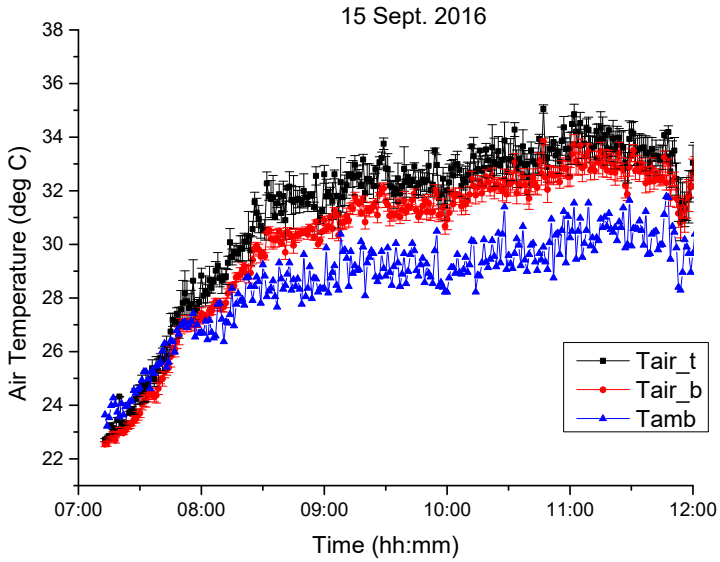

Figure 3.61. The temperature of the air in the bottom and top of the air gap, and the ambient temperature on 15/9/16.

3.6.3 Flow Measurements

The measurements for the air velocity of the air duct for the experiment of 15th September 2016 are shown Figure 3.62 and show that the average air velocity is 0.8-0.9 m/s. This is higher than the air velocity measured in the indoor experiments of 0.3 m/s which was only due to buoyancy effect, with no wind.

In Figure 3.62 the wind speed on that particular day is shown as well. As can be seen, the higher the wind speed, the bigger is the spread of the values measured of the air velocity in the air gap which proves that the air movement in the duct is affected by the external wind.

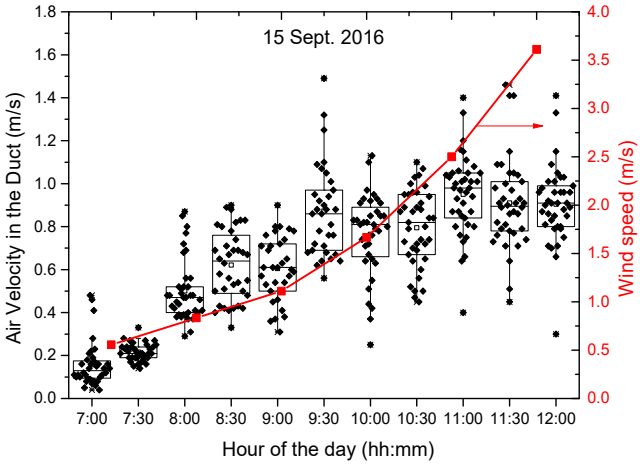

Figure 3.62. The air velocity in the air gap on 15/9/16.

3.6.4 Measured PV Electrical Characteristics

Figure 3.63 shows the I-V and P-V curves of the PV panel recorded on the experiment of September 15th every 30 minutes.

From these graphs, the effect of the PV overheating on the power of the PV panel is not obvious since the radiation is not constant as it was previously in the indoor experiments.

Examining the I-V and P-V curves collected by the PVPM device in the curves of Figure 3.63, it can be observed that short circuit current drops due to the reduction of radiation, shown in Figure 3.57. The change in the open circuit voltage is almost zero. Thus, the temperature of the PV surface did not affect the overall performance of the PV, which mainly affects the open circuit voltage. This means that the 0.10 m air gap was adequate to create sufficient air speed to remove the excess heat behind the PV panel, to prevent overheating and loss of efficiency. The best curve is observed from 9:00 to 9:30 am where solar radiation was at maximum (perpendicular) which also lead to higher PV temperature, which is shown in Figure 3.59.

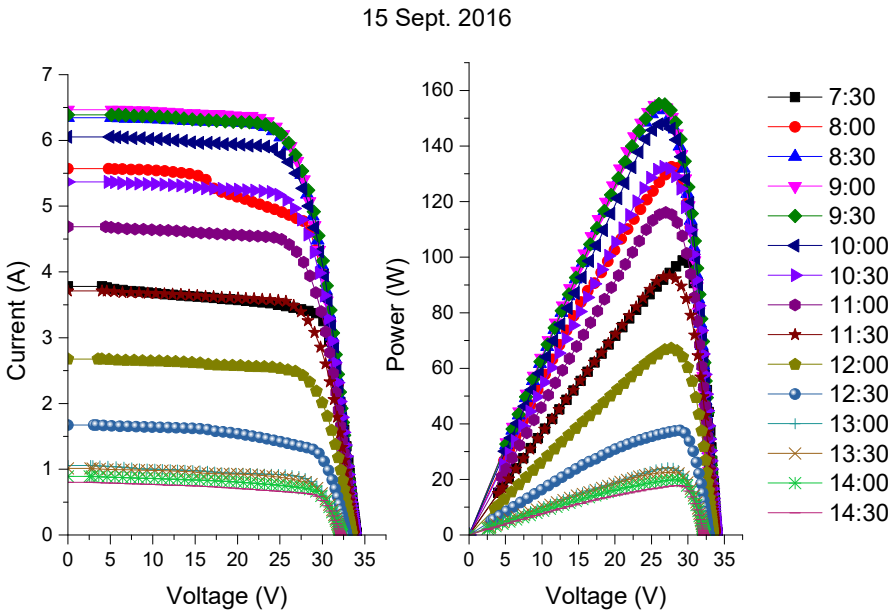

Figure 3.63. The Current-Voltage and Power-Voltage curves of the PV panel during experiment on 15/9/16.

3.6.5 Air Gap Heat Transfer Analysis- Convective Heat Transfer Coefficients CHTC

As done previously for indoor experiments, the experimental Nu number data are compared with the Nu number estimated with the use of the equation proposed by Bar-Cohen and Rohsenow (1984). Figure 3.64 shows the experimental Nu number in comparison with the estimated Nusselt from the Bar-Cohen and Rohsenow (1984) correlation for asymmetric heating.

As can be observed, the equation results are not consistent with the experimental data. Thus, the same procedure is followed as done previously in section 3.5.6. The experimental data from all days of experiments are plotted and fitted with power fitting curve and a new Nusselt number equation is derived:

$$Nu = 0.002\ (Ra^{*}(d/L))^{0.65} \qquad 3.13$$

The Ra* is given previously in Eq. 3.10. Figure 3.65 shows the experimental data with the estimated Nu numbers from the derived equation. The CHTC for the outdoor experiments vary from 2.5 - 5.5 W/m^{2}K. The estimated PRE between the experimental and the estimated Nu values is less than ±20%.

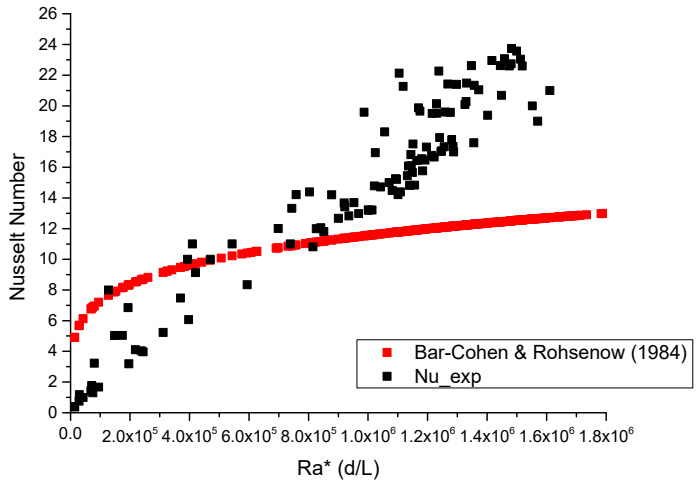

Figure 3.64. Experimental Nu number Vs estimated Nu from Bar-Cohen and Rohsenow (1984) *for outdoor experiments.*

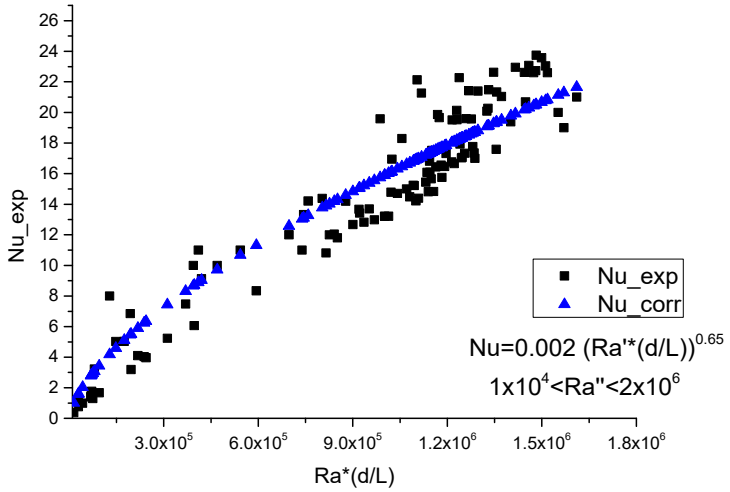

Figure 3.65. The Nu number from the proposed correlation in relation with the experimental Nu number for outdoor experiments.

Figure 3.66 shows the estimated Nu numbers in comparison with the experimental ones. The plot shows that the derived equation gives consistent values with the experimental data with less than ±20% PRE between the experimental and the estimated Nu.

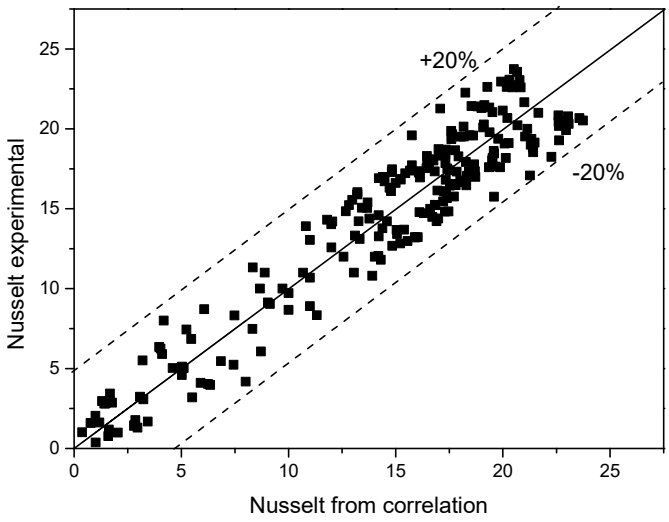

Figure 3.66. Air gap Nusselt number estimation and experimental Nusselt number.

3.7 Discussion & Conclusions

This chapter presented the experimental analysis of the thermal behaviour of a BIPV system, with the use of experimental apparatuses as a basic testing device. The first section of the experimental part presented the results from the indoor experimental procedure carried out in a laboratory with controlled conditions, and the second section presents the experimental analysis carried out in real environmental conditions. From both experimental analyses, a heat transfer analysis is carried out, for the estimation of the CHTC and the Nusselt number values. From this analysis, two correlations for the estimation of the Nusselt number are derived. From the indoor experiments the Nu number correlation can estimate the CHTC in the air gap of a BIPV system in no wind conditions, while from the outdoor experiments the proposed correlation can estimate the CHTC for a BIPV system exposed to wind.

The correlations are based on power fitting curves in the form of $Nu = a\ (Ra^*\ (d/L))^b$ and the constants are shown below in Table 3.8. These correlations are derived considering natural air flow between two parallel plates, one of them considered as isoflux surface (PV panel) and the other as adiabatic surface (wall).

Table 3.8. Air gap average CHTC estimation for indoor and outdoor experiments with no wind and windy conditions respectively.

Conditions*	***a***	***b***
No wind	1.23	0.168

Wind	0.002	0.65

*$10^4 < Ra^*(d/L) < 2 \times 10^6$

Figure 3.67 shows the Nu number data from two new correlations in comparison with the equation from Bar-Cohen and Rohsenow (1984). As can be seen, the correlation obtained from the indoor experiments with no wind is very close to the data obtained from the Bar-Cohen and Rohsenow (1984) correlation. Both equations, the one proposed for non-windy conditions and the equation proposed by Bar-Cohen and Rohsenow (1984) are more appropriate for natural convection since they do not consider any wind disturbances. For the correlation which considers the wind disturbances, the Nusselt number is higher and thus the CHTC will be higher. Concluding, the no-wind correlation should be used in estimating the thermal conditions of the system and carry out heat transfer analysis. However, the engineers working on the field should be aware that the CHTC are increased in the case of windy conditions.

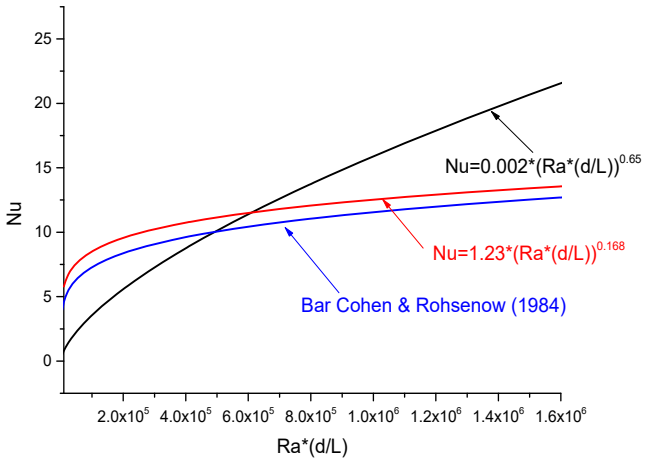

Figure 3.67. Comparison of the new correlations with the correlation proposed by Bar-Cohen and Rohsenow (1984).

General conclusions:

- The open-ended air duct of 10 cm formed between the PV panel and the back wall, is adequate to maintain temperatures lower than 70°C of the PV panel as shown in the experimental measurements presented in this chapter.
- The high temperatures cause loss of electrical efficiency of the PV panel. It is shown that the power drops by 0.4%/°C.

- Considering the single BIPV system, it is observed that the temperature of the PV panel is not the same at all its surface. The bottom side of the PV panel is cooler than the top because it is affected by the air inlet from the bottom opening of the duct.
- The openings of the duct have an important role on the thermal behaviour of the system. It is important to have both top and bottom openings for better air circulation and to keep the temperature of the system at low levels.
- Buoyancy effect occurs in the system as proved by the indoor experiments. The system developed an average air velocity of 0.3 - 0.35 m/s in indoor controlled environmental conditions without external disturbances and wind.
- The PV panel in the system under investigation can be considered as isoflux surface and the wall of the system can be considered as isothermal adiabatic surface since its temperature does not change during the exposure of the system at the sun.
- The convective heat transfer coefficients h for naturally ventilated vertical BIPV system are estimated and can be used for a building energy efficiency analysis to estimate the energy rates and the U-value estimation of the building's construction components. The analysis for building energy efficiency assessment is compulsory for all the buildings since 2008.

CHAPTER 4

4 Simulation Analysis

In this chapter, the aim is to develop a simulation model, validated with the experimental data presented before and then use the validated model to test the system regarding the air gap width, the height of the duct and the air velocity in the duct. As Versteeg and Malalasekera (1995) said, the combination of a fluid flow and heat transfer modeling cannot be sufficient without reference to experimental validations.

According to Linfield and Mudry (2008) computational fluid dynamic (CFD) simulations is the only option for complex temperature problems involving conduction, convection or radiation heat transfer mechanisms. CFD models in heat transfer field can run for temperature variations and take into account changes in fluid density, viscosity, thermal conductivity and heat transfer coefficient. Consequently, COMSOL Multiphysics 4.3b software is selected for simulation in this study because it is a promising software in CFD and finite element method (FEM) simulations and is widely used for thermal modeling of various systems over the years.

Thus, COMSOL Multiphysics software was used, with 3D geometry, in order to simulate the model which is already experimentally assessed. A BIPV model was created to simulate a system of the same size as the experimental apparatus and equations from the theory are applied to the model in order to simulate the heat transfer mechanisms and the air flow in the duct.

4.1 COMSOL Multiphysics

COMSOL is a powerful interactive environment for modelling and solving all kinds of scientific and engineering problems based on partial differential equations (PDEs). Thanks to the built-in physics modes it is possible to build models by defining the relevant physical quantities such as material properties, loads, constraints, sources, and fluxes rather than by defining the underlying equations (Multiphysics Cyclopedia, 2017).

COMSOL is a multiphysics simulation software with many tools able to model a large number of applications with many concurrently physical effects. Its platform is capable to model a wide range of fields; electrical, mechanical, chemical, under various interfaces. The interfaces to describe best the model tested in this study are the Fluids and Heat Transfer.

The finite element method (FEM) is used and the description of the laws of physics for space- and time-dependent problems are usually expressed in terms of partial differential equations (PDEs). For the vast majority of geometries and problems, these PDEs cannot be solved with analytical methods. Instead, an approximation of the equations can be constructed, typically based upon different types of discretizations. These discretization methods approximate the PDEs with numerical model equations, which can be solved using numerical methods. The solution to the numerical model equations are, in turn, an approximation of the real solution to the PDEs.

The GUI (Guided User Interface) provides full access to all steps in the modeling process which are:

1. Selection of the appropriate flow description
2. Creation of the Model Geometry
3. Definition of the properties of the materials which comprise the model and the fluid
4. Addition of equations representing the fluid flow or the heat source of flow
5. Selection of the mesh elements and control the density of the mesh at different positions
6. Selection of solver and time step

4.2 Model Geometry

The geometry of the BIPV model is shown in Figure 4.1. The model is built in the same dimensions as the experimental apparatus presented in the previous chapter and consists of three volumes separated as domains, the PV panel, the air and the wall. The dimensions of the PV panel, air gap and wall are 1642 x 992 x 4 mm, 1642 x 992 x 100 mm and 1642 x 992 x 200 mm respectively.

The PV and the wall domains are solid domains but the air domain is set to have openings at the top and bottom sides of the domain so as to allow boundary conditions for air inflow and outflow.

The geometry of the system is very simple but the physics that apply make its solution complicated. This is mostly because of the uncontrolled air flow in the air duct due to the natural convection.

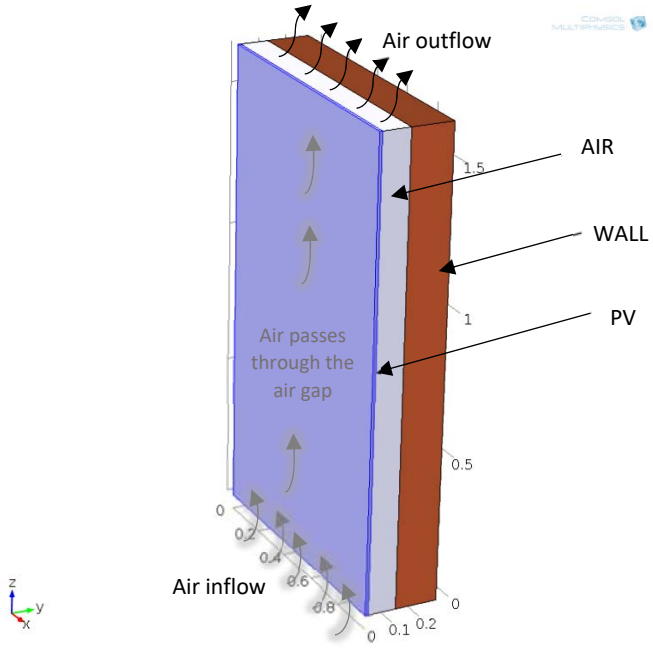

Figure 4.1.The 3D model in COMSOL showing the PV panel, the air gap and wall of the building.

4.3 Theoretical Analysis of the System

The case of heat transfer between the horizontal and vertical planes is not something new. It is referred into many heat transfer books and published papers related to heat transfer. One could say that the BIPV facades could be analysed mathematically in terms of the heat transfer and flow, in the same way as two vertical plates with the known empirical formulas from books. Another possibility could be to analyse the system as finned surfaces with parallel plates. Usually in the heat transfer problems considering natural convection between parallel plates, the two plates are considered either to be both isothermal or both with uniform heat flux. However, this is not the case in BIPV/T facades. As proved earlier from the experimental measurements, the PV is cooler at the bottom where the air enters the duct and thus it is not isothermal. Additionally, BIPVs as well as DSF have two skins from which the one is facing outside and the other facing inside. Likewise, since there are several materials comprising the systems, different heat transfer mechanisms are taking place.

As can be seen in Figure 4.2, the air duct has upper and lower opening to allow the air flow in contact with both sides. The exterior skin is subjected to incident solar radiation which increases the

temperature of the skin while transferring heat in the duct and to the wall. The air, which is in immediate contact with the front hot plate, heats up, expands and becomes less dense from the surrounding air and thus experiences upward thrust. Simultaneously colder fresh air is sucked towards the duct through the lower duct opening.

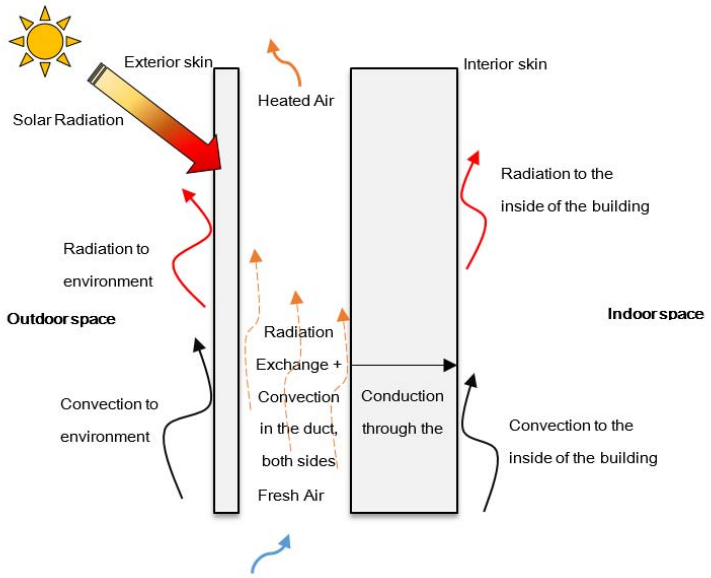

Figure 4.2.Heat transfer mechanisms in a double skin façade or a building integrated photovoltaic system where exterior skin will be the PV panel and interior skin the wall.

In accordance with the schematic diagram in Figure 4.2, Figure 4.3 shows the heat transfer mechanisms of the system in a resistance circuit form.

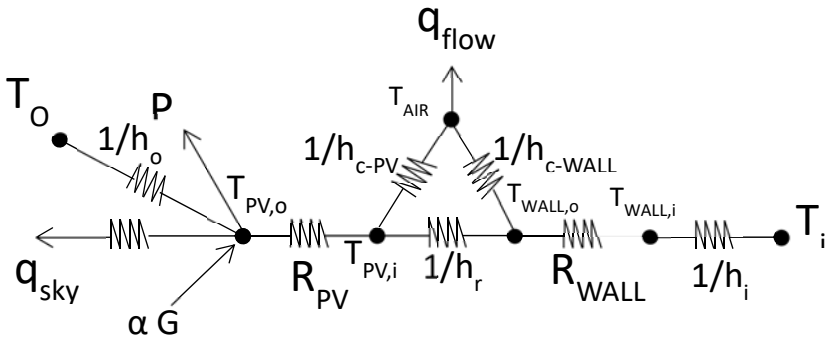

Figure 4.3. Circuit of the thermal resistances and heat transfer mechanisms in a Building Integrated Photovoltaic Façade.

The equations corresponding to a representative control volume in a steady state model are shown below. Equations from 4.1 to 4.5 respectively correspond to energy balances at the top (outer) surface of the PV module, middle of the PV module, bottom (inner) surface of the PV module, air node and the

surface of the wall. Equations 4.6 - 4.10 show the effect of radiation between the PV and the wall, the efficiency of the PV panel and the electrical power, the temperature of the air at the inlet of the duct and the effect of the temperature of the system's parts to the air temperature.

$$\frac{T_{PV,i} - T_{PV,o}}{R_{PV}} - \varepsilon_{PV}\,\sigma\left({T_{PV,o}}^4 - {T_{sky}}^4\right) - h_o\left(T_{PV,o} - T_o\right) = 0 \qquad 4.1$$

$$a\,(\theta)\,G - P_{elec} + \frac{T_{PV,i} - T_{PV,o}}{R_{PV}} = 0 \qquad 4.2$$

$$-q_{rad} - h_{c,PV}\left(T_{PV,i} - T_{AIR}\right) + \frac{T_{PV,i} - T_{PV,o}}{R_{PV}} = 0 \qquad 4.3$$

$$h_{c,PV}\left(T_{PV,i} - T_{AIR}\right) + h_{c,WALL}\left(T_{WALL,o} - T_{AIR}\right) = q_{flow} \qquad 4.4$$

$$q_{rad} + h_{c,PV}(T_{WALLo} - T_{AIR}) + \frac{T_{WALL,o} - T_i}{R_{WALL}} = 0 \qquad 4.5$$

$$q_{rad} = \sigma\,F_{PV}\left(\frac{1}{\varepsilon_{PV}} + \frac{1}{\varepsilon_{WALL}} - 1\right)^{-1}\left({T_{PV,i}}^4 - {T_{WALL,o}}^4\right) \qquad 4.6$$

$$\eta_{PV} = \eta_{STC}[1 - \beta(T_{PV} - 25)] \qquad 4.7$$

$$P_{elec} = \eta_{PV}\,a\,(\theta)\,G \qquad 4.8$$

$$T_{inlet} = T_{outlet} + \frac{A_{gap}\,q_{flow}}{\dot{m}\,C_{p,air}} \qquad 4.9$$

$$T_{AIR} = \frac{1}{\Delta x}\int_0^{\Delta x}\left(\frac{h_{c,PV}\,T_{PV,i} - h_{c,WALL}\;T_{PV,o}}{h_{c,PV} + h_{c,WALL}} + e^{\frac{-w_{PV}\left(h_{c,PV} + h_{c,WALL}\right)}{\dot{m}\,C_{p,air}}x}\right)dx \qquad 4.10$$

The sky temperature T_{sky} (K) to calculate the radiative heat losses to the exterior can be obtained with the formula given by Duffie and Beckman (1980):

$$T_{sky} = T_a\left[0.711 + 0.0056\,T_{dp} + 0.000073\,{T_{dp}}^2 + 0.013\,\cos(\pi\,t/12)\right] \qquad 4.11$$

Where T_a is the ambient air temperature (K), T_{dp} is the dew point temperature (°C), t is the time from midnight (h). A simpler empirical equation can be also used to calculate T_{sky} in terms of outside air temperature T_a only: $T_{sky} = 0.0552\,{T_a}^{1.5}$. Here T_a and T_{sky} are in degrees Kelvin.

In radiative heat transfer, the view factor F_{PV}, is the proportion of the radiation which leaves surface that strikes surface and it can be calculated as a function of the geometric parameters of the surfaces.

Using the above theoretical analysis, a time dependent model is built up to validate the experimental data. The mathematical model of the system in relation with time (t) is shown in the next section.

4.4 Mathematical Model for time depended simulation

The modelling of the specific system examines the effect of the air flow in the duct formed by the PV and the building's wall on the temperature profile of the system.

A combination of heat transfer models is done in the heat transfer interface of COMSOL, to describe heat transfer in solids and fluids including fluid flow with laminar and turbulent models.

To formulate the heat exchange process for a fluid flowing between the PV panel and the building's wall, time dependent partial heat transfer differential equations (PDEs) are used. For the heat transfer in fluids, the following heat equation was used:

$$C_p \frac{\partial T}{\partial t} + \rho\, C_p\, u\, \nabla T = \nabla(k\, \nabla T) + \dot{Q} \qquad 4.12$$

Where t (s) is the time, T (K) is the temperature of the fluid, C_p (J/kg K) is the specific heat of the fluid at constant pressure, ρ (kg/m^3) is the fluid density, u (m/s) is the flow velocity, k (W/m K) is the thermal conductivity and Q (W/m^3) includes the heat transfer sources with positive sign if the heat is added to the fluid volume and negative if extracted from the volume (for instance when there is heat loss to the environment). In case of heat transfer in solids, the velocity is set to zero and the governing equation is thus the pure conductive heat transfer:

$$C_p \frac{\partial T}{\partial t} - \nabla(k\, \nabla T) = \dot{Q} \qquad 4.13$$

For steady state problems, the temperature does not change with time and the first term is eliminated.

Thus, the following three equations were solved for the three domains of the model PV, air and wall, considering the heat transfer solver of COMSOL software:

$$\rho\, C_p \frac{\partial T_{PV}}{\partial t} = \nabla(k\, \nabla T_{PV}) \qquad 4.14$$

$$\rho\, C_p \frac{\partial T_{air}}{\partial t} + \rho\, C_p\, u\, \nabla T_{air} = \nabla(k\, \nabla T_{air}) \qquad 4.15$$

$$\rho\, C_p \frac{\partial T_{wall}}{\partial t} = \nabla(k\, \nabla T_{wall}) \qquad 4.16$$

Various boundary conditions are applied to the model in order to simulate the real conditions, as shown in Figure 4.4. The external side of the PV panel gains heat from solar radiation and loses to the environment. In the boundary between the PV panel and the air gap, heat flows from the hotter panel to the stream of air and at the air-wall boundary the hotter air transfers heat to the wall. Constant

solar radiation is assumed at the front surface of the PV while air flows in the duct formed between the PV and the wall, from the bottom side of the system and exits from the top.

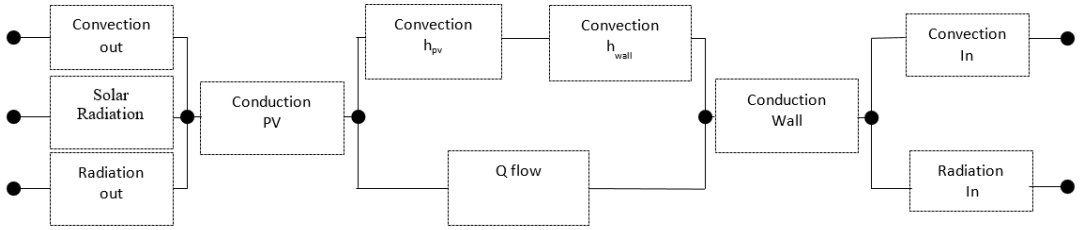

Figure 4.4. The heat transfer mechanisms and basic boundary conditions considered in the system modelling.

The heat transfer interfaces use Fourier's law of heat conduction, which states that the conductive heat flux $\dot{q}$ is proportional to the temperature gradient:

$$-k\frac{\partial T}{\partial x} = \dot{q} \qquad 4.17$$

The convection is set to be natural and it is considered to exist at the front of the PV, the back of the PV, the front of the wall and the back of the wall.

$$\dot{Q} = h\,(T_s - T_\infty) \qquad 4.18$$

The radiation exchange at the outer of the PV panel and the inner of the wall is defined by the following equation, using the appropriate properties and parameters of each domain (PV or wall).

$$\dot{Q} = \varepsilon\,\sigma\,({T_s}^4 - {T_{surr}}^4) \qquad 4.19$$

The convective heat transfer coefficients (CHTC) were estimated each time with the appropriate equation because the conditions in each section of the system are not the same and the coefficients cannot be assumed to be the same everywhere or constant from the bottom to top of the system.

Regarding the convective heat transfer coefficient in the duct, two new Nusselt number correlations (Equations 3.12 and 3.13) derived in Chapter 3 for the estimation of the Nusselt number in the air gap of naturally ventilated BIPV system are used. Equation 3.12 refers to no windy conditions with naturally occurred air velocity in the air gap from 0.26 m/s to 0.34 m/s:

$$Nu = 1.23\,(Ra^*(d/L))^{0.168}$$

While Equation 3.13 refers to windy conditions, with wind speed more than 10 km/h and average air velocity in the air gap 0.8-0.9 m/s. This is given by the following correlation:

$$Nu = 0.002\ (Ra^{*}(d/L))^{0.65}$$

Where the modified Rayleigh number ***Ra**** is given by the Equation 3.10:

$$Ra^{*} = \frac{g\ \beta\ d^{4}\dot{q}_{c}\ \rho\ C_{p}}{v\ k^{2}}$$

Where *d* is the size of the air gap (m), *L* is the height of the duct (m) and v (kg/m s) is the kinematic viscosity of air (equal to μ/ρ).

Accordingly, the CHTC in the air gap can be estimated by the following formula considering D_h the hydraulic diameter of the duct which is $D_h = 4\ A_c/p$:

$$Nu_{gap} = \frac{h_{gap}\ D_h}{k} \qquad 4.20$$

Due to the different heat transfer conditions in the various parts of the system, not all the CHTC are estimated with the use of Equations 3.12 and 3.13. These are applicable only for naural convection in an open-ended duct which is formed by one isoflux plate and one adiabatic which are the PV panel and the back wall respectively.

Thus, the CHTC in the front surface of the PV and the back surface of the wall (facing indoors), are estimated by the use of empirical Nu number equation given by Churchill and Chu (1975) for natural convection over vertical plates:

$$Nu_{out} = \left\{0.825 + \frac{0.387\ {Ra_{L}}^{1/6}}{[1 + (0.492/Pr)^{9/16}]^{8/27}}\right\}^{2} \qquad 4.21$$

Where

$$Ra_{L} = \frac{g\ \beta\ (T_s - T_\infty){L_c}^{3}}{\nu^{2}}\ Pr \qquad 4.22$$

Where L_c is the characteristic length of the geometry (m), in this case the height of the PV.

The Nu number over the outer PV surface and over the inner wall surface, although estimated with the same correlation, they are not assumed to be the same because of the different conditions in the outside and inside and the different temperature of the vertical surface. The CHTC are then estimated by the following relationship considering L to be the height of the model (y-direction in Figure 4.2):

$$Nu_{out} = \frac{h_{out}\, L}{k} \qquad 4.23$$

The properties of the materials used for the simulation are shown in Table 4.1. The properties of air indicated with an asterisk are calculated at every time step in the simulation process with the use of the appropriate equations extracted from the properties given by the graphs in Figure 4.5.

Table 4.1. Physical Properties of the materials consisting the model.

	PV module	Air	Wall	Units
Density, ρ	1500	ρ_air*	2000	[kg/m^3]
Thermal Conductivity, k	0.36	k_air*	0.46	[W/mK]
Emissivity, ε	0.95	-	0.75	[-]
Heat Capacity, Cp=k/ρ*α	1760	Cp*	1500	[kJ/kg K]

**Calculated every time step regarding temperature change of air*

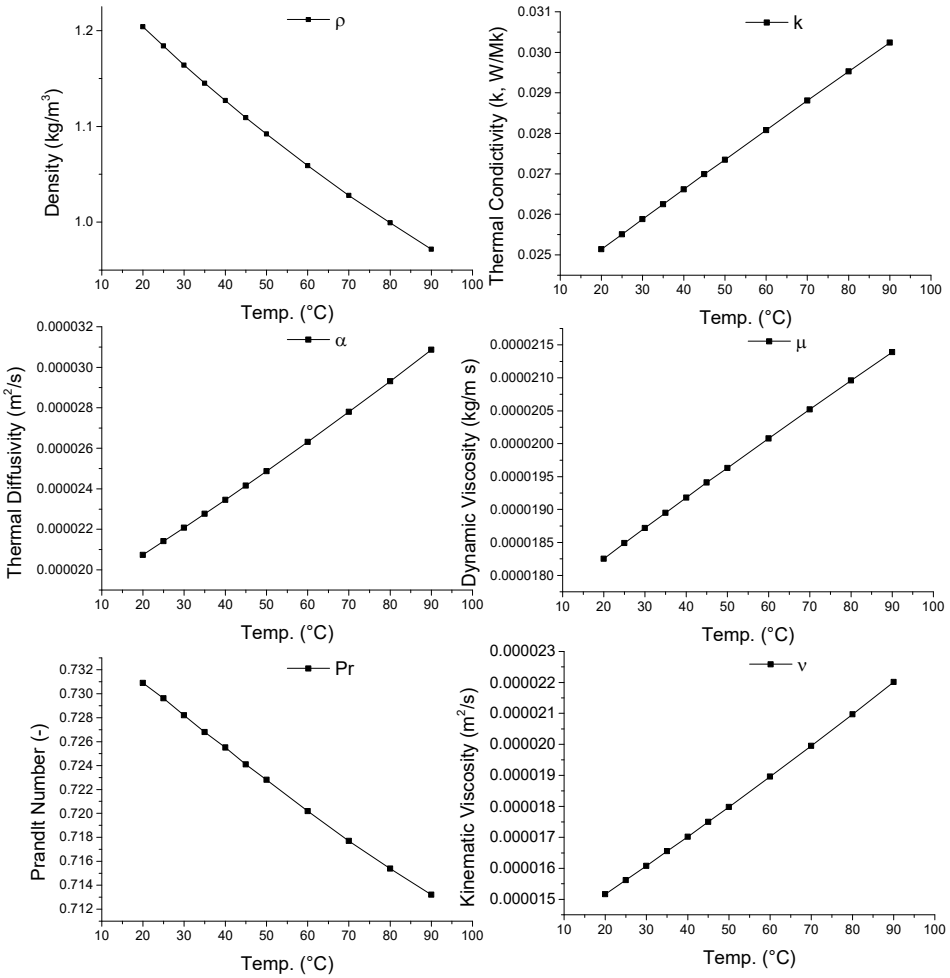

Figure 4.5. Properties of air imported as equations to the model, calculated every time step (data from Cengel and Ghajar, 2011).

4.5 Mesh

Mesh (or grid) generation is one of the most important steps in the process after the definition of the domain and geometry. The model solution requires a subdivision of the domain into a number of smaller non-overlapping sub-domains in order to solve the flow physics within the domain geometry that has been created. This results in the generation of a mesh of cells overlying the whole domain geometry. The accuracy of the solution is strongly influenced by the number of cells in the mesh within the computational domain.

In computational solutions of partial differential equations (PDE), meshing is a discrete representation of the geometry that is involved in the problem. Space is partitioned into elements or cells over which the equations can be approximated.

The grid has a significant impact on the rate of convergence, the solution accuracy and the CPU (central processing unit) time required. The greater the rate of convergence, the better the mesh quality and a better mesh quality provides a more accurate solution. CPU time is a necessary factor. For a highly-refined mesh, where the number of cells per unit area is maximum, the CPU time required will be relatively large. One of the most important problems faced in this study was the CPU time needed, the memory and performance of the hardware although a relatively new generation workstation computer is used. Sometimes if possible, a problem is better to be solved as 2D and select only few models to be simulated 3D, to reduce computing time.

The mesh can be created either manually or automatic by the software. COMSOL software that used in this study has the intelligence to analyze the underlying geometry and generate automatic meshing. However, due to the complex mixture of the heat transfer equations and the fluid flow equations, the solution of the current model required a user controlled mesh with different sizes of grains for each domain. Tetrahedral and triangular cells were used for meshing and extremely fine density of cells are designed at the PV panel and AIR domains to be more accurate, and normal to coarse density at the wall domain (Figure 4.6).

In the current study, the model is solved with 237108 degrees of freedom (DOF) plus 71716 internal DOF. Details on the elements size and number of domain elements are shown in Table 4.2.

Table 4.2. Mesh sizing on the three domains.

	PV	**AIR**	**WALL**
Maximum element size	0.164 [m]	0.0169 [m]	0.131 [m]
Minimum element size	0.0269 [m]	0.00183 [m]	0.0164 [m]
Number of domain elements	31948	245940	98371

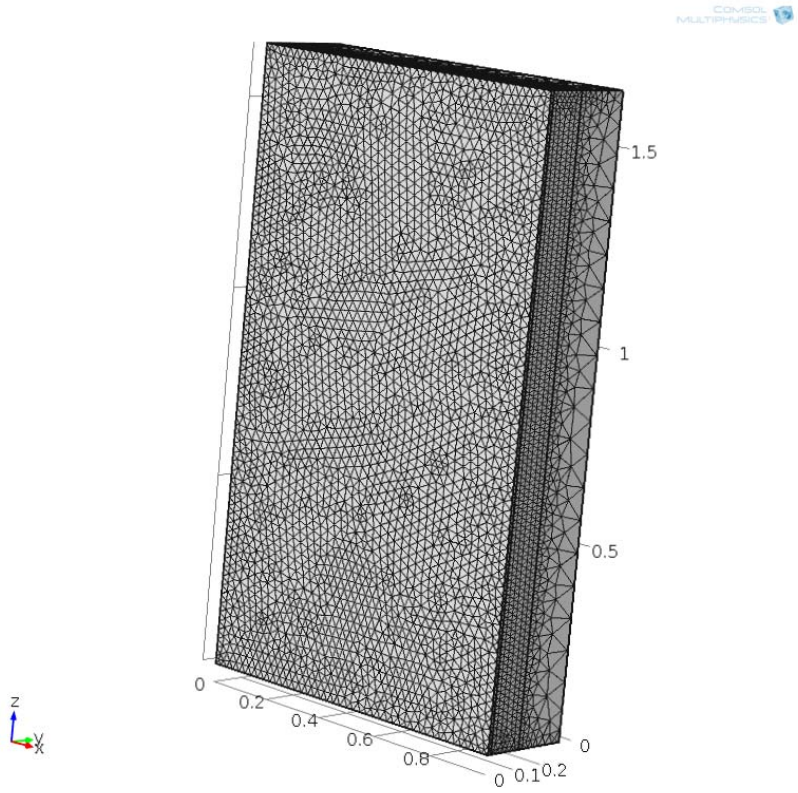

Figure 4.6. The complete mesh on the three model domains with tetrahedral and triangular cells.

4.6 Model Validation

In order to validate the model, a simulation is carried out using the real weather data measured on September 15th, 2016 during the outdoor experimental test on that day. Only radiation and ambient air temperature values were used in the simulation model, and no wind is assumed at the outer side of the PV panel.

The experimental radiation values as well as the ambient air temperature values were plotted and fitted to polynomial curves. As a result, the polynomial equations were imported in COMSOL Multiphysics simulation environment and used to carry out time dependent simulation. Figure 4.7 and Figure 4.8 show the radiation and ambient air temperature used for the simulation in comparison with the experimental measured values on 15/9/16, as well as the derived polynomial equations used in the simulation.

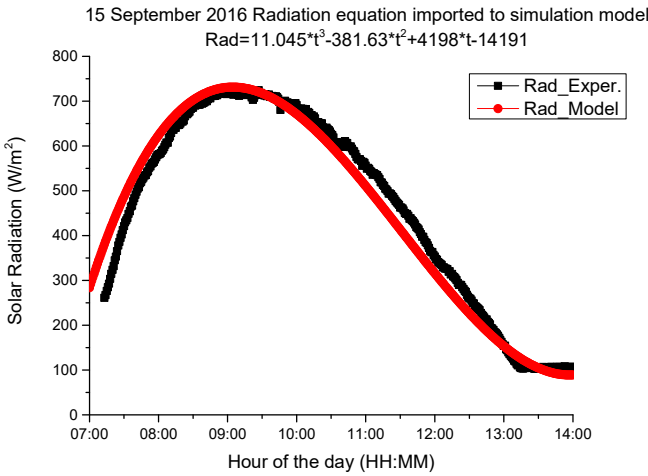

Figure 4.7. The measured experimental solar radiation and the solar radiation used for the simulations.

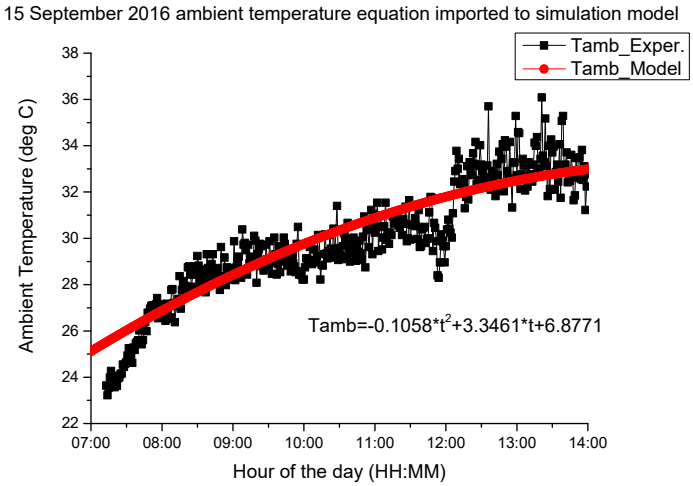

Figure 4.8. The measured experimental ambient air temperature and the ambient air temperature used for the simulations.

All measurements have an uncertainty between the measured or derived value and the true value. The absolute relative error (ARE) of the parameters is calculated to reflect the accuracy of the estimated parameters using the following equation:

$$ARE = \frac{E_{simulated} - E_{measured}}{E_{measured}} \qquad 4.24$$

Figure 4.9 shows the absolute relative error calculated for the solar radiation and ambient temperature shown before in Figure 4.7 and Figure 4.8. As can be seen the percentage relative error (PRE) in both parameters does not exceed 11%.

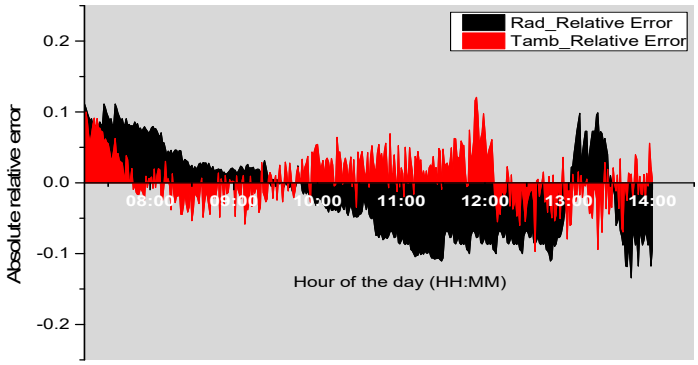

Figure 4.9. The absolute relative error of the estimated and measured values of solar radiation and ambient air temperature.

As already mentioned, there are two equations for the CHTC derived from the experimental analysis given by Equations 3.12 and 3.13 earlier. The results obtained from the simulation model with the use of the two correlations, in comparison with the outdoor measured experimental data regarding the average PV temperature and the average air temperature at the outlet of the air duct are shown in Figure 4.10 and Figure 4.11 respectively.

As can be observed from Figure 4.10, the three lines have the same trend. The small differences between the experimental and simulation data are due to the fact that the simulation estimates the average temperature of the volume of the PV panel which consists of thousands of temperature values, while in the experimental procedure the average is estimated with the 9 temperature measurements from the 9 thermocouples on its back surface. The simulation and measured data are in a good agreement regarding the average temperature of the PV panel. The maximum percentage relative error between the estimated and measured temperature of the PV panel is ±12%.

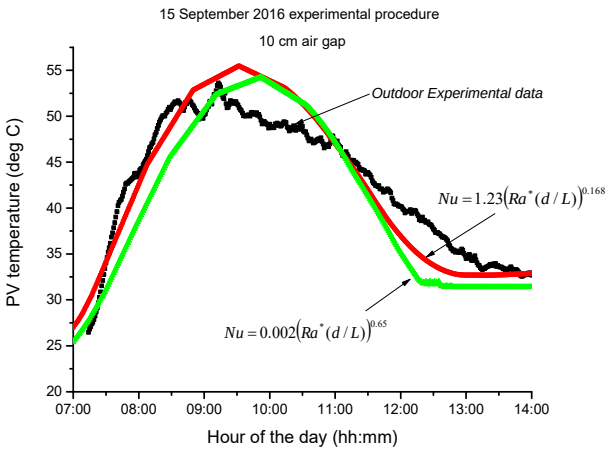

Figure 4.10. The average temperature of the PV panel measured from the outdoor experiment on 15/9/16 Vs the calculated average temperature of the PV panel from the simulation.

Graph 4.11(a) shows the estimated air outlet temperature from the simulation model from the two equations in comparison with the indoor measured experimental values with no wind, and graph 4.11(b) in comparison with the outdoor measured experimental data. As can be seen, the outlet air temperature estimated with Equation 3.12 is closer to the indoor no windy experimental data and the values estimated with Equation 3.13 are closer to the outdoor experimental values which were affected by the ambient wind as expected.

The two graphs show a good agreement between the experimental and simulated values with the two equations. This proves the proximity of the mathematical model and the Nusselt number correlations. The maximum percentage relative error between the estimated and measured temperature of the outlet air is ±8.5% for the indoor experiments and ±12.5% for the outdoor experiments.

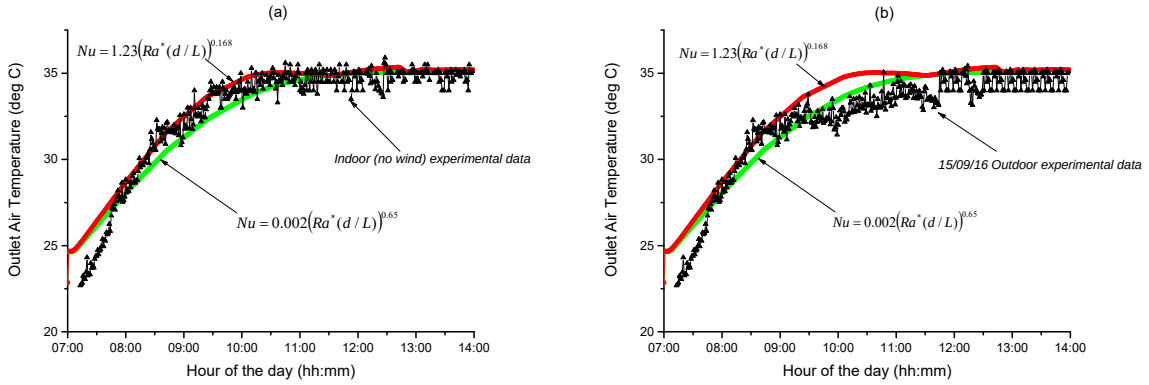

Figure 4.11. The measured outlet air temperature from the windy and non windy experimental procedures shown in graph (a) and graph (b) respectively, Vs the calculated from the simulation with the two correlations from Equations 3.12 and 3.13.

After proving that the experimental data validate the mathematical model, it is believed that for a pure natural ventilation case, Equation 3.12 which gives the Nusselt number in the air gap in no wind conditions is more appropriate. Thus, the following analysis is focused on the model with Equation 3.12.

To evaluate the accuracy of the simulation model with Equation 3.12, Table 4.3 is produced which shows a comparison between the simulated data at constant solar radiation of 800 W/m^2 with Equation 3.12 and the experimental data obtained from the indoor experiments at the same constant solar radiation without wind. As can be seen, the indoor experimental data validate the simulation model since the PRE does not exceed 4.11%.

Table 4.3. The measured temperature of the PV, air and wall during indoor experimental procedure Vs the simulated values with the use of Equation 3.12 considering constant solar radiation and no wind.

	*PV temperature ºC**	*Air gap temperature ºC***	*Wall temperature ºC****

	Tpv_t	*Tpv_m*	*Tpv_b*	*Tair_t*	*Tair_m*	*Tair_b*	*Twall_t*	*Twall_m*	*Twall_b*
Experimental	66.5	63	60	36.5	32	30	26	25.4	25.2
Simulation	68.9	65.3	58	38	32.5	29	25.4	25.3	25
PRE %	3.61	3.65	3.33	4.11	1.56	3.33	2.31	0.39	0.79

** Tpv is measured on the side of the air gap (back side of the PV)*

***Tair measured in the middle of the air gap, equal space from PV and back wall*

****Twall is measured on the outer side of wall facing the air gap*

Taking into account the temperature measurements from the experimental results shown in Chapter 3, which showed that the PV panel surface is not completely isothermal, it is expected that simulation will show that the bottom part of the system has lower temperature than the top as well, at least at the first few centimeters.

Regarding the temperature of the various parts, COMSOL can create detailed contour plots of the temperature of the various domains of the model. The contour plots of Figure 4.12, Figure 4.13 and Figure 4.14 show the temperature distribution of the PV panel, air gap and back wall respectively, which are estimated using real outdoor measured weather data, but with the use of Equation 3.12 for the estimation of the Nusselt number in the air gap considering there is no wind outside.

Since the model with Equation 3.12 is already validated with the indoor experimental data, it can be now used to examine the thermal behaviour of the system in outdoor conditions but without wind. Additionally. it is interesting to see the differences when comparing data estimated with the use of the Equation 3.12 without wind consideration, with measured data under light wind conditions. For comparison purposes, next to each contour plot there is a table showing the experimental measured values from the outdoor experimental procedure carried out in light windy conditions as shown in Chapter 3.

Although comparing the experimental data under windy conditions with the simulation data without wind consideration, in all three figures, there is a good agreement between simulation and experimental measured values. The differences are mainly due to the presence of wind and the different position of measurement as indicated. Thus, it can be said that Equation 3.12 can describe the thermal behaviour of the air gap very well in outside conditions without wind.

From Figure 4.12 it is important to see the temperature difference between the top and bottom sides of the PV panel which is affected from the air inlet in the duct. At this specific plot taken for the results obtained at 9:30 am, the temperature difference between the bottom and top sides of the PV panel is small, about 2.5^{o}C. The contour plot of the air volume in Figure 4.13 shows the temperature of the air near the PV panel to be higher than near the wall as expected. The temperature of the wall volume shown in Figure 4.14, seems to be slightly (1^{o}C) hotter on the side of the air gap, but isothermal regarding its height.

15/9/16 Outdoor experimental data at 9:30	
Tpv_top*	55°C
Tpv_middle*	53°C
Tpv_bottom*	48°C

**measured on the side of the air gap (back side of the PV)*

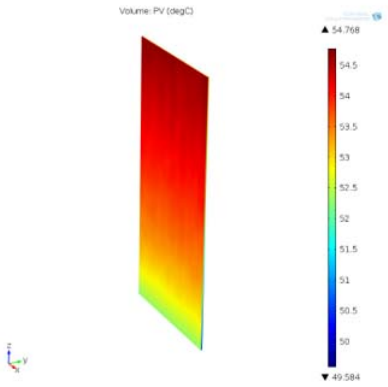

Figure 4.12. The temperature distrribution on the outer side of the PV panel at time 9:30 of simulation.

15/9/16 Outdoor experimental data at 9:30	
Tair_top*	33°C
Tair_middle*	32°C
Tair_bottom*	29°C

**measured in the middle of the air gap, equal space from PV and back wall*

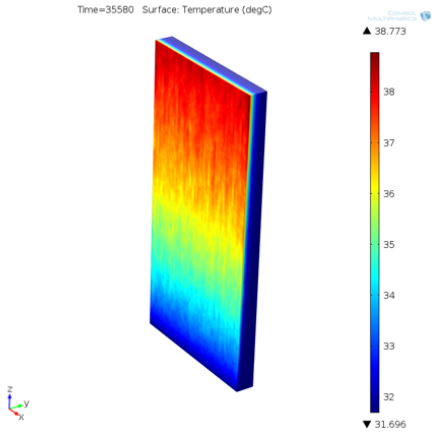

Figure 4.13. The temperature distrribution of the air volume at time 9:30 of simulation.

15/9/16 Outdoor experimental data at 9:30	
Twall_top*	25.6°C
Twall_middle*	25°C
Twall_bottom*	24.7°C

**measured on the outer side of wall facing the air gap*

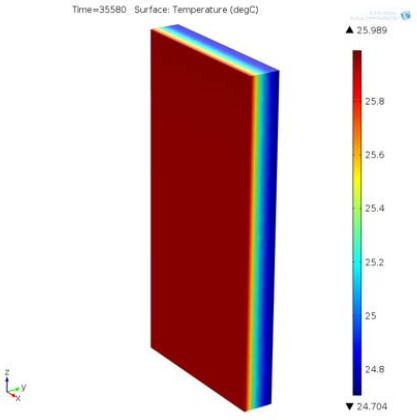

Figure 4.14. The temperature distrribution of the wall volume at time 9:30 of simulation.

For better understanding of the thermal behavior of the system, four boundaries are selected to plot their temperature during the simulation time. The selected boundary surfaces are shown in Figure 4.15 which are the outer and inner surfaces of the PV, and the outer and inner surfaces of the wall.

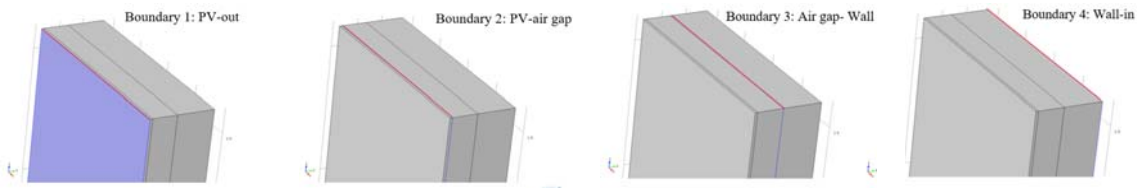

Figure 4.15. Four boundaries of the model.

The temperature at the four boundaries of the system, obtained using Equation 3.12, are shown in Figure 4.16. It is important to note that the temperature difference between the two sides of the wall is very small, and does not increase dramatically through time. On the other hand, the temperature of the PV panel and the temperature of the air in the air duct changes through time and reach maximum the time that the solar radiation is at maximum at 9:30 am because the sun is almost perpendicular to the PV panel (east direction).

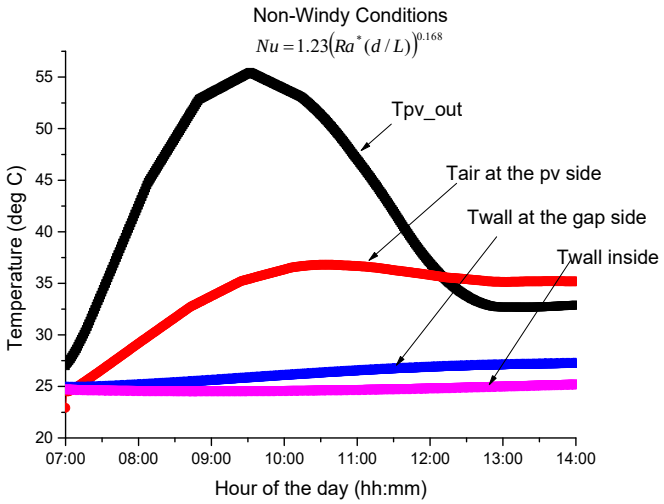

Figure 4.16. The temperature at the four boundaries of the model

The CHTC estimated from the simulation model for every time step during simulation, on the outer side of the PV panel, in the air gap, and on the inner side of the wall are shown in Figure 4.17. As mentioned previously, not all the coefficients are estimated with the same correlation. As can be seen, the CHTC's in the air gap are higher than the coefficients in the outer PV side and the inner wall side.

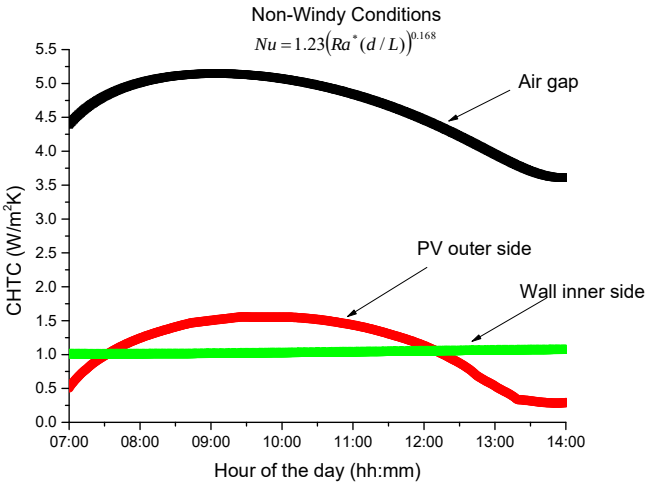

Figure 4.17. Convective heat transfer coefficients on the outer side of the PV panel, in the air gap, and on the inner side of the wall.

4.7 Effect of height and air gap size

In this section, the simulation model is tested under different air gap sizes and heights at constant solar radiation flux of 800 W/m^2. The height of the system depends on the number of modules that are installed one on top of the other without openings in between. Gan (2009) carried out a study to estimate the temperature and velocity of a BIPV system of different heights and concluded that the higher the system is, the higher is the developed temperature on its surface.

As proved from the above investigation, for a single row of PV panels the modules cannot be considered isothermal since the top part of the PV is hotter than the bottom because its temperature is affected by the air inlet and outlet from the two openings.

On the other hand, for a high-rise installation with multiple PV panels consisting one continuous surface without openings in between, the PVs surface will be higher and the big continuous surface can be considered isothermal since it will not be affected by air inlet or outlet except from the first row of panels. However, this is not recommended because it will cause significant high temperatures on the PV panels and loss of efficiency.

Figure 4.18 shows the maximum temperature of the PV panels estimated for different air gaps for the three systems of different heights with one, two and three PV panels one on top of the other. As expected, the bigger is the air gap, the lower is the maximum temperature of the PV panel. On the other hand, the higher is the system the higher is the maximum temperature of the PV panels surface. Consequently, in large applications, it is recommended that a small gap is left between the PV panels

on the height direction so fresh air will enter at the bottom of each PV to keep the temperature of the panels in low levels.

Additionally, from Figure 4.18 it can be seen that for air gap size bigger than 0.1 m, the change in the temperature of the PV panel is small and thus it can be selected as the optimum air gap size for a high-performance system.

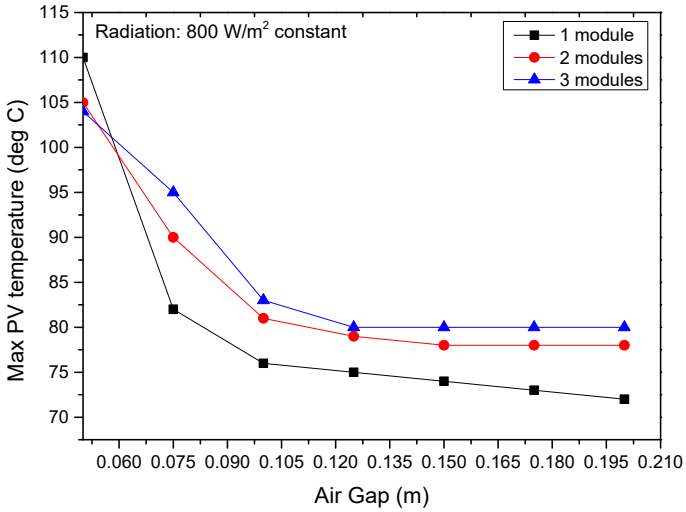

Figure 4.18. Effect of air gap on the PV temperatures of different heights under 800 W/m^2 constant solar radiation

Consequently, in big applications, it is recommended that a small gap is left between the PV panels on the height direction so fresh air will enter and keep the temperature of the panels in low levels.

4.8 Effect of Air Velocity

So far it is shown that air gap has an important role on the temperature distribution of the BIPV system. The experimental procedure carried out in outdoor conditions showed that the average air velocity in the duct was 0.8 m/s. However, it is expected that in less windy conditions, the air velocity in the air gap will be less affected by the wind and thus the excess heated air will be rejected in lower rate. Accordingly, the air velocity in the air gap is an important parameter for the system.

In this section, the validated model is used to investigate the effect of the air velocity in the temperature distribution of the system. The model is tested under various air velocities from 0.05 m/s to 3 m/s at constant air gap of 10 cm.

Figure 4.19 shows the temperature of the outer surface of the PV panel for a BIPV system of 10 cm air gap for various velocities. As can be observed, the higher the air velocity, the lower is the temperature of the PV panel. The faster the air flows in the duct, the more heated air is removed from the duct which is created due to the hot surface of the PV panel. The results show that the air gap of 10 cm is adequate to maintain PV temperature less than 66°C even with a small air velocity of 0.05 m/s.

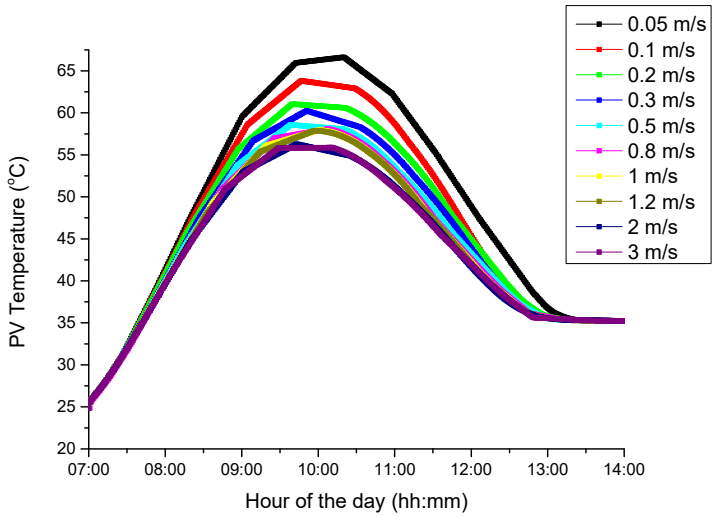

Figure 4.19. The temperature of the outer PV surface for different air velocities in the air duct.

The front and back sides of the PV panel although they are exposed to different conditions, they have almost same temperature due to the small thickness of the panel. Figure 4.20 shows the contour plots of the temperature distribution on the two sides of the PV panel and Figure 4.21 shows the average temperature of the PV panel in the two sides for the simulation with air velocity of 0.1 m/s.

As can be seen from Figure 4.20 the back side of the PV panel seems to be cooler in slightly bigger area at the bottom than in the front side. This is because of the fresh air inlet from the bottom opening of the air duct. At this point it is important to observe the temperature difference from the bottom to the top side of the PV panel, which on the back side, the temperature difference is 10°C.

On the other hand, from Figure 4.21 it can be seen that the average temperature of the surface in the front and back is very similar.

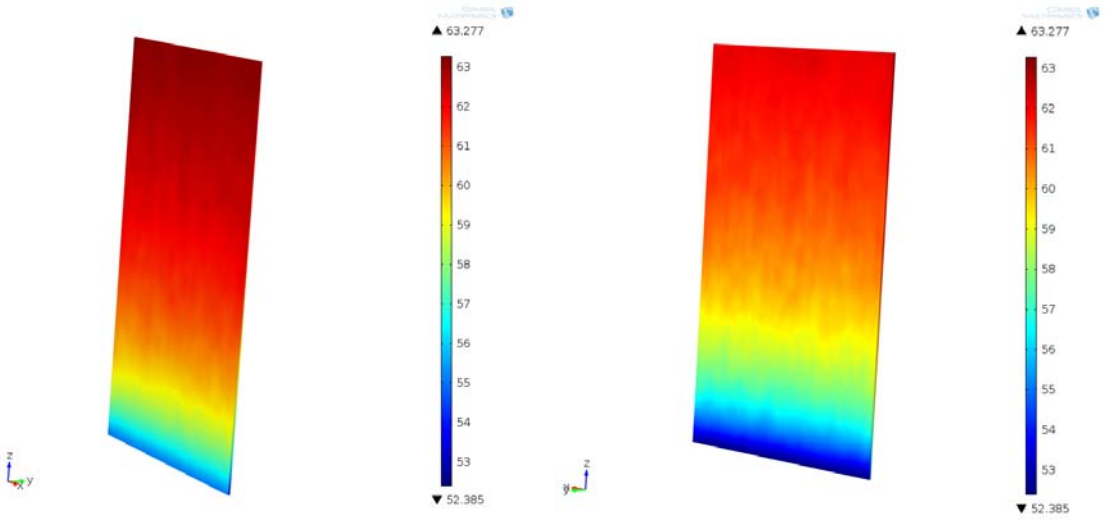

Figure 4.20. The temperature distribution of the front (left) and back (right)surfaces of the PV panel for air gap size of 10 cm and air velocity 0.1 m/s.

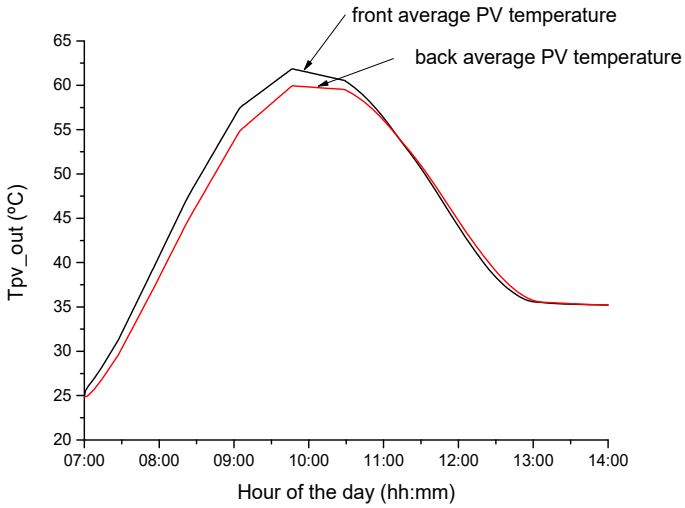

Figure 4.21. The average temperature of the front and back surfaces of the PV panel for air gap size of 10 cm and air velocity 0.1 m/s.

Figure 4.22 shows the temperature of the air in the duct on the boundary air layer near the PV surface. This is the boundary 2 shown before in Figure 4.15. As can be observed the temperature of the air is affected by the temperature of the PV panel and drops when the velocity increases. The effect of the air velocity on the volume of air in the duct is shown in Figure 4.23. The temperatures shown here are lower than the ones shown in Figure 4.22 because this is the average temperature of the whole volume of air in the duct.

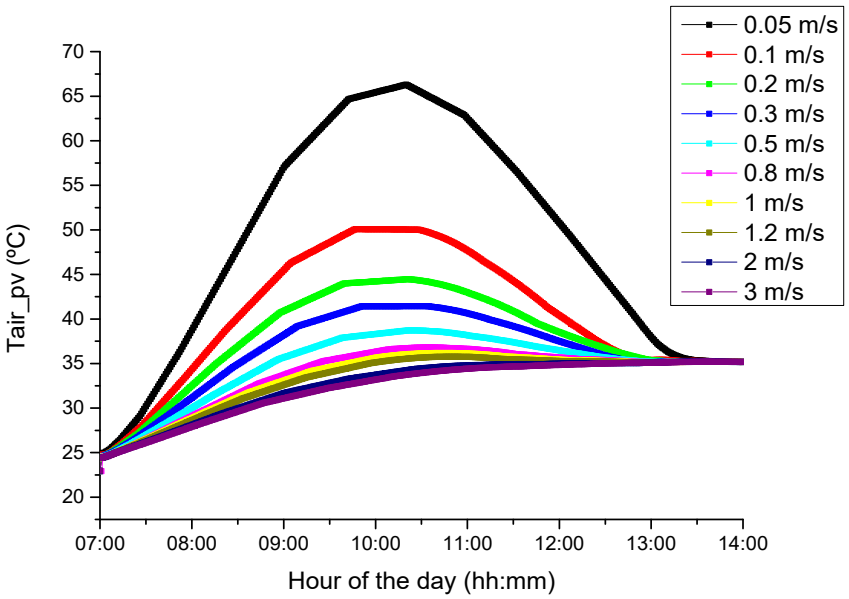

Figure 4.22. The temperature of the air in the duct at the boundary layer of the PV panel at various velocities.

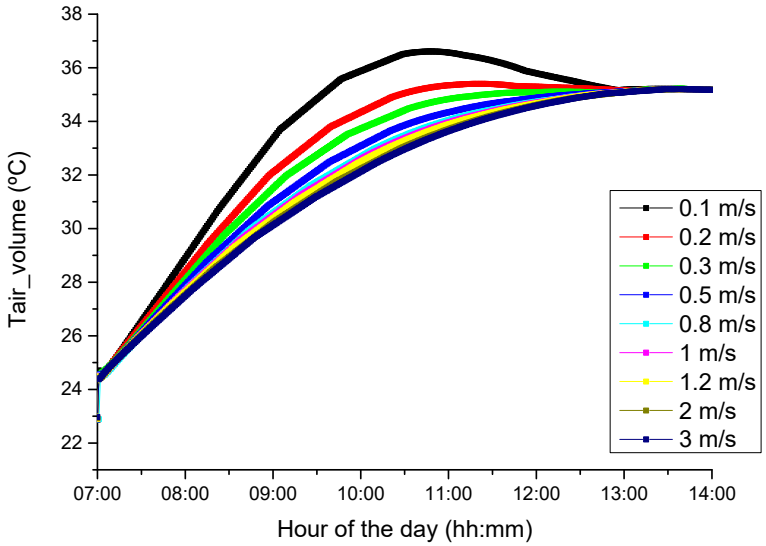

Figure 4.23. The average temperature of the air volume at various velocities.

As mentioned before, BIPV systems can also be modified to be used as BIPV/T systems. The BIPV/T systems use the excess heated air from the duct to heat an indoor space. Thus, in those applications the temperature of the air at the outlet of the duct is an important parameter. Figure 4.24 shows the temperature of the air at the outlet of the duct for various air velocities in the duct. As can be seen, the lower the air velocity, the higher is the temperature of the air at the exit of the duct. This is normal

since with lower velocity the air stays longer in the air duct and it is more affected by the temperature of the PV panel and gets hotter.

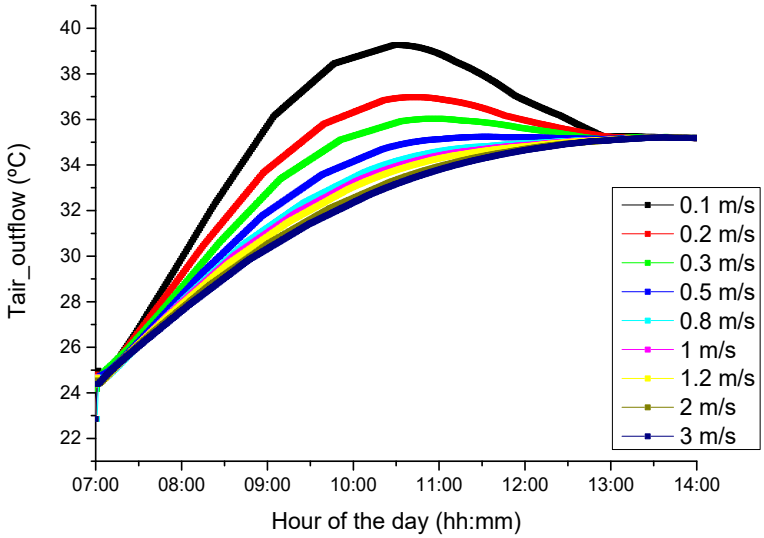

Figure 4.24. The temperature of the air at the outlet of the duct at various velocities.

Figure 4.25 shows the temperature of the wall (boundary 4 in Figure 4.15) under the various tested air velocities in the air duct. As can be observed, there is almost no change at the temperature of the brick wall. This is the reason that the developed correlations refer to natural air flow between two parallel plates one isoflux (PV) and one isothermal (wall).

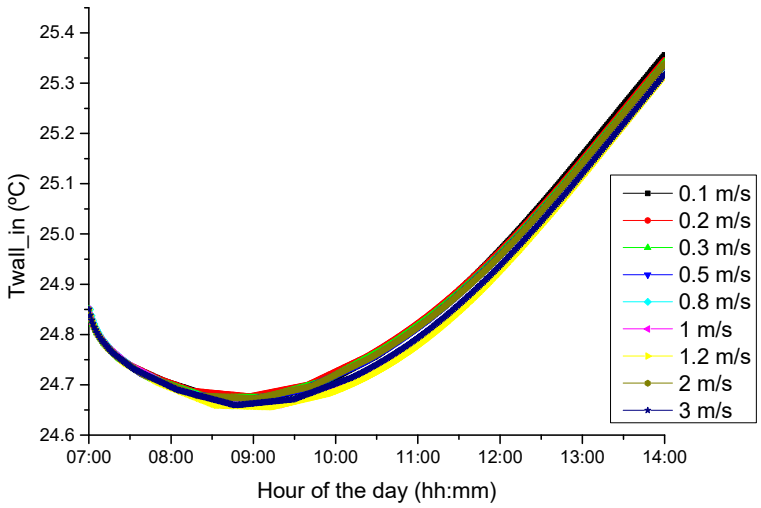

Figure 4.25. The temperature of the wall at the inner side facing indoors, for the various tested air velocities.

As done before in the model validation, in order to understand better the thermal behaviour of the various parts of the system, it is good to see the temperature of the various components at the four boundaries shown in Figure 4.15 which are:

- The temperature of the PV panel at boundary layer at the outer side of the PV panel *(Tair_out)*
- The temperature of the air at the boundary layer at the at the inner side of the PV panel facing the air gap *(Tair_pv)*
- The temperature of the wall at the boundary layer at the outer side of the wall facing the air gap *(Twall_air)*
- The temperature of the wall at the boundary layer at the inner side of the wall facing the indoor spaces *(Twall_in)*

All four temperatures of the boundaries are shown in Figure 4.26 and Figure 4.27 for the lowest simulated air velocity of 0.1 m/s and the highest 3 m/s respectively. It is clear that the temperature of all the components of the system is affected by the air velocity in the air gap. A clearer overall view on the effect of the air velocity on the temperature of the various system parts is shown in Figure 4.28 and Figure 4.29 for two hours 8:00 am and 10:00 am respectively. The temperature of the two sides of the PV panel are shown (Tpv_out, Tpv_gap), as well as the temperature of the air in the duct near the PV side (Tair_pv), the average temperature of the air in the duct (Tair volume), the temperature of the wall on the duct side (Twall_in) and the temperature of the air at the inlet and outlet of the duct (Tair_inflow, Tair_outflow).

It is clear that the temperature of all the components of the system is affected by the air velocity in the air gap. However, after air velocity of about 1 m/s the temperatures are almost stable and no further reduction is observed at higher velocities.

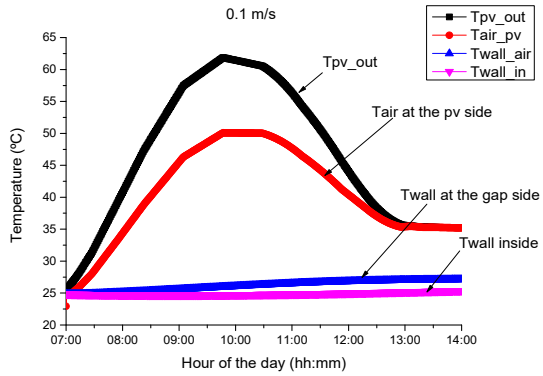

Figure 4.26. The temperature at the four boundaries of the mode for air velocity of 0.1 m/s.

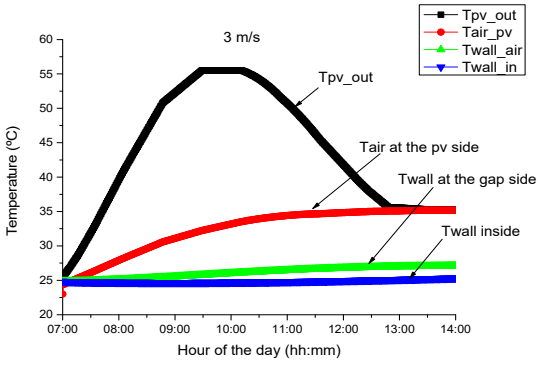

Figure 4.27. The temperature at the four boundaries of the mode for air velocity of 3 m/s.

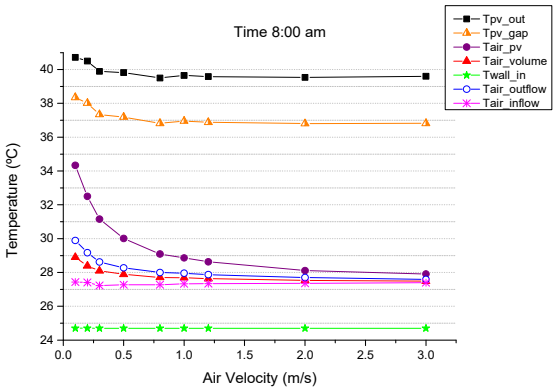

Figure 4.28. The effect of air velocity in the air gap at the temperature of the various parts of the system at 8:00 am.

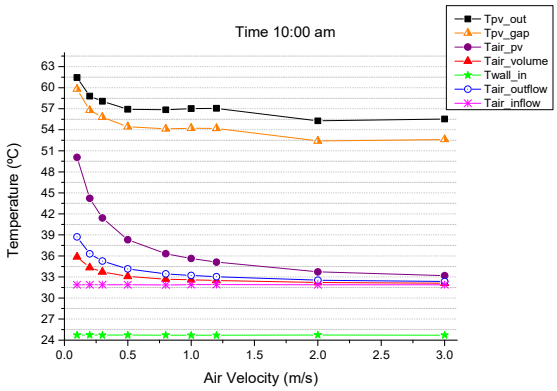

Figure 4.29. The effect of air velocity in the air gap at the temperature of the various parts of the system at 10:00 am.

4.9 CHTC in Building Energy Analysis

Apart from the BIPV system analysis, the convective heat transfer coefficient is a very important parameter for building energy modelling and energy simulations. Especially the last years that it is compulsory for all the buildings to have a Building Energy Efficiency Certificate (BEEC) which sets out the energy efficiency rating of a building or area of a building that is offered for sale, or rent. The certificate indicates the category of energy efficiency of the building which is derived by taking into account all the materials comprising the construction elements, the heating and cooling equipment performance etc.

In order to be able to reach the final result and indicate the correct energy efficiency category, numerous estimations should be carried out. The most important is the estimation of the U-value of all the construction elements of the building. The lower the value, the higher the thermal insulation. With respect to higher operating temperature of BIPV, changes of the thermal characteristics have to be taken into account for the estimation of the U-value of a wall or a roof.

Considering the structure of a BIPV façade wall as shown in Figure 4.30 the U-value can be estimated by the following formula, and the various resistances are shown in Table 4.4.

$$U = \frac{1}{R_{so} + R_{PV} + R_a + R_{WALL} + R_{si}} \ (\mathrm{m^2K/W}) \qquad 4.25$$

Table 4.4. Thermal Resistances of the system components.

The convective thermal resistance on the outer side	(m²K/W)	$R_{so} = \frac{1}{h_o}$

The conductive resistance of the PV panel	(m^2K/W)	$R_{PV} = \frac{d_{PV}}{k}$
The convective thermal resistance of the air in the air duct	(m^2K/W)	$R_a = \frac{1}{h_{air}}$
The conductive resistance of the wall	(m^2K/W)	$R_{WALL} = \frac{d_{WALL}}{k}$
The convective thermal resistance on the inner side	(m^2K/W)	$R_{si} = \frac{1}{h_i}$

Equation 4.25 is a widely used equation for the estimation of the overall U-value of a vertical structure. However, the resistance R_a should be calculated with the use of the convective heat transfer coefficient of the air in the duct between the PV panel and the wall which is named as h_{air}.

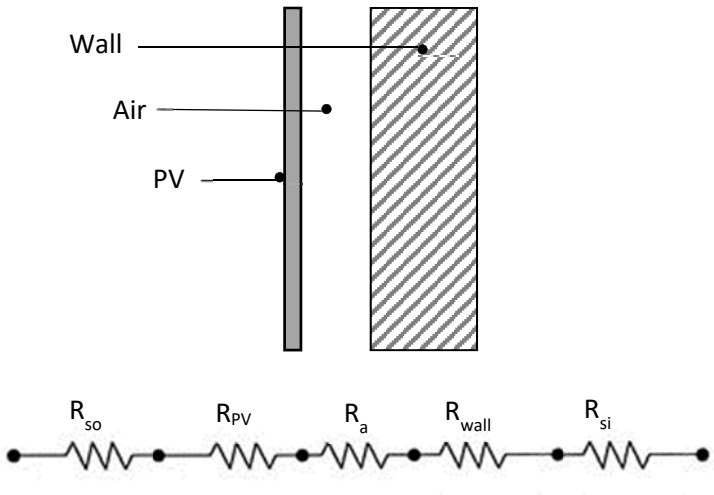

Figure 4.30. Section of a basic BIPV system installed on a brick wall.

According to Wang et al. (2006), BIPV has significant influence on the heat transfer through the building envelope because of the change of the thermal resistance by the various building elements. Using the simulation results of the convective heat transfer coefficients estimated for a vertical BIPV system facing east for weather data of September 15th,2016 from 7:00 to 14:00, the thermal resistances of the various components of the system are shown in Figure 4.31. Figure 4.31 shows the estimated U-value for this system as well.

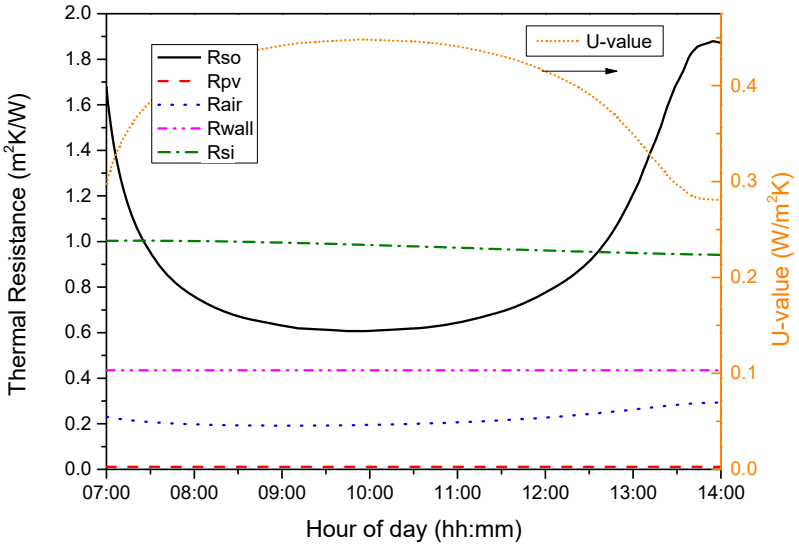

Figure 4.31. The estimated thermal resistances of a BIPV system on a day in September from 7:00 am to 14:00.

The acceptable U-values for each element is given by the building energy authorities of every country as shown in Figure 4.32. The obtained U value is well within the limit specified for most countries.

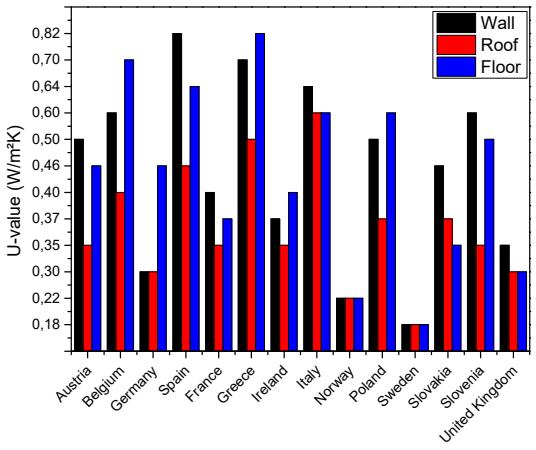

*Figure 4.32. U-values of different construction elements for different countries in Europe (*eurima, 2011*).*

The total heat transfer rate between the vertical façade structure is defined as:

$$Q = \frac{T_{\infty 1} - T_{\infty 2}}{R_{total}} \qquad 4.26$$

Where the $T_{\infty 1}$ and $T_{\infty 2}$ are the temperatures of the air at the two sides of the structure, which are the indoor temperature and outdoor ambient temperature respectively.

Apart from the use of the h_{air} at the building energy analysis, it is also very important for the PV installers and engineers to predict the performance of the system by estimating the convective losses from the system and the effect of the air gap on the total energy of the system. With known CHTC in the air gap, the temperature of the PV panel can also be predicted using the basic convection correlation. The prediction of the temperature of the PV panel can help the installers and engineers to prevent system overheating and building overheating as well as system efficiency losses.

4.10 Discussion & Conclusions

A simulation model of the previously experimentally tested BIPV system is built and validated.

The developed mathematical model includes the empirical correlations for the estimation of the convective heat transfer coefficients in the air gap between the PV panel and the back wall of the system which were presented in Chapter 3. Two equations are considered; one refers to non-windy conditions (Equation 3.12) with low air velocity in the air gap from 0.26-0.34 m/s which is not affected by external wind disturbances, and the other (Equation 3.13) refers to windy conditions which affect the air flow in the air duct and the air velocity in the air duct is 0.8-0.9 m/s.

The mathematical model used in the simulations is validated and shows a good agreement with the experimental data with percentage relative error of 12% of the PV temperature estimation and 12.5% on the air temperature. The error of this order is acceptable in such calculations as mentioned by Gaillard et al. (2014); Hollands et al. (1976), La Pica et al. (1993); Santos and Rüther (2012).

The validated model is also used to investigate the effect of the gap size, duct height and air velocity on the thermal behaviour of the system. It is shown that the higher the system is, the higher is the developed temperature on the PV surface unless there are openings between the various PV panels to import fresh air. Additionally, an air gap of 10 cm is proven to be adequate to keep the temperature of the PV panel at low levels. Regarding the effect of air velocity in the air gap it is concluded that for air velocity bigger than about 1 m/s the temperatures of all the system components (PV, air and wall) are almost stable and no further reduction is observed at higher velocities.

As a final conclusion, it can be said that Equation (3.12) for calm (non-windy) conditions describes better the naturally ventilated systems with natural convection between the PV panel and the back wall, and the results show a good agreement with the experimental data and the literature as well.

General Conclusions:

- For a ventilated system with one PV panel the PV cannot be considered isothermal since its temperature is affected by the air inlet from the bottom opening of the duct formed between the PV and the back wall. It is proved that the bottom side of the PV panel is around 10^{o}C lower than the top.
- Having more than one PVs one on top of the other forming one continuous surface, the height of the system is bigger and thus the height of the air duct is bigger as well. From the simulations, it is shown that the higher is the system without any openings between the PVs, the higher is the developed temperature of the PV panels. However, when multiple PVs are installed one on top of the other leaving openings in between, the height of the system is bigger but the PV panels act like they are independent since each has air inlet at the bottom and air outlet at the top. Thus, lower temperatures are observed in the overall system and the panels can be considered isothermal.

CHAPTER 5

5 Energy and Exergy Analysis

In order to examine the performance of the system, the energy and exergy efficiency need to be estimated[3]. There are numerous studies about energy and exergy efficiency of PV systems, however, most of them are based on PV/T systems, water systems and mechanically ventilated air systems.

The most appropriate way to discuss the performance of a BIPV/T system is to estimate the energy and exergy efficiency of the system. Generally, the exergy is the amount of energy available to be used. When an energy source is at equilibrium with the environment, its exergy is zero. This section presents the energy and exergy analysis of a naturally ventilated BIPV/T system.

The energy efficiency is based on the energy balance, which is the first law of thermodynamics. The exergy efficiency is the ratio of the maximum theoretical work that can be produced by utilizing a heat source. The exergy efficiency is related to the second law of thermodynamics known as the exergy efficiency law.

[3] Part of this study is published as: Agathokleous, R.A., Kalogirou, S.A., Karellas, S., (2017). Exergy analysis of a naturally ventilated Building Integrated Photovoltaic/Thermal (BIPV/T) system. Renew. Energy

This chapter examines theoretically and experimentally the energy and exergy analysis of a naturally ventilated BIPV/T system. For the experimental investigation, the data from the experimental procedures presented earlier in Chapter 3.7 were used.

5.1 Literature Review

A review of exergy analysis of solar thermal systems is presented by Kalogirou et al. (2015) which includes various types of solar collectors and applications of solar thermal systems. Additionally, Kalogirou et al. (2016) presented a comprehensive review on the exergy analysis of solar thermal collectors and processes including PV/T systems and the use of phase change materials. It is concluded that exergy analysis is a valuable method to evaluate and compare possible configurations of the solar thermal systems. Moreover, a review on exergy analysis of various solar energy systems, is carried out by Saidur et al. (2012) summarizing that comparing the thermal efficiency and exergetic efficiency of the systems, it can be concluded that the thermal efficiency is not sufficient to choose the desired system. The systems discussed in this study are solar photovoltaic, solar heating devices, solar water desalination systems, solar air conditioning and refrigerators, solar drying processes and solar power generation. Another review on exergetic analysis and performance evaluation of a wide range of renewable energy resources is presented by Hepbasli (2008).

Chow et al. (2009) made an energy and exergy analysis of a PV/T collector with and without glass cover. The energetic efficiency of the glazed collector was found to be always better than the unglazed collector. The exergetic efficiency of the unglazed collector has been found to be better than the glazed one in the specific range of the tested parameters. It is concluded that if the target is to have either more electrical energy or overall energy output, the second law is more appropriate to assess the system.

Sarhaddi et al. (2010) carried out a study to evaluate the exergetic performance of a PV/T air collector. It is concluded that the thermal efficiency of the PV/T air collector is about 17.18%, the electrical efficiency is 10%, the overall energy efficiency is 45% and the exergy efficiency is 10.75% for sample climatic operating and design parameters.

Saloux et al. (2013) studied the analysis of photovoltaic systems and PV/T systems using the exergy method by developing explicit electrical and thermal models in order to characterize each system. Ceylan and Gurel (2015) performed exergetic analysis of a new design of a PV/T system under specific temperatures at 45^{o}C and 55^{o}C. The results showed that the exergy efficiency obtained for 45^{o}C and 55^{o}C was 17% and 21% respectively.

Jafarkazemi and Ahmadifard (2013) studied the effect of the entire design parameters on the performance of flat plate solar collectors with a theoretical and comprehensive model for energy and exergy analysis. More studies on the energetic and exergetic aspects of solar air collectors is presented by Oztop et al. (2013) and Bahrehmand and Ameri (2015).

5.2 Theoretical Background

Nayak and Tiwari (2008) carried out an energy and exergy analysis of a PV/T integrated system with a solar greenhouse in India. In order to maintain the movement of the air inside the greenhouse, a fan is operated continuously. The exergy analysis calculations of the PV/T integrated greenhouse system show an exergy efficiency of 4% approximately. The exergy efficiency is defined as:

$$\eta_{ex} = \left(\frac{\dot{E}x_{out}}{\dot{E}x_{in}}\right) \times 100 \qquad 5.1$$

Where $\dot{E}x_{out}$ is the exergy output of greenhouse (kWh)

$\dot{E}x_{in}$ is the exergy input for PV modules (kWh)

Fujisawa and Tani (1997) studied the annual exergy on PV/T hybrid collector consisting of a liquid heating flat plate solar collector with mono Si PV on substrate of non-selective aluminium absorber plate. From the experimental evaluation, they concluded that the PV/T collector can produce higher output energy than a unit PV module or liquid heating flat plate solar collector. Assuming that the initial temperature of the fluid medium is equal to the ambient temperature, the overall exergetic efficiency (η_{ex}) of a PV/T system is defined by:

$$\eta_{ex,pvt} = \eta_{ex,pv} + \eta_{ex,th} \qquad 5.2$$

Where $\eta_{ex,pv}$ is the exergetic efficiency of the PV

$\eta_{ex,th}$ is the exergetic efficiency of the thermal collector

Saitoh et al. (2003) calculated the exergy of a hybrid solar collector considering that the electrical energy is equivalent to the exergy. Exergy efficiency equation is given in Equation 5.3 where the exergy of heat Ex_H and exergy from the global solar irradiance Ex_I are given by the Equations 5.4 and 5.5.

$$\eta_{ex,pvt} = \frac{\eta_{conversion} \cdot G + Ex_H}{\dot{E}x_{\text{sun}}} \qquad 5.3$$

Where $\eta_{conversion}$ is the conversion efficiency

G is the global irradiance (W/m^2)

Ex_H is the exergy of heat (W/m^2) shown in Equation (5.4)

$\dot{E}x_{\text{sun}}$ is the exergy from the global solar irradiance (W/m^2) shown in Equation (5.5)

$$Ex_H = \frac{T_{fluid} - T_a}{T_{fluid}} \dot{Q}_s \quad 5.4$$

$$\dot{E}x_{\text{sun}} = 0.95\, G \quad 5.5$$

Where T_a is the ambient temperature (K)

T_{fluid} is the supply temperature of the collector fluid (K)

Q_s is the collected heat amount per unit time per panel area (W/m^2)

The exergy input of solar radiation is determined by different methods. According to Chow et al. (2009), the three most commonly used calculation methods are those suggested by Jeter (1981); Petela (1964); Spanner (1964) shown by Equations 5.6, 5.7 and 5.8 respectively. According to Shahsavar et al. (2012), the differences in the results comparing the three equations are less than 2%.

$$\dot{E}x_{\text{sun}} = \left[1 - \frac{T_{amb}}{T_{sun}}\right] G \quad 5.6$$

$$\dot{E}x_{\text{sun}} = \left[1 + \frac{1}{3}\left(\frac{T_{amb}}{T_{sun}}\right)^4 - \frac{4}{3}\frac{T_{amb}}{T_{sun}}\right] G \quad 5.7$$

$$\dot{E}x_{\text{sun}} = \left[1 - \frac{4}{3}\frac{T_{amb}}{T_{sun}}\right] G \quad 5.8$$

Where T_{amb} is the ambient environment temperature (K)

T_{sun} is the temperature of the sun taken as 5777K

G is the solar radiation per unit area (W/m^2)

Shahsavar et al. (2012) analysed the energy and exergy performance of a naturally ventilated PV/T air collector designed, manufactured and tested in Iran. The tested system had a wooden structure and an inclination angle of 30°. The total exergy efficiency of the studied PV/T system is calculated by:

$$\varepsilon_{tot} = \varepsilon_{el} + \varepsilon_{th} \quad 5.9$$

Where ε_{el} is the electrical exergy efficiency calculated from Equation (5.10)

ε_{th} is the thermal exergy efficiency calculated from Equation (5.11)

$$\eta_{ex,el} = \frac{\dot{X}_{el}}{\dot{X}_{in}} \quad 5.10$$

$$\eta_{ex,th} = \frac{\dot{X}_{th}}{\dot{X}_{in}} \quad 5.11$$

Where $\dot{X}_{in}$ is the $\dot{E}x_{\text{sun}}$ presented in Equation (5.7) by Petela (1964), $\dot{X}_{el}$ is equal to the electrical energy (E_{el}=I V) and $\dot{X}_{th}$ is the thermal exergy as defined by Dubey et al. (2009):

$$\dot{X}_{th} = \dot{Q}_U \left[1 - \frac{T_{amb}}{T_{f,o}}\right] \qquad 5.12$$

Where $\dot{Q}_U$ is the rate of useful energy transfer (kW)

$T_{f,o}$ is the outlet fluid temperature (K)

The analysis by Shahsavar et al. (2012) showed that the total energy efficiency of the system increases with increasing solar radiation intensity but the total exergy efficiency decreases. There is also an optimum channel depth at which total energy and exergy efficiencies of the system are maximum. Finally, it is observed that the total energy and exergy efficiencies of the system increase with the increase of the PV cell efficiency.

Joshi and Tiwari (2007) made an attempt to evaluate exergy analysis of a hybrid PV/T parallel plate air collector for cold climatic conditions in India. The energy and exergy efficiencies of a PV/T air collector were estimated. It is observed that an instantaneous energy efficiency of a PV/T air heater varies between 55-65% and exergy efficiency 12-15%. The results obtained are in agreement with the results predicted by Bosanac et al. (2003) who studied the potential of PV/T solar collectors in Denmark. The exergy efficiency of the PV/T air collector is determined by:

$$\eta_{ex} = \eta_o[1 - \beta\Delta T] + \eta_{th}\left[1 - \frac{(T_{amb} + 273)}{293 + \Delta T}\right] \qquad 5.13$$

Where β is the packing factor of solar cell

η_o is the electrical efficiency under standard test conditions

η_{th} is the thermal efficiency

ΔT is the difference between the ambient temperature and collector outlet temperature

Park et al. (2014) presented a comprehensive literature review on energy and exergy analyses of renewable energy conversion systems including solar air heater, solar water heater, solar photovoltaic and cooking devices. The authors recommended to use PV/T collectors than PVs alone for better performance and economic benefits of these systems. Regarding the PVs, the exergy efficiency was determined by:

$$\eta_{ex} = \frac{V_{mp}I_{mp} - \left(1 - (T_{amb}/T_c)\right)h_c\, A_{PV}(T_c - T_{amb})}{\left(1 - (T_{amb}/T_s)\right)G\, A_{PV}} \qquad 5.14$$

Where V_{mp} is the voltage at the maximum power point (V)

I_{mp} is the current at the maximum power point (Amps)

T_c is the temperature of the cell (K)

T_{amb} is the ambient temperature (K)

h_c is the convective heat transfer coef.; h_c =5.7+3.8v where v is the wind speed

T_{sun} is the temperature of the sun taken as 5777K

A_{PV} is the area of the module (m^2)

The literature review presents various studies on the exergy analysis of PV/T systems and the various correlations obtained for the estimation of the exergy efficiency of the PV/T systems but none was found on naturally ventilated vertical BIPV/T systems and very few found on inclined air PV/T systems. Our objective in this chapter is to present the energy and exergy efficiency of the system.

5.3 Energy Analysis

The actual power output of a PV module is shown in Equation (5.15) as given by Kalogirou (2014):

$$P_{max} = V_{OC}\, I_{SC}\, FF \qquad 5.15$$

Where V_{oc} is the open circuit voltage (V)

I_{sc} is the short circuit current (Amps)

FF is the fill factor

Fill factor describes the quality of solar cells and is defined as the ratio of the maximum power from the solar cell to the product of V_{OC} and I_{SC}.:

$$FF = \frac{P_{max}}{I_{SC}\, V_{OC}} = \frac{I_{mp}\, V_{mp}}{I_{SC}\, V_{OC}} \qquad 5.16$$

Where I_{mp} is the current at maximum power point (Amps) as shown in Figure 5.1

V_{mp} is the voltage at maximum power point (V) as shown in Figure 5.1

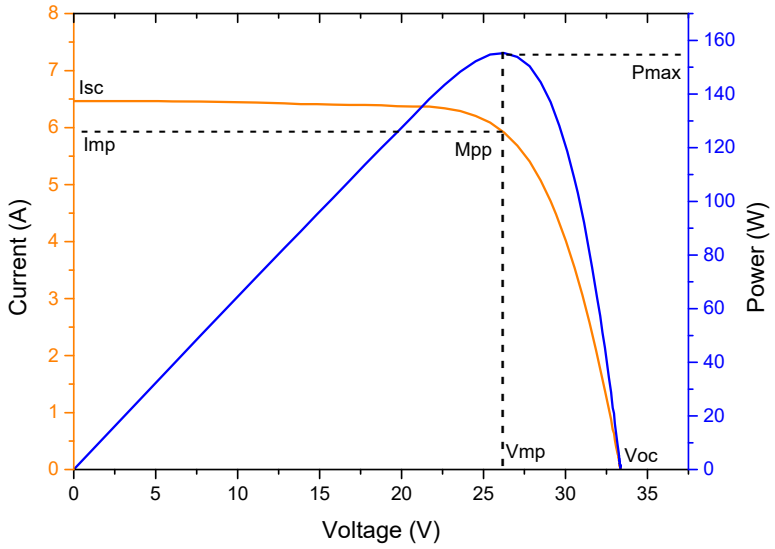

Figure 5.1. Current -Voltage Curve and Current Power Curve for PV module.

The nominal energy efficiency of solar cells and PV module can be defined by:

$$\eta_n = \frac{P_{max}}{A_{PV}\, G} = \frac{FF\; I_{SC}\; V_{OC}}{A_{PV}\, G} \qquad 5.17$$

Where G is the incident solar radiation (W/m^2)

A_{PV} is the area of the PV module (m^2)

The nominal efficiency is always specified under the Standard Test Conditions (STC) at a temperature of 25°C and solar radiation of 1000 W/m^2. The electrical efficiency (η_{el}) at particular irradiance or temperature is the result of the nominal efficiency (η_n) minus the change in efficiency ($\Delta\eta$) due to the temperature effect which is expressed by the cells temperature coefficient (β_c):

$$\eta_{el} = \eta_n - \Delta\eta \qquad 5.18$$

$$\Delta\eta = -\beta_c\,(25℃ - T_C)\,\eta_n \qquad 5.19$$

Accordingly, the electrical conversion efficiency can be defined by:

$$\eta_{el} = \eta_n\left[1 - \beta_c\left(T_C - T_{ref}\right)\right] \qquad 5.20$$

Where T_{ref} is the reference temperature at STC (25°C)

T_c is the cell temperature (K)

β_c is the cells temperature coefficient, shows the drop of efficiency with temperature (%/°C)

The cell temperature can be defined by:

$$T_C = T_{amb} + \left(\frac{NOCT - 20°C}{800\ W/m^2}\right) G \qquad 5.21$$

Where T_{amb} is the temperature at the ambient environment (ºC)

NOCT is the Nominal Operating Cell Temperature reached by open circuit cells in a module under standard operating conditions (°C)

The useful heat gain induced to the system by the air flow is defined by:

$$\dot{Q}_U = \dot{m}\ C_p \left(T_{f,o} - T_{f,i}\right) = \eta_{th}\ G\ A_{PV} \qquad 5.22$$

Thus, the thermal PV efficiency can be defined by:

$$\eta_{th} = \frac{\dot{m}\ C_p \left(T_{f,o} - T_{f,i}\right)}{G\ A_{PV}} \qquad 5.23$$

Where ṁ is the fluid mass flow rate (kg/s)

$T_{f,o}$ is the temperature of the fluid at the outlet (K)

$T_{f,i}$ is the temperature of the fluid at the inlet (K)

C_p is the specific heat of the fluid (kJ/kg K)

The total efficiency can be defined by:

$$\eta_{en} = \eta_{th} + \eta_{el} \qquad 5.24$$

The air mass flow rate for the induced air in the air duct between the PVs and the wall, can be defined by the Equation 5.25 given by Tonui and Tripanagnostopoulos (2008) for the induced mass flow rate of a PV/T collector.

$$\dot{m} = \left(\frac{2\ g\ \beta\ (A_{ch}\ \rho)^2\ A_{ch}\ \eta_{th}\ G\ L\ \sin\theta}{C_p\ \left(f\frac{L}{D_h} + 2\ \beta\ T_{f,o}\right)}\right)^{\frac{1}{3}} \qquad 5.25$$

Where *g* is the acceleration due to gravity (m/s^2)

β is the thermal expansion of air

A_{ch} is the cross-section area of the channel (m^2)

ρ is the fluid density (kg/m^3)

η_{th} is the thermal efficiency of the PV

L is the length of the panel (m)

ϑ is the inclination angle of the system

f is the friction factor

D_h is the hydraulic diameter of the channel (m)

The friction factor *(f)* and the hydraulic diameter *(D_h)* are given by Equations 5.26 and 5.27 respectively.

$$f = 1.906 \left(\frac{Gr}{Pr}\right)^{\frac{1}{12}} \qquad 5.26$$

Where *Gr* is the Grashof number

Pr is the Prandtl number

$$D_h = \frac{4\,A_{ch}}{p} \qquad 5.27$$

Where *p* is the perimeter of the channel (m).

5.4 Exergy Analysis

The exergy analysis is based on the second law of thermodynamics which includes an account of the total exergy inflow, exergy outflow and exergy destructed from the system. The general exergy balance of a BIPV/T system can be written as:

$$\sum \dot{E}x_i - \sum \dot{E}x_o = \sum \dot{E}x_{sys} \qquad 5.28$$

Where $\sum \dot{E}x_i$ is the rate of overall exergy inlet, given by Equation (5.29)

$\sum \dot{E}x_o$ is the rate of overall exergy outlet, given by Equation (5.35)

$\sum \dot{E}x_{sys}$ is the exergy destruction within the system.

The rate of the exergy inlet to the system is the rate of thermal exergy inlet plus the rate of the electrical exergy inlet as given by:

$$\dot{E}x_i = \dot{E}x_{i,air} + \dot{E}x_{i,sun} \qquad 5.29$$

Where $\dot{E}x_{i,air}$ is the rate of thermal exergy inlet to the PV module from the air flow, given by Equation 5.30 as defined by Ceylan and Gurel (2015).

$\dot{E}x_{i,sun}$ is the rate of electrical exergy inlet to the PV module from the sun radiation, given by Equation 5.34 as defined by Petela (1964).

The flow rate of the exergy transferred from the fluid in the inlet that is heated while crossing the duct may be defined by:

$$\dot{E}x_{i,air} = \dot{m}\, e_f = \dot{m}\left[\left(h_{f,i} - h_{amb}\right) - T_{amb}\left(s_{f,i} - s_{amb}\right)\right] \quad 5.30$$

Where the variation of specific enthalpy is given by:

$$h_{f,i} - h_{amb} = C_p\left(T_{f,i} - T_{amb}\right) \quad 5.31$$

And the variation of specific entropy from:

$$s_{f,i} - s_{amb} = C_p \ln\left(\frac{T_{f,i}}{T_{amb}}\right) \quad 5.32$$

Where $T_{f,i}$ is the temperature of the fluid in the inlet.

Thus, Equation 5.30 becomes:

$$\dot{E}x_{i,air} = \dot{m}\, C_p\left[\left(T_{f,i} - T_{amb}\right) - T_{amb} \ln\left(\frac{T_{f,i}}{T_{amb}}\right)\right] \quad 5.33$$

Considering the temperature of the fluid at the inlet equal with the ambient temperature, the term $\dot{E}x_{i,air}$ becomes zero.

The exergy inlet to the system from the sun radiation given by Petela (1964) which is an extension of Equation (5.7) is given by:

$$\dot{E}x_{i,sun} = A_{PV}\, G\left[1 - \frac{4}{3}\frac{T_{amb}}{T_{sun}} + \frac{1}{3}\left(\frac{T_{amb}}{T_{sun}}\right)^4\right] \quad 5.34$$

Where T_{sun} is the temperature of the sun taken as 5777K

The rate of the exergy outlet from the system is defined by:

$$\dot{E}x_o = \dot{E}x_{o,air} + \dot{E}x_{o,sun} \quad 5.35$$

Where $\dot{E}x_{o,air}$ is the rate of thermal exergy outlet of PV module, given by Equation (5.36)

$\dot{E}x_{o,sun}$ is the rate of electrical exergy outlet of PV module, given by Equation (5.37)

By using again Equations (5.31) and (5.32), $\dot{E}x_{o,th}$ may be defined by Equation (5.36) and $\dot{E}x_{o,el}$ by employing η_{el} by Equation (5.37):

$$\dot{E}x_{o,air} = \dot{m}\, C_p\left[\left(T_{f,o} - T_{amb}\right) - T_{amb} \ln\left(\frac{T_{f,o}}{T_{amb}}\right)\right] \quad 5.36$$

$$\dot{E}x_{o,sun} = \eta_{el}\, A_{PV}\, G\left[1 - \frac{4}{3}\frac{T_{amb}}{T_{sun}} + \frac{1}{3}\left(\frac{T_{amb}}{T_{sun}}\right)^4\right] \quad 5.37$$

Where η_{el} is the electrical conversion efficiency defined earlier by Equation 5.20. As can be observed, Equation 5.34 is very similar to the Equation 5.37 with the only difference that it is multiplied by the electrical conversion efficiency. The electrical exergy outlet of the system depends on the efficiency of the PV module to convert the sunlight to electricity.

Accordingly, the exergy balance of a BIPV/T system from Equation (5.28) can be written as:

$$\dot{Ex}_{sys} = \left(\dot{Ex}_{i,air} + \dot{Ex}_{i,sun}\right) - \left(\dot{Ex}_{o,air} + \dot{Ex}_{o,sun}\right) \qquad 5.38$$

Using above equations, the exergy efficiency of the system can be defined by:

$$\varepsilon = 1 - \frac{\dot{Ex}_{sys}}{\dot{Ex}_{i}} \qquad 5.39$$

The experimental procedure and results already presented in Section 3.6 are used also here for the energy and exergy analyses.

5.5 Results

The estimation of the energy and exergy efficiency of the system is made based on some assumptions in order to simplify the analysis:

- The temperature of the PV is considered to be the same in all its area but changing over time (shown in Figure 3.60).
- The solar radiation on the PV surface is considered to be the same in all its area but changing over time (shown in Figure 3.57).
- The temperature of the wall is considered to be the same in all its area remaining constant over time at 26^{o}C.
- The convective heat transfer coefficients range from 3.4 W/m^{2}K to 5.1 W/m^{2}K depending on the variation of the temperature of the PV.

As already mentioned all equations are solved by using the experimental data in order to estimate the energy and exergy efficiency of the system under natural outdoor conditions and natural air gap ventilation.

Figure 5.2 shows the comparison of the PV temperature *(T_{pv})* and the electrical conversion efficiency of the PV *(η_{el})*. As can be observed, the hotter the PV gets, the lower is electrical conversion efficiency.

The electrical efficiency of the system is minimum when the temperature of the PV is maximum. As shown, the electrical conversion efficiency varies between 24%-28.5%.

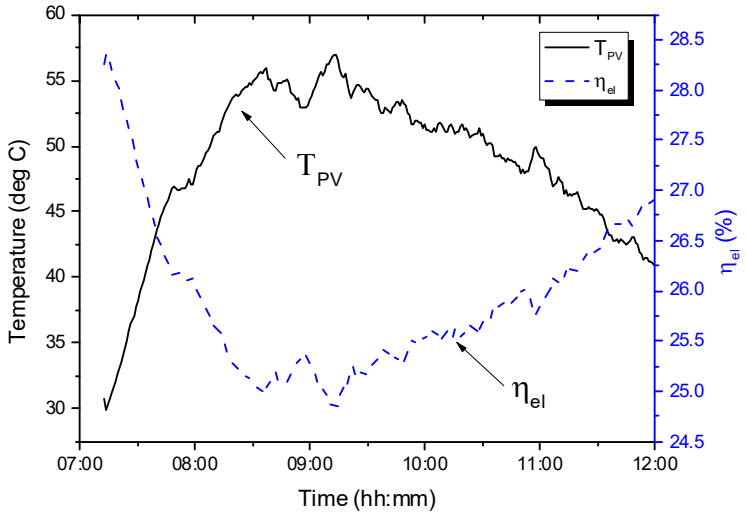

Figure 5.2. The Photovoltaic panel temperature over time in comparison with the electrical efficiency of the PV.

The thermal efficiency *(η_{th})* which is affected by the temperature of the fluid inlet and outlet and the electrical efficiency are shown in Figure 5.3. As can be observed, the electrical efficiency is more dependent on the radiation and the PV temperature because it drops when solar radiation and temperature of the PV is maximum. On the other hand, the thermal efficiency is following an upward trend through time since it is mainly dependent on the temperature difference between the fluid inlet and outlet. This relationship can be seen in Figure 5.4.

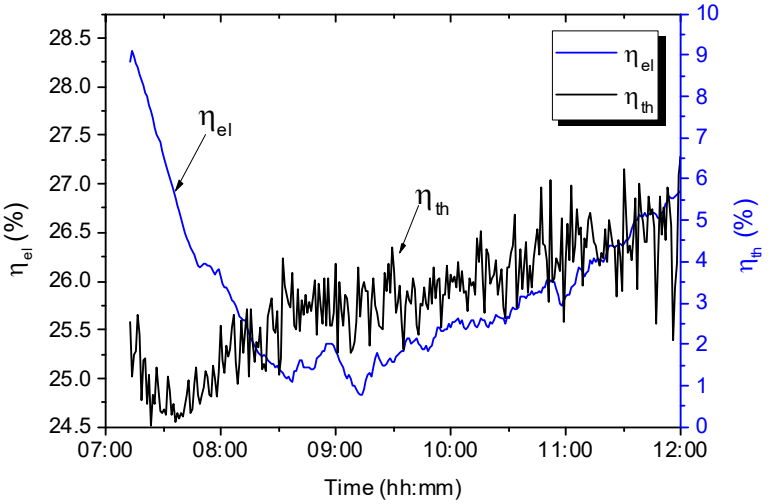

Figure 5.3. The thermal and electrical efficiencies of the system.

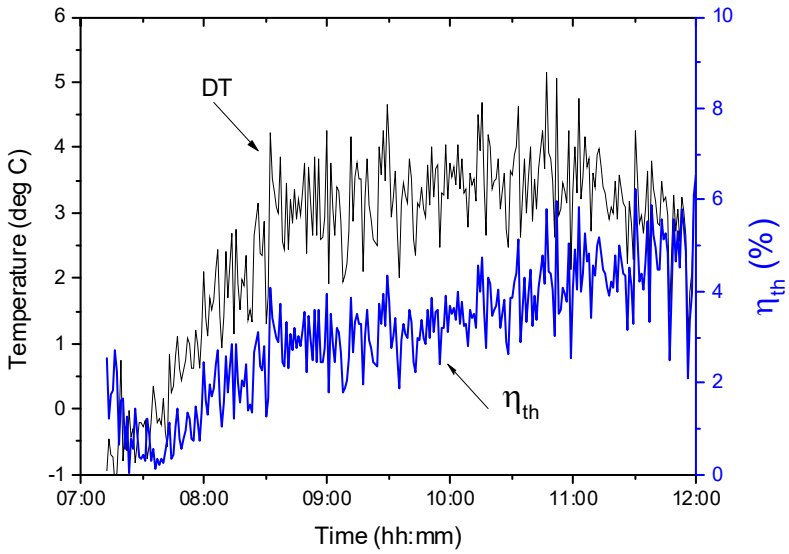

Figure 5.4. Thermal efficiency of the system in comparison with the temperature difference of the fluid inlet and outlet of the air gap.

The overall energy efficiency of the system was 25.5-33.5% although the electrical conversion efficiency of the system drops when the temperature of the PV increases. However, the temperature affects mainly the open circuit voltage. Examining the I-V and P-V curves collected by the PVPM device in the graphs of Figure 5.5, it can be observed that short circuit current drops due to the reduction of radiation. The change in the open circuit voltage is almost zero. Thus, the temperature of the PV surface did not affect the overall performance of the PV, which means that the 0.10 m air gap was adequate to create sufficient air speed to prevent overheating and loss of efficiency. The best curve is observed at 9:00 am where solar radiation was at maximum although at this time the PV temperature was also at maximum.

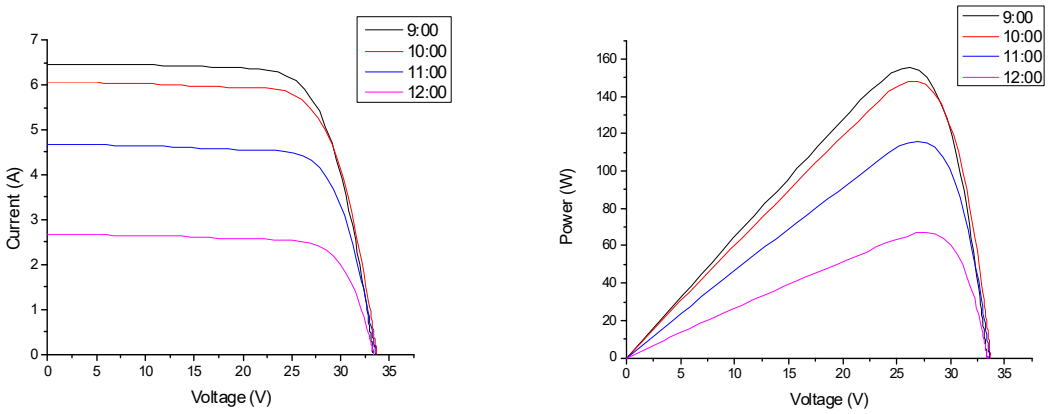

Figure 5.5. Current – Voltage and Power - Voltage curves during experiment.

Earlier it was stated that the amount of energy flowing in and out of a system is the same under thermally steady-state conditions according to the law of energy conservation. This is not happening in exergy since the amount of exergy flowing out *(Ex_o)* is smaller than that flowing in *(Ex_i)*, because exergy is consumed within the system to produce entropy. This is shown in Figure 5.6.

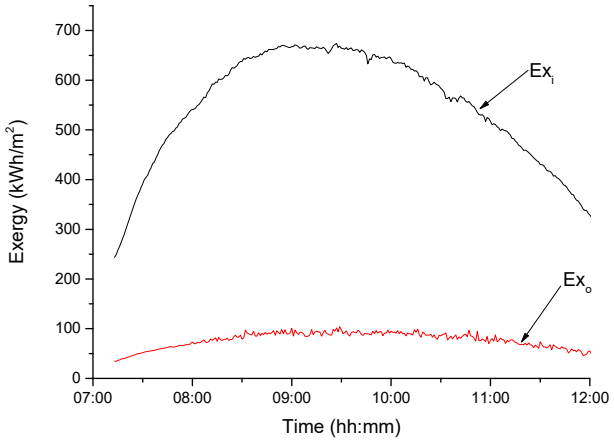

Figure 5.6. The amount of exergy flowing in and out of the system.

Following the equations for the exergy analysis presented earlier in section 5.4, the exergy efficiency of the system *(η_{ex})* is calculated as shown in Figure 5.7 in comparison with the outlet air temperature *(T_{fo})*. As can be observed, the exergy efficiency of the system varies from 13% to 16%. Although, the data do not follow a specific trend, the exergy efficiency shows an increase from 9:30-12:00 where the radiation and PV temperature are high. The range of the exergy efficiency is in agreement with the results obtained by Joshi and Tiwari (2007) who estimated the exergy efficiency of a hybrid air PV/T collector in India. Additionally, as shown in Figure 5.8, the energy efficiency is higher than the exergy efficiency during the whole measurement period.

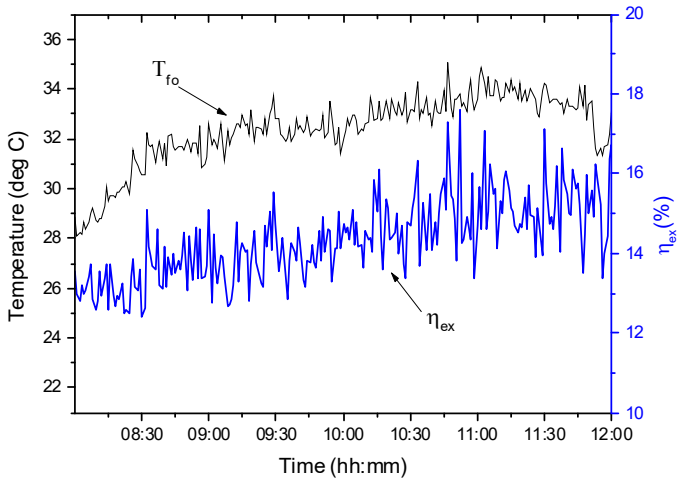

Figure 5.7. The exergy efficiency of the system related to the temperature of the air at the exit of the duct.

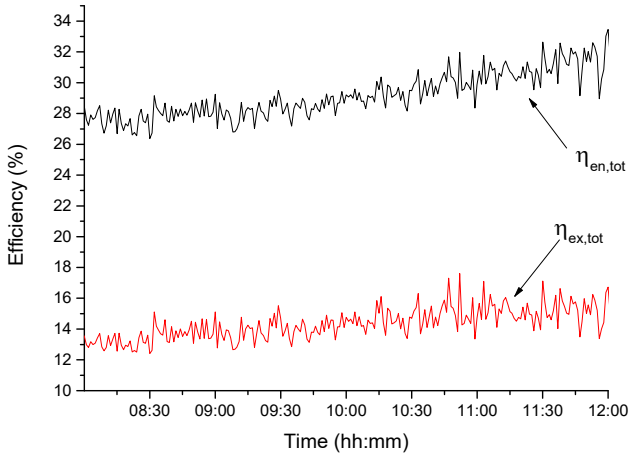

Figure 5.8. The energy and exergy efficiencies.

Unfortunately, no other paper is found on the same system (facade-building integrated naturally ventilated system) to compare the results. These however are of the same order of magnitude as other similar but forced circulation systems, which proves that the penalty paid in terms of exergy spent by the fan (in forced circulation systems) is counterbalanced by the slightly lower performance of the naturally operated system (lower heat transfer values), so the two systems, naturally and forced systems, behave similarly without the disadvantages of the forced system as outlined earlier in the paper.

5.6 Conclusions

Based on the temperature distribution of the system, energy and exergy analyses are carried out and the correlations for the energy and exergy efficiencies are presented. The energy efficiency of the system is estimated to be up to 26.5-33.5% while the exergy efficiency is estimated to be between 13-16%.

Based on the results obtained, the following general conclusions can be drawn:

- The exergy efficiency of the system examined increases by increasing the temperature of the fluid at the outlet.
- The electrical efficiency of the system varies between 24% and 28.5% when the temperature of the PV panel varies between 30-57^{o}C.
- The exergy flowing in the system is bigger than the exergy that exits the system.

CHAPTER 6

6 Building Energy Simulation and System Monitoring

This chapter presents a performance analysis of a real size roof BIPV installation. The knowledge earned from the investigation on the BIPV systems presented earlier in this study is used to recommend the sizing of the air gap of the system and the type of the system's ventilation. Additionally, a simulation model is built before the installation in order to predict the temperature on the PVs surface over a year and the annual energy production of the system considering the proposed measures regarding the air gap width and the type of ventilation. After the estimation of those parameters and the completion of the installation, the estimated results regarding the temperature of the PV surface and the energy production are compared with the monitoring results in order to validate the model and compare the estimated energy production with the measured.

Accordingly, this chapter presents the roofing shingle PV panels installed on a demonstration building, the simulation model developed in TRNSYS to predict the annual performance of the system, the monitoring plan of the system, the results obtained from the simulation and finally the data measured from the monitoring of the system on-site.

This work is developed under the BFIRST (Building integrated Fibre Reinforced Solar Technology) EU FP7 funded project. The aim of the project was to produce new shape (different from flat), lightweight and efficient PV modules for building integration to replace building construction elements such as the roof tiles, the curtain walls, windows, glazings and shading elements. CUT was a partner in the EU project with the responsibility to carry out the thermal analysis of the system.

6.1 Roofing Shingles PV modules

BFIRST project developed a new manufacturing procedure for PV modules for building integration using fibre reinforced composites. As a result, the new PVs are more flexible and lightweight than the conventional PV modules.

Although in the last years the PV manufacturers produce frameless PV modules for BIPV integration, there are many BIPV systems with normal PV panels, aluminum frame, rectangular shape and specific size because they offer better stability and lower price. However, the BFIRST project brings the PV technology in a new level by producing PV modules of variable shape, with same or higher efficiency as the normal PVs, which can be manufactured in different shapes and colors.

The BFIRST project developed PV modules able to replace the building's envelope construction elements such as external façade, roof tiles and glazing. So far, this study is focused on the façade BIPV applications, but this chapter will focus on the thermal analysis of a roof BIPV system in Belgium, with the new roofing shingles (RS) modules. The analysis of the roof BIPV system is done in the same way as the vertical systems, considering only different inclination angle.

The RS element is a frameless rectangular monocrystalline silicon solar panel with characteristic saw tooth shaped profile. The colour of the module is black to reproduce the colour of the natural slate of the roof. Table 6.1 shows some characteristics of the RS module.

Table 6.1. Characteristics of the Roofing Shingle PV modules.

Dimensions	905 x 1395 x 59 mm	**Cell type**	Mono-Si
Weight	7.3 kg	**Cells Efficiency**	18.9%
Power	123 Wp	**Module Efficiency**	11.5%
Cells per module	32		

6.2 Proposed Architectural Concept

The new roofing shingle modules are installed on a demonstration building located in Mons, Belgium (50.4542° N, 3.9567° E) on May 2016. The demonstration building is a new residential building with orientation 10° from south to west. The BIPV system is installed on the two parts of the south roof of the building with 40° slope. The two parts are shown with orange and blue in Figure 6.1. The northern side of the roof is covered with normal tiles.

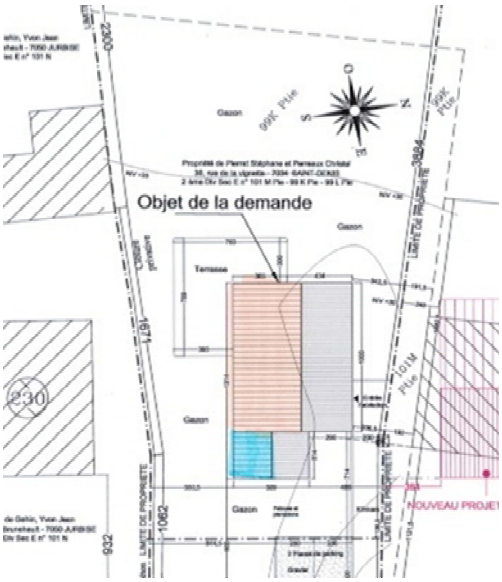

Figure 6.1.The demonstration site in Mons, Belgium, showing the two parts of the roof for BIPV installation.

Considering the size of the RS modules and the size of the two roof parts, a total of 57 RS modules are installed as shown in Figure 6.2, 49 on the big part of the roof and 8 at the small part. The total installed nominal power of the PV plant is 7.01 kWp. The residential house is connected to the electric grid using a 3 x 230 V connection of 12.7 kVA (30 A).

Figure 6.2. The 57 RS modules on the roof of the demonstration building.

The roof is firstly covered with thermal insulation and a wooden structure. Then, aluminium profiles are installed on the wooden structure to fix the PVs. From top to the bottom the modules overlap, to form one large continuous PV surface to cover all the roof's area. From left to right there are no joints in between the panels. Although earlier it was proposed to leave openings between the panels when the application has a large height, in this case it was not possible to install the panels with open joints

in between because it is a roof installation and the aim was to keep the picture of the roof as much as closer to normal tiles and avoid rain water leakage to the insulation. Thus, a continuous PV surface is formed and the air duct is ventilated with bottom and top opening as shown in Figure 6.3. Additionally, the continuous surface of the PV panels in this case is not a major problem because Belgium has a cold climate and it is easier to avoid overheating by leaving an optimum air gap size and openings at the bottom and top of the system only.

As discussed before in this study, an air duct is usually formed in the BIPV applications between the PV panels and the substructure of the building, which is ventilated naturally or mechanically to keep the temperature of the PV panels in effective levels or to produce hot air to be driven into the building for space heating. Taking into consideration the investigation presented so far in the previous chapters, in this system, an air gap of 10 cm is recommended with natural ventilation. As proved earlier, a naturally ventilated air gap of 10 cm is adequate to keep the performance of the system in normal levels.

However, the only way to predict if the design suggestions we made are effective to the particular system is to carry out annually simulations to predict the annual performance of the system and its thermal behavior through a year. This is done with TRNSYS simulation software, which is described in the next section.

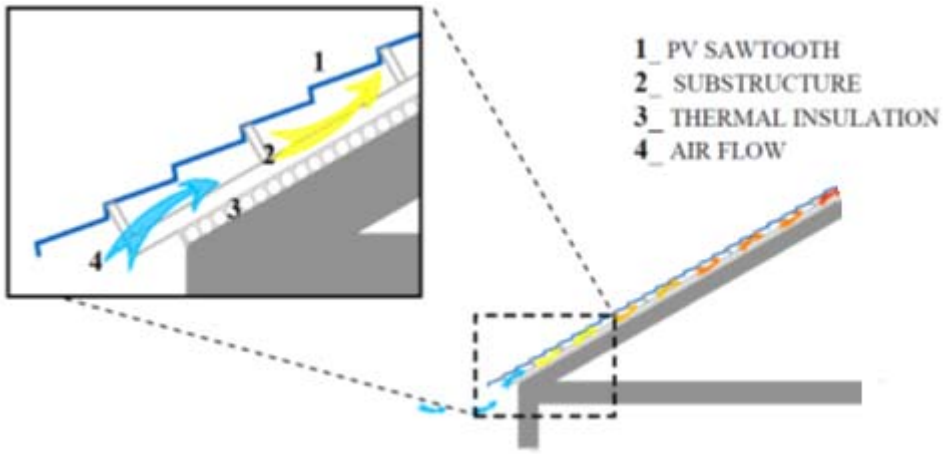

Figure 6.3. The roof structure showing the way of the air flow behind the PV panels.

6.3 TRNSYS as Energy Simulation Software

TRNSYS is used to create a simulation model of the BIPV system installed on the demonstration building in Belgium, using weather data from a TMY (Typical Meteorological Year) file of Brussels, Belgium which is the closest city to Mons where the demonstration building is located, with available TMY files. As mentioned before, this kind of simulation is very useful especially before the installation to estimate

and predict the performance of the system, the annual energy production of the system and the thermal behaviour of the system.

TRNSYS is an acronym for a 'Transient Systems Simulation' software with a standard simulation environment. It is a software used to model and simulate the behaviour of transient energy systems for a large number of applications such as solar systems, HVAC systems with advance design features (e.g., natural ventilation, slab heating), fuel cells, and many other types of systems that require dynamic simulation (TRNSYS17, 2012).

A TRNSYS model consists of individual components, which represents one part of the overall modelled system. Each component, recognized as "type", has its Fortran subroutine program, which is compiled into a Windows Dynamic Link Library (DLL) file. The DLL-based structure allows the user to modify an existing type and create a new custom component model in case that the current TRNSYS modules cannot simulate certain features. The types require time-independent PARAMETERS and time-dependent INPUTS, and generate OUTPUTS. During the simulation, the parameters remain constant. A given output from a type can be used as input for another type. The whole energy model consists of a number of types that are connected and interacted with each other.

Below, the various standard PV components available in the TESS (Thermal Energy System Specialists) libraries for TRNSYS17 are shown:

- TYPE 551: Photovoltaic array shading
- TYPE 560: Fin-tube PV/T solar collector
- TYPE 562: Simple glazed or unglazed photovoltaic panel
- TYPE 563: Unglazed fin-tube PV/T solar collector
- TYPE 566: Building integrated photovoltaic system (interfaces with air zone temperature)
- TYPE 567: Building integrated photovoltaic system (interfaces with TYPE56)
- TYPE 568: Un-glazed building integrated photovoltaic system (interfaces with TYPE56)
- TYPE 569: Un-glazed building integrated photovoltaic system (interfaces with air zone temperature)

Figure 6.4 shows the classification of the existing BIPV/T Types in TRNSYS 17. Both Types 566 and 567 are described as glazed collectors. The cover glass plays a significant role to minimize the top losses, which mainly occur due to wind velocity (Zondag, 2008).

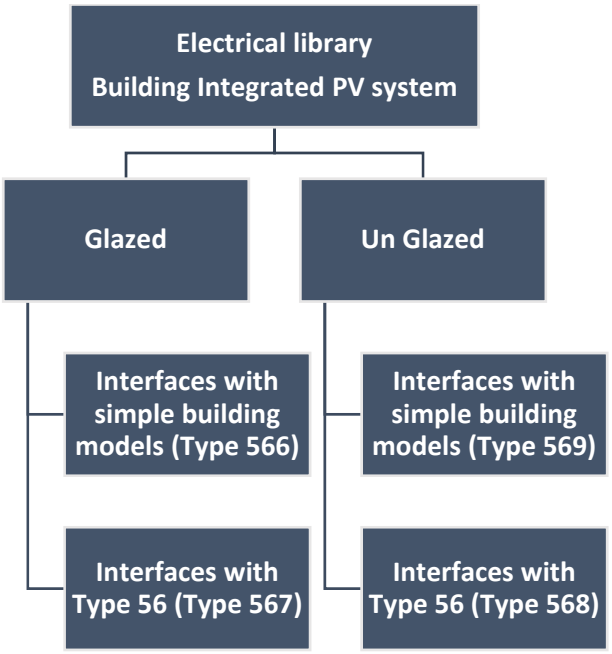

Figure 6.4. Building Integrated PV/T Types in TRNSYS 17.

6.4 Simulation Model

As already mentioned, the BIPV simulation model in TRNSYS was developed prior to the installation of the BIPV system to examine the effectiveness of the proposed design of the system regarding the size of the air gap and the type of ventilation. It is very important to predict the performance and thermal behavior of the system before the installation because it will help the installers and the engineers to make changes to optimize the installation. Apart from the PV surface temperature and the energy production of the system, the developed model can estimate the mean temperature of the air in the duct between the PV panels and the roof's substructure, the temperature of the air in the outlet, the thermal efficiency of the system, the convective and radiative loses, etc.

The main components of the model used are Type 566 and Type 109. Type 566 from the Electrical Library of TRNSYS is used to represent the BIPV system, and Type 109 the weather data.

Type 109 serves the main purpose of reading weather data at regular time intervals from a data file. Weather data in Type 109 are provided in the form of TMY data. A typical meteorological year (TMY) is a collation of selected weather data for a specific location, generated from a data bank much longer than a year in duration. It is specially selected so that it presents the range of weather phenomena for the location in question, while still giving annual averages that are consistent with the long-term averages for the location in question. The TMYs are data sets of hourly values of solar radiation and meteorological elements for a 1-year period.

A simulation is carried out for one year, with one-hour time step, considering the real dimensions of the system, Inclination angle of 40° and orientation of 10 degrees from south. The list of inputs and outputs of the Type 109 is shown in Table 6.2.

Table 6.2. The inputs and outputs of the Type109 for the TMY data

Type 109: Input	**Value**	**Units**
Ground reflectance	0.2	-
Slope of surface	40^o	degrees
Azimuth of surface	10^o	degrees
Type 109: Output		
Ambient temperature	From file	^{o}C
Relative humidity	From file	%
Wind velocity	From file	m/s
Wind direction	From file	degrees
Atmospheric pressure	From file	Pa
Extra-terrestrial radiation on horizontal	From file	kJ/hr m^2
Total radiation on horizontal	From file	kJ/hr m^2
Beam radiation on horizontal	From file	kJ/hr m^2
Sky diffuse radiation on horizontal	From file	kJ/hr m^2
Ground reflected diffuse radiation on horizontal	From file	kJ/hr m^2
Total radiation on tilted surface	From file	kJ/hr m^2
Beam radiation on tilted surface	From file	kJ/hr m^2
Sky diffuse radiation on tilted surface	From file	kJ/hr m^2
Ground reflected diffuse radiation on tilted surface	From file	kJ/hr m^2

Type 566 is intended to model a glazed solar collector that has the dual purpose of creating power from embedded photovoltaic (PV) cells and providing heat to an air stream passing beneath the absorbing PV surface. Figure 6.5 shows a schematic of the PV/T system used in Type 566.

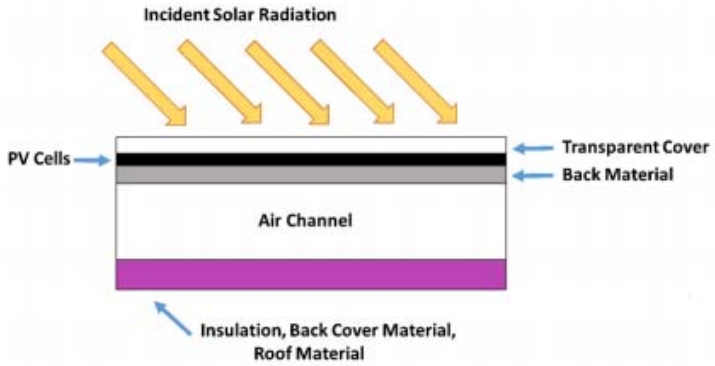

Figure 6.5. A schematic of PV/T system used in Type 566.

This model is intended to operate with simple building models that can provide the temperature of the zone air on the back-side of the collector and provide an estimate of the radiant temperature for

back-side radiation calculations. The cells are assumed to be operating at their maximum power point condition, implying that the voltage and current are not calculated by the model (TESS, 2014).

The thermal models of Type 566 (and Type 567) rely on algorithms given in "Solar Engineering of Thermal Processes" by Duffie and Beckman (1980). The thermal models were developed by energy balances at the cover surface, PV surface, upper air channel surface, and lower air channel surface. The mathematical details are available in TRNSYS TESS models' documentation. The thermal resistance network for both Types 566 and 567 is shown in Figure 6.6.

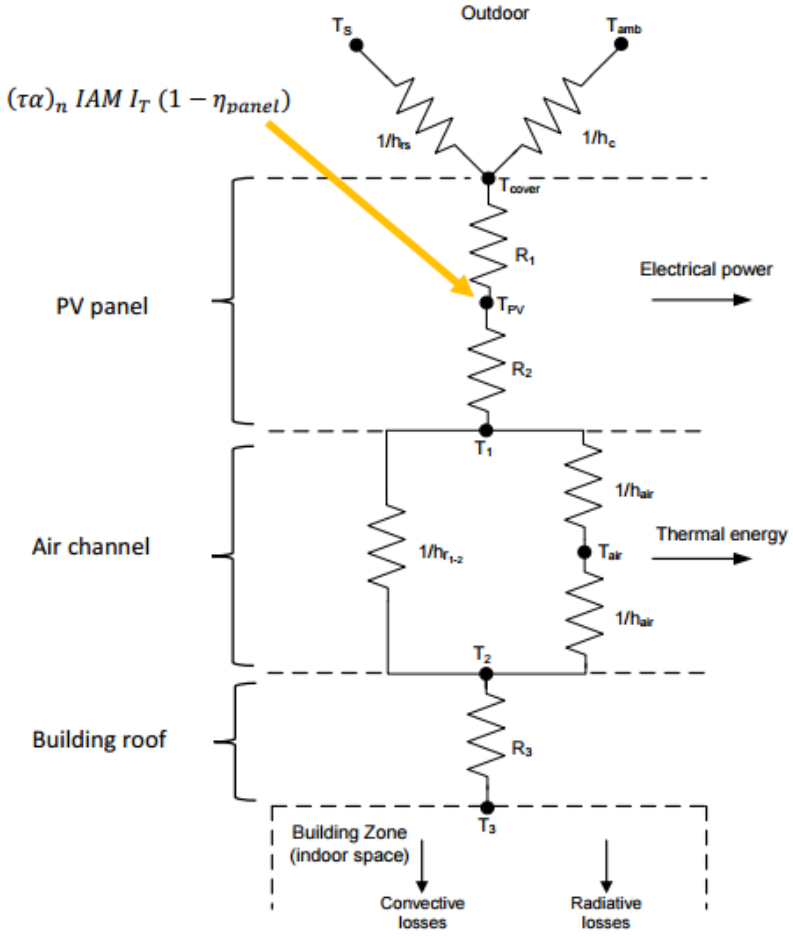

Figure 6.6. Thermal resistance for energy balance of BIPV/T in TRNSYS Type 566.

The CHTC in the mathematical model of Type566 can be estimated by the following equations considering forced ventilation.

$$h = \frac{Nu * k_{air}}{D} \qquad 6.1$$

Where k_{air} the thermal conductivity of air (kJ/h/m/K)

D is the hydraulic diameter of the air duct given by $D = 4\,A_c/p$ (m). A_c is the cross section area of the duct and p is the perimeter of the duct.

When the flow is considered laminar ($Re \leq 2300$), by setting the temperature of the duct as constant, the Nusselt number is given by:

$$Nu = 3.66 \qquad 6.2$$

The Reynolds number in the Type566 model is given by:

$$Re = \frac{4\,\dot{m}}{\pi\,D\,\nu} \qquad 6.3$$

Where $\dot{m}$ is the mass flow rate (kg/hr)

D is the hydraulic diameter of the duct (m)

ν is the kinematic viscosity of air (kg/m hr)

Regarding the Nusselt number for laminar flow, Cengel and Ghajar (2011) give a table with the Nusselt number for laminar flow in noncircular tube. The table shows that the value of 3.66 belongs to the circular tube. For rectangular tubes, the Nusselt number is given regarding the aspect ratio of length/width.

When flow is considered turbulent the Nusselt number is estimated by the following correlation:

$$Nu = 0.023\,Re^{0.8}Pr^{n} \qquad 6.4$$

Where n=0.4 for heating and n=0.3 for cooling of the fluid flowing through the tube. This equation is known as the Dittus and Boelter (1930) equation.

However, in this study the tested system is naturally ventilated and thus natural convection occurs. Consequently, the convective heat transfer coefficients values have been added manually based on the previous experimental analyses, considering naturally ventilated system. The list of the parameters, inputs and outputs of the system and the constant values given in the model are shown in Table 6.3.

Table 6.3. The list of parameters, inputs and outputs of the Type 566.

Type 566: Parameters	**Roof 1**	**Roof 2**	**Units**
Collector width	9.765	2.79	m
Cover length	6.335	3.62	m
Cover conductivity	0.32	0.32	W/mK
Cover thickness	1.8	1.8	mm

Channel height	6.335	3.62	m
Cover emissivity	0.84	0.84	-
Back emissivity	0.9	0.9	-
Channel emissivity top	0.84	0.84	-
Channel emissivity bottom	0.9	0.9	-

Type 566: Input	**Value**	**Units**
Inlet temperature	From file	^{o}C
Inlet flowrate	1400	kg/hr
Ambient temperature	From file	^{o}C
Sky temperature	10	^{o}C
Zone temperature	25	^{o}C
Back radiant temperature	From file	^{o}C
Incident solar radiation	From file	kJ/hr m^2
Total horizontal radiation	From file	kJ/hr m^2
Horizontal diffuse radiation	From file	kJ/hr m^2
Ground reflectance	0.2	-
Incidence angle	40	degrees
Collector slope	40	degrees
Top heat loss coefficient	3.5	kJ/hr m^2 K
Bottom heat loss coefficient	1.2	kJ/hr m^2 K
Atmospheric pressure	14	atm
PV efficiency	0.16	%

Type 566: Output	**Value**	**Units**
Outlet fluid temperature	-	^{o}C
Outlet fluid flow rate	-	kg/hr
Useful energy gain	-	kJ/hr
Thermal efficiency	-	%
Power production	-	kJ/hr
PV efficiency	-	%
Cover temperature	-	^{o}C
PV temperature	-	^{o}C
Upper channel temperature	-	^{o}C
Mean fluid temperature	-	^{o}C
Lower channel temperature	-	^{o}C
Back surface temperature	-	-
Incidence angle modifier	-	%
Convective top losses	-	kJ/hr
Radiative top losses	-	kJ/hr
Convective back losses	-	kJ/hr
Radiative back losses	-	-
Absorbed radiation	-	kJ/hr

6.5 Monitoring: Equipment and Measurements

The PV system set up on the building's roof finished on April 2016 and the sensors and rest of the monitoring equipment were installed during May and June 2016. The monitoring started on June 2016. Thus, most of the data were available from June or July.

One of the most important parameters to measure during monitoring is the temperature of the PVs surface. It is important to record the temperature of the PV surface during the year in order to observe if the PV panels overheat and loose efficiency. In this case, it means that the natural ventilation in a 10 cm air gap is not adequate to cool the PVs and a fan should be installed to drive fresh air in the duct. Ten temperature sensors were installed in various positions on the PV back surface, on the substructure, in the attic etc. Below the instruments used for the monitoring are listed:

- Kipp and Zonen Smart Pyranometer SMP10
- QUADRA Weather Station (Temperature, wind, wind direction, irradiance)
- Relative humidity sensor
- External PT1000 temperature sensors
- Energy meters
- Indoor PT1000 temperature sensors
- Server for data acquisition
- Amazon Cloud storage server

An overview of the complete monitoring equipment is presented in Figure 6.7, showing the outdoor and indoor sensors, and the procedure for connections to save data to the web server storage. The outdoor sensors are the various sensors installed to measure the irradiance and humidity as well as the weather station's sensors. The interface sensors refer to the temperature sensors and data acquisition system installed for the measurements of the PV system. The indoor sensors refer to temperature sensors and energy meters installed to monitor the indoor conditions of the building and the energy consumption of the house. All the sensors transfer information to data loggers through uploading to an online web server, with time step of one minute.

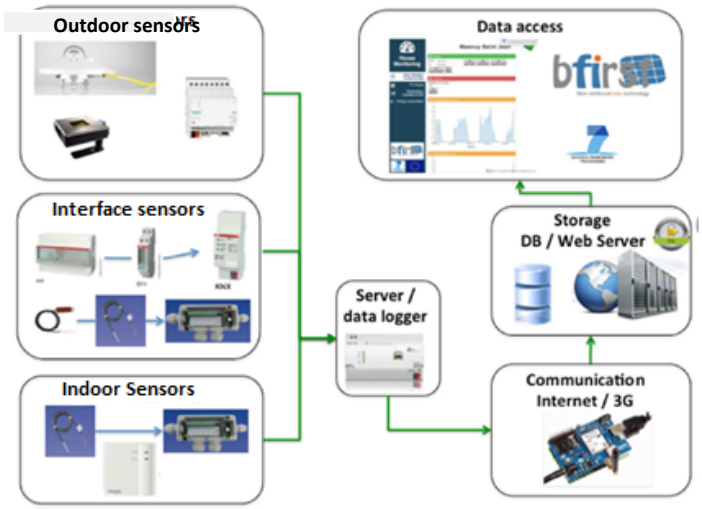

Figure 6.7.The monitoring equipment and the monitoring setup, installed on the demonstration building in Mons, Belgium.

Considering the time interval of 1 minute for all measurements, this means that for one single day of monitoring, for ten random parameters, 14400 values are stored. The amount of data in a month or in a year is extremely huge and the analysis of those data up to the stage to be useful and exploitable is very hard. To do this, a specific code is built in MATLAB in order to filter the data. The filtration and sort of the data is useful not only for presentation purposes but also to be comparable with the simulation results.

6.6 Simulation Results

As mentioned before, the simulation is carried out for one year with the use of real hourly weather data from TMY file of Brussels, Belgium. This section presents the results from the simulation model presented in Section 6.4.

First, it is important to examine the weather data used from the TMY data file. The solar radiation and the ambient temperature of one year are shown in Figure 6.8 and Figure 6.9 respectively.

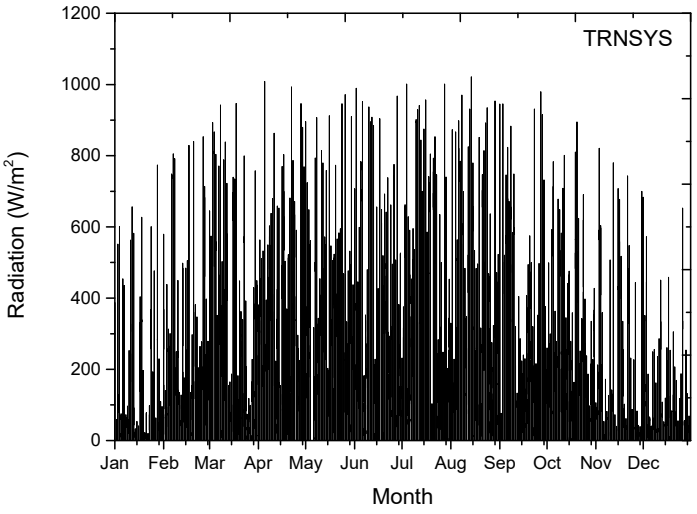

Figure 6.8. The solar radiation on the tilted roof surface from the TMY file for Brussels, Belgium.

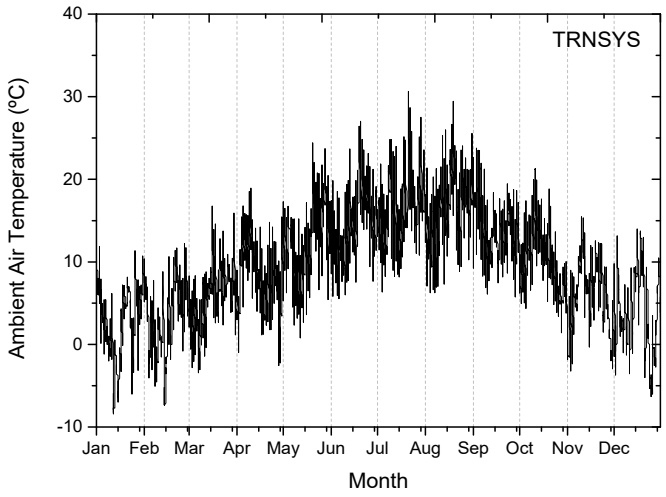

Figure 6.9. The ambient air temperature of Brussels, Belgium for one year from the TMY file.

The aim of the modelling was to predict the temperature of the PV panels through a year and the energy production of the system. It was important to predict the temperature of the system because high PV temperatures affect the performance of the system. Figure 6.10 shows the estimated temperature of the PV panels for one year. As can be observed, the highest temperatures occur in the summer period reaching maximum 67°C. The same observation arises from Figure 6.11 which shows the calculated temperature of the air in the outlet of the air duct between the PV panels and the roof substructure. The air in the inlet of the duct is equal to the ambient air temperature in Brussels, which

varies from 20 to 27°C from June to September. The air in the exit of the duct shown in Figure 6.11, is 5-8°C higher than the inlet, reaching up to 36.7°C in summer months.

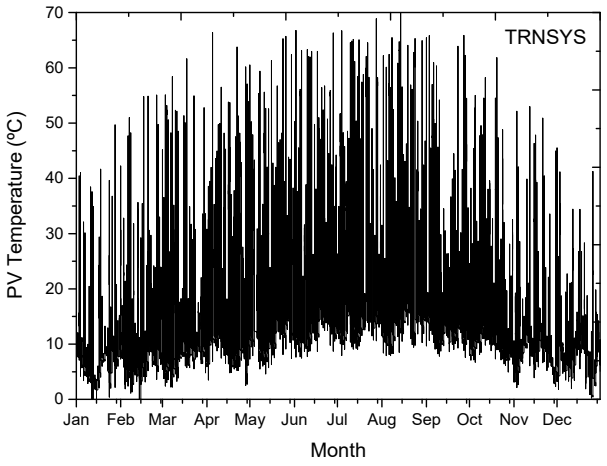

Figure 6.10. The estimated PV temperature for one year simulation..

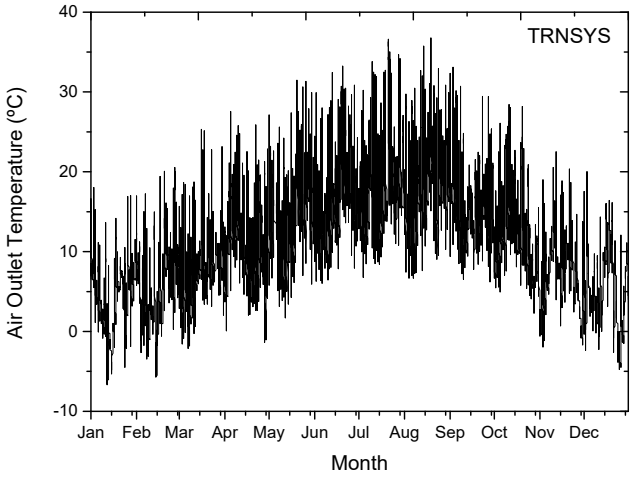

Figure 6.11. The estimated outlet air temperature of the duct, for one year simulation.

So far, the model showed that the proposed air gap size of 10 cm and the natural ventilation can keep the temperature of the PV panels below 67°C during the summer months. The next step is to look on the energy production of the system during these months. The estimated energy production will be compared to the real measured energy production in later section.

Figure 6.12 shows the energy production of the system from the two roofs for one year of simulation. The total production is estimated up to 9507.40 kWh from both roof parts for one year.

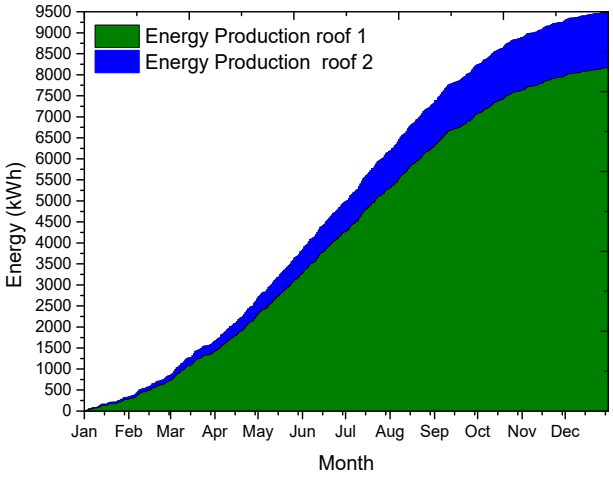

Figure 6.12. The estimated energy production of the system for one year simulation.

From Figure 6.12 it is hard to understand the production of the system each month. Therefore Figure 6.13 shows the energy production of the two roof parts per month. As expected, the maximum production occurs in the summer months and the lower in winter.

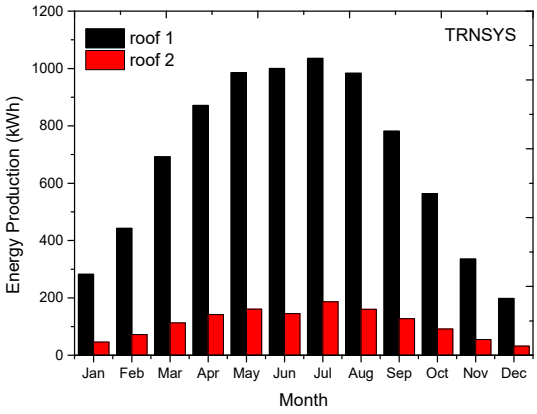

Figure 6.13. The estimated energy production of the system for each month, for one year simulation.

6.7 Results from Monitoring

This section presents the measured data from the monitoring of the real system in Belgium as presented in Section 6.5. As mentioned in previous sections, the installation of the system finished on May 2016 and the monitoring started on June 2016. Thus, the measured data in this section are presented for one year, from June 2016 to June 2017. However, some parameters were available only from July 2016.

The on-site measured solar radiation and ambient air temperature in Mons, Belgium are shown in Figure 6.14 and Figure 6.15 respectively. The radiation is measured on the PV surface slope at 40º so this is the reason that there are values that exceed 1000 W/m^2.

Regarding the radiation measured data, it is observed that it is higher in summer months than the radiation from the TMY file used for the simulation shown previously in Figure 6.8. On the other hand, the measured ambient air temperature shown in Figure 6.15 is very similar to the temperature from the TMY file shown in Figure 6.9 in the previous section.

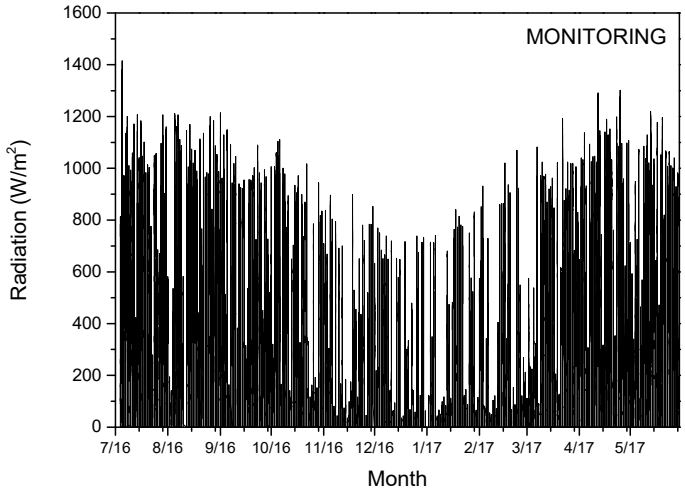

Figure 6.14. The measured solar radiation on the tilted roof surface of the BIPV system in Mons, Belgium.

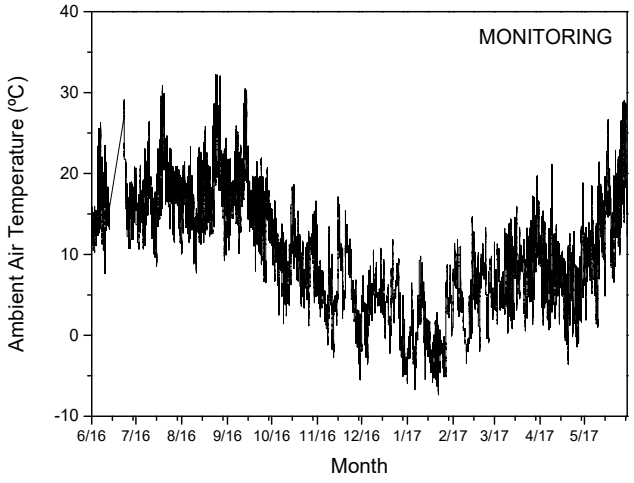

Figure 6.15. The measured ambient air temperature on the site of the BIPV system in Mons, Belgium.

One of the most important parameters of monitoring is the temperature of the PV panels. Various sensors were installed on the back side of the PV panels. However, to present a graph of the average PVs temperature, the average values of all sensors were collected.

Figure 6.16 shows the average measured temperature of the PV panels from June 2016 to June 2017. As can be observed, the maximum temperature observed is 64^{o}C and occurs during the summer months. Comparing Figure 6.16 with the measured PV temperature and Figure 6.10 with the estimated PV temperature, it can be observed that the simulation gives maximum temperature of 67^{o}C.

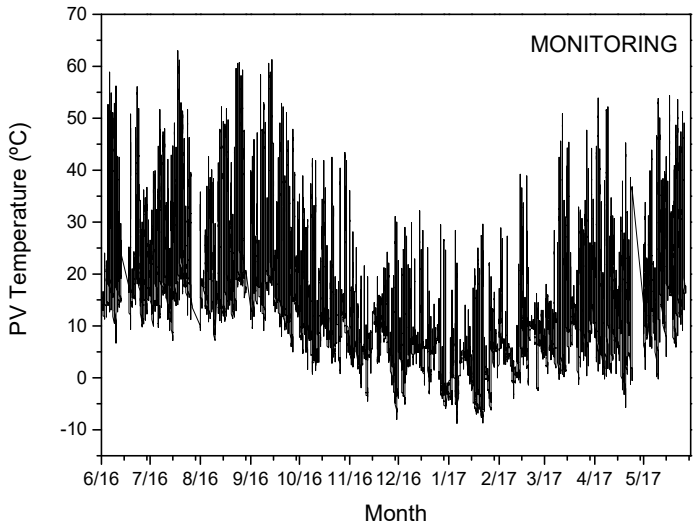

Figure 6.16. The measured PV temperature of the BIPV system in Mons, Belgium.

Figure 6.17 shows the measured temperature of the air in the outlet of the air duct between the PV panels and the roof substructure. It was expected to observe maximum values during the summer months such as the PVs temperature. From Figure 6.17 it can be concluded that the estimated temperature of the air in the outlet of the duct, from the simulation has a good agreement with the measured data regarding the maximum values. The maximum estimated temperature is 36.7^{o}C while the measured is 36.1^{o}C.

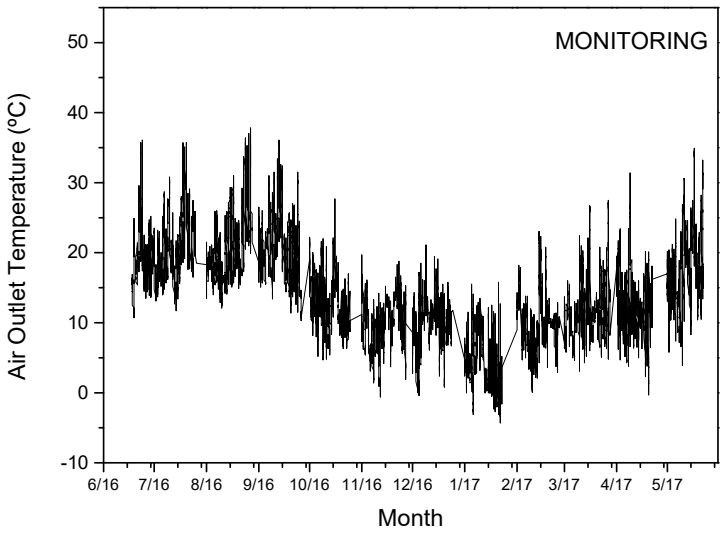

Figure 6.17. The measured air outlet temperature of the BIPV system in Mons, Belgium.

A month to month comparison of the PV temperature and the outlet air temperature will be shown in the next section of this chapter.

The most important measurements of the monitoring plan are the measurements regarding the energy consumption of the house and the energy production of the BIPV system. Figure 6.18 shows the energy consumption of the system from the first month of the BIPV system operation which is July 2016 until June 2017 for all the appliances of the house. As can be seen, the total energy consumption reaches 4500 kWh in one year. Comparing the energy consumption of the house with the energy production of the system shown in Figure 6.19, it can be observed that the system produced double the energy that the house consumed in one year.

The monthly energy production of the system measured from two inverters is shown in Figure 6.20. The maximum production is recorded during the summer months.

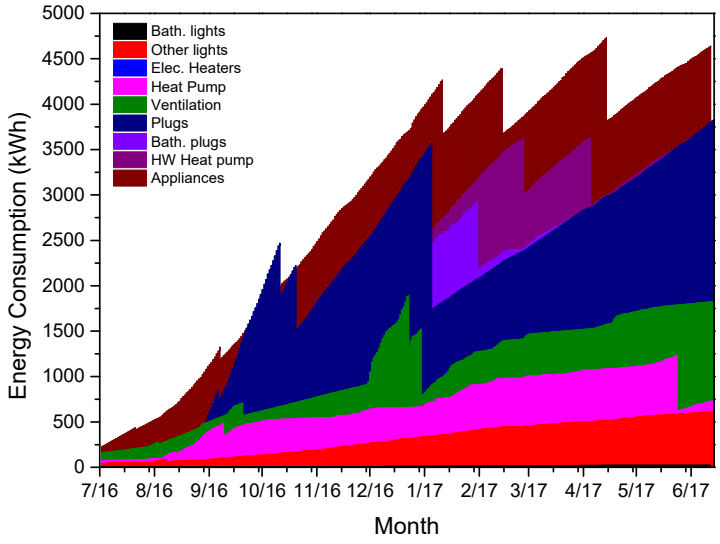

Figure 6.18. The measured energy consumption of the demonstration house in Mons, Belgium.

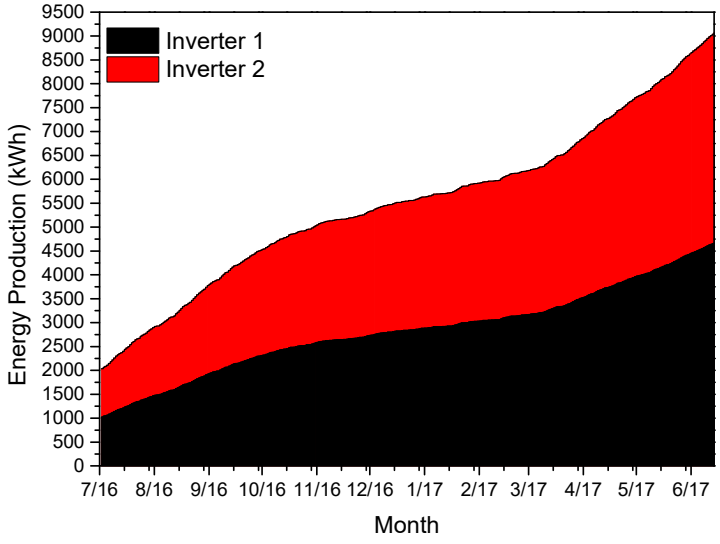

Figure 6.19. The measured energy production of the BIPV system in Mons, Belgium.

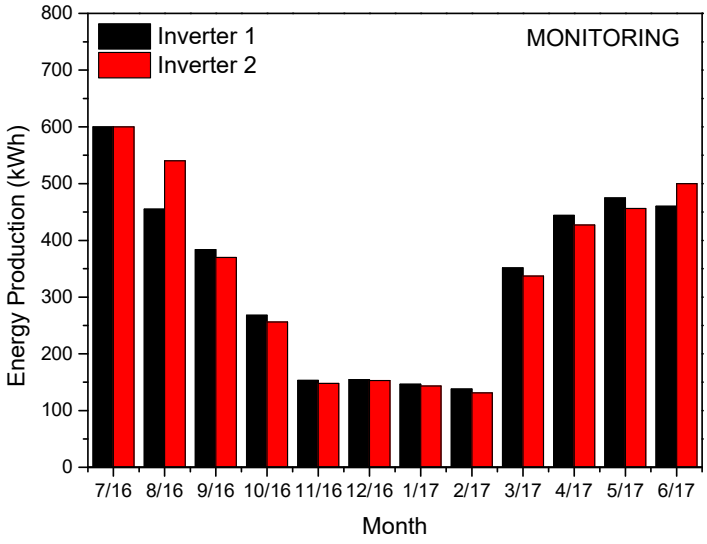

Figure 6.20. The monthly measured energy production of the BIPV system.

6.8 Discussion & Conclusion

This section presents an overall discussion on the estimated and measured results for the BIPV demonstration building in Mons, Belgium. So far, the annual calculated and measured data are presented. In this section, all the values are sorted month to month for better understanding and comparison purposes.

Figure 6.21 and Figure 6.22 show the calculated and measured, average and maximum values of PV temperature and outlet air temperature per month, for one year.

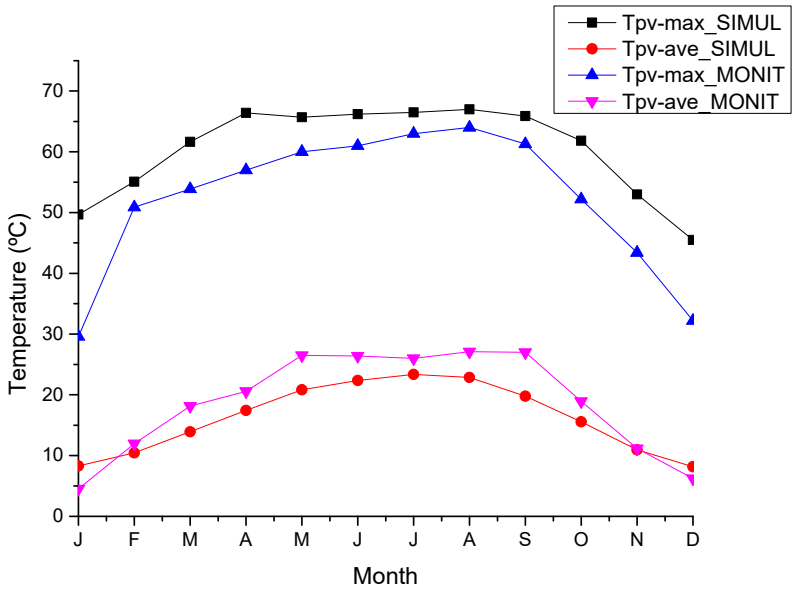

Figure 6.21. Comparison of the maximum and average monthly values of the PV temperature for the calculated and measured data.

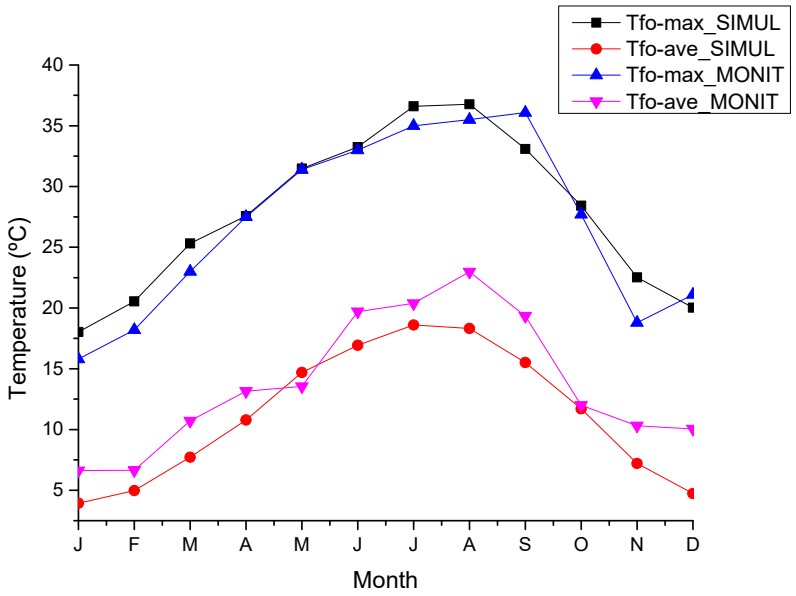

Figure 6.22. Comparison of the maximum and average monthly values of the outlet air temperature for the calculated and measured data.

Overall, there is a good agreement between the simulation and measured data. The total numbers and the estimated percentage differences are shown in Table 6.4. The annual estimated energy production from the system is very close to the measured one. However, in monthly based data the amount of energy is different. This is because the TMY data are usually used for mean annual performance evaluation of thermal systems and does not necessarily coincide with the actual weather data for

particular days. The PRE between the predicted and measured energy production of the system for one year is 1.46% which is very small. This means that the model with type 566 of TRNSYS can representatively predict the annual energy performance of a BIPV system when the various modification regarding the air gap design are made. As previously mentioned, Type 566 is designed to simulate a forced convection system, while in this study, the values of the CHTC are imported manually considering natural ventilation.

Table 6.4. Comparison between the simulation and measured data and the estimated percentage relative error (PRE).

	Simulation	**Measured**	**PRE**
1 year energy production	9507.40 kWh	9648.2 kWh	1.46%
Maximum PV Temperature	67^{o}C	64^{o}C	4.47%
Maximum Outlet Air Temperature	36.7^{o}C	36.1^{o}C	1.66%
Most productive month	July	July	-
Less Productive month	December	February	-

CHAPTER 7

7 Conclusions

The most important outcomes of this study are summarized below:

- A successful heat transfer analysis of the system is carried out and the thermal behaviour of the system is recorded.
- The correlations can be used from the engineers to predict the temperature of the systems and take measures to avoid overheating as well as to estimate the thermal resistances of the construction materials with BIPV.
- Two correlations for the estimation of the Nusselt number in the air gap between the PV panel and the back wall are derived. One for no wind conditions and one for windy conditions.
- At the end, the no-wind correlation is proposed to be used in estimating the thermal conditions of the system and carry out heat transfer analysis when the ventilation of the system is completely dependent on buoyancy forces. However, the engineers working on the field should be aware that the CHTC are increased in the case of windy conditions.
- The open-ended air duct of 10 cm formed between the PV panel and the back wall, is adequate to maintain temperatures lower than 75^{o}C at the PV panel under constant solar radiation experiments.
- The high temperatures cause loss of electrical efficiency of the PV panel. It is shown that the power drops 0.4%/^{o}C.

- Considering a BIPV system with one row of PV panels, it is observed that the temperature of the PV panels is not the same at all their surface. The bottom side of the PV panels is cooler than the top because it is affected by the air inlet from the bottom opening of the duct. It is proved that the bottom side of the PV panel is around 10^{o}C lower than the top.
- Having more than one PV one on top of the other, forming one continuous surface, the height of the system is bigger and thus the height of the air duct is bigger as well. From the simulations, it is shown that the higher the system is without any openings between the PVs, the higher is the developed temperature of the PV panels.
- The openings of the duct have an important role on the thermal behaviour of the system. It is important to have both top and bottom openings for better air circulation and to keep the temperature of the system at low levels.
- Buoyancy effect occurs in the system as proved from the indoor experiments. The system developed average air velocity of 0.3 - 0.35 m/s in indoor controlled environmental conditions without external disturbances and wind.
- The PV panel in the system under investigation is isoflux surface but not isothermal, while the wall of the system is isothermal adiabatic surface since its temperature does not change during the exposure of the system at the sun.
- The estimated convective heat transfer coefficients h for any naturally ventilated vertical BIPV system can be used for the building energy efficiency analysis to estimate the energy rates and the U-value estimation of the building's construction components.
- A simulation model which can estimate the temperature distribution of the system under various conditions is developed and verified with real experimental data.
- The air velocity has an important role on the thermal behavior of the system. For air velocity of bigger than about 1 m/s the temperatures of all the system components (PV, air and wall) are almost stable and no further reduction is observed at higher velocities.
- The size of the air gap affects the temperature distribution of the system and the developed air velocity in the duct. An air gap of 10 cm is the optimum to keep the temperature of the PV panel in effective levels concerning power drop.
- The energy efficiency of the system is estimated to be up to 26.5-33.5% while the exergy efficiency is estimated to be between 13-16%.
- A simulation model for annual prediction of energy production of a BIPV system is developed with good prediction of energy production and temperature of the PV panels.
- There is a good agreement between the annual performance simulation data from TRNSYS and the measured data. The annual estimated energy production from the system is very close to

the measured one so the model can be adopted to predict the annual production of the system under different parameters such as the air gap size and the type of ventilation.

Future work

The subject can be further investigated from the following points of view:

- Experimental investigation of a higher BIPV system without openings and with open joints.
- Experimental investigation with PCM in the air gap between the PV panel and the wall.
- Built an experimental BIPV house to test the BIPV system in different orientations and different angles and use it as an energy collector system for space heating as well.
- Carry out economic analysis and LCA of a real BIPV system considering the energy consumption prices, the energy production, the price of the construction materials replaced by the PV panels and the price of the PV system.

Publications from this Study

Journal Publications

- **Pending**

Agathokleous, R.A., Kalogirou, S.A., (2017) 'Part II: Simulation-Based thermal analysis of a Naturally Ventilated BIPV System: A validated model from experimental data'. Submitted in SOLAR ENERGY.

Agathokleous, R.A., Kalogirou, S.A., (2017) 'Part I: Experimental Based thermal analysis of a Naturally Ventilated BIPV System and new correlations for the estimation of the convective heat transfer coefficients'. Submitted in SOLAR ENERGY.

- **Published**

Agathokleous, R.A., Kalogirou, S.A., (2017). Simulation-Based Investigation of the Air Velocity in a Naturally Ventilated BIPV System. In: Visa, I., Duta, A. (Eds.), Nearly Zero Energy Communities. CSE 2017. Springer Proceedings in Energy. Springer, Cham, pp. 201–217.

Kyritsis, A., Roman, E., Kalogirou, S.A., Nikoletatos, J., **Agathokleous, R.,** Mathas, E., Tselepis, S., (2017). Households with Fibre Reinforced Composite BIPV modules in Southern Europe under Net Metering Scheme. Renew. Energy.

Agathokleous, R.A., Kalogirou, S.A., Karellas, S., (2017). Exergy analysis of a naturally ventilated Building Integrated Photovoltaic/Thermal (BIPV/T) system. Renew. Energy.

Agathokleous, R.A., Kalogirou, S.A., (2016). Double skin facades (DSF) and building integrated photovoltaics (BIPV): A review of configurations and heat transfer characteristics. Renew. Energy 89, 743–756.

Peer Review Conferences

Agathokleous, R., Kalogirou, S.A., (2017). 'A Building Integrated Photovoltaic (BIPV) Demonstration Building in Belgium: Analysis with Simulation and Monitoring data', *Proceedings of SDEWES 2017,* Dubrovnik, Croatia.

Agathokleous, R., Kalogirou, S.A., (2017). 'Simulation Based Investigation of the air velocity in a Double Skin Naturally Ventilated BIPV System', *Proceedings of CSE 2017*, Brasov, Romania.

Agathokleous, R., Kalogirou, S.A., Karellas, S., (2017). 'Convective heat transfer coefficients of a naturally ventilated building integrated photovoltaic (BIPV) system', *Proceedings of ECOS 2017*, San Diego, California.

Agathokleous, R., Kalogirou, S.A., (2017). 'A Passive House with Building Integrated Photovoltaic (BIPV) system', *Preoceedings of Savenergy 2017*, Nicosia, Cyprus.

Agathokleous, R., Kalogirou, S.A., Pierret, S., (2017). 'A Building Integrated Photovoltaic (BIPV) demonstration building in Belgium with new Fibre Reinforced Solar Technology PV modules: Analysis with Simulation and Monitoring data', *Proceedings of BIRES2017*, Dublin, Ireland.

Agathokleous, R., Kalogirou, S.A., (2017). 'Thermal testing of a new photovoltaic (PV) module for building integration encapsulated with glass fibre reinforced composite materials and comparison with conventional Photovoltaic', *Proceedings of BIRES2017*, Dublin, Ireland.

Agathokleous, R., Kalogirou, S.A., (2017). 'Energy Investigation on households with BIPV modules under Net Metering Scheme', *Proceedings of BIRES2017*, Dublin, Ireland.

Agathokleous, R., Kalogirou, S.A., (2016). 'Thermal Analysis of a Building Integrated Photovoltaic (BIPV) system', *Proceedings of ECOS2016*, Portorož, Slovenia.

Agathokleous, R., Kalogirou, S.A., (2016). 'Exergy analysis of a Naturally Ventilated Building Integrated Photovoltaic (BIPV) System', *Proceedings of ECOS2016*, Portorož, Slovenia.

Agathokleous, R., Kalogirou, S.A., (2014). 'Indoor Testing of Solar Systems: A Solar Simulator for Multidisciplinary Research on Solar Technologies', *Proceedings of PRES, CHISA 2014,* Prague, Czech Republic.

Agathokleous, R., Kalogirou, S.A., (2014). 'The Effect of the Air Flow on the Temperature of the PV Panel Examined for Two BIPV Panels of Different Shape', *Proceedings of PRES, CHISA 2014,* Prague, Czech Republic.

Kalogirou, S.A., **Agathokleous, R**., Florides, G., Aresti, L., (2013). 'Air flow effect on the temperature of a building integrated PV-panel', *Proceedings of 2013 COMSOL Conference,* Rotterdam, Netherlands

References

Agathokleous, R.A., Kalogirou, S.A., (2016). Double skin facades (DSF) and building integrated photovoltaics (BIPV): A review of configurations and heat transfer characteristics. Renew. Energy 89, 743–756.

Al-Kayiem, H.H., Yassen, T.A., (2015). On the natural convection heat transfer in a rectangular passage solar air heater. Sol. Energy 112, 310–318.

Arons, D.M.M., Glicksman, L.., (2001). Double Skin, Airflow Facades: will the Popular European Model work in the USA? In: International Conference on Building Envelope Systems and Technologies. Ottawa, Canada, pp. 203–207.

Ayyaswamy, P.., Catton, N., (1973). The Boundary-Layer Regime for Natural Convection in a Differentially Heated, Tilted Rectangular Cavity. J. Heat Transfer 95, 116–123.

Bahrehmand, D., Ameri, M., (2015). Energy and exergy analysis of different solar air collector systems with natural convection. Renew. Energy 74, 357–368.

Bar-Cohen, A., Rohsenow, W.M., (1984). Thermally Optimum Spacing of Vertical, Natural Convection Cooled, Parallel Plates. J. Heat Transfer.

Barbosa, S., Ip, K., (2014). Perspectives of double skin façades for naturally ventilated buildings: A review. Renew. Sustain. Energy Rev. 40, 1019–1029.

Bazilian, M.D., Kamalanathan, H., Prasad, D.K., (2002). Thermographic analysis of a building integrated photovoltaic system. Renew. Energy 26, 449–461.

BBRI (Belgian Building Research Unit), (2002). Source book for a better understanding of conceptual and operational aspects of active facades.

Benemann, J., Chehab, O., Schaar-Gabriel, E., (2001). Building-integrated PV modules. Sol. Energy Mater. Sol. Cells 67, 345–354.

Boake, T.M., (2003). The Tectonics of the Environmental Skin. Canada.

Bosanac, M., Sørensen, B., Katic, I., Sørensen, H., Nielsen, B., Badran, J., (2003). Final Report EFP project 1713 / 00-0014 Photovoltaic / Thermal Solar Collectors and Their Potential in Denmark, Solar Energy.

Brinkworth, B.., (2000). Estimation of flow and heat transfer for the design of PV cooling ducts. Sol. Energy 69, 413–420.

Brinkworth, B.., Cross, B.., Marshall, R.., Yang, H., (1997). Thermal regulation of photovoltaic cladding. Sol. Energy 61, 169–178.

Brinkworth, B.J., (2006). Optimum depth for PV cooling ducts. Sol. Energy 80, 1131–1134.

Brinkworth, B.J., Marshall, R.H., Ibarahim, Z., (2000). A validated model of naturally ventilated PV cladding. Sol. Energy 69, 67–81.

Brinkworth, B.J., Sandberg, M., (2006). Design procedure for cooling ducts to minimise efficiency loss due to temperature rise in PV arrays. Sol. Energy 80, 89–103.

Brown, L., (2009). Mobilizing to save civilization. Norton & Co, New York.

Candanedo, L.M., Athienitis, A., Park, K.-W., (2011). Convective Heat Transfer Coefficients in a Building-Integrated Photovoltaic/Thermal System. J. Sol. Energy Eng. 133, 21002.

Candanedo, L.M., Athienitis, a K., Candanedo, J. a, O'Brien, W., Chen, Y.X., (2010). Transient and steady state models for open loop air based BIPV/T Systems. ASHRAE Trans. 116, 13.

Catton, I., (1978). Natural Convection in Enclosures. In: 6th International Heat Transfer Conference. pp. 13–31.

Cengel, Y.A., Ghajar, A.J., (2011). Heat and Mass Transfer: Fundamentals and Applications, Fourth Edi. ed. Mc Graw Hill Higher Education, New York.

Cerón, I., Caamaño-Martín, E., Neila, F.J., (2013). "State-of-the-art" of building integrated photovoltaic products. Renew. Energy 58, 127–133.

Ceylan, I., Gurel, A.E., (2015). Exergetic Analysis of a new design photovoltaic and thermal (PV/T) System. Environ. Prog. Sustain. Energy 34, 1249–1253.

Chow, T.T., Pei, G., Fong, K.F., Lin, Z., Chan, A.L.S., Ji, J., (2009). Energy and exergy analysis of photovoltaic–thermal collector with and without glass cover. Appl. Energy 86, 310–316.

Churchill, S.W., Chu, H.H.S., (1975). Correlating equations for laminar and turbulent free convection from a vertical plate. Int. J. Heat Mass Transf. 18, 1323–1329.

Compagno, A., (2002). Intelligent Glass Facades (5th revised and updated edition). Berlin: Birkhäuser.

Crespo, A.M.., (1999). History of Double Skin Facades.

Dittus, F.W., Boelter, L.M., (1930). Heat Transfer in Automobile Radiators of the Tubular Type. Publ. Eng. 2, 443.

Dubey, S., Solanki, S.C., Tiwari, A., (2009). Energy and exergy analysis of PV/T air collectors connected in series. Energy Build. 41, 863–870.

Duffie, J.A., Beckman, W.A., (1980). Solar Engineering of Thermal Processes, 2nd Edition.

Eicker, U., Fux, V., Infield, D., Mei, L., Vollmer, K., (1999). Thermal performance of building integrated ventilated PV façades. In: Proceedings of the ISES Solar World Congress.

ElSherbiny, S.M., Raithby, G.D., Hollands, K.G.T., (1982). Heat transfer by natural convection across vertical and inclined air layers. J. Heat Transf. Trans. ASME 104, 96–102.

eurima, (2011). U-values in Europe [WWW Document]. URL http://www.eurima.org/resource-centre/facts-figures/u-values-in-europe.html

European Commission, (2014a). The 2020 climate and energy package [WWW Document]. Europa.

European Commission, (2014b). Energy Efficiency in Buildings [WWW Document]. Europa.

European Commission, (2014c). Constuction of Products (CPD/CPR) [WWW Document]. Europa. URL http://ec.europa.eu/growth/single-market/european-standards/harmonised-standards/construction-products/index_en.htm (accessed 5.13.14).

European Standard EN 673, (1997). Glass in building: Determination of Thermal Transmittance (U value): Calculation Method, European Committee for Standardization.

Eurostat, (2016). Final energy consumption, EU-28, 2015(% of total, based on tonnes of oil equivalent) [WWW Document]. Eur. Comm. URL http://ec.europa.eu/eurostat/statistics-explained/index.php/File:Final_energy_consumption,_EU-28,_2015_(%25_of_total,_based_on_tonnes_of_oil_equivalent)_YB17.png

Famous Quotations, (2014). Famous Quotations from Thomas Edison [WWW Document]. URL http://www.thomasedison.org/index.php/education/edison-quotes/ (accessed 5.10.14).

Fossa, M., Ménézo, C., Leonardi, E., (2008). Experimental natural convection on vertical surfaces for building integrated photovoltaic (BIPV) applications. Exp. Therm. Fluid Sci. 32, 980–990.

Friedman, T., (2008). Hot, flat and Crowded: Why we need a green revolution- and How It Can Renew America. Farrar, Straus and Giroux; 1 edition.

Fujisawa, T., Tani, T., (1997). Annual exergy evaluation on photovoltaic-thermal hybrid collector. Sol. Energy Mater. Sol. Cells 47, 135–148.

Fux, V., (2006). Thermal simulation of ventilated PV facades. Loughborough Universit.

Gaillard, L., Ménézo, C., Giroux, S., Pabiou, H., Le-Berre, R., (2014). Experimental Study of Thermal Response of PV Modules Integrated into Naturally-ventilated Double Skin Facades. Energy Procedia 48, 1254–1261.

Gan, G., (2009). Effect of air gap on the performance of building-integrated photovoltaics. Energy 34, 913–921.

Gnielinski, V., (1976). New Equations for Heat and Mass Transfer in Turbulent Pipe and Channel Flow. Int. Chem. Eng. 16, 359–367.

Gratia, E., De Herde, A., (2004). Natural ventilation in a double-skin facade. Energy Build. 36, 137–146.

Haleakala Solar, (2014). Brief History of Solar and Hawaii Photovoltaic Highlights [WWW Document]. URL http://www.haleakalasolar.com/hawaii-solar/brief-history-of-solar-hawaii-photovoltaic-highlights/ (accessed 7.8.15).

Hamza, N., (2008). Double versus single skin facades in hot arid areas. Energy Build. 40, 240–248.

Hepbasli, A., (2008). A key review on exergetic analysis and assessment of renewable energy resources for a sustainable future. Renew. Sustain. Energy Rev. 12, 593–661.

Hien, W.N., Liping, W., Chandra, A.N., Pandey, A.R., Xiaolin, W., (2005). Effects of double glazed facade on energy consumption, thermal comfort and condensation for a typical office building in Singapore. Energy Build. 37, 563–572.

Hollands, K.G.T., Unny, T.E., Raithby, G.D., Konicek, L., (1976). Free Convective Heat Transfer Across Inclined Air Layers. J. Heat Transfer 98, 189.

Høseggen, R., Wachenfeldt, B.J., Hanssen, S.O., (2008). Building simulation as an assisting tool in decision making. Case study: With or without a double-skin façade? Energy Build. 40, 821–827.

Jafarkazemi, F., Ahmadifard, E., (2013). Energetic and exergetic evaluation of flat plate solar collectors. Renew. Energy 56, 55–63.

Jeter, S.M., (1981). Maximum conversion efficiency for the utilization of direct solar radiation. Sol. Energy 26, 231–236.

Joshi, A.S., Tiwari, A., (2007). Energy and exergy efficiencies of a hybrid photovoltaic–thermal (PV/T) air collector. Renew. Energy 32, 2223–2241.

Kaiser, A.S., Zamora, B., Mazón, R., García, J.R., Vera, F., (2014). Experimental study of cooling BIPV modules by forced convection in the air channel. Appl. Energy 135, 88–97.

Kalogirou, S.A., (2014). Solar Energy Engineering Processes and Systems, 2nd ed. Academic Press.

Kalogirou, S.A., Karellas, S., Badescu, V., Braimakis, K., (2015). Exergy analysis on solar thermal systems: A better understanding of their sustainability. Renew. Energy 85, 1328–1333.

Kalogirou, S.A., Karellas, S., Braimakis, K., Stanciu, C., Badescu, V., (2016). Exergy analysis of solar thermal collectors and processes. Prog. Energy Combust. Sci. 56, 106–137.

Kalogirou, S., Agathokleous, R., Panayiotou, G., (2013). On-site PV characterization and the effect of soiling on their performance. Energy 51, 439–446.

Kragh, M., (2000). Monitoring of Advanced Facades and Environmental Systems. Bath, UK.

La Pica, A., Rodonò, G., Volpes, R., (1993). An experimental investigation on natural convection of air in a vertical channel. Int. J. Heat Mass Transf. 36, 611–616.

Lau, G.E., Sanvicente, E., Yeoh, G.H., Timchenko, V., Fossa, M., Ménézo, C., Giroux-Julien, S., (2012a). Modelling of natural convection in vertical and tilted photovoltaic applications. Energy Build. 55, 810–822.

Lau, G.E., Yeoh, G.H., Timchenko, V., Reizes, J. a., (2012b). Numerical investigation of passive cooling in open vertical channels. Appl. Therm. Eng. 39, 121–131.

Lee, E., Selkowitz, S., Bazjanac, V., Inkarojrit, V., Kohler, C., (2002). High-Performance Commercial Building Façades.

Li, S., Karava, P., (2012). Evaluation of turbulence models for airflow and heat transfer prediction in BIPV/T systems optimization. Energy Procedia 30, 1025–1034.

Linfield, K.W., Mudry, R.G., (2008). Pros and Cons of CFD and Physical Flow Modeling. Livonia, USA.

Loncour, X., Deneyer, A., Blasco, M., Flamant, G., Wouters, P., (2004). Ventilated double facades – Classification & Illustration of façade concepts.

Luque, A., Hegedus, S., (2003). Handbook of Photovoltaic Science and Engineering. John Wiley & Sons Ltd.

Manz, H., (2003). Numerical simulation of heat transfer by natural convection in cavities of facade elements. Energy Build. 35, 305–311.

Manz, H., Frank, T., (2005). Thermal simulation of buildings with double-skin façades. Energy Build. 37, 1114–1121.

Mei, L., Infield, D., Eicker, U., Fux, V., (2003). Thermal modelling of a building with an integrated

ventilated PV facade. Energy Build. 35, 605–617.

Mercer, W.E., Pearce, W.M., Hithcock, J.E., (1967). Laminar forced convection in the entrance region between parallel flat plates. J. Heat Transfer 89, 251–257.

Multiphysics Cyclopedia [WWW Document], (2017). URL https://www.comsol.com/multiphysics (accessed 5.1.17).

Nayak, S., Tiwari, G.N., (2008). Energy and exergy analysis of photovoltaic/thermal integrated with a solar greenhouse. Energy Build. 40, 2015–2021.

Oztop, H.F., Bayrak, F., Hepbasli, A., (2013). Energetic and exergetic aspects of solar air heating (solar collector) systems. Renew. Sustain. Energy Rev. 21, 59–83.

Park, S.R., Pandey, A.K., Tyagi, V.V., Tyagi, S.K., (2014). Energy and exergy analysis of typical renewable energy systems. Renew. Sustain. Energy Rev. 30, 105–123.

Peng, C., Huang, Y., Wu, Z., (2011). Building-integrated photovoltaics (BIPV) in architectural design in China. Energy Build. 43, 3592–3598.

Petela, R., (1964). Exergy of Heat Radiation. J. Heat Transfer 86, 187–192.

Physics, (2014). Rayleigh -Benard and Benard-Marangoni convection [WWW Document].

Probst, M.C., (2008). Architectural integration and design of solar thermal systems. ÉCOLE POLYTECHNIQUE FÉDÉRALE DE LAUSANNE.

Probst, M.C., Roecker, C., (2012). Solar Energy Systems in Architecture, integration criteria and guidelines.

pve photovoltaik engineering, (2017). PVPM2540C [WWW Document]. URL http://pv-engineering.de/en/products/standard-titel/?tt_products%5Bproduct%5D=1&tt_products%5Bcat%5D=1&cHash=200b1894cbdf303facdd1750b187ded4 (accessed 5.20.05).

Quesada, G., Rousse, D., Dutil, Y., Badache, M., Hallé, S., (2012). A comprehensive review of solar facades. Transparent and translucent solar facades. Renew. Sustain. Energy Rev. 16, 2643–2651.

Redchalksketch, (2011). Sydney's first major "double-skin" high-rise [WWW Document]. Redchalksketch. URL http://redchalksketch.wordpress.com/category/facade/page/4/ (accessed 1.1.15).

Rohsenow, W.M., Hartnett, J.P., Cho, Y.I., (1998). Handbook of Heat Transfer.

Saelens, D., (2002). Energy Performance Assessments of Single Storey Multiple-Skin Facades. KATHOLIEKE UNIVERSITEIT LEUVEN.

Saelens, D., Blocken, B., Roels, S., Hens, H., (2005). Optimization of the Energy Performance of Multiple-Skin Facades. In: Ninth International IBPSA Conference,. Montreal, Canada, pp. 15–18.

Saidur, R., BoroumandJazi, G., Mekhlif, S., Jameel, M., (2012). Exergy analysis of solar energy applications. Renew. Sustain. Energy Rev. 16, 350–356.

Saitoh, H., Hamada, Y., Kubota, H., Nakamura, M., Ochifuji, K., Yokoyama, S., Nagano, K., (2003). Field experiments and analyses on a hybrid solar collector. Appl. Therm. Eng. 23, 2089–2105.

Saloux, E., Teyssedou, A., Sorin, M., (2013). Analysis of photovoltaic (PV) and photovoltaic/thermal (PV/T) systems using the exergy method. Energy Build. 67, 275–285.

Sandberg, M., Moshfegh, B., (2002). Buoyancy-induced air flow in photovoltaic facades. Build. Environ. 37, 211–218.

Sanjuan, C., Sánchez, M.N., Enríquez, R., Del Rosario Heras Celemín, M., (2012). Experimental PIV techniques applied to the analysis of natural convection in open joint ventilated facades. Energy Procedia 30, 1216–1225.

Sanjuan, C., Sánchez, M.N., Heras, M.D.R., Blanco, E., (2011a). Experimental analysis of natural convection in open joint ventilated façades with 2D PIV. Build. Environ. 46, 2314–2325.

Sanjuan, C., Suárez, M.J., Blanco, E., Heras, M.D.R., (2011b). Development and experimental validation of a simulation model for open joint ventilated façades. Energy Build. 43, 3446–3456.

Sanjuan, C., Suárez, M.J., González, M., Pistono, J., Blanco, E., (2011c). Energy performance of an open-joint ventilated façade compared with a conventional sealed cavity façade. Sol. Energy 85, 1851–1863.

Santos, Í.P. Dos, Rüther, R., (2012). The potential of building-integrated (BIPV) and building-applied photovoltaics (BAPV) in single-family, urban residences at low latitudes in Brazil. Energy Build. 50, 290–297.

Sanvicente, E., Giroux-Julien, S., Ménézo, C., Bouia, H., (2013). Transitional natural convection flow and heat transfer in an open channel. Int. J. Therm. Sci. 63, 87–104.

Sarhaddi, F., Farahat, S., Ajam, H., Behzadmehr, A., (2010). Exergetic performance assessment of a solar photovoltaic thermal (PV/T) air collector. Energy Build. 42, 2184–2199.

Schittich, C., (2003). Solar Architecture: Strategies, Visions, Concepts. Birkhauser.

Scognamiglio, A., Røstvik, H.N., (2012). Photovoltaics and zero energy buildings: a new opportunity and challenge for design. In: 27TH EU PVSEC. Frankfurt, Germany, pp. 1319–1336.

Selkowitz, S.E., (1978). Thermal Performance of insulating Window systems. ASHRAE Trans. 85.

Shahsavar, A., Ameri, M., Gholampour, M., (2012). Energy and Exergy Analysis of a Photovoltaic-Thermal Collector With Natural Air Flow. J. Sol. Energy Eng. 134, 11014.

Sharples, S., Charlesworth, P.S., (1998). Full-scale measurements of wind-induced convective heat transfer from a roof-mounted flat plate solar collector. Sol. Energy 62, 69–77.

Single Aspects, (2014). Sustaining: Tower Blocks [WWW Document]. Single Asp. URL http://singleaspect.org.uk/sustower/SOA-present.htm (accessed 1.1.15).

Spanner, D.C., (1964). Introduction to Thermodynamics. Academic Press, London New York.

Sparrow, E.M., Azevedo, L.F. a., (1985). Vertical-channel natural convection spanning between the fully-developed limit and the single-plate boundary-layer limit. Int. J. Heat Mass Transf. 28, 1847–1857.

Streicher, W., Heimrath, R., Hengsberger, H., Mach, T., Waldner, R., Flamant, G., Loncour, X., Guarracino, G., Erhorn, H., Erhorn-Kluttig, H., Santamouris, M., Farou, I., Duarte, R., Blomsterberg, Å., Sjöberg, L., Blomquist, C., (2004). State of the Art of Double Skin Facades in Europe:The results of WP1 of the BESTFACADE Project.

Tan, H.M., Charters, W.W.S., (1970). An experimental investigation of forced-convective heat transfer for fully-developed turbulent flow in a rectangular duct with asymmetric heating. Sol. Energy 13, 121–125.

TESS, (2014). Component Libraries General Descriptions 1–76.

Test, F.L., Lessmann, R.C., Johary, a., (1981). Heat Transfer During Wind Flow over Rectangular Bodies in the Natural Environment. J. Heat Transfer 103, 262.

The Eppley Laboratory, (2017). Eppley: A complete Eppley Solar Station [WWW Document]. URL http://www.eppleylab.com/ (accessed 6.20.05).

Thomas, R., (2001). Photovoltaics and architecture. Spon press, London, UK.

Tiwari, G.N., (2002). Solar Energy, Fundamentals, Design, Modelling and Applications. Narosa Publishing House, New Delhi.

Tonui, J.K., Tripanagnostopoulos, Y., (2008). Performance improvement of PV/T solar collectors with natural air flow operation. Sol. Energy 82, 1–12.

TRNSYS17, (2012). TRNSYS 17 Reference Manual.

Uuttu, S., (2001). Study of Current Structures in Double-Skin Facades. Helsinki University of Technology (HUT).

Versteeg, H.K., Malalasekera, W., (1995). An introduction to computational fluid dynamics. Longman Scientific & Technical.

Wang, Y., Tian, W., Ren, J., Zhu, L., Wang, Q., (2006). Influence of a building's integrated-photovoltaics on heating and cooling loads. Appl. Energy 83, 989–1003.

Wright, J.L., (1996). A correlation to quantify convective heat transfer between vertical window glazings. ASHRAE Trans. 106, 940–946.

Xamán, J., Álvarez, G., Lira, L., Estrada, C., (2005). Numerical study of heat transfer by laminar and turbulent natural convection in tall cavities of façade elements. Energy Build. 37, 787–794.

Yang, T., Athienitis, A.K., (2014). A study of design options for a building integrated photovoltaic/thermal (BIPV/T) system with glazed air collector and multiple inlets. Sol. Energy 104, 82–92.

Yin, S.H., Wung, T.Y., Chen, K., (1978). Natural convection in an air layer enclosed within rectangular cavities. Int. J. Heat Mass Transf. 21, 307–315.

Zhao, Y., Goss, W.P., Curcija, D., Power, J.P., (1997). New Set of Analytical correlations for Predicting Convective Heat Transfer in Fenestration Glazing Cavities. Proc. CLIMA 2000 305–316.

Zogou, O., Stapountzis, H., (2011a). Energy analysis of an improved concept of integrated PV panels in an office building in central Greece. Appl. Energy 88, 853–866.

Zogou, O., Stapountzis, H., (2011b). Experimental validation of an improved concept of building integrated photovoltaic panels. Renew. Energy 36, 3488–3498.

Zogou, O., Stapountzis, H., (2012). Flow and heat transfer inside a PV/T collector for building application. Appl. Energy 91, 103–115.

Zöllner, a., Winter, E.R.F., Viskanta, R., (2002). Experimental studies of combined heat transfer in turbulent mixed convection fluid flows in double-skin-façades. Int. J. Heat Mass Transf. 45, 4401–4408.

Zondag, H.A., (2008). Flat-plate PV-Thermal collectors and systems: A review. Renew. Sustain. Energy Rev. 12, 891–959.

Rafaela Agathokleous

rafaela.agathokleous@cut.ac.cy